Design, Development and Performance Investigations of High-Temperature Latent Heat Storage Systems

A thesis submitted in partial fulfilment of the requirements for the degree

of

DOCTOR OF PHILOSOPHY

Submitted by

GURPREET SINGH SODHI

(Roll No. 156103007)

DEPARTMENT OF MECHANICAL ENGINEERING

INDIAN INSTITUTE OF TECHNOLOGY, GUWAHATI

GUWAHATI-781039, ASSAM, INDIA

JUNE 2021

Indian Institute of Technology Guwahati
Department of Mechanical Engineering
Guwahati-781039, Assam, India

STATEMENT

This is to certify that the research work presented in this thesis entitled “Design, Development and Performance Investigations of High-Temperature Latent Heat Storage Systems” has been carried out by me at the Department of Mechanical Engineering, Indian Institute of Technology Guwahati, under the esteemed supervision of Prof. P. Muthukumar.

I hereby confirm that there is no conflict of interest related to the research work and the results documented in this thesis are achieved by me and have not been submitted to any other Institute or University for the award of any other degree or diploma.

In keeping up with the general practice of reporting scientific observations, due acknowledgements have been made wherever the work described is based on the findings of other investigations.

(Gurpreet Singh Sodhi)

Roll No.: 156103007
Department of Mechanical Engineering
Indian Institute of Technology Guwahati
Guwahati-781039, Assam, India
June 2021

Indian Institute of Technology Guwahati
Department of Mechanical Engineering
Guwahati-781039, Assam, India

THESIS CERTIFICATE

This is to certify that the work contained in this thesis entitled "Design, Development and Performance Investigations of High-Temperature Latent Heat Storage Systems" submitted by **Mr. Gurpreet Singh Sodhi** (Roll. No. 156103007) for the award of Ph.D. degree, is a record of bonafide research carried out by him at the Department of Mechanical Engineering, Indian Institute of Technology Guwahati, under my guidance and supervision. The work embodied in this thesis has not been submitted to any other University or Institute for the award of any other degree or diploma.

(Prof. P. Muthukumar)

Professor

Department of Mechanical Engineering
Indian Institute of Technology Guwahati
Guwahati-781039, Assam, India
June 2021

Dedicated

to

my father

Lt. S. Bikramjit Singh Sodhi

Acknowledgements

I would like to express my deepest gratitude to my supervisor Prof. P. Muthukumar, whose sincere guidance has brought me this far and successfully complete my thesis. His esteemed guidance and encouragement has always inspired me to think critically and work with complete devotion. I feel fortunate to be working in a conducive environment where he has always provided me with a free hand to explore different aspects of my research. At the same time, he has provided me with precious inputs and ideas to work persistently and achieve my research objectives. He has always lent me his experience which will be an innumerable asset for the rest of my career.

I want to express my appreciation to the Ministry of Human Resource Development, Government of India, for their constant support in the form of Ph.D. Scholarship through IIT Guwahati. The research in this thesis is funded by the Department of Science and Technology (DST), Government of India, and I am grateful for their financial support (Project No: DST/TMD/SERI/D12(C)).

I would like to thank my thesis supervisor, the head of the department at Mechanical Engineering and the Indian Institute of Guwahati to permit me for a 12 weeks visit to conduct research at the Laboratory for Alternative Energy Conversion (LAEC), Simon Fraser University (SFU), Surrey, Canada upon receiving the MITACS graduate research fellowship. My stay at SFU was further extended under the Queen Elizabeth Scholarship-Advanced Scholars (QES-AS) Program due to the consistent support from my thesis supervisor and the institute to sanction me the leave extension. I am highly grateful to MITACS and QES-AS for funding my research at Canada. The research at LAEC was carried out under the guidance of Prof. Majid Bahrami. I am obliged to him for his mentorship and providing me with the opportunity to work at his revered lab facility. I would like to thank all the lab colleagues at LAEC for their support during my visit.

I am thankful to my doctoral committee members Prof. Niranjan Sahoo, Dr. Amaresh Dalal and Dr. R. Anandalakshmi for their continuous support and encouragement during the course of my PhD. I am also grateful to Dr. S. Senthilmurugan, Department of Chemical Engineering, under whose mentorship I have spent some useful time while carrying out joint research with his students. I highly appreciate the head of the departments and the office bearers (ex and present) in the Department of Mechanical Engineering for imparting the facilities to carry out the research and providing conference visit grants. The support from the technicians and staff at the central workshop, IIT Guwahati was unparalleled. I specially thank Mr. N.K. Das, Mr. Dilip Chetri, Mr. Mrinal Sarma, Mr. Nip Borah and Mr. Jogan Nath for their consistent support while fabricating the experimental setup and conducting experiments.

My journey at IIT Guwahati has been joyful, thanks to my colleagues at Prof. P. Muthukumar's lab. I would like to thank my colleagues Dr. K. Vigneshwaran, Dr. US Hakeem Niyas, Dr. C.R.C. Rao, Mr. Sureandhar Guna, Mr. Nithin Narmada, Mr. Jenne Sunku Prasad, Mr. Tat Suraj and Mr. Umapathi and all other lab mates for their support and suggestions. I would like to give a special thanks to past Masters (M-Tech) student under Prof. P. Muthukumar's supervision, Mr. Bhuwanesh Kumar, Mr Abhishek Kumar and Mr. Vishnu Kumar who have always cooperated and provided their invaluable assistance while conducting the research work. I also extend my gratitude to my mentor Dr. Vijender Singh who motivated me to join the Ph.D. program.

Finally, I give my heartiest gratitude and obedience to my family members for their support, encouragement and eternal love. I thank my parents, Lt. S. Bikramjit Singh Sodhi and Mrs. Rajinder Kaur, my brother and his family for believing in me and supporting me in my adverse times. I also thank the rest of my family and fraternity outside IIT Guwahati.

Sincerely,

GURPREET SINGH SODHI

June 2021

Abstract

The demand and supply of energy go hand in hand, however, major consequences of the increasing energy demands are the depletion of fossil fuel reserves and their impact on the environment. In the current scenario, the energy sector is plausibly dependent upon natural resources for minimizing the instability in the market. Among all the renewable energy resources, solar energy is one of the most prominent sources due to its ample availability and use in numerous applications such as thermal comfort in buildings, solar water heating, solar cooking, solar drying and power generation.

Due to the intermittent nature of solar energy, it cannot meet a continuous supply and storage of energy becomes essential. Thermal energy storage (TES) acts as a temporary reservoir to store energy and assist the operation of the application system during peak demand. This enables stable grid performance added with a decreased reliance on non-renewable energy resources. Concentrated solar power (CSP) technology integrated with TES is a promising solution to develop a stand-alone renewable power generation system. Thermal energy can be stored by various methods; Sensible, Latent and Thermochemical storage. Among all, latent heat storage (LHS) is the most customary storage technique due to its relatively high energy density and a wide range of operating temperatures. LHS systems use phase change materials (PCMs) which absorb the energy due to phase change for energy storage. The isothermal behaviour of phase change leads to a stable power output delivered by the PCMs. Since the thermal conductivity of most PCMs is generally low (0.1-1 W m^{-1} K^{-1}), most of the research works have focused on improving the thermal performance of LHS systems.

The present research work explores the high-temperature LHS systems keeping in mind their integration to applications such as CSP and direct steam generation (DSG). The design, development and performance investigations of high-temperature LHS systems have been scarcely reported in the literature. The thesis work focusses on two major objectives;

(i) Thermal modelling, design, development and testing of high-temperature shell and multi-tube and fin and non-finned encapsulated PCM LHS systems.

(ii) Development of novel LHS system designs to improve the heat transfer rate in conventional high-temperature LHS systems.

To conduct the performance investigations of high-temperature LHS systems, we have designed and developed an experimental test facility at the Indian Institute of Technology Guwahati. The system uses air as the heat transfer fluid (HTF) suitable for maximum operating temperatures and flow rates of 450 ºC and 120 m^3/h, respectively. Sodium nitrate with a melting temperature of 305 ºC is chosen as the PCM. To study the charging and discharging heat transfer behaviour of the LHS system, experimentally validated 2-dimensional (2D), 2D axi-symmetric and 3D numerical models were developed for different geometries using the commercial modelling software COMSOL Multiphysics.

To develop a shell and multi-tube LHS system (storage capacity: ~20 MJ), a 2-dimensional (2D) numerical model was developed to study the heat transfer characteristics of a multi-tube heat exchanger. Three LHS configurations with 13 (1-inch), 17 (3/4-inch) and 25 (1/2-inch) HTF tubes were modelled by fixing the PCM quantity and the HTF tube surface area. The natural convection was neglected for the discharging model. It was found that by increasing the HTF tubes from 13 to 25, the charging and discharging times were reduced by 20% and 48%, respectively. Based on the modelling study, a multi-tube LHS module with 25 HTF tubes was fabricated and experimental investigations were conducted to study the axial/radial temperature distributions, and performance parameters such as charging/discharging time, energy stored/discharged and output power by varying the flow rate and inlet temperature of the air.

To test the performance of high-temperature cylindrical PCM encapsulations (storage capacity: ~0.6 MJ), five different designs were fabricated namely; basic capsule (Case 1), annular capsule (Case 2), annular capsule with straight longitudinal fins (Case 3), annular capsule with tapered longitudinal fins having a decreasing height (Case 4), and annular capsule with tapered longitudinal fins having an increasing height (Case 5). Experimental and numerical investigations were carried out to compare the charging and discharging performances of basic and annular capsules (capsule with hole). The results show that adding a hole in the basic capsule leads to better surface contact due to an increase in the heat transfer area and improves the flow dynamics of the incoming air. Further, experimental investigations were conducted to estimate the charging and discharging performances of all the Cases 1-5 by varying the air inlet flow rate and temperature during charging and discharging.

To improve the charging and discharging heat transfer rates in conventional shell and tube LHS systems, two heat transfer enhancement techniques with simple design modifications such as

effective PCM and fin distribution along the length of conventional shell and tube LHS are proposed.

In the first enhancement technique, the design of the LHS system is modified from a cylindrical shell to a conical shell LHS system. A numerical model of the 3D geometry was developed to analyze the charging and discharging characteristics of both designs. The system comprises of single HTF tube system with Sodium Nitrate as the PCM in the shell side and air as the HTF. The shell dimensions were varied by changing the cone angle and fixing the total PCM volume (or fixed LHS capacity). The conical shell system with a cone angle of 3.4° was found to reduce the charging/discharging times by 17%/28% than the conventional cylindrical shell system. The improvements in the heat transfer rates occur due to the uniform melting and solidification along the system length due to the effective distribution of PCM. Further, the effect of adding straight or tapered fins attached to the HTF tube on the performance of the conical shell system was also analyzed.

In the second enhancement technique, a 2D axi-symmetric numerical model of a vertical shell and tube LHS system comprising of three blocks of PCMs having melting point temperatures (T_m) 360 °C, 335.8 °C and 305.4 °C, respectively, is developed. A non-uniform distribution of fins in three PCM blocks is initially employed to study the performance of the single PCM system ($T_m = 335.8$ °C). The effect of inlet HTF temperature on the charging and discharging performances of the single PCM and multiple PCM (m-PCM) systems were analyzed by varying a Stefan number (Ste_{ref}) parameter, calculated based on the single PCM system. The charging and discharging times for the m-PCM system are either similar or lesser than the single PCM system for $Ste_{ref} \geq 1$, however, there is an improvement of 21-25% in the specific energy charged and discharged by the m-PCM system for all the Ste_{ref} values (0.5, 1, 1.5 and 2) considered. By employing a compound enhancement technique, which is a combination of non-uniform fin-distribution and PCM blocks length ratio optimization for the m-PCM system, 30% and 9% reduction in the charging and discharging time, respectively, over the single PCM system is achieved.

The present thesis work highlights the performance of high-temperature LHS systems. The developed LHS systems can be integrated to high-temperature applications such as CSP and DSG. The important parameters affecting the performance of the LHS system are studied based on experimental and numerical investigations. The research works on high-temperature LHS systems are presently limited and the research output from the present investigations will serve as a benchmark for the development of high-temperature TES devices in the future. The different heat transfer enhancement techniques proposed in the thesis work are simple and can be effectively employed to improve the performances of high-temperature LHS systems.

Nomenclature

A_m	:	Mushy zone constant
c_p	:	Specific Heat [J kg^{-1} K^{-1}]
D_o	:	Shell diameter [m]
d_o	:	Outer tube diameter [m]
g	:	Acceleration due to gravity [m s^{-2}]
Δh_f	:	Latent heat of phase change [J kg^{-1}]
k	:	Thermal conductivity [W m^{-1} K^{-1}]
L_s	:	Length of the system [m]
m	:	Mass [kg]
N	:	Number of HTF tubes
P	:	Power [W]
Q_L	:	Latent heat stored by the PCM [J]
$\dot{Q}$	:	Mass flow rate [m^3 s^{-1}]
T	:	Temperature [K]
t	:	Time [s]

Subscripts/Superscripts

ch	:	charging
dch	:	discharging
in	:	inlet
i	:	initial
L	:	liquid
l	:	local
M	:	melting
max	:	maximum
min	:	minimum
out	:	outlet
ref	:	reference
S	:	solid

Greek Symbols

ρ	:	Density [kg m^{-3}]
δ	:	Melt fraction
μ	:	Dynamic viscosity [Pa s]
β	:	Thermal expansion coefficient [K^{-1}]
ϑ	:	Kinematic viscosity [m^2 s^{-1}]

Abbreviations

CSP	:	Concentrated solar power
DSG	:	Direct steam generation
HTF	:	Heat transfer fluid
LHS	:	Latent heat storage
m.p.	:	Melting point
PCM	:	Phase change material
SHS	:	Sensible heat storage
TES	:	Thermal energy storage

Table of Contents

List of figures

List of Tables

Chapter 1

Introduction

Preface

The world is facing a whammy of crisis in today's date. The COVID19 outbreak has knocked at the doors of the policy makers/governments worldwide to brainstorm and arrive at solutions for a sustainable human life. No wonder the environmental crisis is an ongoing one along with other challenges.

To everyone's good fortune, there has been an adequate response to address the environmental crisis in the past decades. The current investments in green energy have seen a sharp rise and are dominating the energy market. The scientists and researchers worldwide have focused on the development of clean energy technologies to regulate the carbon footprint in the environment.

In this chapter, the background, current status and the future outlook of renewable energy technologies is presented. The role of emerging green technologies such as energy storage, different storage types, conceptualization and their integration with solar thermal technologies such as concentrated solar power is presented.

The thesis work presented here is a small milestone while advancing towards a larger objective.

The ‘Kyoto Protocol’ was adopted in 1997 and most of the developed, industrialized countries had agreed upon the mandate to control the greenhouse gas (GHG) emissions. While some nations, especially the European union (EU) nations had shown positive developments, the others fell short of their targets. A nearly two decades later, recognizing the risks and impacts of the climate change, the ‘Paris Climate Agreement’ of 2015 had asked for the nations globally to work in unison and control the increase in the global average temperature to well below 2 °C compared to pre-industrial levels (REN21, 2019). The global population growth and the energy demands have gone hand in hand in the recent decades (Charriau et al., 2020). Hence, comprehensive efforts are needed to attain the sustainable energy goals.

1.1 Global outlook of energy

Energy is a primary component which binds the ecology and the environment together. Any perturbation in the energy sector has massive impacts on the mankind and the environment. The industrial revolution which happened in the mid-18th century led to historic inventions, however, the human dependency on the non-renewable energy resources increased (Ahuja and Smith, 2016). Fossil fuel reserves have been a major source for satisfying the human energy needs for the past three centuries. Till the late 1990s, coal, natural gas and oil supplied more than 80% of energy worldwide (Kelvii Wei Guo, 2011). The continuous reliance on fossil-fuels has not only exhausted the reserves, but the GHG emissions have had tremendous impacts on the environment.

The climate scientists predicted a 1.3 °C rise in the global temperature between 1850 and 2017 (“Warming Stripes for GLOBE from 1850-2019,”). The CO_2 concentrations in the atmosphere have increased by approximately 27% since 1958 to 400 ppm in 2012 (Farmer and Cook, 2013) and to 414 in 2020 (Copernicus, 2021). The problems of climate change, global warming and their repercussions such as melting of the polar ice, floods and increase in the global temperature have alarmed the nations worldwide. Further, the global electricity consumption has doubled in the last two decades (REN21, 2019). Throughout this time, the majority of this consumption has been observed in Asian countries such as India and China, and the United States.

1.2 Role of renewable energy

Globally, 78% of the GHG emissions are linked with the production or consumption of energy (Natural Resources Canada, 2018-2019). The detrimental impacts of non-renewable energy production have driven a massive quest in the research community to look out for alternatives to fossil fuels. Utilizing the renewable energy resources is a way forward towards achieving sustainable human development. Imbibing this idea, the nations have moved forward and promoted the use of clean technologies.

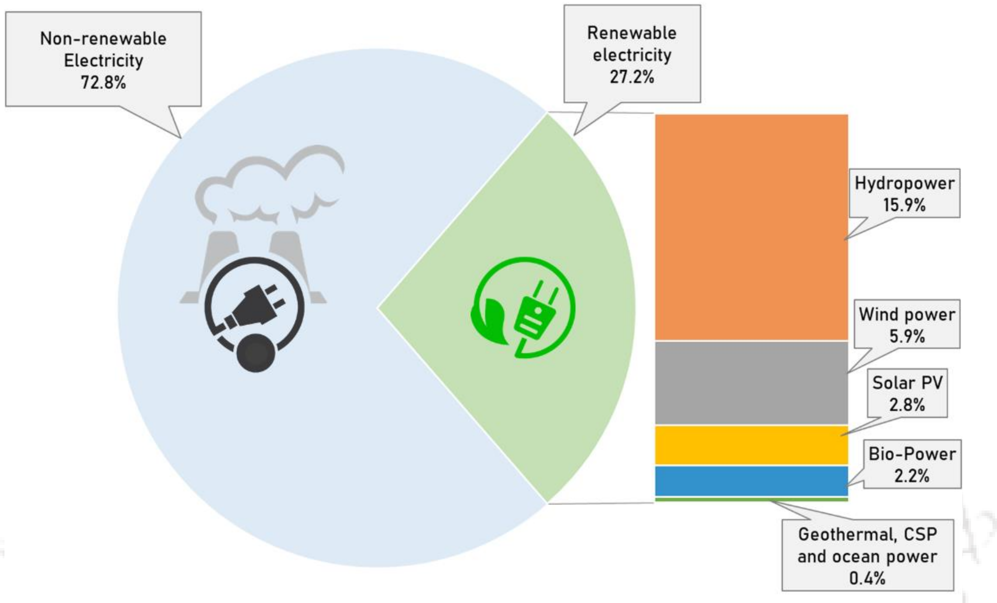

Figure 1.1. Share of renewable and non-renewable electricity production for the year 2019* (REN21, 2020).

In 2019, the global renewable electricity production accounted for approximately 27% as shown in Figure 1.1 (REN21, 2020). The major contributions to renewable electricity were from hydropower, wind and solar photo-voltaic (Solar-PV) technologies. The growth of renewables in electricity production has seen a rising trend over a decade's period (2009-2018) (see Figure 1.2). This has happened due to an upsurge in the development of renewable technologies by the major consumers of energy. In the United States and China, there has been a rise of nearly 31% and 43% in the total yearly renewable electricity production between 2014 and 2018. In India, coal has been the major power generation source from decades, however, the share of renewable electricity was 17.2% in 2017, and 21.1% in 2018, which is not far from the global average (International Energy Agency [IEA], 2019). As per the recent data of the Ministry of New and Renewable Energy, Government of India, the share of renewables out of the total installed generation capacity stands at 23.39% ("MNRE, Govt. of India, 2021").

* The data reported in Figure 1.1 is as per the most recent statistics available.

There have been rapid developments in the renewable energy sector in India, since the declaration of National Determined Contribution (NDC) under the Paris Agreement which aims for 40% power generation from renewables by 2030. The immediate proposal is the installation of 175 GW renewable electricity capacity by 2022, majority of which (approximately 57%) will be accomplished using solar-PV technology. The majority of India's renewable energy production contributions come from hydropower and wind power with installed capacities of 50 GW and 37.2 GW. However, the solar installed capacity has grown at an outstanding pace by nearly twelve times to 32.5 GW in 2019 from 2013 (International Energy Agency [IEA], 2020).

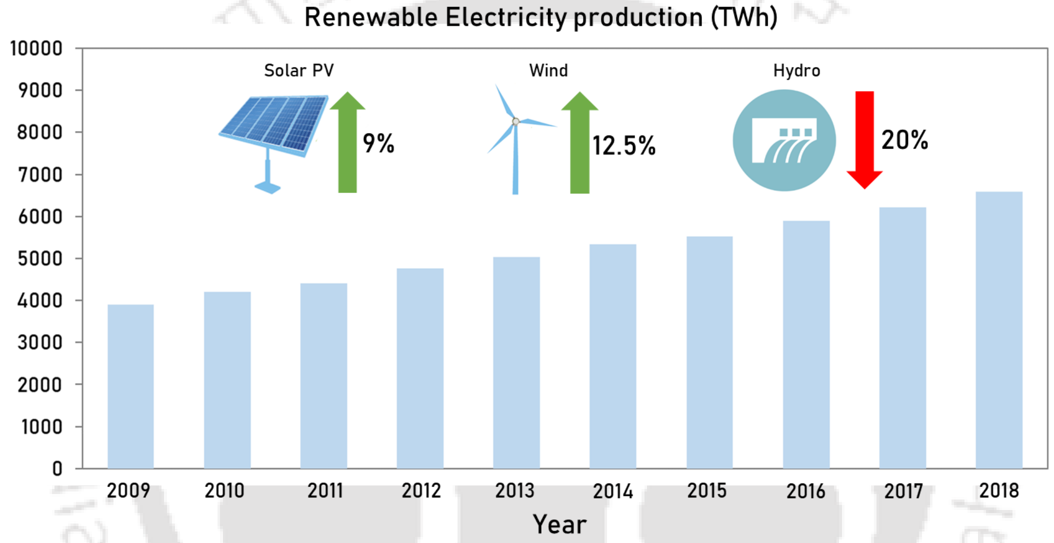

Figure 1.2. Growth in the global renewable electricity (in TWh) production between 2009 to 2018† (International Renewable Energy Agency, 2020).

With a consistent growth in the renewable electricity generation globally, there has been a 20% drop in the hydropower share in 2018 as compared to 2009 as shown in Figure 1.2 (International Renewable Energy Agency, 2020). The major reason is that hydropower is geographically dependent due to resource inadequacy. Further, it carries huge infrastructure cost and environmental consequences such as damage to river ecosystem and habitats. On the other hand, solar and wind power generation have seen a rise, and are currently the most reliable renewable energy sources to meet the surge in the global demand. However, effective load management is severely affected due to their daily and seasonal variance. Further, the choice between the solar and wind depends upon several factors such as availability, cost and stability.

† The data reported in Figure 1.2 is as per the most recent statistics available.

Solar energy has unique characteristics such as its widespread availability, extremely possibility of localization/de-centralization, clean energy and has less ecological impacts. Despite the immense potential of solar technologies, they are unable to deliver a continuous energy supply. This stresses the need of an energy buffer in order to develop self-sustained renewable energy power houses. The convenience of the renewable resources provided by the mother nature to the mankind is inspirational and hence, statutory investments in renewable technologies such as solar power is the necessity of the hour.

1.3 Solar Power: Technologies and challenges

The Sun is a gigantic energy source and the total radiation received by the Earth is a sum of the direct or beam radiation, reflected radiation and diffused radiation. The earth receives nearly 885 million TWh of solar energy annually, which is roughly 6200 times more than the commercial energy demand globally (Bijarniya et al., 2016). The peak radiance received at peak solar period is 1000 W/m^2 (Sumathi et al., 2015). Undoubtedly, solar energy can sustain the entire energy needs if harnessed appropriately.

The solar technologies are broadly classified into solar photovoltaic (solar-PV) and solar thermal. The solar-PV directly converts the energy from the solar radiation to electric energy using the photovoltaic effect. Solar thermal technologies convert the solar energy into usable heat or to power. Solar-PV uses solar panels, whereas, solar collectors are used in solar thermal. According to a report, the solar-PV has experienced a remarkable drop in the installation cost in the previous decade and the trend is expected to continue in the upcoming three decades (International Renewable Energy Agency - IRENA, 2019). However, the e-waste coming from PV panels is expected to reach 60-78 million tonnes till 2050 and the consequences are congruent with the e-waste generated from battery storage (Stephanie Weckend et al., 2016). Further, solar-PV systems suffer a reduction in power output with rising ambient temperature and strongly depend upon solar radiation (Ju et al., 2017). Nevertheless, the direct comparison between solar-PV and solar thermal technologies is not justified as both involve different mechanisms of power generation and instead, recent technological innovations suggest a hybridization of solar-PV with solar thermal technologies (Ju et al., 2017; Peinado Gonzalo et al., 2019; Powell et al., 2017; Pramanik and Ravikrishna, 2017). The objective behind their integration is to obtain maximum regeneration of solar panel heat and stable power output for a full day.

Solar thermal technologies are environmentally friendly and are useful in developing numerous applications such as thermal comfort in buildings, solar water heating, solar cooking, solar drying and power generation. Solar thermal technologies are clean and have an inherent advantage of integration with energy storage systems to develop stand-alone power generating facilities. The most common method of harnessing energy from solar thermal route is through concentrated solar power (CSP). The radiations from the Sun are focussed on the operating medium such as a fluid from where the thermal energy is transported to the power plant directly or through an energy storage mechanism.

1.3.1 Concentrated solar power (CSP) technology

In 2019, there was an estimated increase of 34% in CSP generation ("International Energy Agency,"). CSP technology has been growing at an appreciable pace, however, significant efforts are required to achieve the sustainable development scenario. Presently, USA and Spain are the major contributors to CSP technology, however, developing nations such as India have also made significant investment in the technology (Islam et al., 2018). In USA, the total installed CSP generation capacity is expected to reach 1504 GW by 2050 (Trieb, 2009). Other emerging economies such as South Africa and Morocco have developed largest plants with longer storage time (Achkari and El Fadar, 2020). CSP technology has the capability to satisfy both thermal energy and electricity demands (Espinosa-Rueda et al., 2016; Zou et al., 2017). Based on direct normal irradiance (DNI), the Middle East, Mediterranean, North Africa, Arizona, Nevada, New Mexico have been described as the 'Sun Belt (Trieb, 2009).

The CSP technologies require a minimum irradiance of 200 W/m^2 for generating power (Dugaria et al., 2015). The received solar radiation is concentrated on a small area of focus which generates heat at medium-to-high temperatures. The higher operating temperature results in larger thermodynamic efficiency and hence, smaller is the surface area required to absorb the heat thus preventing heat losses due to conduction or convection (Fuqiang et al., 2016). However, the CSP technology is still dependent upon solar radiance and is significantly affected by the solar intermittency. Therefore, the potential of generation using CSP technologies is enriched after integrating it with thermal energy storage technology.

Following are the few merits of CSP plants integrated with TES (Achkari and El Fadar, 2020; González-Roubaud et al., 2017; Prieto and Cabeza, 2019; Xu et al., 2015); (i) round the clock energy supply, (ii) improvement in operational plant efficiency, (iii) reduction in GHG emissions, (iv) effective load management thus preventing undesirable load fluctuations, and

(v) economical operation. A typical CSP power plant as shown in Figure 1.3 comprises of three major components i.e. solar concentrator, thermal energy storage (TES) unit and the heat to power conversion unit (“Parabolic trough power plants”).

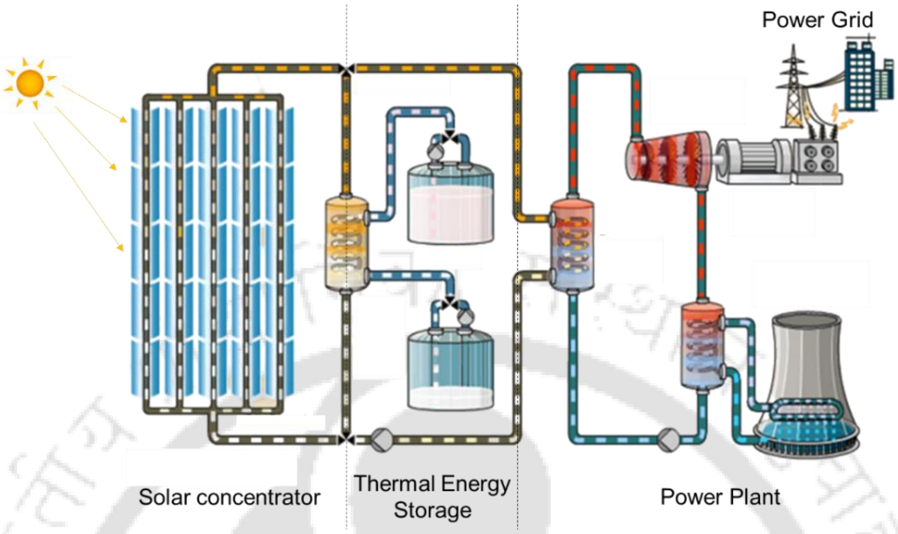

Figure 1.3. Typical concentrated solar power plant with integrated thermal energy storage system (“Parabolic trough power plants”).

1.3.1.1 Solar concentrators

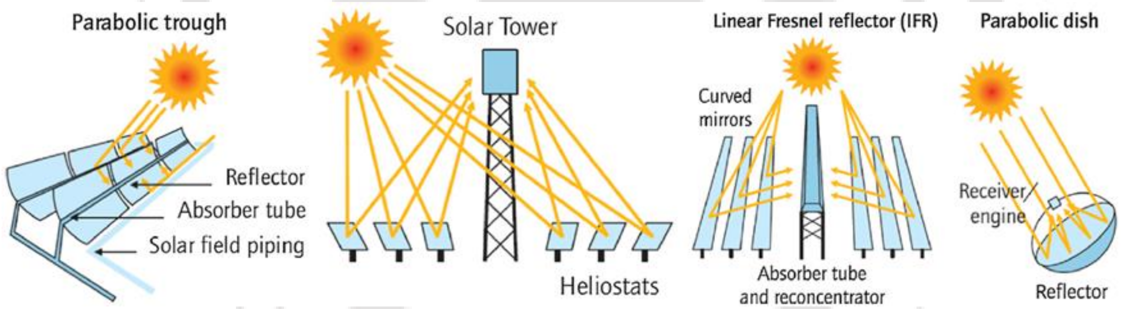

Figure 1.4. Classification of solar collectors (Behar et al., 2013).

The solar concentrators consist of a solar tracking system which continuously aligns the reflective surfaces of the solar panels towards the sun to receive maximum solar radiance. The solar concentrators are either line-focusing technologies; parabolic trough collector (PTC) and Linear Fresnel Reflector (LFR), or point-focusing technologies; Solar Power Tower (SPT) and Parabolic Dish Collector (PDC). The different CSP technologies are shown in Figure 1.4 and described below;

Parabolic trough collector (PTC): The parabolic trough collectors have parabolic reflectors/mirrors. The incident radiations are reflected from the reflectors towards a linear receiver, which are evacuated glass tubes absorbing maximum radiation. The energy carrier fluid commonly termed as the heat transfer fluid (HTF) passes through the absorber tube and carries the absorbed heat. PTCs have an operating temperature between 20 and 400 °C, have a low thermal efficiency and require a very large installation land area. They can be used for both process heating (100-250 °C) or power generation (300-400 °C) (Liang et al., 2015).

Linear Fresnel Reflector (LFR): Similar to PTC, LFR has parabolic mirrors, however, the receiver is a separate receiver tower located away from the mirrors. To make the collector compact, several design modifications have been tried and tested to develop a compact LFR (CFLR) having parallel towers in a single row of LFRs. Their operating temperature lies between 50 and 300 °C, have a low thermodynamic efficiency and cost (Zhang et al., 2013).

Solar Power Tower (SPT): It consists of an array of mirrors called heliostats which focus the incident radiation at a single point and hence, they are categorised under point-focusing collectors. They operate in a relatively high temperature range between 300 and 565 °C (Barlev et al., 2011).

Parabolic Dish Collector (PDC): They have bi-directional capability to absorb solar radiation and have highest efficiency among different solar concentrators (Kumar et al., 2017). They require a small installation area and can operate in a broad range between 120 and 1500 °C. The PDCs are the most expensive kind of solar concentrators, however, they are most promising for small-scale power generation (Bijarniya et al., 2016).

1.4 Energy storage systems (ESS)

The history of the energy storage technique dates back to 1909, when the first pumped-hydro storage facility of capacity 1 MW started in Switzerland (Whittingham, 2012). The energy storage is a regeneration technique which maintains an energy ‘buffer’. Ideally, the power delivered by the electricity grid varies based on demand throughout the day. The storage system levels the supply and demand and helps in ‘peak shaving’ of the load on the electricity generation unit. A simple demonstration is illustrated in Figure 1.5, wherein, as the demand reduces, the energy supplied to the grid can be directed towards the ESS which can be charged. With a surge in demand, the ESS can discharge the energy, thereby reducing the load on the power plant. This technique improves the safety of the power plant operation, reduces the grid cost, stabilizes the grid supply and reduces the GHG emissions. Further, if the power plant is equipped with a CSP technology, the benefits are tremendous such that the load is reduced further during peak sunshine hours.

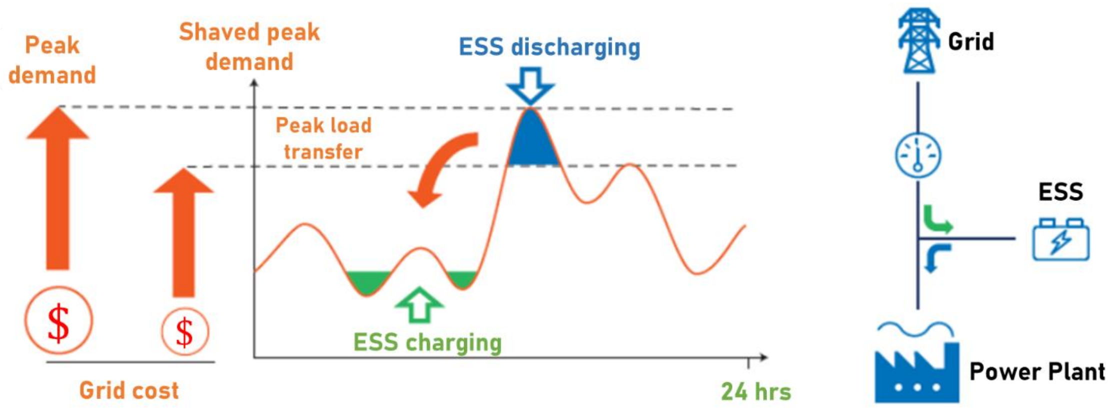

Figure 1.5. Demonstration of load peak shaving using an energy storage system (ESS) .

Energy can be stored via distinct mechanisms such as mechanical, chemical, magnetic, biological and thermal, however, based on the storage technology they are broadly classified as mechanical, electrical and thermal energy storage (Koohi-Fayegh and Rosen, 2020). Mechanical energy storage involves pumped hydropower storage, compressed air energy storage and energy stored in flywheels. Electrical energy storage involves storage in different types of batteries namely; Li-ion and Ni-Cd, etc. Thermal energy storage (TES) is a technique which involves energy storage in the form of heat which can be later used for distinct applications. The objective of the present thesis work is focused on the development and performance enhancements of TES systems.

1.4.1 Thermal energy storage (TES) technology

The TES involves storage of heat/cold in a medium known as the storage medium, and consists of an equipment referred to as the storage system for the exchange of the stored energy whenever desired. The storage mediums are either naturally existing, for example, water stored in natural lakes or underground natural reservoirs, or they can be artificially manufactured containments/tanks to prevent heat exchange with the surroundings. The important aspects while selecting a TES system for its integration to a CSP plant are as follows (González-Roubaud et al., 2017; Renewable and Agency, 2013);

(i) Storage capacity- It depends on the type of storage medium, method and size of the storage system.

(ii) Power- It is the rate of energy stored or discharged

(iii) Overall efficiency (%)- It is the ratio of energy discharged to the energy charged, thus considering the thermal losses.

(iv) Charging and discharging time- It is the time taken to charge or discharge the energy from the TES to the main system, and is generally estimated in hours for the CSP technology.

(v) Storage cost- The cost can be calculated both at the material level or the system level and is generally calculated in USD/kW or USD/kWh. The most used indicator to estimate the economic benefits from a TES integrated CSP plant is the levelized cost of electricity (LCOE) (EPA, 2020). LCOE reflects the competiveness between different technologies and represents the revenue per unit of the electricity that can recover the technology cost including the building and operation cost.

All the afore-mentioned factors govern the performance of the TES integrated CSP plants. With effective integration, the development of a fully sustained and clean energy generation capacity is highly feasible.

1.4.2 Storage conceptualization

TES systems are integrated to a variety of applications such as thermal conditioning of buildings, solar process heating systems, thermal management of power electronics, process steam and power generation (Sharma et al., 2009). Most of the applications have specific requirements such as the type of storage medium, size and type of heat exchanger units. For high-temperature energy storage, the developed storage concepts are classified into active and passive TES systems and are elaborated below (Gil et al., 2010).

1.4.2.1 Active storage system

The active storage system is designated based on the heat transfer due to forced convection into a storage medium. It is further sub-divided into direct and indirect storage. In case of an active direct storage system, the heat transfer fluid (HTF) which circulates to the receiver is also the heat storage medium. The example shown in Figure 1.6(a) is a two-tank active direct storage system ("Informe anual 2006 -Plataforma Solar de Almeria," 2006). The commonly used HTF for active direct storage are synthetic oils or molten salts (Vignarooban et al., 2015). The active direct storage system prevents the cost of additional heat exchangers and hence, they are economical, however, the HTF is required to have the properties of a good storage material. Molten salts when used as HTF are effective, but they require an auxiliary heating system to prevent them from freezing (Gil et al., 2010). Further, the system cannot be employed for direct steam generation due to requirement of equipment to handle the HTF gas (Achkari and El Fadar, 2020). The 20 MW Gemasolar CSP Plant in Spain is an example of active direct storage system (Comité Internacional De La Cruz Roja (CRIC), 2007).

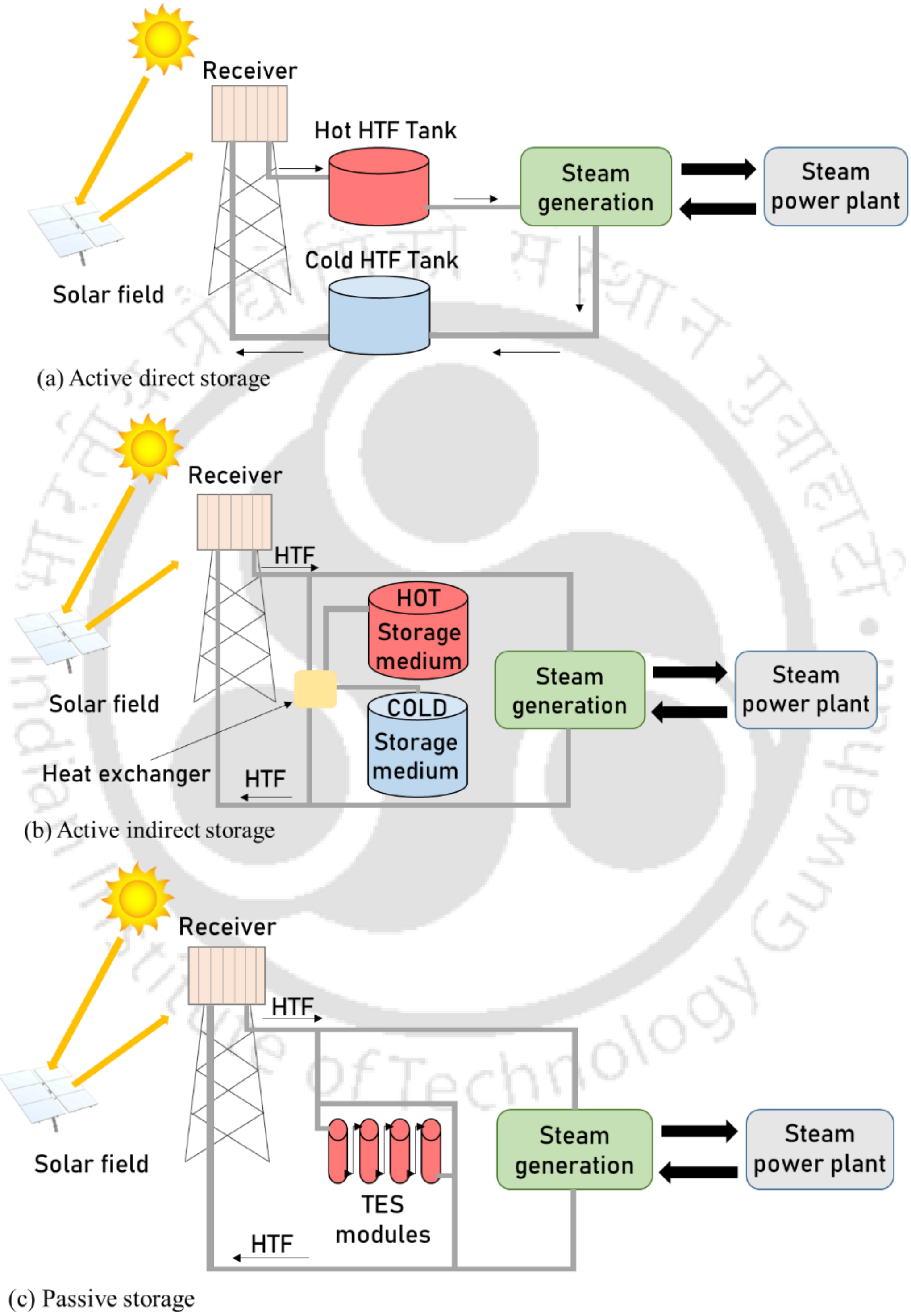

Figure 1.6. Different thermal energy storage concepts namely, (a) active direct storage, (b) active indirect storage, and (c) Passive storage (Gil et al., 2010).

An active indirect storage system employs a separate medium for energy storage. The example illustrated in Figure 1.6(b) shows a two-tank storage system, where the HTF (generally oil) receives the heat from the solar field and transfers the heat to the storage medium (generally molten salt) through a heat exchanger. The two-tank system can also be replaced by a single tank known as a thermocline system which operates on the principle of thermal stratification of the hot and the cold storage medium in the same tank, thereby reducing the cost (Medrano et al., 2010).

1.4.2.2 Passive storage system

In a passive storage system (refer Figure 1.6 (c)), the function of the HTF is only to charge/discharge the storage medium, however, the storage medium is stationary. Generally, passive storage involves a solid storage medium such as concrete and may also have dual storage mediums. The major disadvantage of this type of storage is low heat transfer rate and cooling down of the storage medium while discharging, thus causing a drop in the HTF temperature (González-Roubaud et al., 2017).

Both the active or passive storage are successfully operational storage systems and aid in effective management of the plant load.

1.4.3 Types of TES systems

The TES systems are primarily divided into three types based on the storage medium involved namely; sensible, latent and thermochemical energy storage. The selection of a TES material is based upon several factors such as operating temperature, thermo-physical properties of the storage medium, size of the storage system and cost. The different types of storage systems are described below;

1.4.3.1 Sensible heat storage (SHS)

In the sensible heat storage (SHS) systems, the energy is stored by virtue of temperature difference or sensible heat transfer. The amount of heat stored/discharged is proportional to the mass, specific heat and the temperature increase of the SHS medium as shown in Eq. (1.1)

$$Q_S = mc_p\Delta T \tag{1.1}$$

where m (kg) and c_p(J/kg K) are the mass and specific heat of the SHS material

Different types of solid and liquid storage mediums have been identified as potential SHS materials. Solid mediums include rocks, concrete, soil, metals, whereas, liquid SHS mediums include synthetic oils, molten salts and water (Gil et al., 2010). The SHS mediums have wide range of operation with a maximum temperature of 1200 ºC for magnesia fire bricks (Kuravi et al., 2013). SHS storage is beneficial for the conditions where there is a sudden rise in demand, however, they are unable to deliver stable power output.

1.4.3.2 Latent heat storage (LHS)

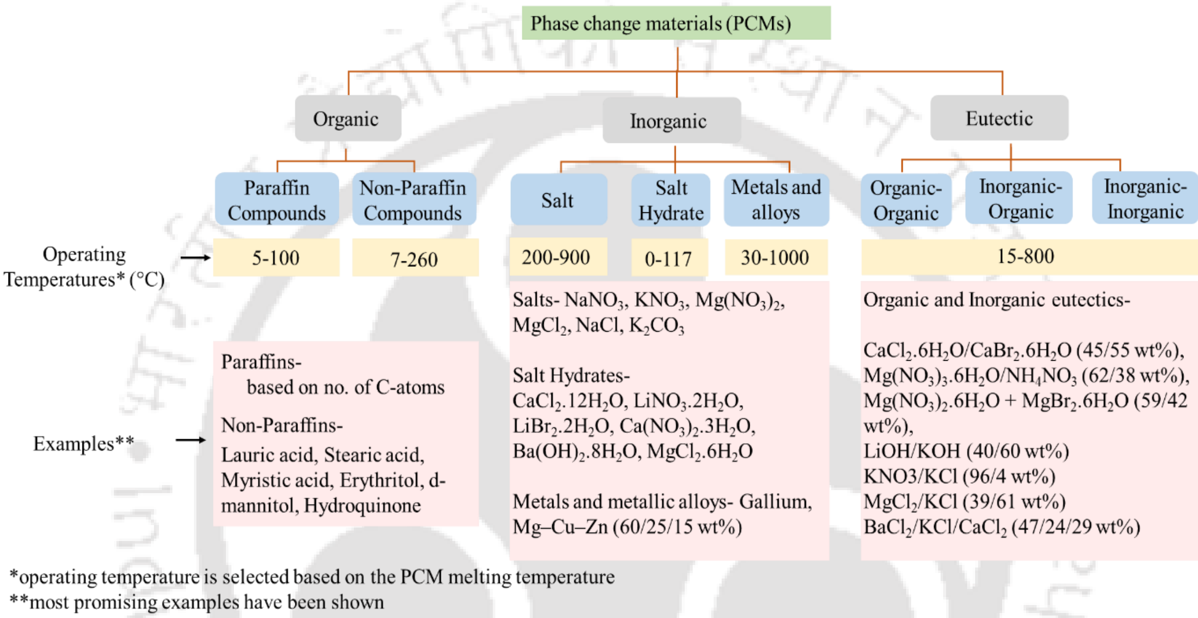

Figure 1.7. PCM classification, operating temperatures and most promising examples.

As the name suggests, the LHS systems store energy due to the latent heat absorbed by materials commonly termed as phase change materials (PCMs). PCMs possess a high volumetric energy storage density and hence, useful in developing compact storage units. They have excellent cyclic stability and do not lose their storage property over thousands of cycles (Liu et al., 2012). They are most suitable for stable power output as the phase change is an isothermal process. The solid-liquid and liquid-vapour transitions are most common for storage. However, most of the literature has been reported on solid-liquid phase change as liquid-vapour transitions lead to high volumetric expansion and increase the size of the equipment. The energy stored/discharged by the LHS systems is shown in Eq. (1.2).

$$Q_L = m_{PCM}(\Delta h_f) \quad (1.2)$$

where m_{PCM} (kg) and Δh_f(J/kg) are the mass and latent heat of phase change of the PCM

The selection of PCM is similar to SHS material, however, the most important criteria is the melting point temperature and the phase change enthalpy of the PCM which has to be consistent with the developed application. One important advantage of PCMs is their capability of storing sensible heat, thereby increasing the overall energy storage output. The biggest challenge for the development of the LHS systems is that the PCMs have a low thermal conductivity (0.1-1 W m^{-1} K^{-1}) (Mahdi et al., 2019), which affects the charging/discharging performance of the system. Hence, majority of research in the LHS domain has been focused on improving their heat transfer characteristics. PCMs are suitable for a wide variety of applications and available in diverse categories. A detailed classification based on the data collected from literature is shown in Figure 1.7 (Gil et al., 2010; González-Roubaud et al., 2017; Kenisarin and Mahkamov, 2016; Liu et al., 2012; Myers et al., 2015; Myers and Goswami, 2016; Pereira da Cunha and Eames, 2016; Sharma et al., 2009; Xie et al., 2017).

1.4.3.3 Thermochemical heat storage (TCHS)

The thermochemical energy is stored due to endothermic or exothermic heat released during the reversible chemical reactions. Figure 1.8 illustrates the various steps involved in TCHS system (Sunku Prasad et al., 2019). The energy stored and discharged is dependent upon formation and breakage of molecular bonds. The storage capacity is proportional to the reaction enthalpy and number of reactant moles as shown in Eq. (1.3). TCES has the highest energy storage density than other storage methods, however, the technology suffers due to high medium and equipment costs (Herrmann and Kearney, 2002).

$$Q_T = n\Delta H \tag{1.3}$$

where n is the number of moles and ΔH is the reaction enthalpy

Although, all the afore-mentioned TES methods are conceptually proven technologies, their implementation is highly competitive. In terms of operability, SHS has touched the industrial scale, LHS is at both the pilot and industrial scale, whereas, TCES is still being explored by researchers and is at the laboratory scale. A recent review study (Achkari and El Fadar, 2020), presented a comparison between the three technologies in terms of cost and efficiency, thereby predicting the feasibility of implementation (refer Figure 1.9). It is observed that both the LHS and TCHS have a high efficiency, however, SHS suffers from low efficiency. The cost of LHS lies in between both the other technologies, whereas, TCHS is extraordinarily expensive.

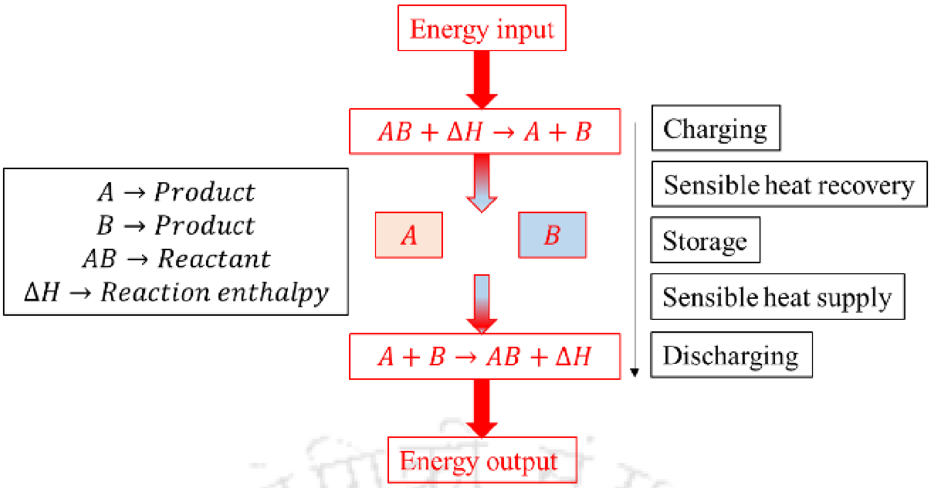

Figure 1.8. Sequence of steps involved in thermochemical energy storage process (Sunku Prasad et al., 2019).

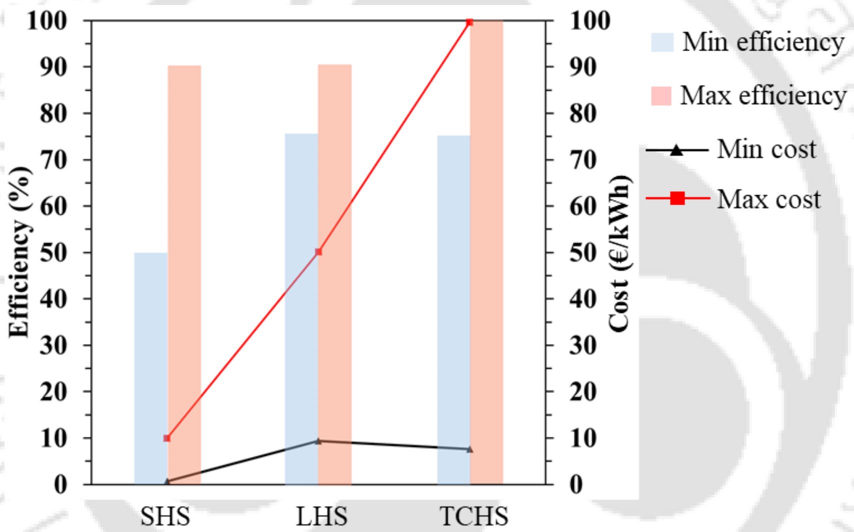

Figure 1.9. Efficiency and cost ranges for different TES technologies (Achkari and El Fadar, 2020).

1.5 CSP-TES systems: Developmental status and challenges

Till 2016, Spain and USA were the largest producers of CSP based electricity with total operational capacity of 2.304 GWe (50 CSP plants) and 1.64 GWe (19 CSP plants), respectively, and had a combined installed capacity of 73% of the global CSP capacity. Thereafter, South Africa, Morocco, India and China emerged as major investors in CSP technology (Mark Mehos et al., 2016). Amongst different CSP technologies, the SPT and PTC have been the most preferred technologies, whereas PDC has been implemented scarcely due to its high cost. In India, most of the installed capacity employs the LFR technology (Palacios et al., 2020) such as in Dadri ISCC Plant (Uttar Pradesh), Dhursar (Rajasthan).

According to a recent report by the National Renewable Energy Laboratory (NREL), 45.5% of the operational CSP capacity and 83.3% of the CSP capacity under development worldwide is equipped with a thermal energy storage (TES) capacity (Madaeni et al., 2012). The CSP-TES integration was less prevalent until 2016, however, the advent of new storage materials and significant research and development in the TES technology have led to an extremely high feasibility of CSP-TES integration. Table 1.1 presents detailed characteristics of the CSP technology, operational parameters, TES integration and the most successful CSP plants operational worldwide.

CSP technology is a proven technology for renewable energy production and has an efficiency higher than the solar-PV technology, however, there are a few techno-economic barriers which restrict its dominance in the energy market. The most important challenges for developing a CSP technology are as follows;

(i) Competence with solar-PV: The decreasing cost of the solar PV panels has had a significant impact on the CSP market (Power, 2010). For typical CSP plants, the operating temperature are high (~250-700 °C), whereas, solar-PV system operates at ambient temperatures (Ju et al., 2017). The high temperature operation increases the initial cost significantly due to high cost of heat exchangers and other equipment.

(ii) Degradation of CSP components: The CSP components such as absorber tubes, tanks and mirrors undergo continuous degradation of various forms. The absorber tubes experience cracks and deformation. The thermal losses, thermal stresses and corrosion are the common degradation mechanisms in tanks. The mirrors are degraded due to soiling, erosion, corrosion, atmospheric transmission losses and focusing issues arising due to their weight (Peinado Gonzalo et al., 2019).

(iii) Choice of heat transfer fluids (HTFs): HTFs are needed for both the CSP and CSP-TES systems. The most common HTFs are water, steam, air, molten salts and synthetic oils. Water is a natural HTF, however, its availability and high corrosion effect on carbon steels are some of its demerits. Steam and air come under the category of gaseous HTFs and can also be used as storage materials (Islam et al., 2018; Pelay et al., 2017). Apart from high equipment cost, steam has high corrosion effects. Air as an HTF is a naturally available substance with zero cost and no corrosion effects, but has a poor thermal conductivity and low energy density.

Table 1.1. Detailed summary of CSP technology and various CSP-TES plants operational worldwide.

CSP Technology	**Operating temperature (°C)**	**Heat transfer fluid**	**Relative cost**	**CSP-TES integration**	**Efficiency (%)**	**Land requirement (km^2/MW)**
Parabolic trough collector (PTC)	290–390	Synthetic oil, water/steam (DSG), molten salts	Low	Possible	10-15	0.025
Linear Fresnel reflector (LFR)	250–390	Water/steam	Very low	Possible	9-15	0.008
Solar power tower (SPT)	250–500	Water/steam, molten salt, air (demonstration)	High	Highly possible with low cost	14-17	0.036
Parabolic dish collector (PDC)	250–700	Air, hydrogen, helium	Very high	Difficult	18-25	0.011

Characteristics of high capacity CSP-TES plants operational worldwide

Project and country	**Type of solar concentrator**	**Installed capacity (MWe)**	**Type of HTF**	**Type of energy storage system, storage capacity**
Solana, USA	PTC	280	Therminol VP-1	Two tank indirect (molten salt), 6 h
Arcosol 50 (Valle 1), Spain	PTC	49.9	Diphenyl/Diphenyl Oxide	Two tank indirect (molten salt), 7.5 h
Noor II Ouarzazate CSP Power Station, Morocco	PTC	200	Synthetic oil	Two tank indirect (molten salt), 7 h
Dhursar, India	LFR	125	Synthetic oil	-
Shouhang Dunhuang 100 MW Phase II, China	SPT	100	Molten salt	Two tank direct (molten salt), 11 h
Kathu Solar Park, South Africa	PTC	100	Thermal oil	Two tank indirect (molten salt), 4.5 h

The use of air in CSP technology is presently limited to demonstration units such as in Jülich Solar Tower plant, Germany (“Solar PACES,”). Molten salts are successfully employed in the CSP plants due to their low cost, inherent energy storage feature and wide range of availability. The only issue lies with their handling, as most of the molten salts have high freezing temperatures and need auxiliary heating mechanisms to maintain them in liquid phase (Gil et al., 2010). Finally, the synthetic oils are the most prevalent in the operational plants. Although they have thermally accustomed properties, their cost is a major concern (Vignarooban et al., 2015).

(iv) Choice of TES method (Renewable and Agency, 2013): Sensible heat storage materials has been the more favourable choice in most of the developed CSP technology due to their low cost and minimum complexity. The problem that lies with PCMs is their handling, whereas, their moderate cost and high energy density makes them the most appreciable choice. Thermochemical energy storage still lacks as a suitable TES system due to extremely high cost of the equipment and materials.

(v) Storage and discharge rates: The heat transfer characteristics of different TES methods decides their ability to compliment the CSP technology. Presently, exhaustive research and development is undergoing to improve the thermal characteristics of TES systems to make them viable for integration with the CSP technology.

By considering all these challenges and finding appropriate solutions, the CSP-TES systems have long-lasting benefits and there is an immense potential of developing a stand-alone CSP technology with minimum harm to the environment.

1.6 Motivation of the thesis work

The LHS systems are the most comprehensive and competitive energy storage solutions due to their high energy storage density, moderate cost and stable power output characteristics. The past decade has seen a significant admittance of PCM-based storage systems in solar power technologies. However, optimum thermal performance requires a high rate of charging and discharging. Therefore, there is a need of developing high-performance and cost-effective TES solutions in the future.

In the present thesis work, the performances of high-temperature LHS systems are analysed. Different heat transfer enhancement techniques to improve the heat transfer rate in conventional LHS systems are explored. The developed numerical models aid in the design and development of LHS systems before the development of large-scale experimental prototypes.

The major objective of the thesis work is to develop an LHS system for high-temperature applications such as concentrated solar power and direct steam generation. The research works on the development of LHS systems are presently limited to temperatures of below 200 ºC and no attempt has been made to develop a high-temperature and high-capacity LHS prototype. The developed thermal energy storage (TES) facility aims to analyse the performances of TES systems in the temperature range of 450 ºC using air as the heat transfer fluid. A shell and multi-tube heat exchanger of energy storage capacity ~20 MJ is designed and developed based on a numerical model of the multi-tube LHS system. The thermal performance of a lab-scale LHS prototype is analysed to determine the feasibility of integration with high-temperature applications. The present study will serve as a benchmark to design and develop a high-capacity lab-scale prototype in the temperature range of 450 ºC and also explore various heat transfer enhancement techniques. Further, experimental and numerical investigations are conducted to study new PCM encapsulation designs of storage capacity ~0.6 MJ suitable for high-temperature applications. A major focus is laid on improving the heat transfer rate in conventional LHS systems using simple design modifications such as introducing a conical shell heat exchanger design or by employing non-uniform distribution of fins in the system. These novel designs can complement the high-temperature applications and improve their performance in the future.

1.7 Thesis structure

In the present thesis work, the design, development and performance investigations of high-temperature LHS systems is presented by varying different operating conditions. The thesis is organized into eight chapters.

Chapter 1 gives a brief introduction about the global energy scenario, drawbacks of non-renewable energy resources and developmental status of different renewable technologies. Different types of TES concepts, merits and demerits of different types of TES systems are discussed. The classification of PCMs and motivation of the present thesis work is presented.

In Chapter 2, the state-of-art is presented, which majorly focuses on LHS systems using PCMs and the desirable features of commercial PCMs are introduced. The effective implementation of LHS systems, different PCM containment methods, modelling techniques, heat transfer enhancement techniques, problems and applications of PCMs are discussed in significant detail. The various gaps in the literature are identified and the objectives of the present thesis work are formulated.

Chapter 3 describes the modelling technique used to develop the numerical model of the LHS system. The complete numerical procedure includes the governing equations, assumptions and validation of the numerical data with the experimental data. Further, experimental methodology and procedures for conducting the experimental investigations are presented. This includes the description of the experimental test facility, the PCMs and HTF used, property estimations and uncertainties associated with the experiments.

Chapter 4 discusses the design, development and performance investigations of high-temperature multi-tube LHS system. Important performance parameters namely charging/discharging time, energy stored/discharged, and output power were estimated by varying the flow rate and inlet temperature of air which is used as the HTF. The practical implications of the LHS systems and their comparison with different high-temperature sensible heat storage systems are also discussed.

In Chapter 5, experimental and numerical investigations on high-temperature cylindrical PCM capsules are conducted. Charging and discharging performances of five capsule designs namely; basic cylindrical capsule, annular capsule, annular capsule with straight longitudinal fins, annular capsule with tapered longitudinal fins having decreasing height and annular capsule with tapered longitudinal fins having increasing height are analysed.

The upcoming chapters propose various designs that can be implemented to improve the heat transfer characteristics in conventional LHS designs.

In Chapter 6, a heat transfer enhancement technique is proposed, wherein, a novel LHS system is developed using a 3D numerical model. The LHS system design is optimized by modifying a cylindrical shell into a conical shell heat exchanger system.

In Chapter 7, another heat transfer enhancement technique is proposed, wherein, a multi-PCM system with non-uniform fin distribution is developed using a 2D axi-symmetrical model. The practical implications of the developed multi-PCM system and its advantages over single PCM system are discussed.

Chapter 8 presents the major conclusions from the thesis work. The major outcomes of the present research work, the scope and recommendations for the future are discussed.

1.8 Summary

The introduction section first describes the present energy scenario and the role of renewable energy in the development of sustainable energy systems. Later, the different systems for harnessing the solar energy are discussed, followed by the technologies used for solar power generation. Finally, the most important asset of modern day solar thermal technologies i.e. thermal energy storage is described in detail. Different concepts, types and effective integration of thermal energy storage to concentrated solar power technology is discussed and finally, the motivation and objectives of the present work are elaborated.

Chapter 2

State of the Art: A review of the literature

Preface

The history of the energy storage technique dates back to 1909, when the first pumped-hydro storage facility of capacity 1 Megawatt started in Switzerland. Till date, the energy storage systems have evolved comprehensively with the advent of new materials, processes, applications, equipment and improved techniques.

In this chapter, the background of research on the latent heat thermal energy storage systems is discussed in detail. The literature review discusses the evolution of phase change materials, storage techniques, thermal modelling techniques, heat exchangers and heat transfer enhancement techniques.

2.1 Phase change materials (PCMs)

The idea of using Phase Change Materials (PCMs) for energy storage is not new. PCMs have been an evolving field in the past four decades and has become a separate domain of study for the material scientists. The selection of PCMs for various end-user applications is based on important criteria such as; operational temperatures, thermal stability and thermo-physical properties. Apart from easy and cheap availability, PCMs should ascertain the following for their best selection (Abhat, 1983);

1. Thermodynamic nature-
    - Desired melting temperature and range of melting/solidification
    - High phase change enthalpy per unit volume for high energy storage density
    - High density for smaller equipment size
    - High specific heat for added sensible heat storage
    - High thermal conductivity
    - Melting should be consistent with uniform material composition in the solid or liquid phases.
    - Low volumetric expansion/contraction upon melting
2. Kinetic nature-
    - Minimum or zero sub-cooling
3. Chemical nature-
    - Chemically stable
    - Minimum decomposition for high cyclic stability
    - Non-corrosive
    - Non-flammable, non-toxic and non-explosive

Significant research and development works have been conducted on the analysis and discretion of PCMs with data reported in different review studies in the literature.

2.2 Forms of PCM

The PCMs used for different applications are broadly classified based on their physical interaction with the heat source and the method of PCM containment which are described below (Bland et al., 2017).

2.2.1 PCMs for bulk storage

The different categories of PCMs namely; organic, inorganic, eutectic mixtures of organic and inorganics and liquid metals have been commonly used in most of the applications such as cold storage, air-conditioning, water heating, solar drying, solar cooking, electronic thermal management, process steam and power production (Sharma et al., 2009). The use of paraffins, fatty acids and most of the salt hydrates is limited up to 250 °C, whereas, molten salts, metals, alloys and eutectic mixtures are suitable up to 1000 °C. All common PCM technologies need a heat exchanger/storage tanks for the melting and solidification of PCMs during the storage and discharge of energy, respectively.

Abhat et al. (Abhat, 1983) presented a review study of PCMs in the operational temperature range between 0-120 °C and found that paraffins, salt hydrates and organic/inorganic eutectics are commonly preferred due to their low-cost. Organics have low chemical stability, whereas inorganic salt hydrates possess high phase change enthalpies.

Zalba et al. (Zalba et al., 2003) had previously discussed the thermal stability and corrosion aspects of PCMs based on the research works up to 2003, and paraffins were found to be extremely stable based on the thermal-cycling tests. On the other hand, most salt hydrates were found to have corrosive effects on copper, brass, aluminium, whereas, stainless steel suffered minimum corrosion impacts (Cabeza et al., 2001; Farrell et al., 2006; Xie et al., 2017). More details relevant to corrosion of different container materials using different PCMs have been discussed in the review conducted by Khan et al. (Khan et al., 2016) and Rathod and Banerjee (Rathod and Banerjee, 2013). A number of PCMs made it to the list of commercial PCMs as reported by Sharma et al. (Sharma et al., 2009) in 2009. In their review study, they presented thermo-physical properties and applications of commercial PCMs in the temperature range of 0-150 °C.

The use of PCMs for high temperature (> 200 °C) applications such as direct steam generation (DSG) and concentrated solar power (CSP) became prevalent only after the advent of CSP-TES using latent heat storage technology (Nomura et al., 2010a; Steinmann and Eck, 2006). Comprehensive review studies were presented by Gil et al. (Gil et al., 2010) and Medrano et al. (Medrano et al., 2010), where they highlighted the use of molten salts and eutectics for high-temperature range. Later, Agyenim et al. (Agyenim et al., 2010b) enlisted PCMs for use in complete temperature range of 0-800 °C and discussed their suitability for various TES applications.

With rapid development of PCM applications, significant research has been focused on their cyclic thermal stability and techniques for property determination. The thermal stability is ensured if the change in the PCM latent heat and melting point are negligible after consistent thermal cycling. Rathod and Banerjee (Rathod and Banerjee, 2013) discussed the thermal and chemical stability of organic, inorganic and eutectics and found that organic PCM have a good thermal stability, whereas, inorganic PCMs especially salt hydrates, undergo phase-separation and super-cooling. Amongst the measurement techniques, the differential scanning calorimetry (DSC) and differential thermal analysis (DTA) are most common to measure the latent heat and melting temperature of small PCM sample sizes (1-10 mg) , whereas, the T-history method is more suitable for bulk materials (Yinping and Yi, 1999). In DSC and DTA, a reference material (alumina is recommended) and the PCM sample are subjected to a constant heating rate and the heat flow between the materials is recorded to generate the DSC curve. The area calculated under the DSC curve peak represents the latent heat, whereas, the temperature at the peak represents the melting point (Sharma et al., 2009). In T-history method, the PCM sample is initially kept at a temperature higher than the PCM melting temperature and suddenly exposed to a temperature lower than the PCM melting temperature. The temperature versus time graph is plotted and the specific heat and latent heat is determined through mathematical formulations. The complete theory and procedures to calculate the thermo-physical properties using DSC, DTA and T-history method have been described elsewhere (Kuznik et al., 2011; Yinping and Yi, 1999).

Mohamed et al. (Mohamed et al., 2017) recently presented a review study and compared different organic and inorganic PCMs. They concluded that inorganic PCMs are the best choice for high-temperature applications as the demerits such as phase-separation and corrosion are minimized. Further, Nazir et al. (Nazir et al., 2019) reported the recent advancements in the organic and inorganic PCMs and concluded that the heat transfer using PCMs could be improved by various encapsulation techniques and by adding nano-materials. These methods are found to increase the heat transfer surface area and also ascertain the compatibility with the heat exchanger materials.

2.2.2 Encapsulated PCMs: Macro, micro/nano encapsulated (MEPCMs/NEPCMs)

Macro-encapsulation techniques involve the use of typical PCM materials as used for bulk storage, however, the PCMs are enclosed in specific container shapes such as rectangular, cylindrical and spherical. This technique provides benefits such as; easy handling and compatibility with air and liquid HTFs, limited phase-separation and compactness (Ã et al., 2008). Macro-encapsulations are best suited for specific applications such as packed-bed storage and steam generation (Laing et al., 2011). Non-reactive polymers with good stability up to 2200 cycles have been identified as encapsulates for the temperature range 120-350 °C by Alam et al. (Alam et al., 2015). For storage at higher temperatures up to 650 °C, ceramic encapsulates possessing high thermal and chemical stability have been developed by Wickramaratne et al. (Wickramaratne et al., 2018).

Micro/nano encapsulated PCMs comprise of small particles (~0.1-1000 µm) with PCM as the core material enclosed by organic/inorganic shells. Zhao and Zhang (Zhao and Zhang, 2011) presented a comprehensive review highlighting the various physical and chemical encapsulation techniques such as spray drying, in-situ polymerization, interfacial polymerization, suspension-like polymerization and complex coacervation. The micro-encapsulation methods have been classified in Figure 2.1. The size of the micro-encapsulated particles ranges between 1 and 100 µm and have distinct advantages such as shape-stability, thermal-stability and negligible interaction with the surrounding environment as the PCMs are enclosed in polymeric shell materials (Milián et al., 2017).

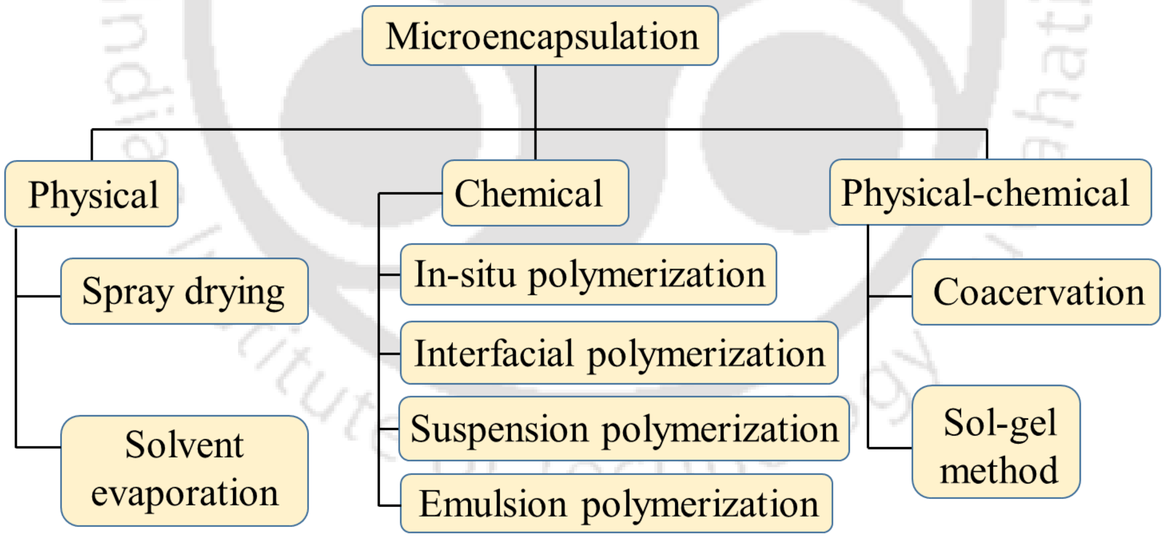

Figure 2.1 Classification of PCM encapsulation methods (Peng et al., 2020).

In another review study by Su et al. (Su et al., 2015), they touched upon important factors that limit the use of MEPCMs. They investigated that shells made from inorganic materials led to better thermal conductivity, however, they have low encapsulation efficiency which lowered the energy storage density. The most vital parameter that substantiates the use of MEPCM/NEPCM in various applications is the ability to undergo shape-stabilization which improves the energy storage density and prevents leakage of PCM from the core of the capsules. Umair et al. (Umair et al., 2019) discussed various novel approaches to improve the stabilization and thermal properties of MEPCMs. Hybrid organic-inorganic shells constituting inorganic additives such as silver or iron nano-particle led to improvement in thermal conductivity of the organic shell materials. MEPCM can be used for diverse applications, however, their shape-stabilization feature makes them more prevalent in textile, building comfort and thermal management applications (Leong et al., 2019; Peng et al., 2020).

2.2.3 Emulsions and PCM slurries

The emulsions or PCM slurries are not very different from MEPCMs. PCM slurries consist of MEPCM mixed with a carrier fluid (generally water). The major advantage of PCM slurries is that they eliminate intermediate heat exchange mechanism between the HTF and the PCM, and due to their flow properties they can be pumped as an HTF with inherent storage capability (Shao et al., 2015).

Jurkowska and Szczygieł (Jurkowska and Szczygieł, 2016) recently conducted a detailed review on the different thermo-physical properties of PCM slurries. The MEPCMs require higher pumping power due to increase in the fluid viscosity when added to the carrier fluid. However, the ratio of power required for pumping the MEPCM slurry (90% water) to the heat transported by it is higher than that of water alone by an order of 1-5 times.

PCM slurries are a convenient technology for developing applications such as cold storage and heating ventilation and air conditioning in buildings (Shao et al., 2015). However, their stability and rheological aspects determine their behaviour when subjected to high mechanical forces while pumping. Depending upon the amount of MEPCM in the slurry and viscosity of the resultant slurry, it may behave as a Newtonian or Non-newtonian fluid and suffer from problems such as creaming, sedimentation, agglomeration and capsule rupture. The stability and rheological characteristics of the PCM slurries have been discussed in detail in the review study presented by Delgado et al. (Delgado et al., 2012).

The use of the different forms of PCMs described above is explicitly dependent upon the application. The PCMs for bulk storage and macro-encapsulations are used for the complete range of solar thermal applications depending upon their compatibility with the containment material. The micro-encapsulations, emulsions and slurries are suitable for low-temperature solar thermal applications (0-100 ºC) such as building conditioning, textile and pharmaceutical industries due to higher thermal and chemical stability in this operating temperature range.

2.3 LHS heat exchange systems

Based on the different forms in which PCMs can exhibit energy storage, the heat exchange systems involve the direct or indirect interaction of PCM with the end use applications in the temperature between 0 and 1000 °C. Primarily, the heat exchange systems are divided into three basic forms as described below;

2.3.1 Shell and tube heat exchangers

Shell and tube heat exchangers are one of the most common and most intensely studied designs for LHS due to minimum design complexity, lower thermal losses and flexibility to design variations for heat transfer enhancement (Agyenim et al., 2010b; Li et al., 2019). Typically, the design incorporates a HTF tube surrounded by a PCM on the shell side, however, various designs may also have HTF flowing on the shell side and PCM contained inside tubes known as the pipe model. The former design is preferred over the latter due to better heat transfer characteristics and lower PCM melting time (Esen et al., 1998). Further, most of the heat from the HTF is transferred to the surrounding PCM as the HTF flows inside the pipe, thus preventing heat loss to the environment. A further improvement in the heat transfer rate is achieved by using a multiple HTF tube system. Agyenim et al. (Agyenim et al., 2010a) initially analysed the comparison between single and multi-tube systems experimentally for a fixed quantity of PCM. Both the rate of storage and discharge were found to improve for the multi-tube system. During PCM melting, the number of convective cells increases due to the multi-tube system, thus improving the overall natural convection heat transfer in the system. Whereas during PCM solidification, more number of tubes reduce the resistance to conduction heat transfer due to an increase in the heat transfer surface area. The improved performance for the multi-tube system was also confirmed from the numerical investigations conducted by Esapour et al. (Esapour et al., 2016). They developed a heat exchanger design with PCM enclosed in between the inner and outer HTF passages. By increasing the number of inner HTF tubes from single to four, the melting time was found to reduce by approximately 30%.

Based on the literature reviewed on multi-tube storage systems, it is observed that most of the studies analysed the multi-tube system through numerical investigations. For example, Liu et al. (Liu et al., 2017) compared the arrangements with PCM enclosed in a flat panel, parallel and staggered HTF tubes. For the same PCM quantity, the staggered tube arrangement reduced the melting time significantly. Sodhi et al. (Sodhi et al., 2019b) analysed the impact of increasing the number of tubes for a fixed heat transfer surface area and fixed PCM volume.

They observed that increasing the number of tubes from 13 to 25, the rate of natural convection in the system improved, thus leading to a charging time reduction by 20%. Zheng and Wang (Zheng and Wang, 2019) demonstrated a similar effect of increasing the number of tubes on the heat transfer characteristics for a varying heat transfer surface area.

Experimental investigations on multi-tube systems have been carried out by only a few researchers (Niyas et al., 2017a; Raul et al., 2018; Riahi et al., 2018; Shen et al., 2019; Zauner et al., 2017). Most of the experimental investigations are limited to the use of 4-5 HTF tubes i.e. low capacity storage systems. Only a few studies namely; Niyas et al. (Niyas et al., 2017a) and Zauner et al. (Zauner et al., 2017) have studied high capacity multi-tube storage systems with 25 and 19 HTF tubes, respectively.

2.3.2 Packed-bed storage units

The packed bed storage systems comprise of a storage media contained inside capsules and the heat transfer takes place with the HTF flowing in the periphery of the capsules. The capsule shells are generally made of high thermal conductivity materials such as aluminium, stainless steel and copper (Singh et al., 2010), however, very few researchers have studied the impact of shell coatings such as Silicon dioxide, Nickel alloy and Zinc with thermal conductivities ranging between 1.5 and 116 W m^{-1} K^{-1} on the TES system performance (Bellan et al., 2015). Packed bed systems have been in continuous use for energy storage applications from long, however, no significant evolution in the field has been done in terms of the capsule design. The packed bed storage systems are limited to only a few capsule shapes such as spherical and cylindrical due to their high heat transfer surface area (Alam et al., 2014; Wickramaratne et al., 2016). These shapes offer simplistic designs for handling PCMs than other bulk storage methods (Ã et al., 2008). Further, the packed bed systems have high heat transfer efficiency due to close contact heat transfer between the HTF and the capsule surface and low thermal losses (Zanganeh et al., 2012).

A significant research has been focused on developing theoretical (Nithyanandam et al., 2014) and numerical models (Gao et al., 2020; Peng et al., 2014) to optimize the performance of packed bed storage systems. Packed bed storage systems charge/discharge due to thermal stratification i.e., change in temperature in the layers of PCM capsules across the length of the bed. The inlet/outlet conditions, porosity, shape of storage media and pressure drop are important factors determining the performances of packed bed storage systems (Trahana et al., 2014). Many researchers have contributed to improve the exergy efficiency of the packed bed system by using stratified capsules, such that there is a maximum thermal interaction between the HTF and the PCM layers (Elfeky et al., 2018; Yang et al., 2014; Yang and Zhang, 2012).

Bains and Singh (Bains and Singh, 2018) conducted a parametric experimental study to test the performance of spherical capsules with three commercial waxes: microcrystalline, bees and paraffin wax. Increasing the HTF flow rate, significantly improved the heat transfer efficiency and the charging/discharging rates, however, the exergy efficiency dropped. Further, more amount of energy could be stored using three PCMs than the single PCM. M.J. Li et al. (M. J. Li et al., 2018) conducted numerical and experimental investigations on a packed bed storage system with spherical capsules for high temperature (400 °C) application. The overall charging/discharging efficiency and the charging/discharging rates were predicted to be higher than shell and tube storage system by 1.9-2.4 times and 1.8-3.2 times, respectively.

2.3.3 Tank storage

The tank storage is an example of bulk PCM storage where the PCM is stored in large tanks. Although there is no practical limitation to their use, they are most commonly used in concentrated solar power (CSP) technology or district level energy networks (Herrmann et al., 2004). The tank based PCM storage is similar to hot and cold water storage buffers used in combined power and heat and district level heating systems used to reduce the peak load on the grid or the central air-conditioning systems. The most important design considerations in such systems is the thermal stratification levels maintained in the tank, the storage temperatures and the efficacy of the insulation (Baker, 2008). Haller et al. (Haller et al., 2009) presented a detailed review to determine the stratification efficiency for a tank storage system which was found to be affected by both the internal entropy generation due to mixing and external entropy generation due to heat losses. Dickinson et al. (Dickinson et al., 2013) presented the charging and discharging strategies of a multi-tank storage system. They studied configurations namely; series charge/discharge, parallel charge/discharge and series charge with parallel discharge. They found parallel discharge and series charge to be the most viable options.

The different LHS heat exchange systems are shown in Figure 2.2 and their use is dependent upon the application and scale of energy storage. The tank storage is generally used for high-capacity storage systems for solar power applications discussed in Section 1.4.2. The shell and tube heat exchangers and the packed-bed system can be used for lab-scale to industrial-scale TES systems for power production or as auxiliary storage devices to assist different solar thermal applications.

Tank storage | Shell and tube heat exchanger | Packed bed system with spherical PCM capsules

Figure 2.2. Different type of LHS heat exchangers namely; Tank storage (Herrmann and Geyer, 2002), shell and tube heat exchanger (Zauner et al., 2017) and packed bed system with spherical capsules (Bains and Singh, 2018).

2.4 Phase change modelling techniques

Modelling is an engineering tool that provides physical insight of the melting and solidification behaviour, and aids in the design and analysis of storage system before the development of the actual prototypes. The phase change phenomenon is a coherent process which takes place during the energy charging and discharging processes of the PCM. Various analytical and numerical modelling techniques have been developed and discussed in the literature. Dhaidan and Khodadadi (Dhaidan and Khodadadi, 2015) presented a detailed review of different modelling techniques for analysing the melting inside rectangular, cylindrical and spherical shaped containers.

2.4.1 Analytical solutions

The phase change problem is a highly non-linear problem, therefore obtaining a closed-form analytical solution is a challenging task and thus, a very few of them have been developed. Although, a few studies have developed closed-form analytical solutions, the approach is subjected to extensive assumptions. Most closed-form solutions have been developed based on one-dimensional (1D) steady-state fluid flow mathematical domains (Dutil et al., 2011; Hong et al., 2015). The Stefan problem is one of the oldest solution which predicts the movement of the phase change boundary as a function of time. The exact solution exists in the form of a similarity solution where the independent variables i.e. the phase change front (x) and time (t) merge together to form a single variable of the form $x/t^{1/2}$ (Ã–zisik MN and Özışık MN, 1993).

Veerapan et al. (Veerappan et al., 2009) developed an analytical model of EPCM with spherical shell for solar energy storage. The studied parameters included the variation in the capsule size, PCM type, initial PCM temperature and the temperature boundary condition imposed on the outer surface of the shell. The model neglected the melting variations in the angular and azimuthal directions and also the buoyancy driven PCM flow. It considered a melting front moving radially inward towards the centre of the sphere. The pure heat conduction based melting was found to over-predict the melting time, with a maximum deviation of 20%.

Hamdan and Hinti (Hamdan and Al-Hinti, 2004) developed an approximate solution for phase change in a rectangular cavity including the buoyancy effects. The interface was considered straight and its inclination was only considered with respect to time and not with respect to height of the cavity. Bareiss and Beer (Bareiss and Beer, 1984) developed an experimentally validated analytical solution for PCM in a cylindrical tube and provided correlations for the solution validity. The analytical solutions are quick and convenient than numerical solutions, however, their application is limited due to approximations and assumptions.

2.4.2 Numerical solutions

The numerical solutions are fairly accurate as compared to the analytical solutions and have the capability to be employed for complex 2D and 3D geometries. The different numerical schemes that have been extensively used to solve the phase change problem are finite volume method (FVM), finite element method (FEM), finite difference method (FDM), tridiagonal matrix algorithm (TDMA), Gauss–Seidel iterative scheme (G-S), explicit time stepping marching (EM), resistance–capacitance (R-C) method (Al-Saadi and Zhai, 2013; Goldstein et al., 1997). During phase change, the PCM flow and heat transfer are solved using the mass, momentum and energy equations. However, the equations are non-linear partial differential equations with source terms to inculcate the buoyancy effects and the latent heat absorbed/released during phase change.

The common methods adopted to include the latent heat of phase change are (Al-Saadi and Zhai, 2013);

(i) Enthalpy method: In the enthalpy method (Jegadheeswaran and Pohekar, 2009), the total enthalpy accounts for the sensible and the latent enthalpy and is incorporated in the energy equation. The method has been used extensively in the literature (Shamsundar and Sparrow, 1975; Yang et al., 2012). The method is quick and can deal with and sharp and gradual phase transitions, however, it is not effective for super-cooling problems.

(ii) Heat capacity method: In this method, the heat capacity accounts for both the sensible and latent heat (Al-Abidi et al., 2013). The specific heat is defined as a function of temperature, generally as a Gaussian distribution curve (Zhang et al., 2014). The method is suitable for only gradual phase change and not suitable for the case of single phase change temperature or for a small phase change temperature range.

(iii) Heat source method: The latent heat is separately treated as a source term and can deal with both sharp and gradual phase transitions. However, it lacks computational efficiency and not effective for PCMs melting in a temperature range.

The biggest disadvantages of the various numerical methods are that they are time consuming, incur significant computation cost and need sophisticated processors and computers to handle the numerical simulations.

2.5 Phase change heat transfer mechanisms

The energy storage and discharge using PCMs occurs due to energy charged and discharged by the PCM during the melting and solidification processes. The heat transfer takes place due to the heat transferred from the source fluid (HTF) to the PCM through various heat exchange systems discussed previously. During melting, the PCM changes its phase from solid to liquid and the heat transfer inside the PCM takes place due to the combination of conduction and convection heat transfer. Initially, the heat transfer initiates at the surface of the heat source in contact with the PCM due to conduction. In case the PCM initial temperature is lower than its melting temperature, sensible heat is transferred to the PCM which raises its temperature. As the PCM starts melting, the viscosity decreases and the fluid PCM exchanges heat with the surrounding PCM due to advection. As more and more PCM melts, the bulk flow leads to convection heat transfer which increases the temperature of the liquid PCM. Natural convection heat transfer occurs due to non-uniformity in material density, and if this non-uniformity is due to temperature non-uniformity, the induced motion is called as thermal gravitational convection (Frank Kreith, Raj M. Manglik, 2011). The density difference of the hot and cold PCM leads to formation of convection currents which in turn enhances the overall heat transfer inside the PCM region.

During solidification, as the low temperature HTF interacts with the PCM, the heat transfer takes place from the PCM to the HTF. Initially, sensible heat transfer takes place and the PCM loses heat due to conduction. Similar to melting, the heat is also transferred due to natural convection only during the beginning of solidification, however, as the PCM solidifies, the convection effect diminishes with the growing solid layer. Therefore, the convection heat transfer is much pronounced during charging, whereas conduction is the dominant heat transfer mode during solidification. The summary of some of the previous and recent studies highlighting the role of natural convection and conduction heat transfer while melting and solidification in differently shaped PCM enclosures is listed in Table 2.1.

Table 2.1 Summary of studies highlighting the effect of natural convection and conduction heat transfer during the PCM melting and solidification.

Author (Year)	Heat exchange configuration	Brief summary
Sparrow et al. (Sparrow et al., 1981, 1979)	Short PCM column with inner HTF tube submerged in a water bath	• natural convection accelerates melting and occurs regardless of solid PCM temperature • during solidification, natural convection prevailed only in case the PCM temperature was below fusion value and did not affect heat transfer rate significantly
Bénard et al. (Bénard et al., 1985)	Melting in a rectangular enclosure with isothermal wall boundary conditions	• melt front interface was initially linear and tilt increased with time • high curvature in the top part due to natural convection effect
Agyenim et al. (Agyenim et al., 2010b)	Shell and tube: single and multiple HTF tube	• higher natural convection effect due to multiple convection cells formed in multi-tube system
Hoesseinizadeh et al. (Hosseinizadeh et al., 2013)	PCM Melting in a sphere with isothermal wall boundary condition	• melting occurs initially due to close contact and heat transfer rate is high and diminishes with time • natural convection dominates the heat transfer in the upper hemisphere • PCM sinks to bottom of the sphere followed by slow conduction in the bottom half
Hosseini et al. (Hosseini et al., 2015)	Shell and single tube heat exchanger with and without longitudinal fins	• heat transfer initially dominated by conduction followed by natural convection domination throughout charging • fins improve the heat transfer rate especially during initial stages. • more fins lead to blockage of natural convection vortices and also reduce the overall energy storage density of the system.
Murray and Groulx (Murray and Groulx, 2014)	Vertical shell and tube system with longitudinal fins	• melting is natural convection dominated and solidification is conduction dominated • fins need to be carefully designed and positioned so as to prevent natural convection suppression
Wang et al. (Y. Wang et al., 2016)	Vertical shell and tube system	• during melting, natural convection effect is concentrated in the upper most region of the shell • solidification initially starts at the bottom and then progresses radially outward in a symmetrical manner

Most of the studies suggest that natural convection effect dominates the heat transfer during melting. Therefore, the heat exchanger needs optimal design to benefit from the natural convection effects induced in the storage system. The typical melt front patterns in horizontal and vertical shell and tube system are described in Figure 2.3. Apart from convection and conduction, radiation heat transfer becomes prominent for high-temperature applications and leads to an additional reduction in the phase change time of PCMs (Archibold et al., 2015, 2014; Pirasaci et al., 2017).

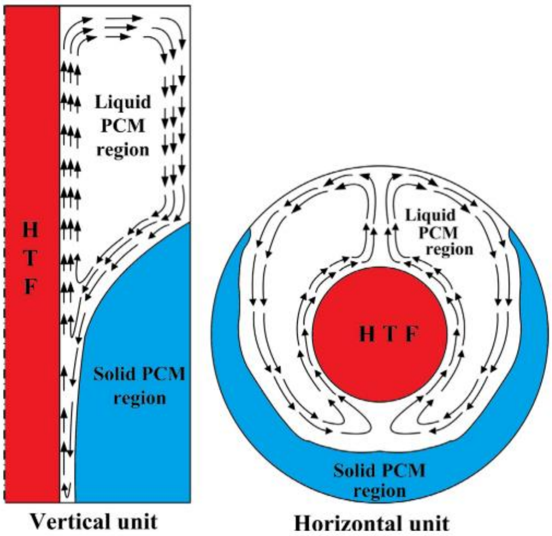

Figure 2.3. Typical shapes of melting fronts in a vertical (left) and horizontal (right) shell and tube storage system (Longeon et al., 2013; Ng et al., 1998).

2.6 Heat transfer enhancement techniques for LHS systems

PCMs have high energy storage capability, however, they offer low heat transfer rates due to their low thermal conductivity (Lim et al., 2019). To maintain an ideal balance of quantity of energy stored and heat transfer rate, enhancement of the heat transfer characteristics in the LHS systems have been of key interest to many researchers. Some of the important techniques include; adding extended surfaces or fins (Lim et al., 2019), Macro/Micro/Nano scale additives to enhance the thermal conductivity of PCMs (Lin et al., 2018; Liu et al., 2016; Rehman et al., 2019), PCM cascading (multiple-PCMs) (Lakshmi Narasimhan N, 2019) and specially designed heat exchange devices. Further few studies have also discussed hybrid enhancement techniques which are a combination of two or more enhancement methods. The different heat transfer enhancement methods and related research studies have been discussed in detail below.

2.6.1 Fins or extended surfaces

Various researchers have investigated different fin shapes to improve the rate of heat conduction in the LHS system (Abdulateef et al., 2018b).

Zhang and Faghri (Zhang and Faghri, 1996) developed a numerical model with internal fins i.e. fins in the HTF side. Their study suggested that for air being used as the HTF, the rate of forced convection in the tube side was the major bottleneck to the overall heat transfer rate and hence, fins were installed on the HTF side and not on the PCM side. Further, the range of heat transfer enhancement factor over plain-tube system was found to improve from 1 to 1.8 by adding more number of fins having high thickness and width.

Mat et al. (Mat et al., 2013) investigated an experimentally validated numerical model of a triplex tube heat exchanger with PCM enclosed in inner and outer HTF tubes. The performance of the system using fins in the PCM region protruding from internal HTF tube, external tube and both internal-external HTF tubes was analysed. They concluded that the charging rate was not affected by the fin structure, and rather increasing the fin length from 10 mm to 42 mm led to the melting time reduction by 43.3%.

Khalifa et al. (Khalifa et al., 2014) compared fin-based heat pipe system with a bare heat pipe system and observed that with the increase in the number of fins, the increase in the overall effectiveness was more predominant than the decrease in the energy storage capacity.

Hosseini et al. (Hosseini et al., 2015) studied the effect of longitudinal fin height on the charging performance of a horizontal shell and tube LHS system. The fins were found to alter the shape of the convection currents and the melting was more symmetric by using fins with a longer height. A better charging performance was observed for longer height fins with a compromise in the energy storage capacity and blockage of convection currents.

2.6.1.1 Fins with specially designed features

Sciacovelli et al. (Sciacovelli et al., 2015) developed a numerical model of tree-shaped fins with single and double bifurcations (Y-shaped fins) to improve the heat transfer rate during the discharging process. The optimization techniques were based on the transient behaviour of the solidification process and led to the development of a fin design with 24% improvement in efficiency. Using similar fin-topology optimization techniques, Pizzolato et al. (Pizzolato et al., 2020, 2017) developed fins based on natural convection and conduction heat flow patterns for single and multi-tube systems. The fin designs for melting and solidification were comprehensively distinct and the studies provide a remarkable insight of the performance improvement using fin-topology optimization and 3D printing based fabrication techniques. Zhang et al. (Zhang et al., 2020) later tested a fabricated unit composed of tree-shaped fins. The most important observation was that, the solidification time reduced by 66.2 % for the radial fin system, however, the melting time had barely changed. Amongst other fin-shapes explored by various authors were triangular fins (Abdulateef et al., 2017), helical fin (Rozenfeld et al., 2017), V-shaped fins (Alizadeh et al., 2019), star-shaped fins (Hosseinzadeh et al., 2020) and spider-web like fins (Wu et al., 2020). Another interesting study was published by Karami and Kamkari (Karami and Kamkari, 2020) featuring perforated fins, having the ability of improving the natural convection heat transfer than the system with solid fins.

2.6.1.2 Fin distribution

Kazemi et al. (Kazemi et al., 2018) numerically investigated the effect of position of longitudinal fins in a horizontal shell and tube system. They reported that as the natural convection heat transfer dominates the upper region in the PCM domain, fins should be positioned in the bottom section to cause uniform melting and thus improve the overall heat transfer rate. Yagci et al. (Yagci et al., 2019) experimentally investigated the effect of varying height of longitudinal fins from the inlet to the outlet section of the vertical LHS system. For a fixed total surface area of the fins, they observed an improvement of 21% for the case with greater distribution of fin surfaces near the outlet section of the system, and thus improved the overall heat transfer during charging, whereas discharging was found to be unaffected due to the fin distribution. Similarly, Shahsavar et al. (Shahsavar et al., 2020) developed a numerical model to study the effect of non-uniform distribution of circular fins in a vertical shell and tube system and found that the charging performance improved by employing fins near the outlet section. The non-uniform distribution of fins amplify the conduction heat transfer in the domains which possess a low heat transfer rate otherwise, and further it also promotes the buoyance induced PCM flow.

Most of the research works on LHS systems with specially designed fins have been studied using numerical investigations and are shown in Figure 2.4(a). The implementation of these designs in LHS systems is subjected to constraints such as cost of manufacturing and complex system design. The distribution of fins with conventional designs in the LHS system has been studied using both numerical and experimental investigations by various researchers as shown in Figure 2.4(b) and are relatively simple designs with low manufacturing cost.

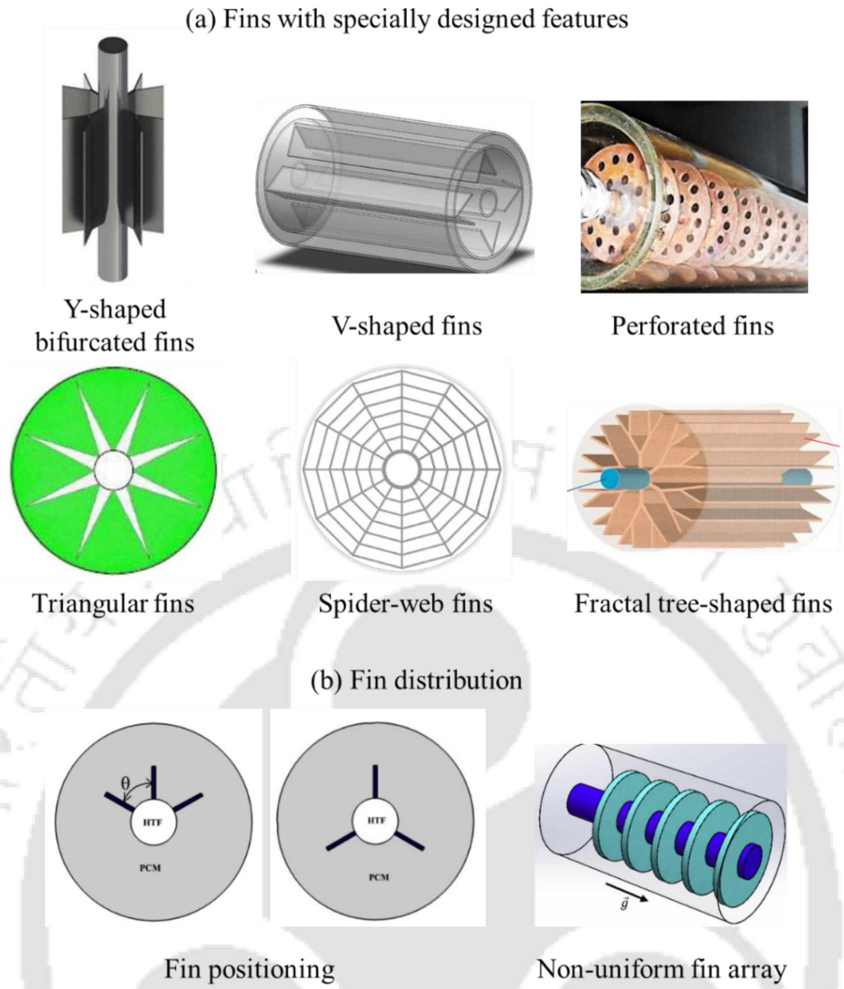

Figure 2.4. (a) Specially designed fin shapes (Abdulateef et al., 2017; Alizadeh et al., 2019; Karami and Kamkari, 2020; Wu et al., 2020; Yagci et al., 2019; Zhang et al., 2020) and (b) fin distribution (Kazemi et al., 2018; Shahsavar et al., 2020) employed by various researchers to improve the heat transfer rate in LHS systems.

2.6.2 High thermal conductivity additives to PCM

2.6.2.1 PCM composites/blends

Pure-PCMs have high energy storage densities and stable operation over thousands of cycles however, low thermal conductivity limits their potential. Further, some of the applications, especially thermal management of electronic devices and batteries require a leak-proof energy storage mechanism (Patel and Rathod, 2020; Qureshi et al., 2018). Additionally, PCMs are used in wall-boards for temperature control in human-comfort application (X. Wang et al., 2016). The additives are added to improve both the thermal conductivity and the form-stability of the resultant composite. Natural graphite has high in-plane thermal conductivity and has been identified as an excellent thermal management material (Inagaki et al., 2014). Allotropic forms of carbon such as graphite, graphene and nano-tubes have been studied as additives to increase the thermal conductivity of PCM blends (Mantilla Gilart et al., 2012; Reddy et al., 2018). PCM-composites increase the thermal conductivity, however, compromise the energy storage density. Some of the studies with different forms of additives into different PCMs and the important property changes for the resultant composites are listed in Table 2.2.

Table 2.2. Research on the variation of thermally conductivity and latent heat by adding different additives to PCM.

PCM	Additive type wt%	λ (W m^{-1} K^{-1}) PCM	Blend	h (kJ kg^{-1}) PCM	Blend	T_m (°C) PCM	Blend	Ref.
Paraffin	GNS 1%, 3%, 5%	0.33	1.45, 3.26, 4.47	143.9	132.1, 128.5, 120.4	53.5	53.3, 52.9, 53.6	(Chen et al., 2013)
Myristic acid	GnP, MWCNT, NG 3%	0.22	0.60, 0.32, 0.318	194.9	187.1, 188.4, 188.9	54.4	54.3, 54.4, 54.6	(He et al., 2019)
Paraffin	EG 1%, 10%	0.3	0.41, 3.83	132	136.1, 115.5	55	55.8, 61.3	(Xia et al.,
Polyethylene glycol	EG 4%, 6%, 8%, 10%	0.3	2.1, 2.91, 4.53, 6.11	169.5	165.1, 153.2, 116.2, 108.1	50.9	50.4, 46.9, 42.9, 41.8	(Lv et al., 2016)
n-docosane (Paraffin)	EG 2%, 4%, 7%, 10%	0.22	0.39, 0.52, 0.68, 0.82	194.6	192.6, 188, 181.9, 178.3	41.6	41.1, 41.0, 40.7, 40.2	(Sari and Karaipekli, 2007)
Paraffin	GO 51.7%, 52.2%, 52.61, 55.29%,	0.287	0.932, 0.952, 0.964, 1.32	131.9	63.7, 63.1, 62.5, 59.1	53.4	53.5, 54.6, 51.5, 52.3	(Mehrali et al., 2013)

Abbreviations: Multi-walled carbon nano-tubes (MWCNT), graphene nano-plates (GNP), graphite nano-sheet (GNS), nano graphite (NG), graphene oxide (GO), thermal conductivity (λ), latent heat (h), melting point temperature (T_m)

Table 2.2 shows that different additives when added to PCM lead to an increase in the thermal conductivity of the resultant composite, whereas, there is a decrease in the latent heat.

Lv et al. (Lv et al., 2016) studied the effect of adding EG in polyethylene glycol (PEG) and found that the thermal conductivity increased by a factor of 20.5, and latent heat reduced by approximately 35%, after adding 10 wt% EG. They also tested the heat transfer characteristics of pure PEG and composites in a rectangular container system and observed that the additive had an adverse effect on the natural convection based PCM flow, however, the massive improvements in the rate of conduction were justifiable for using EG composite for energy storage or retrieval.

2.6.2.2 Metal foams/wool/rings

Metal foams are porous structures of high thermal conductivity metals such as aluminium, nickel and copper, where the copper foams have been most widely implemented due to their high thermal conductivity (Rehman et al., 2019). The performance of a PCM-copper foam (porosity 97.3%) combination was tested by Wang et al. (C. Wang et al., 2016) and a reduction of 40% in the charging time was reported. Similarly, Zhang et al. (Zhang et al., 2017) reported up to 57% reduction in the charging time than pure PCM by using an aluminium foam (porosity 90%, pore size 2.8 mm). Hu et al. (Hu et al., 2019) studied the performance of PCM impregnated in a low porosity (67%) aluminium metal foam and obtained up to 45% and 83.3 % reduction in charging time and temperature, respectively. Further, the pore size had a direct dependence on the thermal performance, where low porosity had led to uniform heat distribution. Joshi and Rathod (Joshi and Rathod, 2020) compared three configurations of PCM in a rectangular enclosure with isothermal wall boundary condition namely; pure PCM, fins-PCM and copper foam-PCM. Both the fin-PCM and the foam-PCM systems delivered fast charging than pure PCM, however, the foam-PCM hindered the natural convection flow significantly. Some of the easiest and effective methods such as adding metal (copper) wool and metallic rings to PCM to improve the thermal performance during melting and solidification have been proposed in the literature (Gasia et al., 2019; Velraj et al., 1999). Similar to other blends/composites, the natural convection flow is hindered with metal foams, especially for a smaller metal foam pore size (Jin et al., 2017).

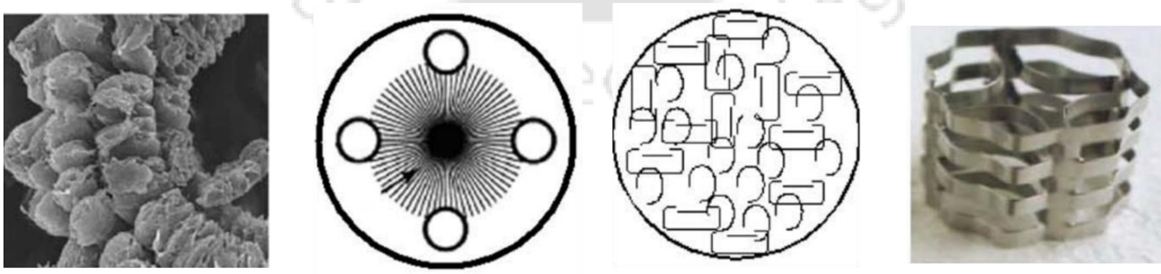

Graphite flakes Carbon brushes Metal rings Metal matrix

Figure 2.5. Some of the high thermal conductivity materials added to PCM (Khan et al., 2016).

The different types of high-thermal conductivity materials to enhance the heat transfer rate in PCMs are shown in Figure 2.5. However, in most of the cases, adding these materials leads to hindrance of the natural convection inside the PCM region.

2.6.3 Nano enhanced PCMs (NEPCMs)

Different types of nano-particles, especially allotropic forms of carbon are added to the PCM to increase the thermal conductivity and thus improve the heat transfer rate. NEPCMs are either embedded in the PCM and used as encapsulations or used in the form of emulsions (Huang et al., 2019). Despite their advantages, they are suitable for applications such as thermal management of electronics and comfort conditioning due to excellent chemical stability of emulsions and micro-capsules in the desired temperature ranges (Cheng et al., 2020).

Most recent studies have showcased the performance of LHS systems using different nano-particles through various numerical techniques, whereas, only a few studied the performance of LHS through experimental investigations (Xiong et al., 2020). Tao et al. (Tao et al., 2015) developed composites of a carbonate salt with different nano-materials namely; single-walled carbon nano-tube (SWCNT), fullerene, multi-walled carbon nano-tube (MWCNT) and graphene. The energy storage capacity did not reduce significantly by adding the nano-materials up to 2.5 wt% and SWCNT was found to be most suitable to improve the PCM thermo-physical properties. In another study, Tao et al. (Tao et al., 2019) discussed that except for improving the thermal conductivity, adding these nano-materials improves the specific heat, thereby enhancing the sensible heat storage capacity.

Graphene nano-platelets based encapsulated PCM ensure form-stability, but encapsulations contain only ~50% active PCM (Praveen et al., 2019). However, graphene nano-particles require very low concentration (0.5 wt%) to enhance the thermal conductivity by up to 60%, and thus huge energy savings can be achieved as reported by Joseph and Sajith (Joseph and Sajith, 2019). Fang et al. (Fang et al., 2015) prepared a PCM composite with graphite nano-sheets (GNS) of different sizes. The heating and cooling performance improved, thermal conductivity increased by a factor of 2.58 and the viscosity had increased 21 times compared to parent PCM by adding 5 wt% GNS. Krishna et al. (Krishna et al., 2017) integrated a Al_2O_3 (nanoparticles)-Tricosane (PCM) based composite as a thermal management material. Due to excess energy storage (up to 30% of the input power) during the heating-cooling cycle, the parasitic fan power consumption reduced to half. Similarly, Praveen and Suresh (Praveen and Suresh, 2018) investigated copper oxide (CuO) nanoparticles based PCM nano-composite and it was found to improve the temperature control in a heat sink application. The CuO nanoparticles are also useful to improve the thermal conductivity and thermal diffusivity when added in small amounts (2% by volume) in nitrate salts (Myers et al., 2016).

2.6.4 Cascading of PCMs (multiple-PCM arrangement)

Table 2.3. Summary of studies on m-PCM systems.

Ref.	LHS system configuration	Key findings
(Wang et al., 2015)	Shell and tube	• Designed HTF tube zig-zag pattern with improved surface area with heat transfer enhancement of multi-PCM over single PCM. • Performance improves using unequal PCM mass ratio.
(Aldoss and Rahman, 2014)	Packed bed with capsules	• m-PCM performs better than intermediate T_m single PCM • Single PCM with low T_m and single PCM with high T_m perform better than m-PCM during charging and discharging, respectively
(Rady, 2009)	Packed bed with granular phase change composites (GPCCs)	• Mixture of GPCCs perform better than m-PCM in terms of charging rate and exergy • GPCC with small phase change temperature range has the highest charging rate. • Low T_m GPCC and high T_m GPCC performs better than m-PCM during charging and discharging, respectively.
(Farid et al., 1990)	Packed bed with cylindrical capsules	• m-PCM has a charging rate higher than intermediate T_m single PCM unit by 15% • Narrow phase change range leads to better system performance.
(Elfeky et al., 2018)	Packed bed with spherical capsules	• m-PCM has high energy and exergy efficiencies than all single PCM systems. • Single PCM with low T_m and single PCM with high T_m perform better than m-PCM during charging and discharging, respectively
(Chiu and Martin, 2013)	Shell and tube	• Reported ~40% improvement in complete charge-discharge cycle heat transfer rate using m-PCM. • m-PCM is found better than single PCM only for part-load performance (70% of the discharged energy)
(Singh and Verma, 2020)	Shell and tube	• Reported ~35% improvement in cumulative charge-discharge rate than single PCM.
(Kurnia et al., 2013)	Shell and tube	• Proposed novel festoon design for vertically and horizontally arranged m-PCMs. • Reported ~30% improvement in charging rate than single PCM using the festoon design and m-PCMs stacked vertically.

The cascading concept arises based on the deficit of heat transfer that occurs between the HTF and the PCM along the favourable heat transfer path. Different PCMs are cascaded in order of their melting point temperatures to enhance the heat transfer rate between the HTF and the PCM. In most plausible scenario, the thermal potential diminishes significantly as the HTF flows along the LHS system. However, in case of cascaded system, the HTF interacts with PCMs with their melting point temperatures in series (during charging), which maintains a continuous and more uniform heat transfer (Michels and Pitz-Paal, 2007; Yan and Yang, 2019).

Some researchers have extensively studied the performance enhancements using multiple-PCMs (m-PCMs) for various applications. Cheng et al. (Cheng and Zhai, 2018) designed a cold storage system for the application temperature range between 13 and 17 ºC and observed a charging rate enhancement of ~35% than a single-stage system. Mostafavi et al. (Mostafavi Tehrani et al., 2018) identified 12 storage groups for concentrated solar power application (~300-550 ºC) with both sensible and latent heat storage mediums and proposed a combined system with high-temperature PCM (melting point of 525 ºC)-concrete-low temperature PCM (melting point of 525 ºC) in the volume fraction ratio of 0.25:0.5:0.25. Similarly, Li et at. (X. Y. Li et al., 2018) investigated m-PCMs in different proportions and an optimum volumetric ratio of 1:2:3 was found to have the highest charging capacity. Peiró et al. (Peiró et al., 2015) developed a heat exchanger design with m-PCM (150-200 ºC) having effectiveness higher than a single PCM by ~19.5%. Another possible outcome by using m-PCM systems is the reduction in the fluctuation of the output (Cui et al., 2003).

Few studies have proposed mathematical formulations based on thermodynamic optimization of energy and exergy of m-PCMs (Gong and Mujumdar, 1997; Mosaffa et al., 2014; Watanabe and Kanzawa, 1995). All these studies have shown a superior m-PCM system performance over a single PCM system. The performance comparison between single and m-PCM LHS systems can be often inexplicable. The comparison between single and m-PCM systems conducted by different authors is summarised in Table 2.3.

2.6.5 Special heat exchanger features

The heat transfer rate in the LHS system can also be accelerated by varying different heat exchanger design features. The most common method is by employing fin-coil shell and tube heat exchanger designs.

2.6.5.1 Improvements in shell and coil heat exchangers

Koukou et al. (Koukou et al., 2018) proposed a staggered tube fin-coil heat exchanger device to improve the natural convection heat transfer during melting. However, they also recommended the design to reduce the thermal resistance offered by the PCM during the solidification process. The helical coil design with HTF flowing inside the coil and PCM in the outer periphery was proposed by Kabbara et al. (Kabbara et al., 2018) and Korti et al. (Korti and Tlemsani, 2016). Both the studies found that charging was natural convection dominated, whereas, it was suggested to improve the heat exchanger design focusing on enhancement of the discharging characteristics. Mahdi et al. (Mahdi et al., 2020) modified a normal spiral coil design to a conical spiral coil design. The objective of conducting the experimental investigations was to improve the surface area of heat transfer in the domain having low heat transfer and they found 28.3% improvement in the charging rate due to the design modification. Ahmadi et al. (Ahmadi et al., 2018) conducted numerical investigations on a spiral coil LHS system and found that the melting rate improved in the bottom portion of the horizontal heat exchanger system by increasing the diameter of the spiral coil.

2.6.5.2 Plate heat exchangers

Plate heat exchanger (PHE) design has been studied by GÜREL (GÜREL, 2020) and Palomba et al. (Palomba et al., 2019) and they found that the heat transfer rate can be enhanced significantly by optimizing the PCM layer thickness in between the plates in comparison to the shell and tube LHS systems.

2.6.5.3 Improvement in external heat exchanger factors

Zipf et al. (Zipf et al., 2013) demonstrated a proof-of-concept of a screw heat exchanger employed to improve heat transfer by imparting rotations in the PCM domain. Nepustil et al. (Nepustil et al., 2016) demonstrated a heat exchanger design with a scraper mechanism to remove the PCM layer deposited at the heat exchange surface.

2.6.5.4 Triplex tube heat exchanger (TTHX)

Recently, triplex tube heat exchanger (TTHX) with HTF flow in the inner and the outer tube and PCM in the intermediate tube has gained significant attention of the researchers. Mat et al. (Mat et al., 2013) improved the TTHX design by adding internal-external fins which led to 43.3% improvement in the melting rate. Later, Sefidan et al. (Sefidan et al., 2017) developed a numerical model to study the solidification characteristics of a TTHX LHS system with HTF in the inner tube and similar or dissimilar PCMs in the other two tubes. Commercial PCMs RT 35 and RT 50 were used in a fin based aluminium heat exchanger. It was found that employing RT 50 in the outermost tube and RT 35 in the intermediate tube led to maximum reduction in the solidification period. Further, Abdulateef et al. (Abdulateef et al., 2018a) experimentally investigated a TTHX system and a validated numerical model was developed to observe the effect of triangular fins attached to inner and outer HTF tube in different configurations. The results concluded that triangular fins had shown better solidification rate than longitudinal fin design. The improvements in the TTHX design have been investigated by Mahdi and Nsofor (Mahdi and Nsofor, 2018), who have added Alumina (Al_2O_3) nano-particles to improve the PCM thermal conductivity, thus improving the solidification rate. Recently, Alizadeh et al. (Alizadeh et al., 2019) investigated V-shaped fins in the PCM region of a TTHX with added single-walled carbon nano-tubes. Using up to 5 wt% of the SWCNT, enhancements up to 1.5 times in the solidification rate have been reported.

Most of the afore-mentioned studies have performed numerical simulations to predict the TTHX performance and most of the studies have considered a two-dimensional domain, thus neglecting the variations along the length of the LHS system.

2.6.5.5 Variation in heat exchanger design parameters

Another important concept to improve the melting heat transfer is by incorporating an eccentric inner HTF tube by lowering its position in a horizontal shell and tube system. The proof-of-concept has been experimentally demonstrated by Cao et al. (Cao et al., 2018) and Yazici et al. (Yusuf Yazici et al., 2014) with melting time reduction by 57% and 67% in their respective studies. The improvements occur as the eccentric tube design facilitates greater PCM movement in the upper region where the effect of natural convection heat transfer is significant, and simultaneously reducing the PCM amount in the lower region having weak conduction effect.

The orientation of the LHS system has a notable impact on the melting characteristics due to variation in the natural convection heat transfer effect. The experimental investigations conducted by Mehta et al. (Mehta et al., 2019) comparing both the horizontal and vertical shell and tube LHS systems shows that the horizontal configuration experiences faster melting up to 50% melting than vertical system, however, the poor heat transfer rate in the bottom section of horizontal system delays the overall melting time. Recently, a similar observation was made by Kalapala and Devanuri (Kalapala and Devanuri, 2020), where again, faster melting was observed in the horizontal system up to 65% of the total melting. The numerical analysis conducted by Pahamli et al. (Pahamli et al., 2017) had shown that the melting was always faster in the vertical system than the horizontal system throughout the process. It is also important to note that the diameter of the PCM shell is also one of the important factors to determine the melting time, which was not discussed in these comparative studies. In a rectangular enclosure with the larger dimension as the heat transfer surface, the melting time is significantly less in horizontal system as compared to the vertical system. This happens as the vertical reach of the natural convection vortices is limited, which leads to a faster melting.

The different heat exchanger design modifications employed to improve the heat transfer rate in LHS systems are shown in Figure 2.6. The selection of a particular design depends upon a number of factors such as cost of manufacturing, simplicity of design and feasibility of capacity upscaling. Simple designs with effective distribution of PCM or heat transfer surfaces along the favourable heat transfer path are found to satisfy the selection criteria.

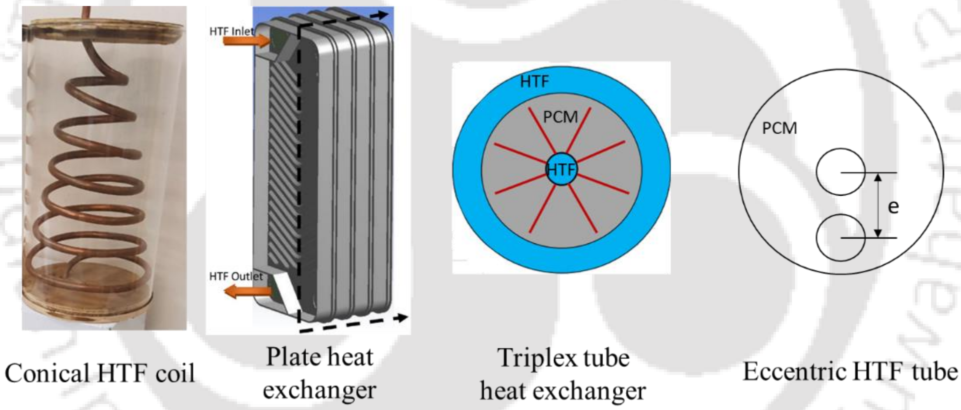

Figure 2.6. Special heat exchanger design features to improve heat transfer rate in PCMs (Abdulateef et al., 2018a; Cao et al., 2018; GÜREL, 2020; Mahdi et al., 2020).

2.7 Problems with using PCMs

(i) Supercooling:

The drop in the PCM temperature below its solidification temperature without the actual starting of the solidification process is termed as supercooling and occurs mostly in inorganic salt hydrates (Wei and Ohsasa, 2010). However, some of the microencapsulated organic PCMs have been found to show this effect. Supercooling adversely affects the solidification process in the thermal energy storage system as the solidification does not initiate at the desired temperature and the amount of latent heat released is reduced. The degree of supercooling depends upon the sample size, cooling rate and homogeneity of the sample and can be minimized by adding nucleating agents. In most cases, macro-encapsulation is preferred over micro-encapsulation to prevent the super-cooling effects (Bland et al., 2017).

(ii) Phase change hysteresis

The difference in temperature between the solidification and the melting temperature of the melting and the solidification curves is known as hysteresis. The phase change hysteresis may affect the long term PCM operation (Rubitherm, 2017).

(iii) Phase segregation

The phase segregation occurs due to composition of the PCM and separation of the constituents based on their density difference. Phase segregation adversely affects the thermal cycling of the PCM and can be eliminated by adding nucleating and thickening agents (Bland et al., 2017).

2.8 Applications of PCMs

Anisur et al. (Anisur et al., 2013) presented a detailed study of the possible use of PCM technology to minimize the CO_2 emissions in different applications. The most important applications of PCM based storage systems are thermal comfort in buildings and vehicles (Zhou et al., 2012), solar thermal power plants (Gil et al., 2010), solar cookers (CSH India, 1999), waste heat transportation systems (Nomura et al., 2010b), solar drying (Rabha and Muthukumar, 2017) and thermal management of electronics (Sodhi et al., 2020). Some of the studies highlighting important PCM applications and their operating conditions are shown in Table 2.4.

Table 2.4. Important PCM applications.

Application	System Description	PCMs used	HTF's used	References
Thermal Comfort in Buildings	• Shape stabilized PCM used in flooring. • PCM Roof Panels • PCM tiles and ceilings • PCM melting temperature range between 15-35 °C	Paraffins (Rubitherm (RT) 25, RT 25, RT 32), inorganic eutectic mixtures, multi-component mixture of hydrocarbons of paraffinic composition	Water	(Anisur et al., 2013; Cerón et al., 2011; Lin et al., 2005; Pasupathy et al., 2008)

Table 2.4 continued…

Thermal management in heat sinks and batteries	• Heat sinks filled with micro-encapsulated and composite PCMs.	Paraffins and composites	-	(Acar and Dincer, 2019; Deng et al., 2018; Iradukunda et al., 2020; Khan et al., 2017; Lanahan and Tabares-Velasco, 2017; Patel and Rathod, 2020)
Domestic water heating	• Finned tube heat exchangers • Hot water storage tanks • PCM integrated with solar water heater • PCM melting temperature range between 40-70 °C	Dodecanoic Acid, Paraffins (RT 65), mixture of hydrate salts	Water, water/ glycol mixtures	(Frazzica et al., 2016; Kabbara et al., 2016; Seddegh et al., 2015b)
Solar Drying	• PCM in shell of multi-tube heat exchangers • Finned tube heat exchangers • PCM melting temperature range between 55-90 °C	Paraffins (RT 58)	Air, water/ glycol mixtures	(Bal et al., 2011; Rabha and Muthukumar, 2017)
Steam Generation	• PCM in shell of multi-tube heat exchangers • PCM capsules used in steam accumulators. • PCM melting temperature range between 100-600 °C	Molten salts, eutectic mixtures, mineral/synthetic oils	Molten salts, eutectics, mineral/synthetic oils	(Bayón et al., 2010; Crespo et al., 2018)
Solar power (CSP or waste heat)	• PCM used in thermocline tank system. • Cascading of PCM's • Encapsulated PCM. • PCM melting temperature range between 100-600 °C	Molten salts, eutectic mixtures	Air, molten salts, water/steam	(Gil et al., 2010; Herrmann and Geyer, 2002)

Apart from the extensive literature discussed on the applications of PCMs in the CSP technology, the maximum use of the PCM technology has been in the district heating/cooling networks, domestic hot water generation systems and load management systems. Most popular examples of energy storage systems implemented in real-time applications are listed below (PCM Products, 2020);

- The Royal Wolverhampton Hospital, UK: Hot and chilled water energy storage system, 930 kWh heating load and 1500 kWh cooling load
- Saudi Arabian Haramain High Speed Train Stations, K.S.A. PCM Energy Storage System: Jeddah (3200 kWh), Madhina (3200 kWh), Kaec (3200 kW h), Makkah (10000 kWh)
- Western Sydney University, Australia: PCM Energy Storage System, 550 kWh
- STAOIL HQ, Bergen: Norway Central Cooling PCM Energy Storage, 1300 kWh
- Royal Physcian HQ, London, UK: Chilled Water PCM Energy Storage, 2000 kWh
- Netherland Cancer Institute, Amsterdam, Holland: 2000 kWh
- Cleantech-2 Zero Energy Building, Singapore: 7200 kWh
- Bergen Airport, Norway-T3: Energy Centre TES Application, 2840 kWh
- National Theatre, London, UK: 2000 kWh
- Norwegian University of Life Sciences, Campus, Norway: 9000 kWh
- Western Norway University, Campus Kronstad, Bergen, Norway: Large Scale District Cooling Application, 12000 kWh
- Eidos, Italy: Heat Pump Application, 1200 kWh
- Gosnel City District Cooling, Australia: 4000 kWh
- Western Sydney Building 24, Australia: TES Load Shifting Application, 550 kWh
- DEKRA-HQ, Stuttgart, Germany: Office Building TES, 600 kWh
- Federal Center South, Seattle, USA: US General Administration Building, 1050 kWh

2.9 Literature closure

Based on the detailed literature survey, the following conclusions are made;

- The shell and tube heat exchangers and design improvements such as triplex tube heat exchangers have been reported in the literature recently. However, most of the studies were limited to 1D or 2D numerical models and an in-depth experimental analysis was limited. The multi-tube shell and tube design and experimental analysis of high capacity industrial-scale storage system has not been reported extensively.
- Majority of the research has been focused on developing low-temperature LHS applications. Due to limitations such as cost of equipment, HTFs and PCMs, the

development of LHS systems for high-temperature applications have been scarcely reported.

- Different macro/ micro/ nano PCM encapsulations have been studied by various researchers. The research studies on micro and nano-PCM encapsulations have been limited to material development and the related LHS technologies are not widely commercial. Macro capsules are widely commercial in DSG and CSP applications, however, the capsule shapes are limited to basic designs such as basic cylindrical and spherical capsules.
- Numerous studies reported recently have explored different fin-based LHS designs such as tree-shaped fins (Zhang et al., 2020), corrugated fins (Aly et al., 2019), perforated fins (Karami and Kamkari, 2020), spiral fins (Mehta et al., 2020), spider-web fins (Wu et al., 2020) and wire-wound fins (Khan and Khan, 2020) and V-shaped fins (Alizadeh et al., 2019). Most of these designs were developed using numerical modelling techniques, whereas, large-scale prototyping can only be achieved using expensive 3D-printing techniques.
- Very few studies have reported simple heat transfer enhancement techniques such as effective PCM distribution in conventional cylindrical shell and tube LHS designs to improve the charging and discharging rates.
- Most of the heat transfer enhancements using fin-based LHS designs have been discussed in the literature, however, their in-depth experimental analysis is presently limited. Moreover, development of designs employing effective heat transfer surface distribution using simple fin shapes such as longitudinal and circular fins is lacking.

Taking into account the above-mentioned aspects and gaps from the literature, the objectives of the present thesis work are defined. The thesis work is focused on two major aspects. First, the experimental and numerical investigations of high-temperature LHS systems which are useful in commercial applications such as CSP and DSG. The following are the important goals for this part of the research;

- Design and development of a high-temperature experimental test facility for investigating the performance of LHS systems.
- Developing a 2D numerical model to optimize the number of HTF tubes in multi-tube LHS system.

- Design, fabrication and performance investigation of a multi-tube LHS system design of LHS capacity 10.7 MJ.
- Experimental validation and heat transfer analysis of a cylindrical PCM capsule using a 2D axi-symmetrical numerical model.
- Design, fabrication and performance investigation of cylindrical PCM capsules carrying different longitudinal fin-designs.

Secondly, an attempt is made to develop novel techniques to improve the heat transfer characteristics in conventional horizontal and vertical shell and tube high-temperature LHS systems. Two different heat transfer enhancement techniques are conceptualized and proposed as described below.

- To develop a 3D numerical model of a conical shell and tube LHS system and explore heat transfer characteristics of straight and tapered longitudinal fin designs.
- To develop a 2D axi-symmetrical model of a multi-PCM LHS system with non-uniform fin distribution in different PCM blocks.

2.10 Summary

This chapter presents a detailed survey of the literature concerning LHS systems. Different aspects of PCMs such as physical form of existence, PCM enclosures, PCM melting and solidification heat transfer mechanisms are studied. The various modelling techniques and their role in designing LHS systems is explored. Finally, the heat transfer enhancement in LHS systems, the commercial aspect of various LHS designs and different applications of PCMs are discussed. Based on the developments in LHS systems studied in the literature, the objectives of the PhD thesis work are framed and presented.

Chapter 3

Methodology and procedures of LHS system development

Preface

Optimum design of latent heat storage (LHS) systems is extremely vital for the development of cost-effective solar thermal technologies. The rate of heat transfer between the heat transfer fluid (HTF) and the phase change material (PCM) is governed by important factors such as flow rate of the HTF, heat transfer surface area and the heat transfer enhancement method used. Apart from these parameters, the thermo-physical properties of PCMs, and storage temperature are imperative to application specific design. The numerical modelling techniques help to establish the physical behaviour and optimization of the LHS systems before manufacturing the actual storage prototypes. This reduces the initial cost and also useful in up-scaling the system to high capacity storage systems. As the designs are finalized, experimental investigations are conducted for analysing the system performances at different operating parameters to decide the operational feasibility. This chapter describes the design methodology for the development of cylindrical shell and tube LHS systems.

3.1 Design of the LHS system

The storage capacity of the LHS system is fixed (Q_L) and based on the latent heat (Δh_f) of the PCM, the PCM volume (V) is calculated using Eq. (3.1).

$$Q_L = \rho V \Delta h_f \tag{3.1}$$

where ρ is the density of the PCM

Fixing the length (L_s) of the storage system, outer diameter (D_o) of the heat exchanger shell is calculated using Eq. (3.2).

$$V = \frac{\pi}{4}(D_o^2 - N d_o^2) L_s \tag{3.2}$$

where N is the number of HTF tubes and d_o is the outer diameter of the HTF tube.

For a single tube system, N=1.

3.2 Numerical modelling

Based on the afore-mentioned calculated dimensions, the numerical model of the LHS system is developed.

3.2.1 Governing Equations

In the present thesis work, 2-dimensional (2D), 2D axi-symmetric and 3D LHS models are developed for different geometries and comprising the HTF and the PCM domains. The interaction between the PCM and the HTF is a non-linear problem. The model is solved as a conjugate heat transfer problem where both the HTF flow and the heat transfer between the HTF and the PCM is solved simultaneously. Solving the phase change problem is challenging than solving the PCM in the solid and liquid phases. To incorporate the phase change enthalpy, different methods are employed as discussed in Section 2.4.2. In the present work, the effective heat capacity method is employed, where the heat capacity during phase change constitutes a combination of the specific heat and the latent heat as shown in Eqs. (3.8-3.9). Effective heat capacity method was implemented initially by Bonacina et al. (Bonacina et al., 1973) and has been validated by several authors (Niyas et al., 2017a; Ogoh and Groulx, 2012; Sunku Prasad et al., 2018; Yang and He, 2010) to account for heat capacity variation during phase change.

The flow and energy interactions in the PCM region are governed by Eqs. (3.3-3.5) (Chung, 2018). The source terms added in the momentum equation govern the phase change and natural convection process. Eq. (3.6) signifies the Boussinesq approximation (Demuren and Grotjans, 2009) which eliminates the variation in density between the hotter and the colder PCM fluid and approximates to source term $\vec{S}_b$, representing the effect of natural convection in terms of temperature variation in the PCM region. During phase change of PCM, both the solid and liquid phase co-exist and the condition of the PCM is termed as mushy zone. The source term mentioned in Eq. (3.7) is taken from Kozeny-Carman equation (Brent et al., 1988), which accounts for smooth transitions between the solid and the liquid velocities. For higher values of mushy zone constant (A_m), the convection strength inside PCM decreases, which reduces the melting rate. Several literature works have recommended different values of A_{mushy} varying between 10^3 to 10^7 (Kumar and Krishna, 2017) and the value considered in the present study is 10^5. ϵ is a very small number to prevent the division of source term by zero and its value is 10^{-3}.

Continuity Equation

$$(\nabla.(\rho\vec{v}))_{PCM} = 0 \tag{3.3}$$

Momentum Equation

$$\left(\frac{\partial(\rho\vec{v})}{\partial t} + \rho(\vec{v}.\nabla)\vec{v}\right)_{PCM} = \left(-\nabla P + \nabla.(\mu\nabla\vec{v}) + \vec{S}_b + \vec{S}_m\right)_{PCM} \tag{3.4}$$

Energy Equation

$$\left(\frac{\rho c_p}{k}\right)_{PCM}\frac{DT}{Dt} = \nabla^2 T \tag{3.5}$$

Source Terms

$$\vec{S}_b = -\rho\vec{g}\beta(T - T_0) \text{ (Boussinesq Approximation)} \tag{3.6}$$

$$\vec{S}_m = -\frac{(1-\delta^2)}{(\delta^3+\epsilon)}A_m\vec{v} \text{ (Kozeny-Carman equation)} \tag{3.7}$$

Specific Heat of PCM

$$(c_p)_{PCM} = \begin{cases} (c_p)_S \; for\; T < T_S \\ (c_p)_{eff} \; for\; T_S \le T \le T_L \\ (c_p)_L \; for\; T \ge T_L \end{cases} \tag{3.8}$$

Effective Specific Heat of PCM

$$(c_p)_{eff} = \frac{(c_p)_S + (c_p)_L}{2} + \frac{\Delta h_f}{T_L - T_S} \tag{3.9}$$

Melt Fraction

$$\delta = \begin{cases} 0, for\; T < T_S \\ \frac{T-T_S}{T_L-T_S}, for\; T_S \le T \le T_L \\ 1, for\; T \ge T_L \end{cases} \tag{3.10}$$

The governing equations (Eqs. 3.11-3.13) for the HTF flow are given below;

Continuity Equation

$$\nabla.(\rho\vec{v})_{air} = 0 \tag{3.11}$$

Momentum Equation $$\left(\frac{D(\rho\vec{v})}{Dt}\right)_{air} = (-\nabla P + \mu\nabla^2\vec{v})_{air} \quad (3.12)$$

Energy Equation $$\left(\frac{\rho c_p}{k}\right)_{air}\frac{DT}{Dt} = \nabla^2 T \quad (3.13)$$

The energy equation for the heat transfer surface (tube material or fins) is given by Eq. (3.14) below;

Energy Equation for the heat transfer tube or fins $$\left(\frac{\rho c_p}{k}\right)_{m}\frac{DT}{Dt} = \nabla^2 T \quad (3.14)$$

3.2.2 Assumptions

The following assumptions are made while developing the model.

- PCM is homogeneous and isotropic.
- HTF flow is assumed to be laminar.
- Density variation in the PCM flow is introduced using the Boussinesq approximation.
- Natural convection process is symmetric about the vertical axes.
- The natural convection effect during discharging is neglected (Niyas et al., 2017b; Seddegh et al., 2015a).

The above said assumptions are valid for all the numerical modelling work conducted in the present thesis work unless stated otherwise.

3.2.3 Numerical procedure

The finite element based software COMSOL Multiphysics 4.3a ("COMSOL Inc.,") has been employed to solve the governing equations (Eqs. 3.3– 3.14). The system of equations at each Newton-Raphson step are solved using a direct linear solver (PARDISO). Euler Backward difference formula (BDF) is employed for time stepping. The time step is adaptive in nature and varies based on the error values at previous iterations. The initial minimum and maximum time steps chosen are 0.001 s and 0.1 s, respectively. The chosen maximum time step helps to solve the problem in minimum computational time. The problem is highly non-linear and the solution diverges for convergence criteria less than 10^{-3}. Hence, the convergence criterion is set as 10^{-3}. The simulations are performed using a Dell precision T7610 workstation, equipped with two Intel Xeon E5-2650 v2 processors and 64 GB 1866 MHz RAM (refer to the section Appendix D for additional information).

3.2.4 Experimental validation of the numerical model

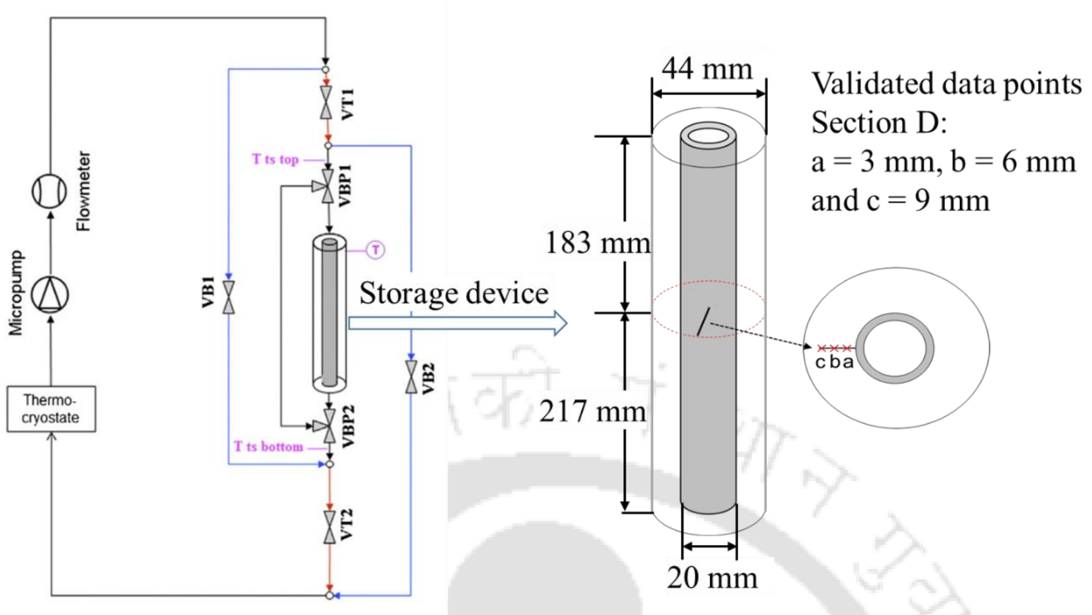

Figure 3.1. Experimental test facility, LHS device, dimensions and thermocouple positions of the validated experimental data (Longeon et al., 2013).

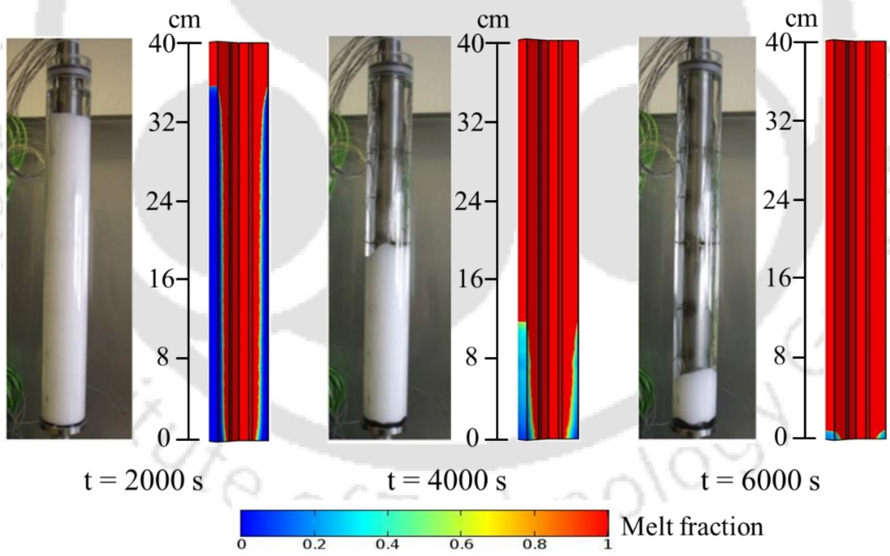

Figure 3.2. Comparison of progression of melt front from the experimental data (Longeon et al., 2013) with numerical simulation data.

The effective heat capacity method described above is validated with the experimental data reported by Longeon et al. (Longeon et al., 2013). Figure 3.1 shows the layout of the experimental system developed by Longeon et al. (Longeon et al., 2013). Paraffin (RT35) having a melting point of 35 ºC was used as PCM in the reported work and was enclosed in the annular region of a concentric tube system. The inner diameter of the outer Plexiglas transparent shell was 44 mm, whereas the inner HTF tube was made of Stainless steel having inner diameter and thickness of 15 mm and 2.5 mm, respectively. The length of the storage system was 400 mm. Water was used as the heat transfer fluid in the study.

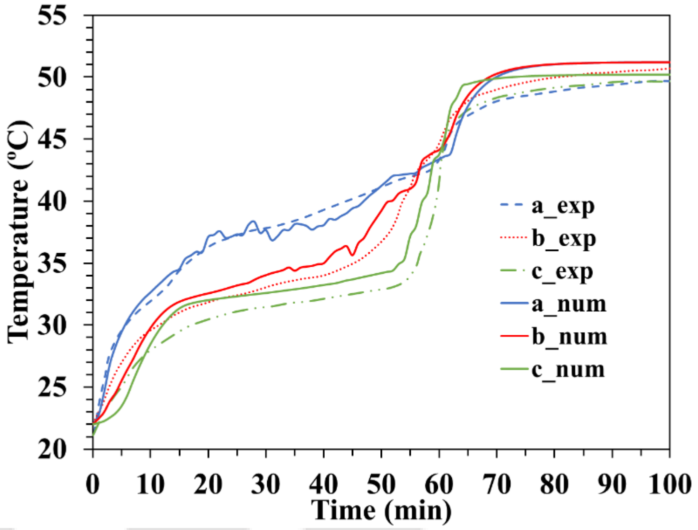

Figure 3.3. Validation of the numerical data with the charging process.

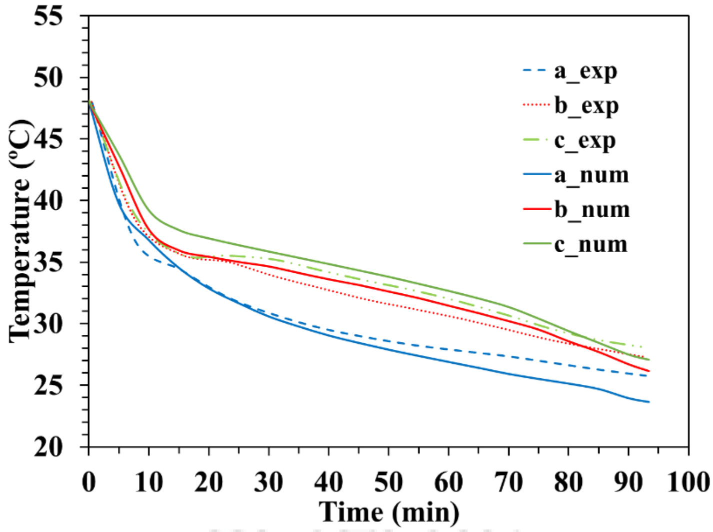

Figure 3.4. Validation of the numerical data with the discharging process.

The inlet HTF temperature of 52 ºC is the experimental condition selected for the validation purpose during the charging process. Water flows from top to bottom of the storage device and the valves VT1 and VT2 are in open condition. Initially, the PCM was maintained at 22 ºC and the average velocity of water at tube inlet was 0.01 m/s, thus maintaining a laminar flow (Reynolds number < 2300 as reported by Longeon et al. (Longeon et al., 2013)) condition. In the reported work, temperature was recorded at several angular (0°, 90°, 135°, 180°, 225° and

270°) and radial positions (a=3 mm, b=6 mm and c=9 mm) at seven sections (A-G) along length. The variation at different angular positions was found to be negligible. The evolution of melting front computed numerically after different time intervals is shown in Figure 3.2, and is observed to be slightly faster than in the experimental observations. This happens primarily due to the fact that the heat transfer is considered ideal, such that there is no heat loss to the surroundings, which is not possible during real-time experiments. Figure 3.3 shows the deviation of temperature profile obtained through simulations from experimental data at axial location D with radial distances of a, b and c from the outer surface of the inner tube. Numerically predicted values are found to closely match with experimental data with a maximum deviation of ±3.5 ºC.

The numerical model for the discharging process has been validated for location D with the discharging experiment reported by Longeon et al. (Longeon et al., 2013) and shown in Figure 3.4. The PCM initial temperature was fixed as 47 ºC during the discharging experiment. It is observed that the numerical data closely matches with the data obtained from the experiments with a maximum error of ±2.5 ºC.

3.3 Experimental setup

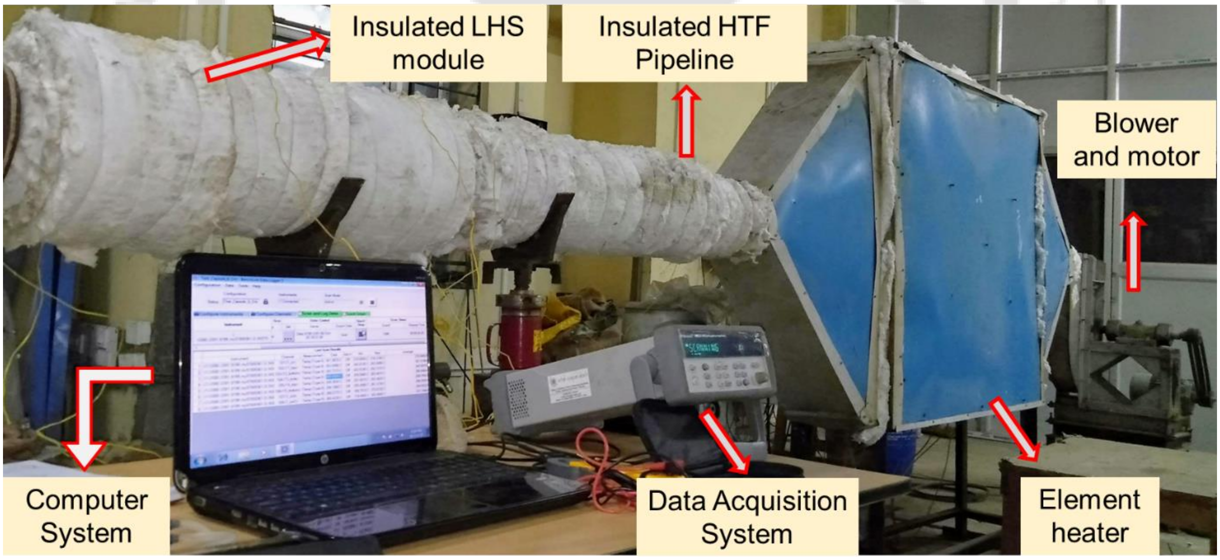

Figure 3.5. Photograph of the thermal energy storage (TES) test facility.

A custom fabricated experimental test facility has been designed and commissioned at the Indian Institute of Technology Guwahati to study the performance of TES systems. The setup has been developed to provide wide range of flow conditions (0-120 m^3/h) while operating at high temperatures (up to 400 °C). The schematic of the experimental test bed is shown in Figure 3.5.

3.3.1 Components of the experimental system

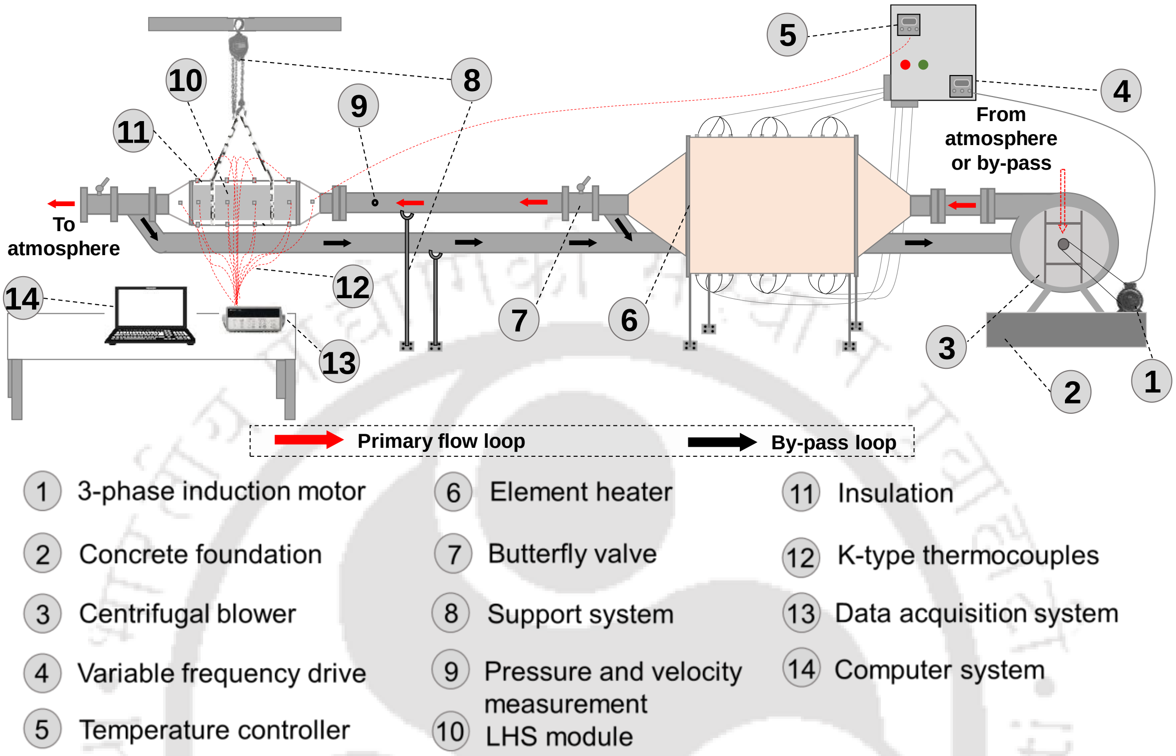

Figure 3.6. Layout of the thermal energy storage (TES) test facility with important components.

The layout describing the essential components and flow directions in the TES system is shown in Figure 3.6 and the specifications for the various labelled components are described in Table 3.1. The system comprises of a primary flow loop (red arrows in Figure 3.6) in which the suction of the atmospheric air (HTF) takes place at blower inlet. The air is then passed to the heater section which consists of three rows, each having 16 number of 1 kW electric element heaters. The heated air is then passed to the LHS module where it passes through the HTF tubes of the LHS module. After charging or discharging, the HTF at the exit of the module is either released to the atmosphere or passed through the by-pass loop (black arrows in Figure 3.6). The by-pass loop is operated through by-pass flow valves and is operational only under the following conditions i.e. (a) HTF circulation back and forth between the heater and by-pass at heater exit to maintain the required HTF temperature, and (b) utilizing the heat available at the exit of the primary flow loop and passing the air back to the blower suction. The desired HTF flow rate conditions are achieved using a variable-frequency drive connected to the motor which runs the blower. The HTF flow rate is measured at the LHS module inlet using a pitot-tube device. The HTF temperature required during the charging/discharging experiments is maintained using a temperature controller which controls the heater operation using the LHS module inlet temperature as the input. The HTF is circulated in the system in a 101.6 mm (4-inch) channel insulted with a 4-inch (~100 mm) thick layer of ceramic wool blanket (k = 0.12 W m^{-1} K^{-1}, as provided by the supplier).

Table 3.1. Specifications of the different components of the experimental test facility.

Label number (refer Figure 3.6)	Specifications (refer to the section Appendix A)
1	3 phase induction motor, Make – ABB, Capacity - 2 hp
2	Concrete foundation for blower support
3	Custom fabricated stainless steel centrifugal blower, Capacity – 120 m^3/h
4	Variable frequency drive, Make – ABB, Rating – 2 hp
5	Temperature controller, Make - SELEC
6	Custom fabricated element heater equipped with power supply using flame-retardant glass fibre single core cables (Make - ÖLFLEX® HEAT 650 SC) supplied by LAPP India, Heater capacity – 48 kW
7	Flow control butterfly valves
8	System support
9	Pitot tube velocity/flow measurement, Make – Testo, Model - 512
10	LHS module
11	Ceramic wool insulation
12	Custom made K-type thermocouples, Accuracy - ±0.5 °C
13	Data acquisition system, Make – Agilent, Model – 34970A
14	Computer system for data logging and processing

3.3.2 Phase change material (PCM), heat transfer fluid (HTF) and tube material

Molten salt Sodium Nitrate ($NaNO_3$) was used as the PCM. The differential scanning calorimetry (DSC) analysis was performed to determine the phase transitions of the PCM using DSC Analyzer (Make: Perkin Elmer) at a heating rate of 10 °C/min. The heat flow variation versus PCM sample temperature is plotted in Figure 3.7. The melting temperature of the PCM was estimated as 305.1 °C (T_M), and the phase change enthalpy was 175.1 kJ/kg. Air was used as the HTF considering its benefits such as high stability, low viscosity, zero cost and free availability (Vignarooban et al., 2015). The HTF tubes and the LHS module were custom fabricated using stainless steel grade SS 310S due to its high corrosion resistance. The thermo-physical properties of Sodium nitrate and SS 310S are described in Table 3.2, whereas the thermo-physical properties of air (refer Table 3.3) are adopted from the standard property charts (Incropera et al., 2007).

Table 3.2. Thermo-physical properties of Sodium nitrate and SS 310S.

Property	Value	
	Sodium Nitrate (Conference	SS 310S
Melting point temperature (°C)	305.1*	-
Thermal conductivity (W m^{-1} K^{-1})	0.5	14.2
Density (kg m^{-3})	2260 (solid), 1910 (liquid)	
Specific heat (J kg^{-1} K^{-1})	1600 (solid), 1655 (liquid)	500
Thermal expansion coefficient (K^{-1})	3.65×10^{-4}	
Latent heat (kJ kg^{-1})	175.1*	-
*properties estimated from the DSC analysis (refer Figure 3.7)		

Table 3.3. Thermo-physical properties of air (Incropera et al., 2007).

Property	**Expression**
Density (kg m^{-3})	$0.0034845PT^{-1}$
Thermal conductivity (W m^{-1} K^{-1})	$-0.00227583562 + 1.15480022\,\mathrm{E}(-4T) + 7.90252856\,\mathrm{E}(-8T^2) + 4.11702505\,\mathrm{E}(-11T^3) - 7.43864331\,\mathrm{E}(-15T^4)$
Specific Heat (J kg^{-1} K^{-1})	$1047.63657 - 0.372589265T + 9.45304214\,\mathrm{E}(-4T^2) - 6.02409443\,\mathrm{E}(-7T^3) + 1.2858961\,\mathrm{E}(-10T^4)$
Dynamic Viscosity (10^{-5} Pa s)	$-8.38278\,E(-7) + 8.35717342\,E(-8T) - 7.69429583\,E(-11T^2) + 4.6437266\,\mathrm{E}(-14T^3) + 1.06585607\,E(-17T^4)$

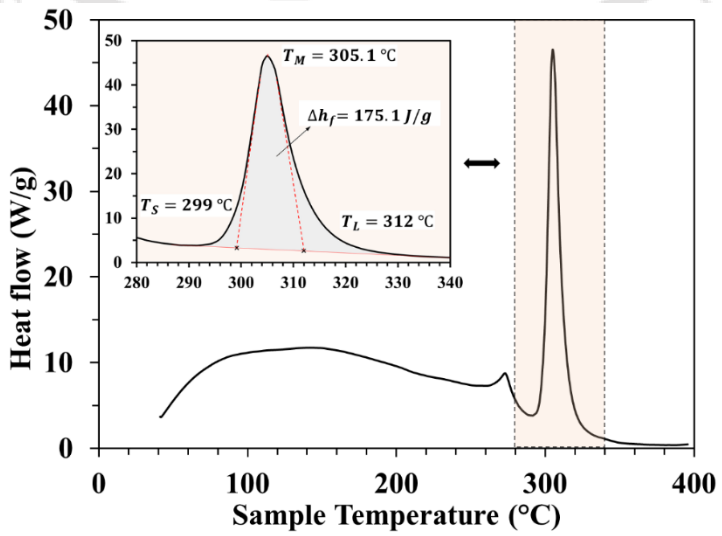

Figure 3.7. Differential scanning calorimetry (DSC) curve for sodium nitrate.

3.3.3 Uncertainty analysis

The uncertainty occurred in the calculation of different quantities such as flow rate, energy stored and energy discharged due to err or in the measured quantities. The different measured quantities include temperature, PCM weight and the HTF velocity. The temperature was measured using calibrated K-type thermocouples having accuracy ±0.5 °C. The accuracy of pitot tube based velocity meter used for velocity measurements is ±0.1 m/s, respectively. The uncertainty is calculated using the Kline and McClintock (Moffat, 1988) method described in Eqs. (3.15-3.16) (refer to the section Appendix B for sample uncertainty calculations).

Uncertainty in calculating a single quantity:

$$\delta R_X = \frac{\partial R}{\partial X}\delta X \tag{3.15}$$

where R is the dependent quantity and is a function of the measured quantity X.

Total uncertainty in the calculated quantity R is given by

$$\delta R = \left(\sum\left(\frac{\partial R}{\partial X_i}\delta X_i\right)^2\right)^{1/2} \tag{3.16}$$

where R is a function of independent or measured quantities X_i.

3.4 Summary

This chapter presents the general procedures followed for the design and development of the high-temperature LHS systems. The governing equations to develop the numerical model, the basic assumptions, numerical procedure and the experimental validations are discussed. Later, the various components of the high-temperature thermal energy storage experimental test facility developed at the Indian Institution of Technology Guwahati are described. The procedure to conduct the experimental investigations, material selection and the error analysis is described in detail.

Chapter 4

Performance investigations of high-temperature LHS system: Multi-tube design[‡]

Preface

High-temperature thermal energy storage (TES) systems improve the reliability and performance of solar-powered technologies due to their ability to levelize the gap between energy supply and demand. The shell and tube heat exchanger design is an effective TES solution, especially for developing high-temperature pilot-plant scale industrial and commercial applications due to low heat loss to the surroundings and higher heat transfer characteristics (Li et al., 2019). Optimizing the number of HTF tubes aids in developing a compact LHS system with improvement in the heat transfer dynamics. This happens due to an increase in the heat transfer surface area and the intensification of natural convection in the system (Mastani et al., 2019).

The work presented in this chapter focuses on the design, development and performance investigations of a high-temperature latent heat storage (LHS) system. A 2-D numerical model is developed to optimize the number and size of HTF tubes in a multi-tube LHS system by fixing the total heat transfer surface area. Further, experimental investigations were carried out on a developed multi-tube LHS module with sodium nitrate used as the phase change material (PCM) filled in the shell side and air was used as the HTF. Important performance parameters such as charging/discharging time, energy stored/discharged, and output power were estimated by varying the flow rate and inlet temperature of air. The energy storage of ~19.5 MJ was achieved with maximum PCM temperature reaching up to 365 ºC.

[‡] A portion of the findings reported in this chapter are published as the following research article:

Sodhi GS, Vigneshwaran K, Jaiswal AK, Muthukumar P. Assessment of heat transfer characteristics of a latent heat thermal energy storage system: Multi tube design. Energy Procedia. 2019 Feb 1;158:4677-83.

4.1 Design and performance evaluation parameters

A multi-tube LHS module is developed and performance investigations are carried out using the experimental test facility described in Section 3.3. The dimensions of the multi-tube LHS system with PCM on the shell side and HTF on the tube side are shown in Figure 4.1. The outer shell diameter (D_o) is calculated by fixing the LHS capacity (Q_L), length (L_s) and size of the inner HTF tubes (d_o) using Eqs. (3.1-3.2) described in Section 3.1.

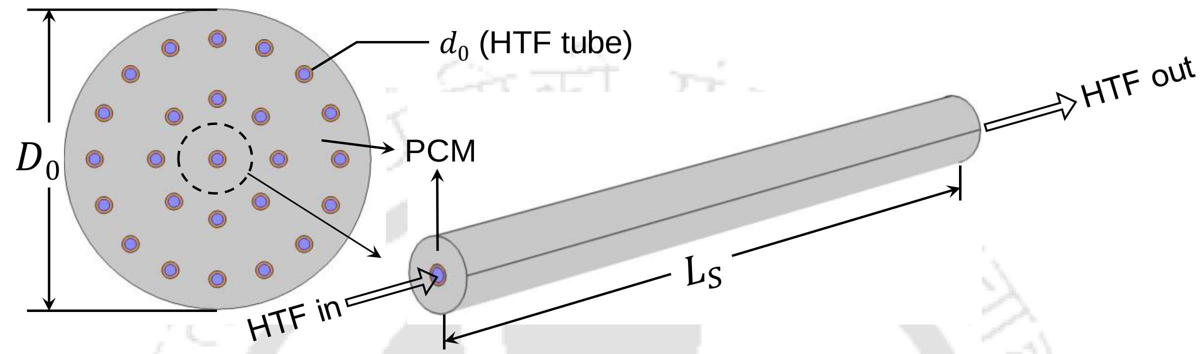

Figure 4.1. Schematic of the multi-tube LHS system.

The following parameters are considered as important while analysing the performance of the multi-tube LHS system;

Melt fraction (δ) – The melting fraction is the fraction of the PCM melted or solidified during charging or discharging, respectively, as shown in Eq. (4.1). The melt fraction varies between the melting temperature range ($T_L - T_S$) of the PCM.

$$\delta = \begin{cases} 0 & for\ T_{pcm} < T_S \\ \dfrac{T_{pcm} - T_S}{T_L - T_S} & for\ T_S \leq T_{pcm} \leq T_L \\ 1 & for\ T_L > T_{pcm} \end{cases} \tag{4.1}$$

Charging and Discharging time – The charging time is estimated based on the melting condition throughout the LHS module. The LHS module is said to be fully charged as the value of δ is 1 i.e. the average of temperature at all the temperature measuring locations reaches T_L. Similarly, the discharging time is estimated as the time taken for the LHS module to solidify completely i.e. the value of δ at all the temperature measuring locations based on Eq. (4.1) is 0.

Energy charged and discharged – During charging, the LHS module is charged by the HTF as the heat transfer takes place due to the temperature difference between the HTF and PCM (T_{in}-

T_i). Initially, the energy is stored in the form of sensible heat, whereas, as the PCM melts, it absorbs the latent heat and changes its phase from solid to liquid. Later, the liquid PCM stores the sensible heat and reaches a maximum temperature denoted by T_f. The sensible, latent and the total heat absorbed by the LHS module are given in Eqs. (4.2-4.4).

$$Q_{C,sensible} = m_{pcm}c_s(T_M - T_i) + m_{pcm}c_L(T_{pcm} - T_M) \tag{4.2}$$

$$Q_{C,latent} = (\delta)m_{pcm}\Delta h \tag{4.3}$$

$$\begin{aligned} Q_{C,total} &= Q_{C,sensible} + Q_{C,latent} \\ &= m_{pcm}(c_s(T_M - T_i) + (\delta)\Delta h_f + c_L(T_{pcm} - T_M)) \end{aligned} \tag{4.4}$$

During discharging, the PCM is initially in the liquid state and since the HTF temperature is lower than the PCM temperature, the LHS module discharges energy till it reaches a minimum temperature. The sensible, latent and the total heat discharged by the LHS module are given in Eqs. (4.5-4.7).

$$Q_{D,sensible} = m_{pcm}c_L(T_i - T_M) + m_{pcm}c_S(T_M - T_{pcm}) \tag{4.5}$$

$$Q_{C,latent} = (1 - \delta)m_{pcm}\Delta h_f \tag{4.6}$$

$$\begin{aligned} Q_{D,total} &= Q_{D,sensible} + Q_{D,latent} \\ &= m_{pcm}(c_L(T_i - T_M) + (1 - \delta)\Delta h_f + c_s(T_M - T_{pcm})) \end{aligned} \tag{4.7}$$

The charging or discharging power is calculated as a derivative of the cumulative total energy charged or discharged with respect to time as shown in Eq. (4.8).

$$P_c(or\ P_d) = \frac{\mathrm{d}Q_{C,total}\,(or\ dQ_{D,total})}{\mathrm{dt}} \tag{4.8}$$

4.2 Numerical model: multi-tube LHS system

A 2D numerical model is developed to optimize the number of tubes in the multi-tube LHS system. Three multi-tube models namely; Case A: 13 (1-inch) tubes, Case B: 17 (3/4-inch) tubes and Case C: 25 (1/2-inch) tubes as shown in Figure 4.2 were developed to analyse the effect of varying the HTF tube size and the number of tubes on the charging and discharging characteristics. In all the three cases, the heat transfer tube surface area and the PCM volume are fixed. The model considers only the PCM domain subjected to the temperature boundary condition of the heat transfer tube surface. Fixing the LHS capacity (Q_L) and the outer HTF tube diameters (d_0) for all the cases, the outer shell diameters (D_0) are calculated per unit length using Eqs. (3.1-3.2).

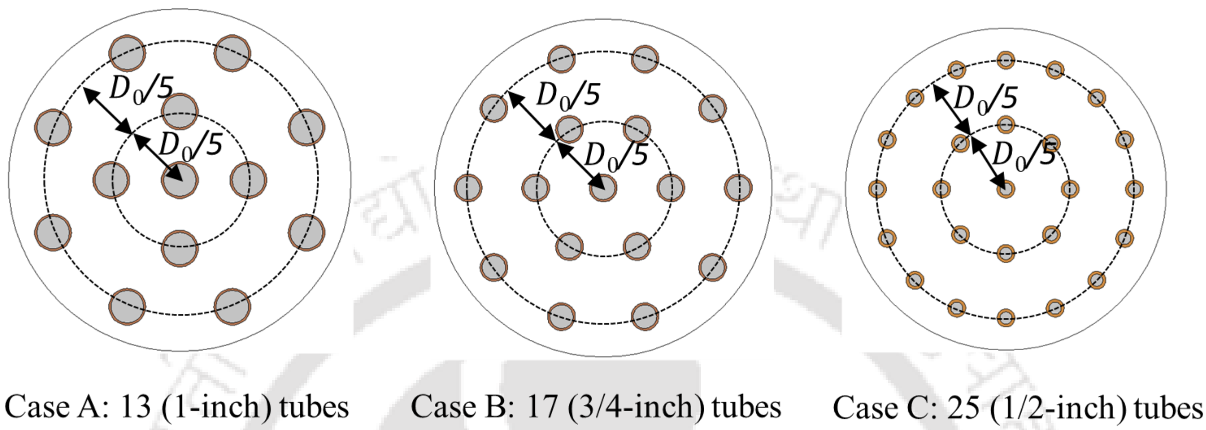

Figure 4.2. 2D numerical model domain of the multi-tube LHS system (Case A: 13 tubes, Case B: 17 tubes and Case 3: 25 tubes).

4.2.1 Boundary conditions

The numerical model is subjected to the following boundary conditions (Eqs. 4.9-4.13):

For charging; $T_{wall} > T_M > T_i$

At $t = 0$ s, $T = T_i = 286$ °C (for all domains) (4.9)

For $t > 0$, $T_{wall} = 326$ °C (4.10)

For discharging; $T_{wall} < T_M < T_i$

At $t = 0$ s, $T = T_i = 326$ °C (for all domains) (4.11)

For $t > 0$, $T_{wall} = 286$ °C (4.12)

Outer shell of the LHS model is adiabatic; $\left.\frac{\partial T}{\partial r}\right|_{r=D_o/2} = 0$ (4.13)

The numerical procedure, governing equations and assumptions for the PCM domain are described in detail in Section 3.2.

4.2.2 Selection of number and size of HTF tubes

The melt fraction variation with time for the charging process is shown in Figure 4.3. The melting time obtained for Case A, Case B and Case C are 232, 210 and 185.5 min, respectively.

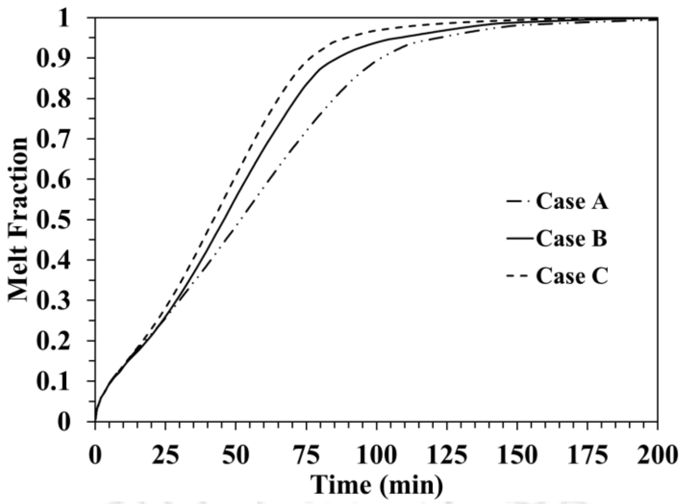

Figure 4.3. Melt fraction variation with time during the charging process.

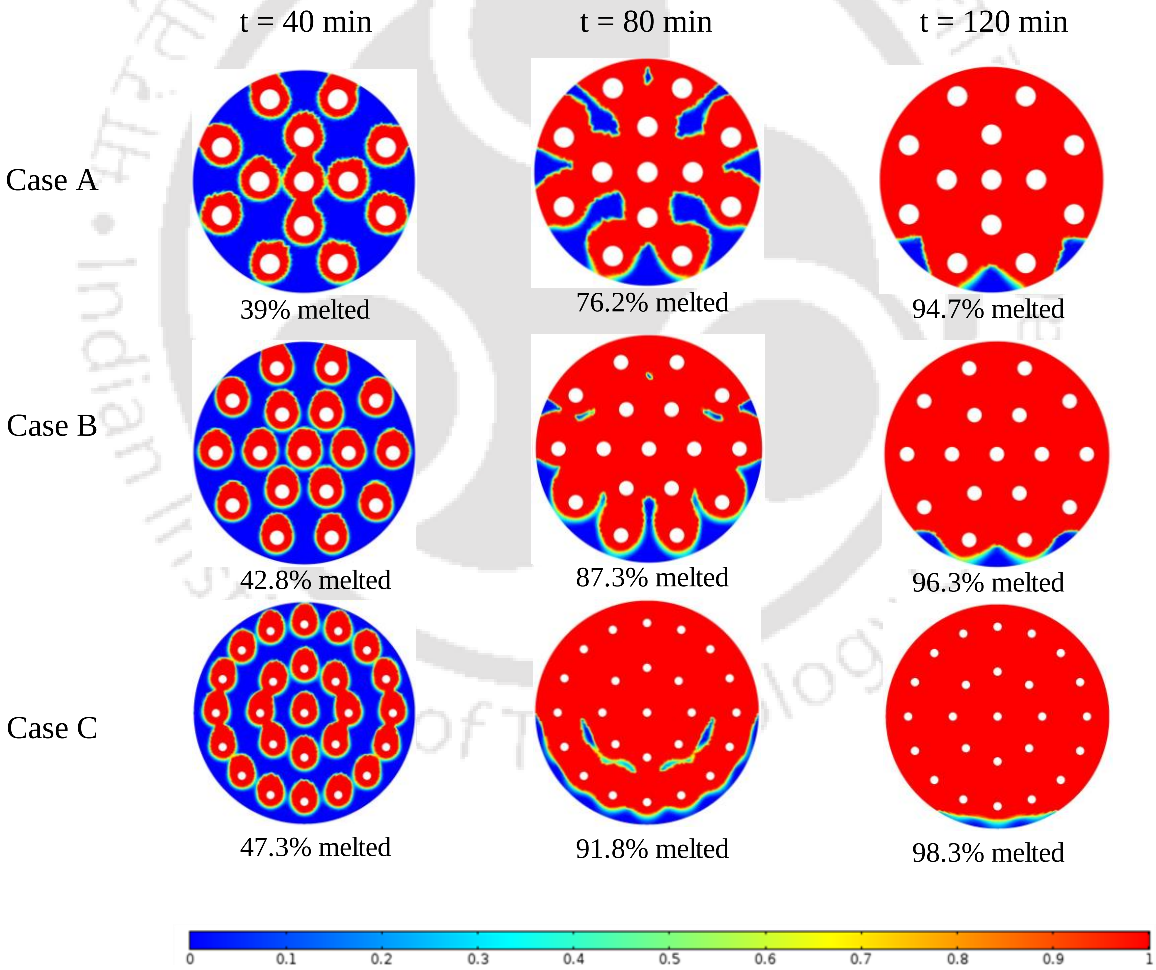

Figure 4.4. Melt fraction contours for Case A, Case B and Case C after time interval of 40, 80 and 120 min during charging.

During the charging process, the heat transfer in the PCM region occurs due to the combined effect of natural convection and conduction. The conduction heat transfer is dominant near the HTF tube walls only initially, however, the heat transfer occurs predominantly due to natural convection at a later stage. The natural convection effect is visualized using the melt fraction contours shown in Figure 4.4. For a constant PCM quantity and fixed heat transfer surface area of tubes, Case C performs better than the other cases. There is a reduction of 9.5% and 20% in the charging time in Case B and Case C than Case A. It is observed that as the number of tubes increases, more convection cells originate from the HTF tubes as shown in Figure 4.4. After 80 min, the merging of the convection cells is visible for all the cases. The rate of natural convection heat transfer increases significantly in Case B (87.3% melted) and Case C (91.8% melted) than Case A (76.2% melted) especially in the upper section of the PCM container as the convection cells merge. The occurrence of this phenomenon in multi-tube heat exchangers has been reported extensively in the literature previously (Esapour et al., 2016). The improvement in the natural convection effect in Case C results in minimum charging time. By increasing the number of tubes from 13 to 17, there is a significant improvement in the charging rate, however, it does not improve notably thereafter by increasing the number of tubes to 25.

During discharging, the PCM loses its heat to the HTF and gets solidified. The melt fraction variation with respect to time during the discharging process is plotted in Figure 4.5. Case A, Case B and Case C are solidified in 280, 228 and 147 min respectively. The solidification contours during the discharging process at the time intervals of 50 min, 100 min and 150 min are shown in Figure 4.6. The natural convection does not affect the rate of heat transfer during discharging significantly and has been neglected (Seddegh et al., 2015a). Initially, the solidification fronts originate at all the HTF tube surfaces. After 100 min, it is observed that the solidification fronts cover a greater region in Case C (81.1% solidified) as compared to Case A (64.3% solidified) and Case B (71.7% solidified). The improvement in conduction heat transfer occurs in Case C than Case A and Case B due to better distribution of heat transfer surfaces throughout the PCM region which reduces the overall thermal resistance.

Both the charging and discharging rate are improved by using more number of smaller size HTF tubes than using less number of larger size tubes due to better distribution of heat transfer surfaces inside the PCM region. The multi-tube LHS module is developed based on the outcomes of the numerical model and the performance investigations were carried out as presented in the upcoming sections.

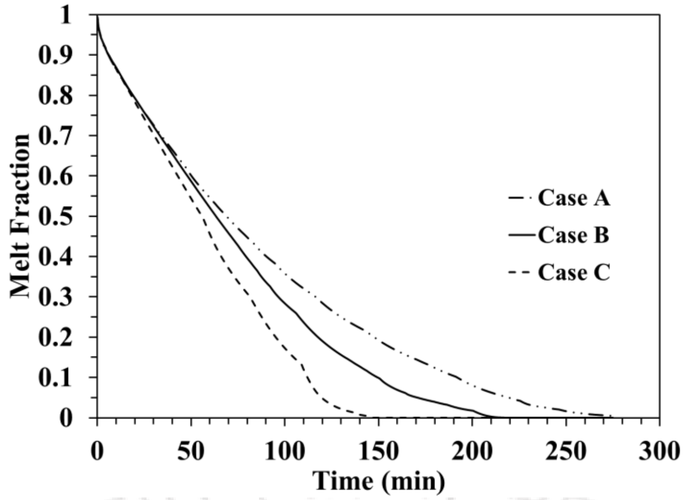

Figure 4.5. Melt fraction variation with time during the discharging process.

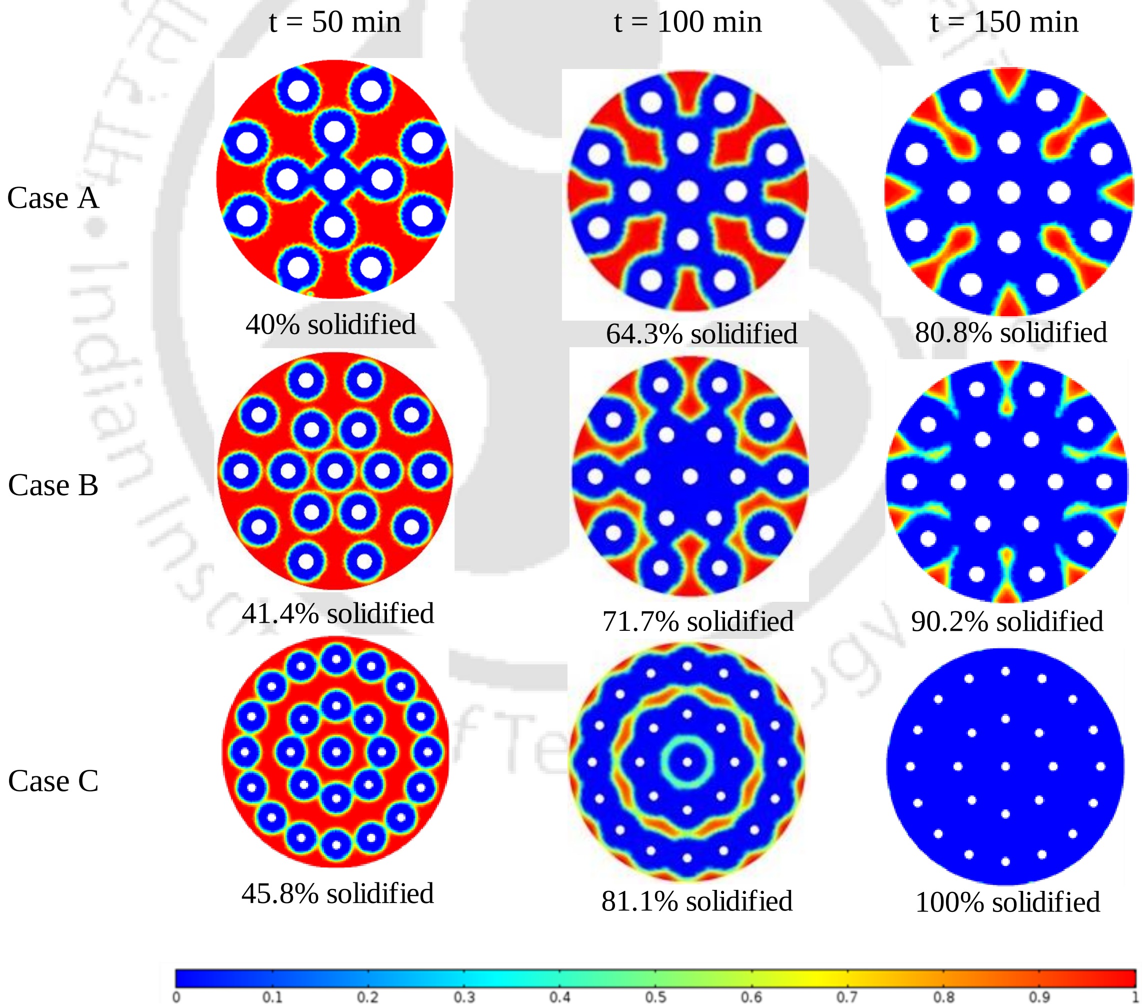

Figure 4.6. Solidification front during the discharging process for Case A, Case B and Case C after time interval of 50, 100 and 150 min.

4.3 Development and performance investigations of the multi-tube LHS module

The design of the LHS module based on the 2D model described above comprises of a shell and tube system. Air is chosen as the HTF and flows through the HTF tubes and sodium nitrate ($NaNO_3$) is chosen as the PCM and filled in the shell side of the module. Air flows through 25 HTF tubes of SS 310S (Stainless steel) material which ensures high-temperature corrosion resistance. The thermo-physical properties of the HTF, PCM and the tube material are described in Section 3.3.2.

The experimental LHS system was designed for a LHS capacity of 10.7 MJ, however, additional sensible energy was charged or discharged during the actual operation. While performing the experimental investigations, approximately 61 kg solid PCM was filled in the LHS module to store the required latent heat. The dimensions of the fabricated LHS module and the location of different thermocouples is described in Figure 4.7(a)-(c). The system performance is analysed through temperature data measured using K-type thermocouples. One thermocouple each was fixed at the LHS inlet and outlet, and additionally one thermocouple connects the LHS inlet and the temperature controller used to monitor and maintain a constant HTF temperature during the experiments. It is practically not possible to maintain a constant HTF temperature while the system is operational as the heater continuously fluctuates between the ON and OFF condition. Three thermocouples at radial positions described in Figure 4.7(c) are installed at each of the module sections 1, 2, 3 and 4 shown in Figure 4.7(b). The picture of the LHS module with thermocouples installed at the described positions before and after insulating is shown in Figure 4.7(d). While conducting the analysis, the recorded thermocouple data shall be denoted as $T_{x,i}$, where x represents the radial locations $a/b/c$, and i represents the axial locations marked by the sections 1/2/3/4.

The charging and discharging experiments were performed for a range of inlet HTF conditions listed in Table 4.1. The schematic and components of the high-temperature LHS system developed to conduct the experimental investigations on the LHS module is described in detail in Section 3.3. The atmospheric air heated using the element heater is allowed to pass through the LHS module to preheat the PCM to the desired initial temperature condition (T_i). The inlet to the LHS module is then closed to continue the HTF heating to the required inlet temperature (T_{in}) condition. During charging, T_{in} is higher than T_i, such that the heat transfer takes place from the HTF to the PCM, whereas, during discharging, T_{in} is lesser than T_i, such that direction of heat transfer is reversed. The air at the outlet is either exhausted to the atmosphere or re-circulated to the element heater.

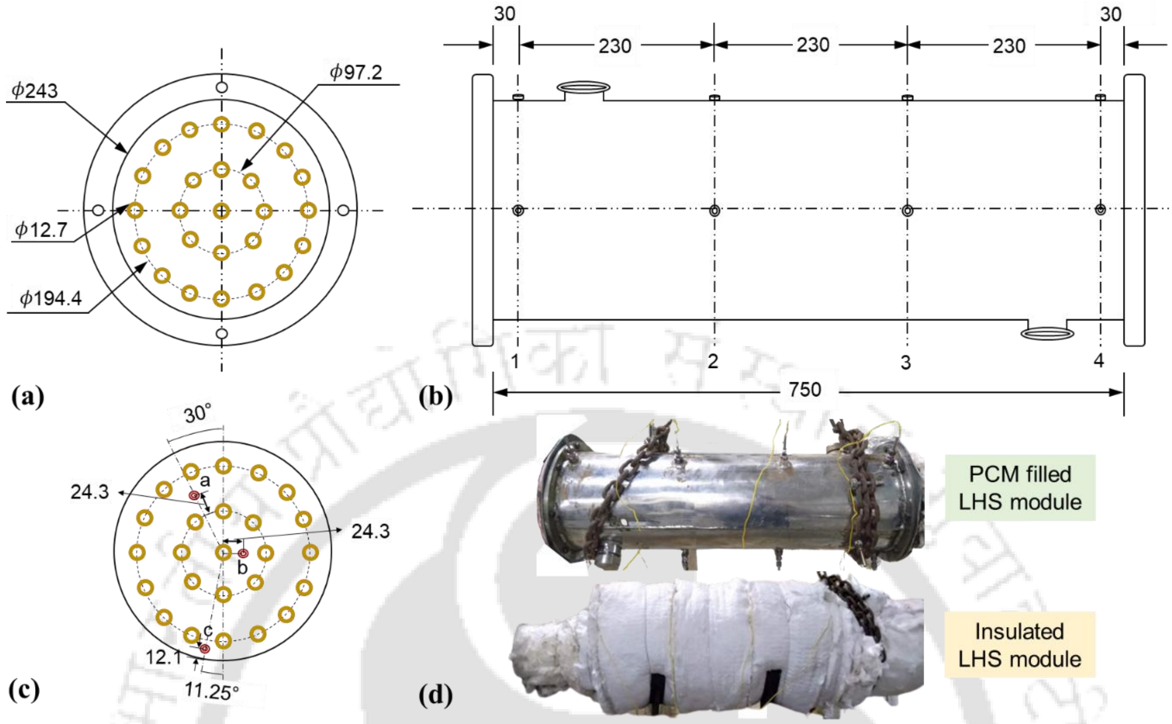

Figure 4.7. (a) Dimensions of the LHS module, (b) thermocouple locations along the axial direction (sections 1,2,3 and 4), (c) thermocouple locations in the radial direction (locations a, b and c), and (d) picture of the LHS module before and after insulation.

The experiments were devised based on rigorous preliminary assessment trials to study the operating conditions of the air heater and the centrifugal blower. It was found that the maximum HTF temperature was the limiting condition for deciding the HTF flow rate. During the real-time operation, both the flow rate and temperature conditions change in a reverse manner with respect to each other, such that increasing the flow rate reduces the inlet HTF temperature and vice versa. Therefore, the maximum flow rate (102 m^3/h) was decided based on the maximum achievable HTF temperature (380 ºC) and further parametric investigations were performed based on lower HTF flow rate values (43.8 m^3/h, 73 m^3/h and 102 m^3/h). The flow rate from the main channel was assumed to distribute uniformly in the HTF tubes. The Reynolds number (Re_{tube}) for the maximum flow rate and temperature condition (102 m^3/h at 380 ºC) during charging is calculated based on the flow through the HTF tubes as shown in Eq. (4.14). During the discharging process, the calculated maximum Re_{tube} (for 102 m^3/h at 225 ºC) is ~3200. Therefore, the flow remains essentially in the laminar regime in most of the experiments, and in the transition regime only during few experiments.

$$Re_{tube} = \frac{4\rho\dot{Q}_{in}}{\pi \times N \times d \times \mu} = \frac{4 \times 0.51 \times 102}{3600 \times \pi \times 25 \times 0.0107 \times 330 \times 10^{-7}} \approx 2085 \qquad (4.14)$$

The uncertainties occurring in the mass flow rate of the air, energy stored and energy discharged due to error in the temperature and flow measurement devices are ±0.0596 kg/min, ±0.5044 MJ and ±0.5043 MJ, respectively.

Table 4.1. List of the charging and discharging experiments conducted.

Experiment no.	HTF Inlet temperature, T_{in} (°C)	LHS module initial temperature, T_i (°C)	HTF flow rate, $\dot{Q}_{in}$ (m^3/h)
Charging			
Exp1	380	275	43.8
Exp2	380	275	73
Exp3	380	275	102
Exp4	360	275	73
Exp5	340	275	73
Discharging			
Exp6	225	330	43.8
Exp7	225	330	73
Exp8	225	330	102
Exp9	245	330	73
Exp10	265	330	73

4.4 Charging and discharging performance of the LHS module

In this section, the results obtained from the charging and discharging experiments are presented in detail. The results are evaluated based on the temporal variation of the temperature data measured by the thermocouples and the profiles for the temperature variations, melt fraction, axial and radial temperature distribution, sensible/ latent/ total energy charged/discharged and power output are presented and analysed.

4.4.1 Charging experiments

4.4.1.1 LHS module temperature variations

The temperature profiles for different thermocouples during charging (Exp2: T_{in}= 380 °C, T_i = 275 °C and $\dot{Q}_{in}$ = 73 m^3/h) are shown in Figure 4.8. The average initial LHS module temperature was maintained as 275 °C during the experiment. The temperatures at different locations were tried to be maintained with minimum fluctuations from the initial temperature through controlled heating before starting the charging experiment, however, practically it was not possible to maintain perfect isothermal conditions throughout the module.

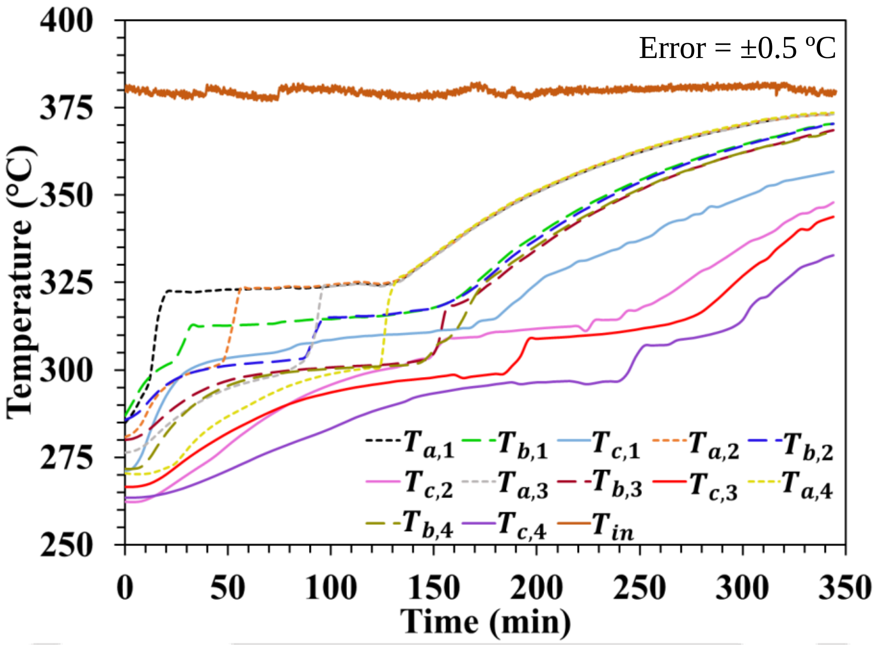

Figure 4.8. Temporal variation of temperature versus time measured at different thermocouple locations (Exp2: T_{in}= 380 °C, T_i = 275 °C and $\dot{Q}_{in}$ = 73 m^3/h; subscript x,i - radial location x = a, b, c and axial location i = 1, 2, 3, 4) during the charging process.

A significant variation in the LHS module temperatures were found during charging and the following important observations can be made;

a) The shape of all the temperature profiles is similar except for the variation in slopes at various transition points. During the initial stages of heating, a steady rise in temperature is observed which indicates heat transfer due to conduction. This is followed by a sharp transition of slope as the temperature rises dramatically, thereby representing the melting and absorption of latent heat by the PCM. The temperature at a certain location rises again after the PCM has melted. The temperature rise in profiles $T_{a,i}$ (i = 1, 2, 3 and 4) are higher than $T_{b,i}$, followed by $T_{c,i}$ indicating a high rate of heat transfer in the upper regions of the LHS module.

b) The radial variation of temperature in the LHS module suggests that the charging in the top region is dominated by the natural convection heat transfer. The natural convection effect is observed due to the buoyancy-driven PCM flow. While heating, the melted PCM mass at a higher temperature and thus having low density, moves towards the top regions and is replaced by the high density PCM at a lower temperature. The high temperature PCM displaces the heat towards the top regions in the LHS module and a flow circulation from bottom to the top regions is formed, which increases the temperature in the top regions. A similar effect for horizontal LHS systems has been highlighted by other studies (Avci and Yazici, 2013; Niyas et al., 2017b; Sodhi et al., 2019a; Yusuf Yazici et al., 2014).

c) The temperature profiles $T_{a,i}$ rise consecutively and remain within a small temperature range (~322-325 °C) for a longer duration. Therefore, after melting, the top PCM layer of the LHS module essentially remains as a pool of liquid PCM at a nearly constant temperature transferring heat to the adjacent PCM. All $T_{a,i}$ attain a specific temperature and rise simultaneously thereafter. A similar behaviour was observed for the temperatures $T_{b,i}$.

d) The temperature profiles $T_{a,i}$ and $T_{b,i}$ are fairly smooth with minimum temperature fluctuations, however, significant temperature fluctuations can be observed in case of $T_{c,i}$ i.e. the thermocouple locations at the bottom of the LHS module.

4.4.1.2 Axial and radial temperature distribution

The charging process affects the heat transfer in the LHS module both in the axial and radial directions. To determine the radial variation, the progression of temperatures $T_{a,3}$, $T_{b,3}$ and $T_{c,3}$ i.e. all the temperature locations at Section 3 are plotted at different time intervals as shown in Figure 4.9(a). Initially at t = 0 min, there occurs a difference (~7-8 °C) between these temperatures due to experimental limitations, however, the temperature evolution with time clearly depicts the heat transfer behaviour. Till 60 min, there is an equal increment in all these temperatures. Beyond this point, the rise in $T_{a,3}$ is higher than $T_{b,3}$ and followed by $T_{c,3}$ throughout the charging process, such that the melting in the top region is faster than the middle and the bottom regions. For the remaining time, the temperature in the top region rises continuously up to steady-state condition, closely followed by the temperature in the middle region, whereas the temperature rise in bottom region is extremely slow. This suggests that the heat transfer in the top regions of the LHS module is faster than the middle and the bottom regions. This occurs due to the natural convection effect during charging, which increases the rate of heat transfer in the top regions, whereas, the heat transfer in the bottom regions is weak due to limited natural convection effect. A similar radial temperature with time was found at all the other sections (Sections 1, 2 and 4) along the length of the LHS module. The heat transfer variation in the axial direction is intuitive as the heat source i.e. the HTF flows along the length of the LHS module. Due to the heat flow from the HTF to the PCM, the PCM temperature increases. Initially, the rate of heat transfer is highest close to the inlet section due to high temperature difference between the HTF and the PCM. As the time progresses, the temperature difference between the HTF and the PCM diminishes along the length and hence, there is a reduction in the heat transfer rate.

The axial temperature distributions are analysed using the temperature rise in the middle region for different axial locations i.e. the progression of $T_{b,1}$, $T_{b,2}$, $T_{b,3}$ and $T_{b,4}$ plotted in Figure 4.9 (b). After 60 min, the temperature rises in the axial location close to the inlet is high, whereas, the temperature at subsequent axial locations is similar. At 120 min, the temperatures $T_{b,1}$ and $T_{b,2}$ are almost similar and higher by ~14 °C than $T_{b,3}$ and $T_{b,4}$. This indicates a decrease in the heat transfer along the system length. The temperatures at all the axial locations nearly equalize at 180 min and beyond this point, the temperature at all the $T_{b,i}$ rises simultaneously until the steady-state is reached. A similar axial distribution exists in the top regions, however, the heat transfer rate in the bottom region is exceptionally low. This happens as the heat transfer in the bottom regions is exceptionally low due to minimum natural convection effect and therefore, the temperature rise is slow.

Apparently, the heat transfer during charging is not restricted to axial or radial directions as the temperature evolution in both the directions is completely inter-linked. The natural convection plays an important role in the heat transfer behaviour of the LHS module during charging.

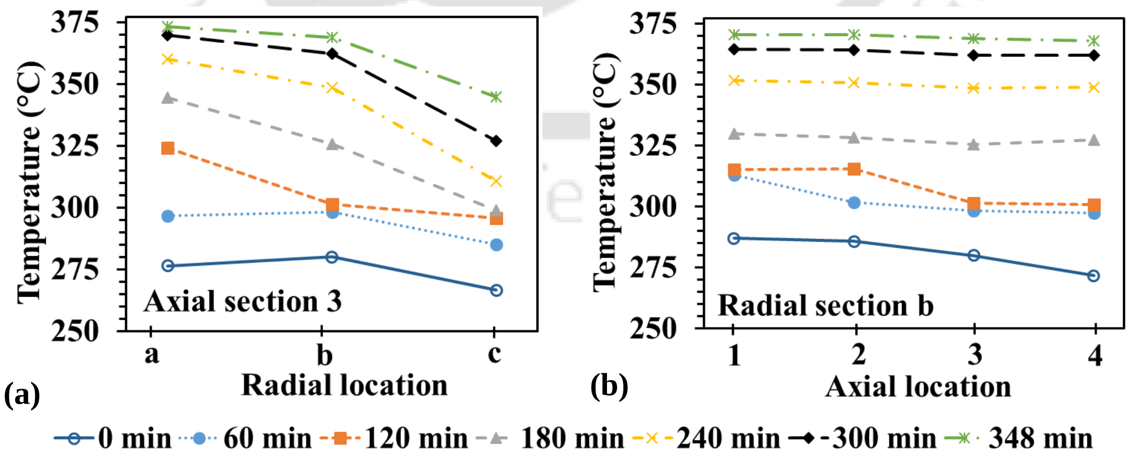

Figure 4.9. Variation of temperature versus time during charging along (a) radial locations a, b and c at axial section 3, and along (b) axial locations 1, 2, 3 and 4 at radial section b.

4.4.1.3 Local and average melt fraction

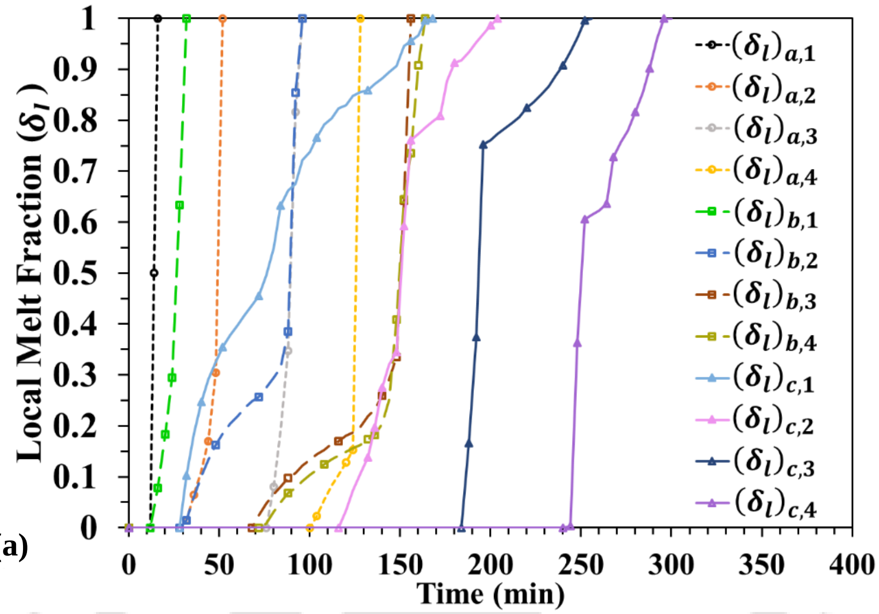

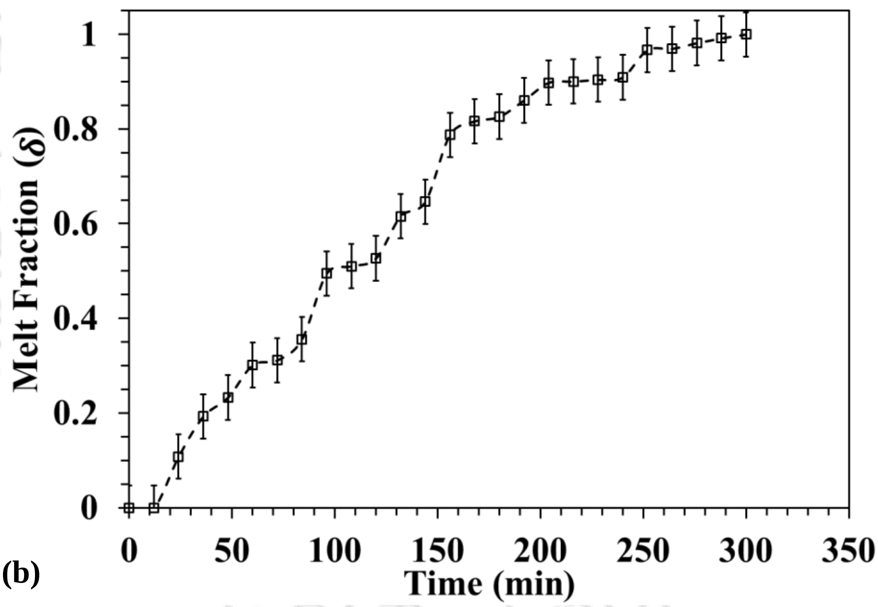

Figure 4.10. (a) Local and (b) average melt fraction throughout the LHS module during charging.

Figure 4.10(a) shows the variation of local melt fraction with time during the charging experiment (Exp2). The temporal evolution of the melt fraction explains that there exists a directional asymmetry in the melting process at various locations of the LHS module. The melting initiates in the top sections first, followed by the middle and the bottom sections. At 128 min, until melting is complete in the top region ($(\delta_l)_{a,1} = (\delta_l)_{a,2} = (\delta_l)_{a,3} = (\delta_l)_{a,4} = 1$) it has only completed partially in the middle region ($(\delta_l)_{b,1} = (\delta_l)_{b,2} = 1$, $(\delta_l)_{b,3} = 0.198$

and $(\delta_l)_{b,4} = 0.163$), and has only started in the bottom region ($(\delta_l)_{c,1} = 0.855, (\delta_l)_{c,2} = 0.106$ and $(\delta_l)_{c,3} = (\delta_l)_{c,4} = 0$). This again reflects upon the effect of domination of natural convection heat transfer in the top region of the LHS module. The melting in the middle region completes in 164 min and is delayed comprehensively in the bottom region as it takes another 128 min for the melting to complete in the LHS module.

Figure 4.10(b) shows the average melting in the LHS module, where it is to be noted that 30% of the total PCM is melted in 60 min. Further, it takes another 67 min for the melting to be completed up to 60%. The average melting rate sustains at an almost linear rate up to 80% of the melting, which is completed in 54% of the total melting time. The rest 20% of the melting is completed in 46% of the total melting time. The comprehensive slowdown occurs close to melting completion due to low temperature gradient between the HTF and the PCM. Only the bottom regions of the LHS module are left out to be melted at this point in time, and the melting is delayed further in this region due to the lack of the natural convection heat transfer. The average melting throughout the LHS module completed in 296 min.

The important observation from the melting characteristics is that melting begins in the top regions close to the inlet section and ends in the diagonally opposite bottom region near the outlet section. Further, it may be desirable to implement partial charging which will have faster heat transfer characteristics.

4.4.1.4 HTF inlet and outlet temperatures

The average PCM temperature (T_{pcm}), inlet HTF temperature (T_{in}) and the outlet HTF temperature (T_{out}) variations during charging (Exp2) are shown in Figure 4.11. The heat transfer during charging occurs due to the temperature difference between the HTF and the PCM. Initially, since the temperature difference ($T_{in} - T_{pcm}$) is high, the rate of heat transfer is higher which leads to a maximum drop in T_{out}. As the charging progresses, the PCM gains more energy such that the temperature difference and consecutively, the heat transfer between the HTF and the PCM reduces. It is important to note that ideally, it is not possible to continue charging up to the HTF inlet temperature due to continuous heat loss from the LHS module to the surroundings. Therefore, the steady-state T_{pcm} will always be lower than T_{in} and will take infinite time to reach T_{in}. The charging process was stopped at the maximum charging temperature (T_f) of 362.9 °C, and the T_{out} at this condition is 371.6 °C.

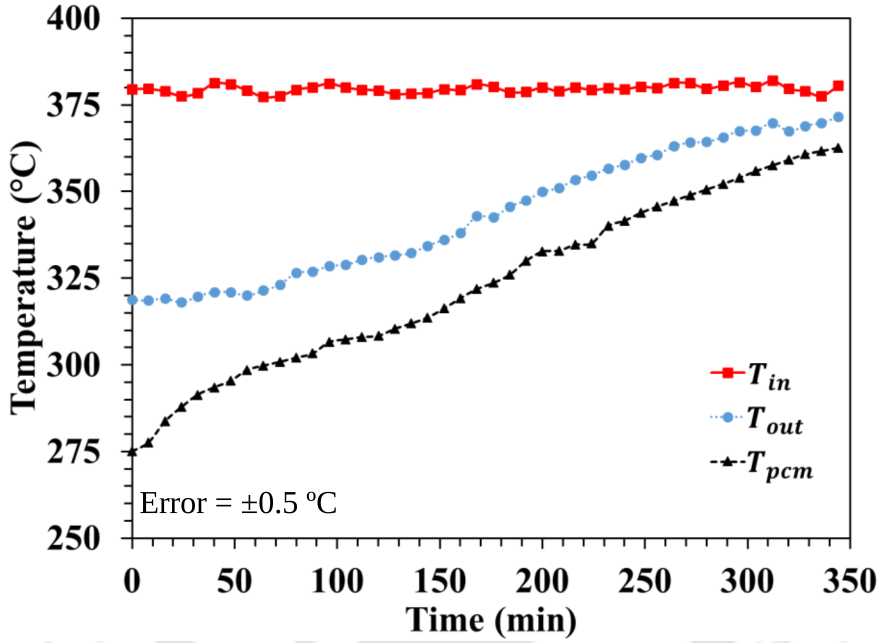

Figure 4.11. Average PCM temperature and the temperature at the inlet and outlet of the LHS module during charging.

4.4.1.5 Energy charged and rate of charging

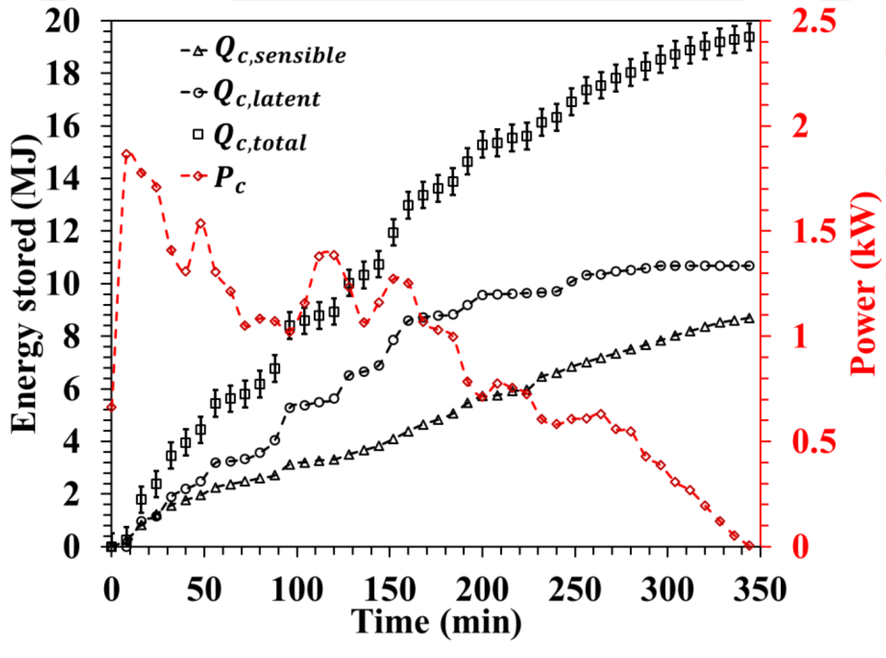

Figure 4.12. Sensible, latent and total energy charged and the charging power.

Figure 4.12 shows the cumulative sensible, latent and total energy stored and the rate of total energy charged by the LHS module. Initially, the PCM is in its solid-state at a temperature of 275 ºC and the HTF is passed through the LHS module at 380 ºC. The amount of energy stored is calculated using Eqs. (4.2-4.4). The LHS module absorbs the sensible heat initially as the solid PCM is heated followed by the latent heat till the melting is complete at 296 min. Again, the liquid PCM stores the sensible heat till it reaches the steady-state temperature condition at 362.9 ºC. The latent heat contributes to approximately 55% of the total energy stored, however the remaining is stored as sensible heat of the solid and liquid PCM.

The cumulative charging power profile shows that peak power is charged initially due to a high temperature difference between the HTF and PCM. This happens due to the sensible heat storage in the PCM. The LHS module delivers steady power during most of the melting process. Later, the rate of heat transfer drops gradually with the decrease in temperature difference between the HTF and PCM, and the charging power decreases continuously up to the end of the process.

4.4.1.6 Effect of inlet HTF conditions on charging

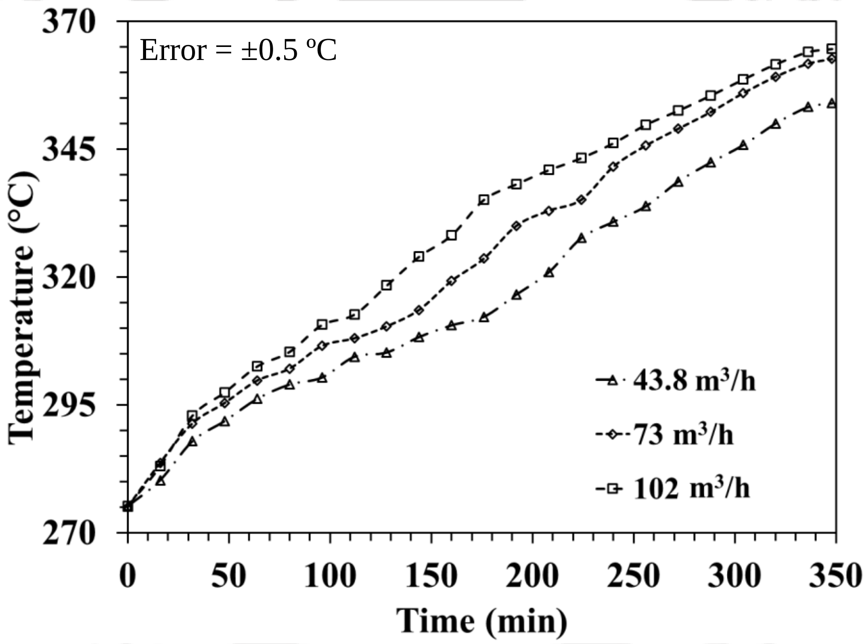

Figure 4.13. Effect of HTF flow rate on the charging performance of the LHS module.

The inlet HTF temperature and flow rate affects the charging performance comprehensively and therefore, a parametric investigation is conducted to analyse the behaviour of the LHS module by varying these parameters. To study the effect of inlet HTF flow rate on the charging performance, the flow rate is varied between 43.8 and 102 m^3/h (Exp1, Exp2 and Exp3), whereas, the initial LHS module temperature and HTF inlet temperature are fixed as 275 ºC and 380 ºC, respectively. Figure 4.13 shows the average temperature profiles of the PCM at different inlet HTF flow rates. Increasing the HTF flow rate, the thermal resistance to heat transfer decreases which leads to an improvement in the overall heat transfer rate. The temperature profiles show that the effect of increase in flow rate on the charging time is significant up to 73 m^3/h, however the heat transfer improves only marginally thereafter. The charging time reduces by ~15% as the flow rate increases from 43.8 m^3/h to 73 m^3/h, whereas, a reduction of only ~8.5% was achieved with further increase in flow rate to 102 m^3/h. The charging times for the flow rates of 43.8 m^3/h, 73 m^3/h and 102 m^3/h are 348 min, 296 min and 271 min, respectively. With increase in the flow rate, the total latent heat stored during these experiments is fixed (10.7 MJ), however, there is an increase in the amount of sensible heat stored due to an increase in the maximum steady-state charging temperature.

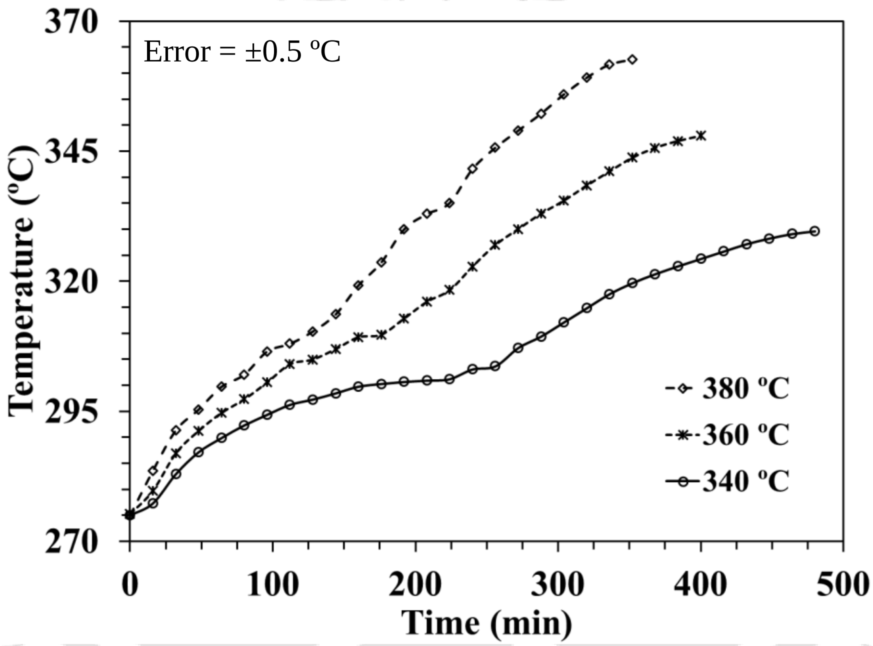

Figure 4.14. Effect of HTF temperature on the charging performance of the LHS module.

Figure 4.14 shows the average temperature variation of the LHS module by varying the HTF inlet temperature. The initial temperature and flow rate in these experiments (Exp2, Exp4 and Exp5) are fixed as 275 ºC and 73 m^3/h, respectively. Increasing the HTF inlet temperature, the temperature difference between the HTF and initial PCM temperature increases, which is the major driving potential for both the natural convection and conduction heat transfer rate in the LHS module. The charging time reduced by ~27% from 485 min to 354 min by increasing HTF inlet temperature from 340 ºC to 360 ºC. With a further increase to 380 ºC, the charging time was reduced further by 16.3 % to 296 min. The amount of latent heat stored was fixed at all T_{in} i.e. 10.7 MJ, however, the share of sensible heat out of total energy stored was increased from 33.3% (5.33 MJ) to 44.8% (8.7 MJ). Therefore, the increase in the temperature difference between the inlet HTF temperature and initial PCM temperature significantly improved the rate and amount of sensible heat stored.

A direct comparison between the effects due to increase in the HTF inlet flow rate or HTF inlet temperature cannot be made as both can be varied distinctively, however, the results show that inlet HTF temperature significantly affects the heat transfer rate. On the other hand, by increasing the inlet flow rate above a threshold value, the heat transfer rate does not improve comprehensively.

4.4.2 Discharging experiments

4.4.2.1 LHS module temperature variations

The temperature variations at different locations of the LHS module for the discharging experiment (Exp7) are shown in Figure 4.15. The inlet HTF temperature was fixed as 225 ºC and the average initial LHS module temperature was 330 ºC. Similar to the charging experiments, the practical issues such as fluctuation in the HTF inlet temperature and variation at different locations of the LHS from the initial PCM temperature could not be eliminated while performing the experiment.

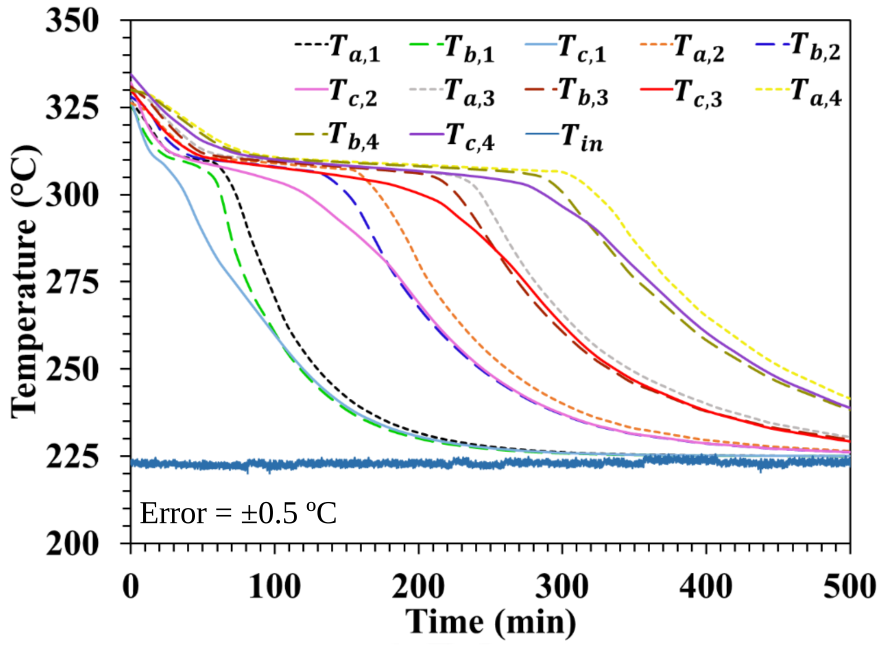

Figure 4.15. Temporal variation of temperature versus time measured at different thermocouple locations (Exp7: T_{in} = 225 °C, T_i = 330 °C and $\dot{Q}_{in}$ = 73 m^3/h; subscript x,i - radial location x = a, b, c and axial location i = 1, 2, 3, 4) during the discharging process.

The discharging temperature profiles are significantly different from the charging temperature profiles and the following important observations can be made;

a) The temperature profiles have similar shape but different slopes at different locations. The heat transfer takes place from the PCM to the HTF due to the temperature difference between them. Initially, there is a drop in temperature at all locations, followed by a sharp transition of slope indicating the initiation of the PCM solidification. After solidification, the temperatures drop gradually until they reach the steady-state temperature.

b) The radial variation of temperature in the LHS module is minimal and can only be observed during the solidification of the PCM at different radial locations. This suggests that the discharging takes place uniformly in the radial direction and the heat transfer occurs due to conduction heat transfer.

The temperature profiles $T_{a,i}$, $T_{b,i}$ and $T_{c,i}$ at each axial section (i = 1, 2, 3, 4) vary only marginally from each other, however, the variation of heat transfer is significant at consecutive sections (Section 1, 2, 3 and 4) along the direction of the HTF flow.

4.4.2.2 Axial and radial temperature distribution

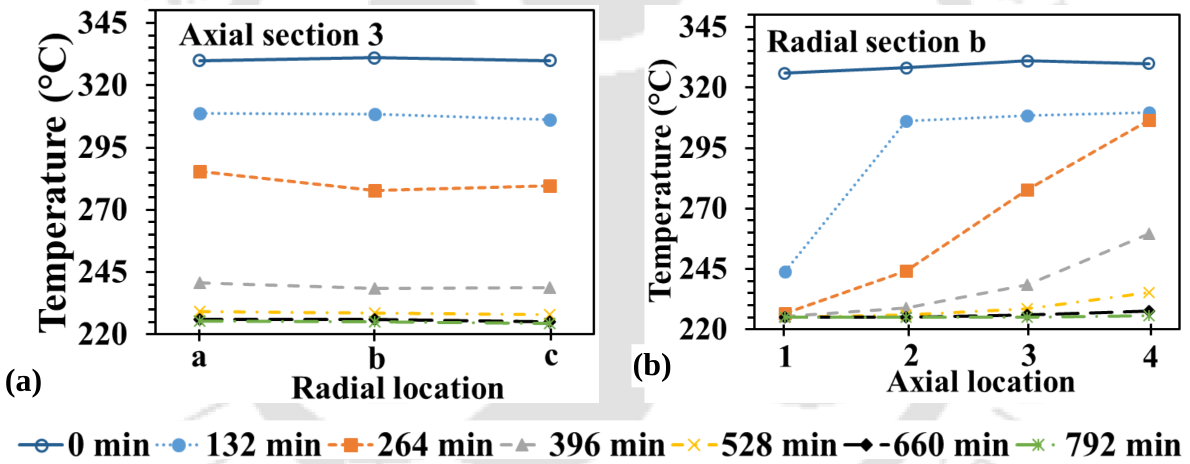

Figure 4.16. Variation of temperature versus time during discharging along (a) radial locations a, b and c at axial section 3, and along (b) axial locations 1, 2, 3 and 4 at radial section b.

The temperature distributions during discharging are comprehensively different from charging. The radial temperature variation is evaluated by plotting the progression of temperatures at axial section 3, i.e. temperatures $T_{a,3}$, $T_{b,3}$ and $T_{c,3}$ with time as shown in Figure 4.16(a). There is a similar decrement in temperature in the top, middle and bottom regions up to 132 min of discharging. At 264 min, discharging for $T_{c,3}$ is marginally slower than the other radial locations. Later, the temperature decreases uniformly at all the radial locations till the discharging completes, however, the rate of temperature drop reduces due to decrease in the heat transfer between the HTF and the PCM. The radial distribution at different axial sections is found to be similar, such that the heat transfer takes place uniformly throughout the system length and negligible thermal stratification occurs along the radial direction in the LHS module.

In the axial direction, the temperature distribution is determined by plotting the temperature evolution in the middle section i.e. temperatures $T_{b,1}$, $T_{b,2}$, $T_{b,3}$ and $T_{b,4}$ at different axial locations as shown in Figure 4.16(b). After the initiation of the discharging process, $T_{b,1}$experiences a significant drop than $T_{b,2}$, $T_{b,3}$ and $T_{b,4}$. The heat transfer rate at this location is high due to high temperature difference between the HTF and the PCM. The temperature drop for $T_{b,1}$ subsides after 264 min as it reaches close to steady-state, and the temperature drop for $T_{b,2}$is higher than $T_{b,3}$, followed by $T_{b,4}$. This behaviour repeats for the subsequent time intervals and along the subsequent axial locations with discharging taking place consecutively along different sections along the system length. The axial variations in the top and the bottom sections are consistent with that of the middle section.

Overall, while discharging, significant temperature variation with time occurs in the LHS module only in the axial direction, whereas, minimum variation occurs in the radial direction.

4.4.2.3 Local and average melt fraction

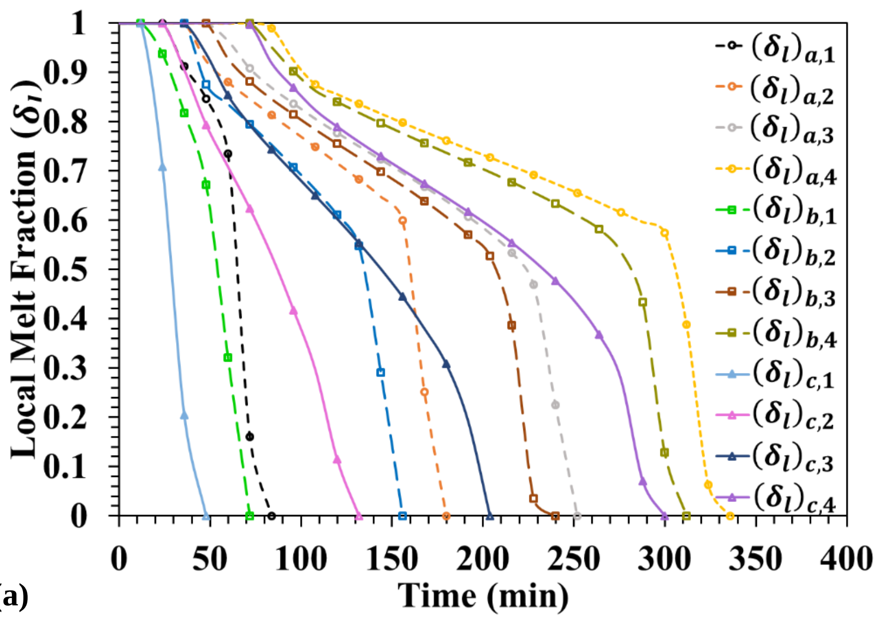

(a)

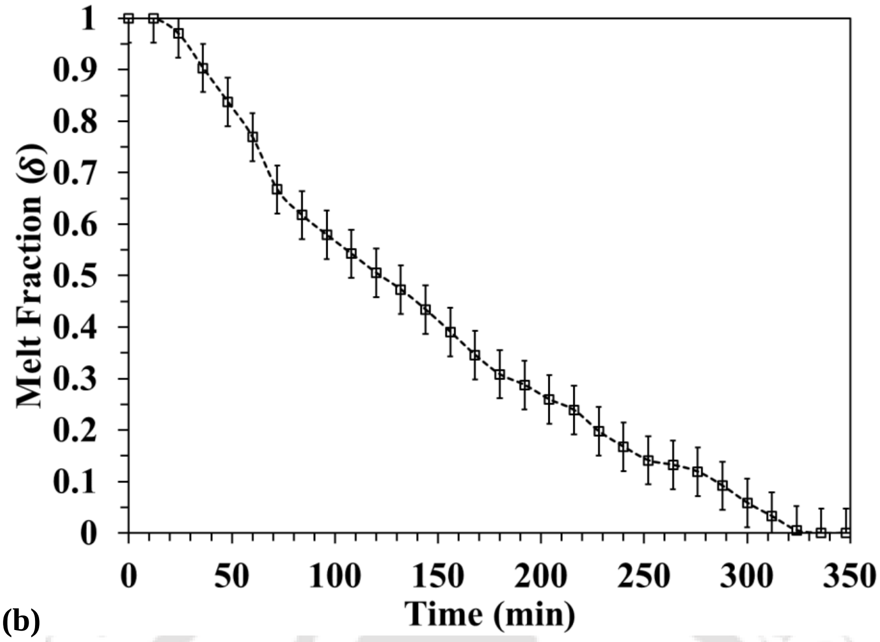

(b)

Figure 4.17. (a) Local and (b) average melt fraction throughout the LHS module during discharging.

Figure 4.17(a) shows the variation in the local melt fraction (δ_l) during the discharging experiment. Unlike melting, the solidification does not vary significantly based on the radial location i.e. top, middle or bottom regions in the LHS module, however, it takes place due to the radial progression of the solidification fronts around every HTF tube. For example, at Section 1, the solidification at $(\delta_l)_{c,1}$is marginally faster than $(\delta_l)_{b,1}$followed by $(\delta_l)_{a,1}$. This symmetry in solidification at different radial locations shows that there is negligible effect of natural convection and heat transfer is dominated by conduction.

Initially, the solidification initiates in the section close to the inlet (Section 1) of the LHS module followed subsequently at different sections (Section 2, 3 and 4) along the axial direction. The local melt fraction profiles drop rapidly at Section 1, such that the solidification completes almost instantly after its initiation. However, the rate of solidification drops consecutively at different sections along the length of the LHS module.

Figure 4.17(b) shows the average melt fraction during solidification and it can be observed that 50% of solidification completed in 120 min, i.e. in 36% of the total discharging time (336 min), whereas, 90% of the solidification is completed in approximately 75% of the total discharging time. It can be inferred that solidification occurs at a faster rate initially, however, it reduces significantly as the time progresses. Therefore, a partial discharging condition may be beneficial during the system operation.

4.4.2.4 HTF inlet and outlet temperatures

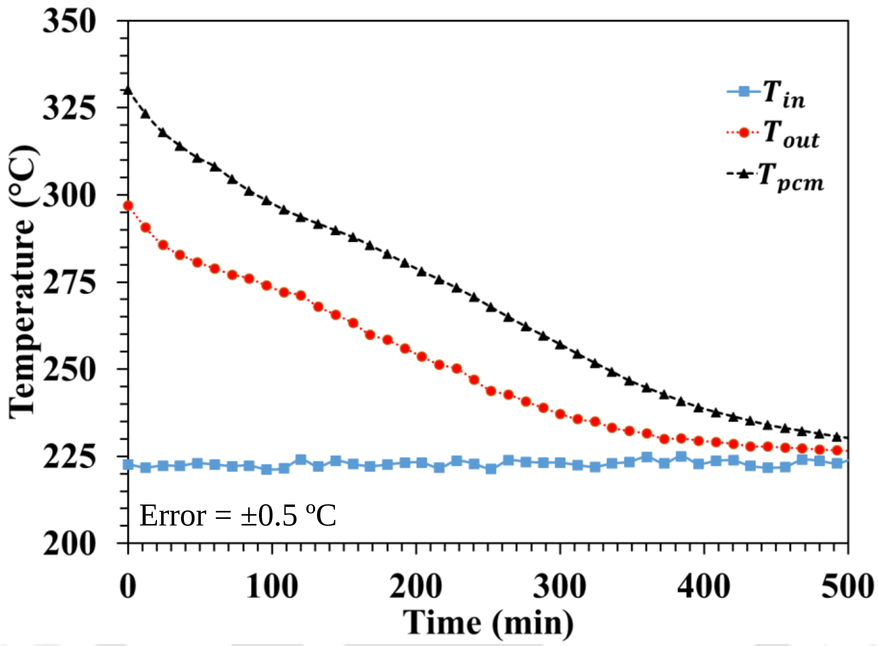

Figure 4.18. Average PCM temperature and the temperature at the inlet and outlet of the LHS module during discharging.

The LHS module average temperature, inlet and the outlet HTF temperatures for the discharging experiment are shown in Figure 4.18. The heat transfer rate is initially high due to a high temperature difference between the PCM and the HTF. As the time progresses, the PCM temperature and the HTF outlet temperature decreases continuously due to diminishing heat transfer. It is to be noted that unlike charging, it is possible for the LHS module temperature to attain a steady-state condition closer to the HTF inlet temperature while discharging. This happens as the LHS module has a tendency to continuously lose heat to the ambient and attain lower temperatures. Ideally, if the discharging is allowed to run for an infinite time period, the average LHS temperature can even become equal to the HTF inlet temperature.

4.4.2.5 Energy discharged and rate of discharging

The sensible, latent and total energy discharged and the rate of energy discharged during the discharging of the LHS module are shown in Figure 4.19. The PCM is initially in the liquid-state at a temperature of 330 °C and the energy is discharged as the HTF is passed through the HTF tubes at 225 °C. As the PCM solidifies, the latent heat is discharged, whereas, the liquid and solid sensible heats are discharged due to the continuous decrease in the PCM temperature. Out of total energy discharged i.e. 20.83 MJ, 48.7% (10.15 MJ) is discharged as sensible heat from the PCM. The latent heat is completely discharged upon the completion of solidification at 336 min. The power delivered by the LHS module is initially high as the rate of heat transfer between the HTF and the PCM is high. However, as the amount of energy discharged increases, the rate of energy delivered reduces due to reduction in the temperature difference between the HTF and the PCM. The peak power delivered during the initial period may be useful in fulfilling the instant demand of the end-user application.

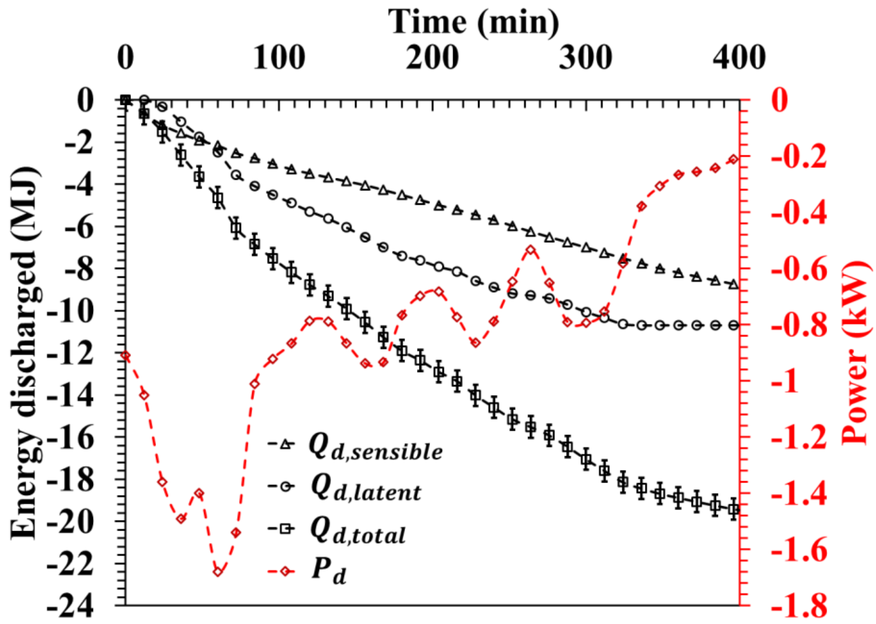

Figure 4.19. Sensible, latent and total energy charged and the discharging power.

4.4.2.6 Effect of inlet HTF conditions on discharging

During the discharging, the inlet HTF temperature and flow rate affect the discharging performance significantly. The effect of inlet HTF flow rate during discharging is studied by varying the HTF flow rate at the inlet of the LHS module between 43.8 m^3/h and 102 m^3/h (Exp6, Exp7 and Exp8). The initial LHS module temperature and HTF inlet temperature were fixed as 330 ºC and 225 ºC, respectively, during these experiments.

Figure 4.20 shows the average PCM temperature profiles at different HTF flow rates. The heat transfer rate was found to improve due to increase in the HTF mass flow rate, however, the improvement was significant only up to a threshold value of the flow rate. The discharging time reduced by ~15% as the flow rate increased to 73 m^3/h, whereas, there was a further reduction by only ~8.5% with increase from 73 m^3/h to 102 m^3/h. The discharging times at 43.8 m^3/h, 73 m^3/h and 102 m^3/h are 348 min, 296 min and 271 min, respectively.

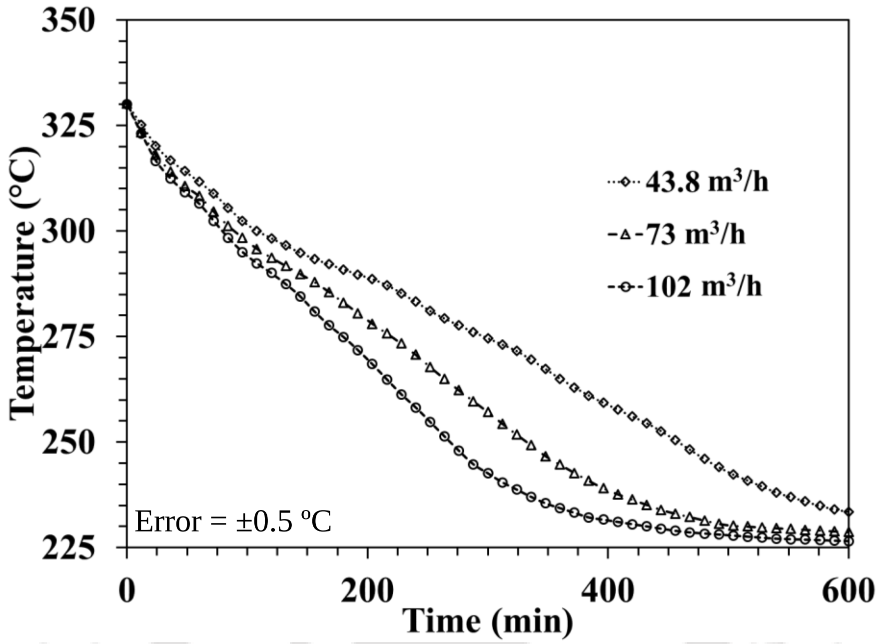

Figure 4.20. Effect of HTF flow rate on the discharging performance of the LHS module.

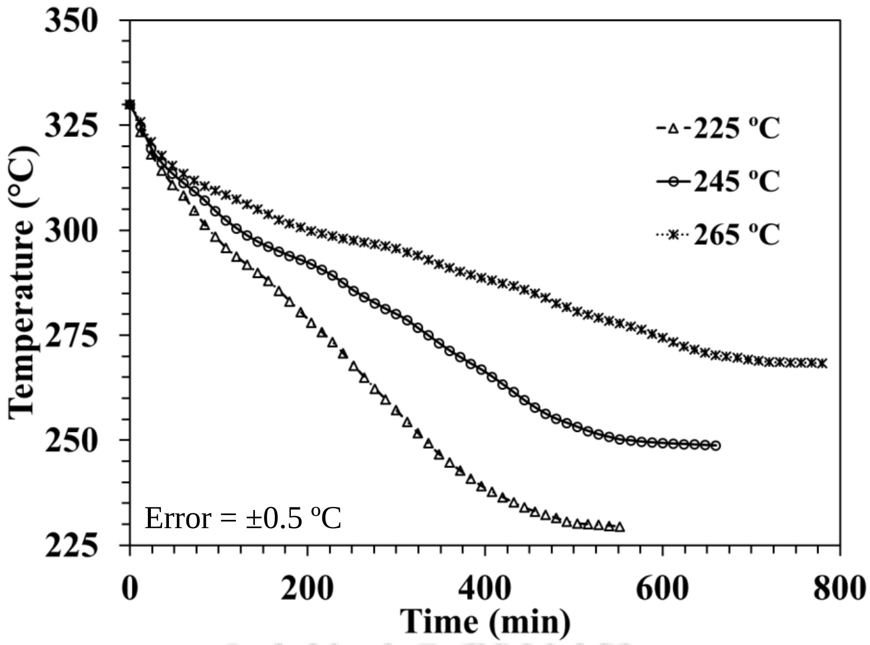

Figure 4.21. Effect of inlet HTF temperature on the discharging performance of the LHS module.

For a fixed HTF flow rate of 73 m^3/h and an initial LHS module temperature of 330 °C, the inlet HTF temperature was varied between 225 °C and 265 °C as shown in Figure 4.21. The discharging time for 265 °C was 608 min, however, it was reduced by 29.6% to 428 min by reducing the inlet HTF temperature to 245 °C. Decreasing the inlet temperature to 225 °C, the heat transfer rate had improved further and the discharging time reduced further by 21.5% to 336 min.

Similar to the charging process, the heat transfer rate during discharging is improved due to increase in the temperature difference between the HTF and the PCM. The amount of latent heat discharged was fixed, however, the sensible heat discharged by the LHS module increased by 63% from 5.92 MJ to 9.64 MJ.

4.4.3 Summary of the charging and discharging experiments

Table 4.2 summarizes the charging and the discharging characteristics such as charging and discharging time and the energy storage and discharged by the LHS module for the complete range of charging and discharging experiments.

Table 4.2. Summary of the charging and discharging characteristics of the LHS module.

Exp no.	T_{in} (°C)	T_i (°C)	T_f (°C)	$\dot{Q}_{in}$ (m^3/h)	t (min)	Q (MJ)	Q (kWh)	Q (kWh/kg)	Q (kWh/ m^3)
Charging									
Exp1	380	275	357.7	43.8	348	18.7	5.2	0.0852	162.5
Exp2	380	275	362.9	73	296	19.2	5.34	0.087	166.8
Exp3	380	275	365.3	102	271	19.4	5.41	0.0886	169
Exp4	360	275	348.9	73	354	17.8	4.97	0.0815	155.3
Exp5	340	275	330	73	485	16.0	4.45	0.073	139
Discharging									
Exp6	225	330	227.5	43.8	460	20.5	5.70	0.0934	178.1
Exp7	225	330	229.4	73	336	20.3	5.64	0.0926	176.5
Exp8	225	330	226.4	102	256	20.6	5.73	0.0939	179.0
Exp9	245	330	248.7	73	428	18.4	5.13	0.0841	160.4
Exp1	265	330	268.3	73	608	16.6	4.61	0.0756	144.1

4.4.4 Comparison with commonly used sensible heat storage (SHS) mediums

Among the sensible heat storage (SHS) mediums, cast steel and concrete are the most common and have distinct properties. Cast steel has high cost and better performance, whereas, concrete has relatively low cost and performance (Herrmann and Kearney, 2002). The detailed experimental investigations on the charging and discharging performance of cast steel and concrete based thermal energy storage systems using the same experimental setup as described in Section 3.3 have been reported in the authors previous studies (Vigneshwaran et al., 2019a, 2019b). A brief comparison for the utilization of cast steel, concrete and sodium nitrate ($NaNO_3$) for storage temperatures up to 400 °C is presented below;

a) Material level comparison: The material level comparison does not depend upon the rate of charging or discharging of the sensible and latent heat storage materials, whereas, it only depends upon the amount of energy charged/discharged, which further depends upon the thermo-physical properties of the storage medium. The thermo-physical properties of $NaNO_3$ are mentioned in Table 3.2, whereas, the properties for concrete and cast steel were reported in our previous studies (Vigneshwaran et al., 2019a, 2019b). The energy discharged by the SHS and LHS mediums in kilowatt-hour per unit mass per unit temperature change (kWh/kg K) and kilowatt-hour per unit volume per unit temperature change (kWh/m^3 K) of the storage medium is given by Eqs. (4.15-4.16) below (refer to the section Appendix C for the detailed illustration of these equations);

$$Q_{discharged}\left({}^{kWh}/_{kg\ K}\right) = \left(c + \frac{\Delta h}{\Delta T}\right) \times \frac{1}{3600 \times 1000} \tag{4.15}$$

$$Q_{discharged}\left({}^{kWh}/_{m^3\ K}\right) = \rho\left(c + \frac{\Delta h}{T_f - T_i}\right) \times \frac{1}{3600 \times 1000} \tag{4.16}$$

Here ρ and c are the density and specific heat of the SHS and LHS mediums and ΔT refers to the change in the medium temperature during energy storage. The sensible heat component (c or ρc) in Eqs. (4.15-4.16) represent the specific heat capacity and the volumetric energy storage capacity of both the SHS and LHS mediums. The latent heat component ($\Delta h/T_f - T_i$) is only valid for the LHS medium, whereas, it is zero for the SHS medium. Practically, the latent heat stored by the PCM is accompanied by a SHS component which is further dependent upon the temperature change in the storage medium. The energy stored by the concrete, cast steel and $NaNO_3$ in kWh/kg K and kWh/m K is shown in Figure 4.22(a)-(b). The specific heat capacity and volumetric energy storage density is shown for $NaNO_3$ while considering it (i) only as a SHS medium, (ii) combined SHS and LHS medium with a 100 ºC temperature change and (iii) combined SHS and LHS medium with a 200 ºC temperature change. It is inferred that the specific heat capacity and the volumetric energy storage density of $NaNO_3$ decreases as the sensible heat component increases due to higher temperature change of the storage medium, however, it is always higher than cast steel and concrete. Therefore, the thermal energy storage system employing $NaNO_3$ can be relatively compact and lighter than cast steel or concrete based storage mediums.

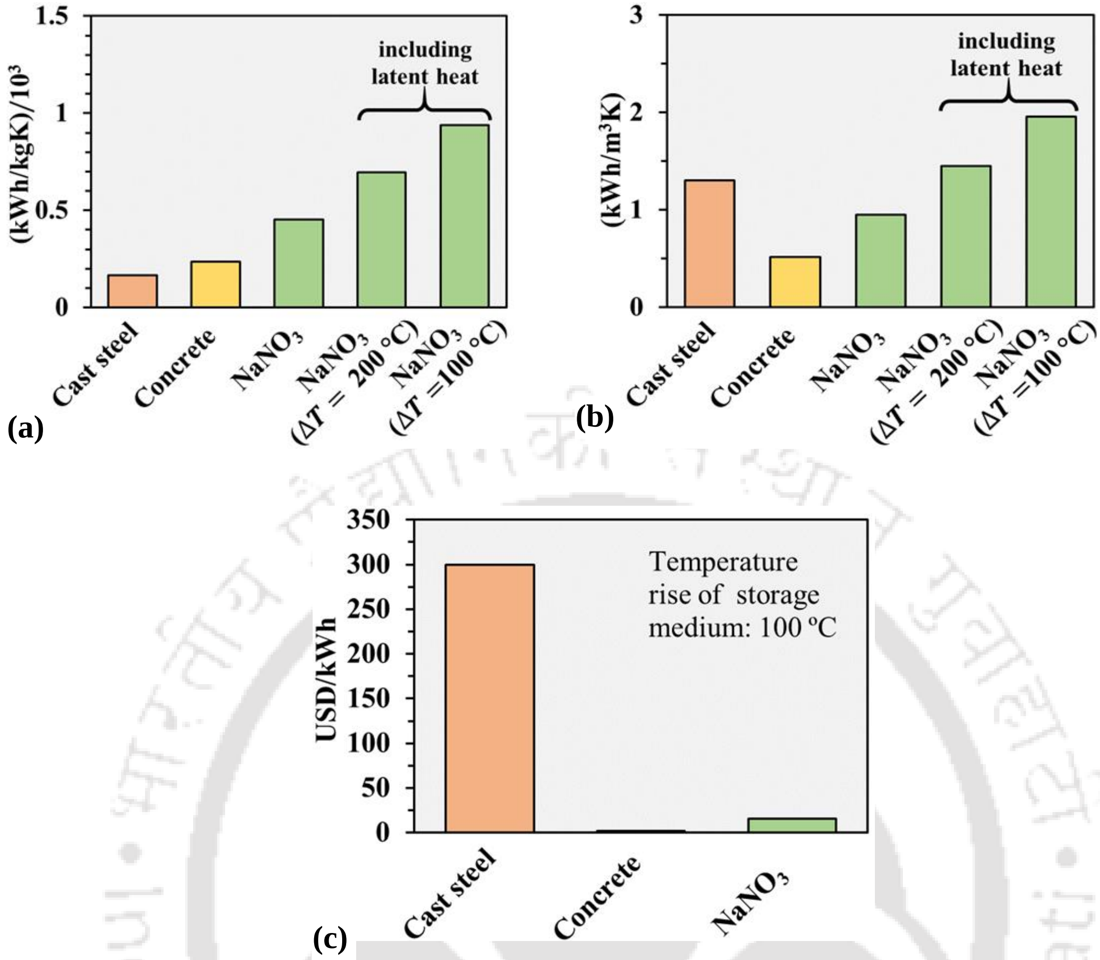

Figure 4.22. Energy discharging capacity of cast steel, concrete and sodium nitrate in (a) kWh/kg K, (b) kWh/m^3 K and (c) cost of energy storage.

The cost of storage for SHS and LHS mediums is based on the temperature change of the storage medium. The material cost of $NaNO_3$ is 1.33 USD/kg. Figure 4.22(c) shows the cost of cast steel, concrete and $NaNO_3$ in USD/kWh for a 100 ºC change in the storage medium temperature. It is observed that both the concrete and $NaNO_3$ have a very low cost of energy storage. Cast steel is relatively expensive with a storage cost of 300 USD/kWh and may not be suitable for developing industrial scale storage systems.

b) System level comparison: At the system-level, the shape of the discharging power profiles and the discharging times are crucial aspects to incorporate the different SHS and LHS mediums with real-time energy storage applications such as concentrated solar power (CSP).

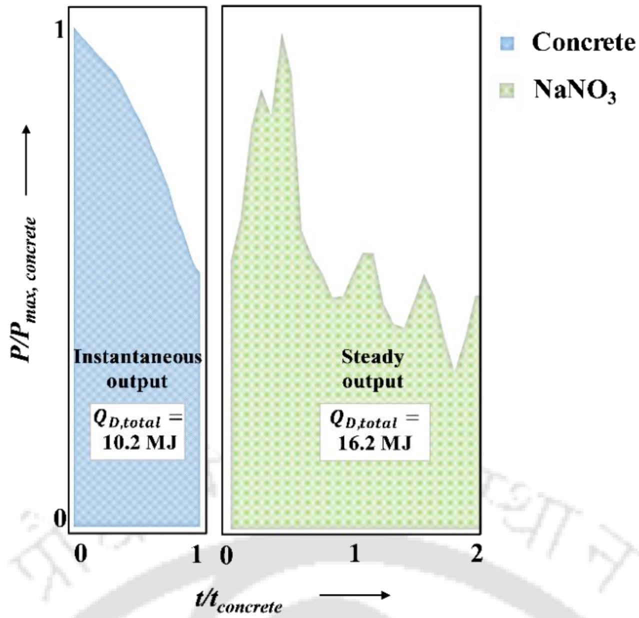

Figure 4.23. Discharging power profiles for concrete and $NaNO_3$.

Figure 4.23 shows the cumulative power profiles for concrete and $NaNO_3$ thermal energy storage systems. The volume flow rate of air in both the cases is 73 m^3/h and the temperature difference between the HTF and the storage material $(T_{in} - T_i)$ for concrete and $NaNO_3$ are 110 °C and 105 °C, respectively. The material discharging temperature range $(T_f - T_i)$ for both the materials is fixed as 70 °C. It is observed that for a fixed temperature range, $NaNO_3$ discharges ~59% more energy than concrete due to the additional sensible heat component, however, this is achieved in twice the discharging time as concrete. Further, the output power profiles show that concrete has an instantaneous discharging and the discharge rate decreases continuously with time. On the other hand, the discharging rate of $NaNO_3$ is high initially due to high amount of latent heat discharged and becomes steady at a later stage. Therefore, SHS medium shall be suitable for instantaneous load demand, whereas, the LHS medium for steady power characteristics. Conversely, LHS medium shall be more convenient in case of a fluctuating load profile. Hence, $NaNO_3$ proves beneficial than concrete and cast steel from the material perspective, whereas, a combination of SHS and LHS medium shall be more desirable to fulfil diverse load requirements of the end-user applications.

4.4.5 Practical implications of the LHS system

While performing the experimental investigations, the following important observations were noteworthy and can be useful in the design and incorporation of the developed high-temperature LHS module to end-user applications.

- The PCM was filled in the solid phase and up to 12% volume was allowed for PCM expansion, thus leaving a small air cavity in the top section of the LHS module.
- During charging, the LHS module steady-state temperatures were much lower than the HTF inlet temperature, whereas during discharging the steady-state temperatures are closer to the HTF inlet temperature. This occurs due to higher energy losses during high temperature charging experiments.

4.5 Summary

In the present work, performance investigations of a high-temperature latent heat storage (LHS) system are carried out. A 2D numerical model was developed to optimize the number and size of heat transfer fluid (HTF) tubes in a multi-tube shell and tube LHS system. The modelling results show that both the natural convection and conduction heat transfer rate improved by using more number of smaller diameter HTF tubes than using less number of larger diameter HTF tubes.

Experimental investigations were carried out to study the charging and discharging characteristics of a LHS system on a high-temperature thermal energy storage (TES) test facility. The LHS module carrying a shell and multi-tube configuration with sodium nitrate (m.p. 306 ºC) used as the PCM filled on the shell side and air used as the HTF passing through 25 HTF tubes was designed and developed. The following important conclusions were made from the experimental investigations;

- The axial and radial distribution of temperatures at different locations showed that the charging process experienced significant variations with natural convection dominating during most of the process. During discharging, the heat transfer was symmetrical in the axial and radial directions and varying significantly along the length of the LHS module. The natural convection effects during the discharging were negligible and most of the process was dominated by conduction heat transfer.
- The rate of PCM melting was higher in the top regions of the LHS module than the bottom regions due to natural convection in the system, whereas during discharging, the solidification occurred simultaneously in the top, middle and bottom regions.
- The charging times at flow rates of 43.8 m^3/h, 73 m^3/h and 102 m^3/h were 348 min, 296 min and 271 min, respectively, and the discharging times were 460 min, 336 min and 256 min, respectively.

- Increasing the inlet HTF flow rate during charging and discharging, it was found that the rate of heat transfer improved only up to a threshold value, whereas, the improvement was insignificant thereafter. The variation in the inlet HTF temperature had a significant impact on the charging and discharging performance. Increasing the temperature difference between the HTF and the initial PCM temperature by 40 ºC during charging and discharging led to a reduction in charging and discharging time by 40% and 45%, respectively.
- The maximum amount of energy charged and discharged by the LHS module were 19.5 MJ and 20.62 MJ, respectively. The power characteristics show that the LHS module charged or discharged at a faster rate initially, followed by steady charging and discharging power.

Chapter 5

Performance investigations of high-temperature PCM capsules[§]

Preface

Macro PCM encapsulations are a customary technique for TES systems used for high-temperature applications such as concentrated solar power (CSP) and direct steam generation (DSG) (Pirasaci et al., 2018; Pirasaci and Goswami, 2016). Typically, cylindrical and spherical capsules are used in bundles or packed-bed configurations to achieve the desired LHS capacity.

In this research work, experimental and numerical investigations were carried out to study the charging and discharging performances of sodium nitrate phase change material (PCM) based cylindrical capsules. The developed experimental test setup utilized air as the heat transfer fluid with operating temperatures up to 400 °C. A validated numerical model was developed to study the impact of adding a hole at the centre of a cylindrical capsule on its heat transfer behaviour. Further, experimental investigations were conducted for different inlet flow rates and inlet air temperatures for five different capsule designs namely; basic capsule (Case 1), annular capsule (Case 2), annular capsule with straight longitudinal fins (Case 3), annular capsule with tapered fins having decreasing height (Case 4), and annular capsule with tapered fins having increasing height (Case 5).

The study explores different possibilities to enhance the heat transfer rate in basic cylindrical capsules which are prevalent in high-temperature applications such as DSG and CSP.

[§] The findings reported in this chapter are published as the following research article:

Sodhi GS, Muthukumar P. Experimental and numerical investigations on the charging and discharging performances of high-temperature cylindrical phase change material encapsulations. Solar Energy, June 2021:224:411-424.

5.1 Design of the PCM capsules

The schematic of typical PCM encapsulations used for thermal energy storage in different high-temperature applications such as steam accumulators and concentrated solar power is shown in Figure 5.1. Each of the PCM capsule modules is capable of storing the latent heat, and a bundle of these capsules are used to develop high capacity storage system. The heat transfer between the PCM and the surrounding HTF takes place through the capsule wall. The cylindrical capsules are the most favourable for commercial applications due to a higher heat transfer surface area than other capsule shapes (Liu et al., 2016). The two dimensional (circular: r-θ) shape of the solidification fronts are symmetrical in the angular direction, however, the natural convection leads to an asymmetry in case of melting. However, the natural convection effect is negligible for smaller diameter capsules and can be neglected (Dhaidan and Khodadadi, 2015; Hariharan et al., 2018; Pirasaci et al., 2018). Considering the axial direction, long and slender cylindrical capsules are found to have a faster melting/solidification due to increase in the surface area to volume ratio of the capsules (Palanisamy and Niyas, 2018). Very few researchers have reported techniques to improve the heat transfer rate in conventional cylindrical PCM capsules.

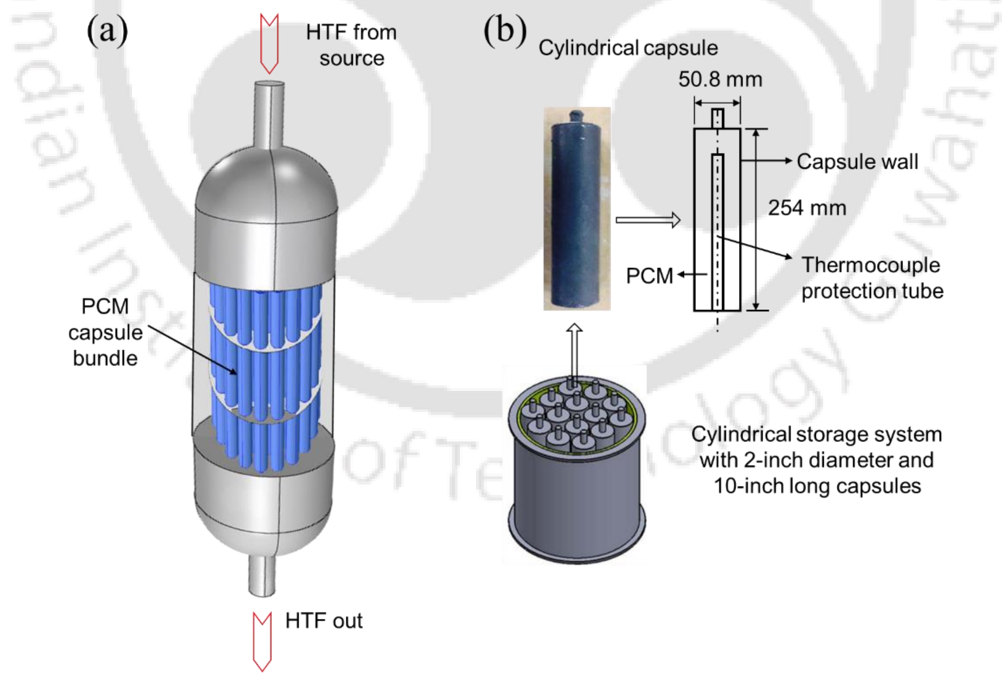

Figure 5.1. (a) Inside view of a typical LHS system with cylindrical PCM encapsulations and (b) example of a cylindrical storage tank with PCM capsules developed by Pirasaci et al. (Pirasaci et al., 2017) .

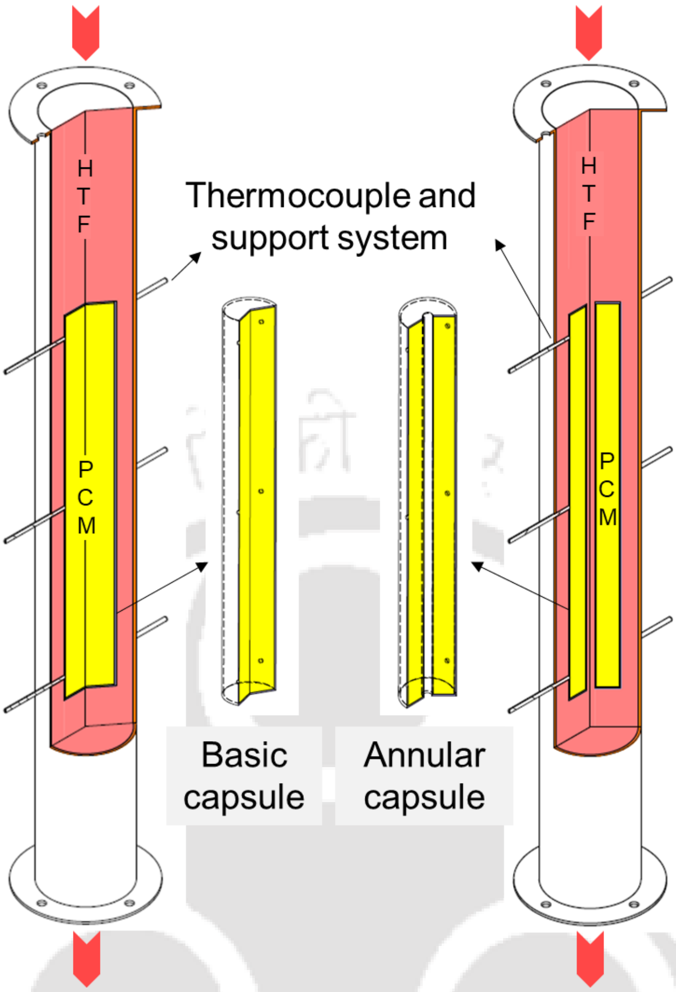

Figure 5.2. Schematic of the PCM capsule designs namely; basic capsule and annular capsule.

In the present work, the performance of PCM capsule modules carrying different designs is analysed. The capsules were developed using SS 310S material which is compatible with high temperature corrosive environment. The schematic of the tested capsule modules is shown in Figure 5.2. The basic PCM capsule design is a cylindrical PCM containment, whereas, the modified design comprises of a hole or recess at the centre of the basic capsule and is termed as the annular capsule. The modification in the design leads to an increase in the surface area exposed to the air which is used as the HTF.

5.2 Numerical model

The numerical model is developed to understand the behaviour of fluid flow and heat transfer in the horizontal PCM capsules. The computational domain of the 2D axi-symmetric numerical model developed for two cases; basic cylindrical capsule and annular capsule is shown in

Figure 5.3(a)-(b). The dimensions of both the cases are described in Table 5.1. The equations governing the HTF flow and the heat transfer between the HTF and the PCM are described in detail in Section 3.2.1. The air flow is assumed to be developed and the heat transfer rate inside the PCM takes place due to conduction. The PCM thickness is very small (< 30 mm) and hence, the natural convection heat transfer due to the buoyancy driven flow is neglected (Dhaidan and Khodadadi, 2015; Hariharan et al., 2018). The model is developed using the commercial modelling software COMSOL Multiphysics and the simulations are conducted using a Dell precision T7610 workstation having Intel Xeon E5-2650 v2 processors and 64 GB 1866 MHz RAM.

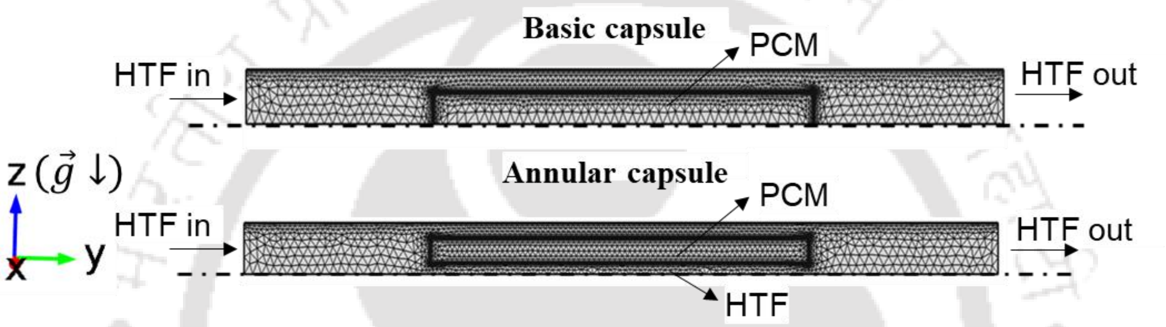

Figure 5.3. Computational domain and meshing features of the basic (top) and the annular capsule (bottom).

The numerical model described above was validated with the experimental data of the charging experiments. For this purpose, charging experiments were performed for the temperature range 50-330 ºC for an inlet air temperature and flow rate of 360 ºC and 58.5 m^3/h, respectively.

5.3 Development and performance investigations of different PCM capsule designs

The layout of the high temperature test facility developed to analyse the performance of different PCM capsules is shown in Figure 5.4. Experimental investigations were carried out to study the charging and discharging performances of different capsule modules described in Figure 5.5. The PCM capsule module was heated to the initial PCM temperature using the hot air from the heater. Later, the air was heated by activating the primary loop before the storage system until the required inlet temperature was achieved. The inlet to the storage module was then opened and the air at the required temperature and flow rate was passed to the PCM capsule module. The complete experimental procedure including the important components of the experimental test facility and the operational features has been described in detail in Section

3.3. However, the tested LHS unit is the PCM capsule module (component label number 6 in Figure 5.4) in the present case.

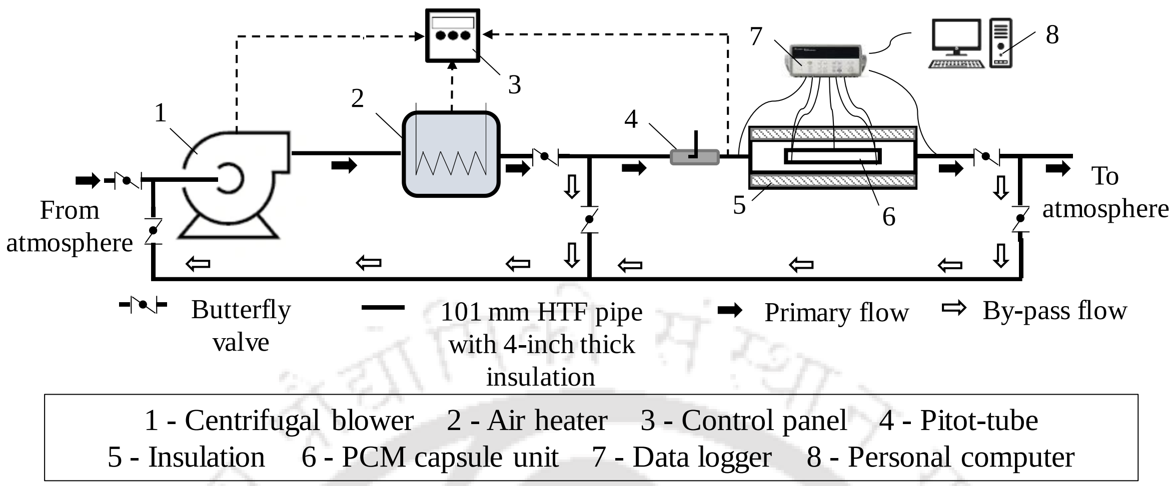

Figure 5.4. Layout of the experimental test facility to test the PCM capsule modules.

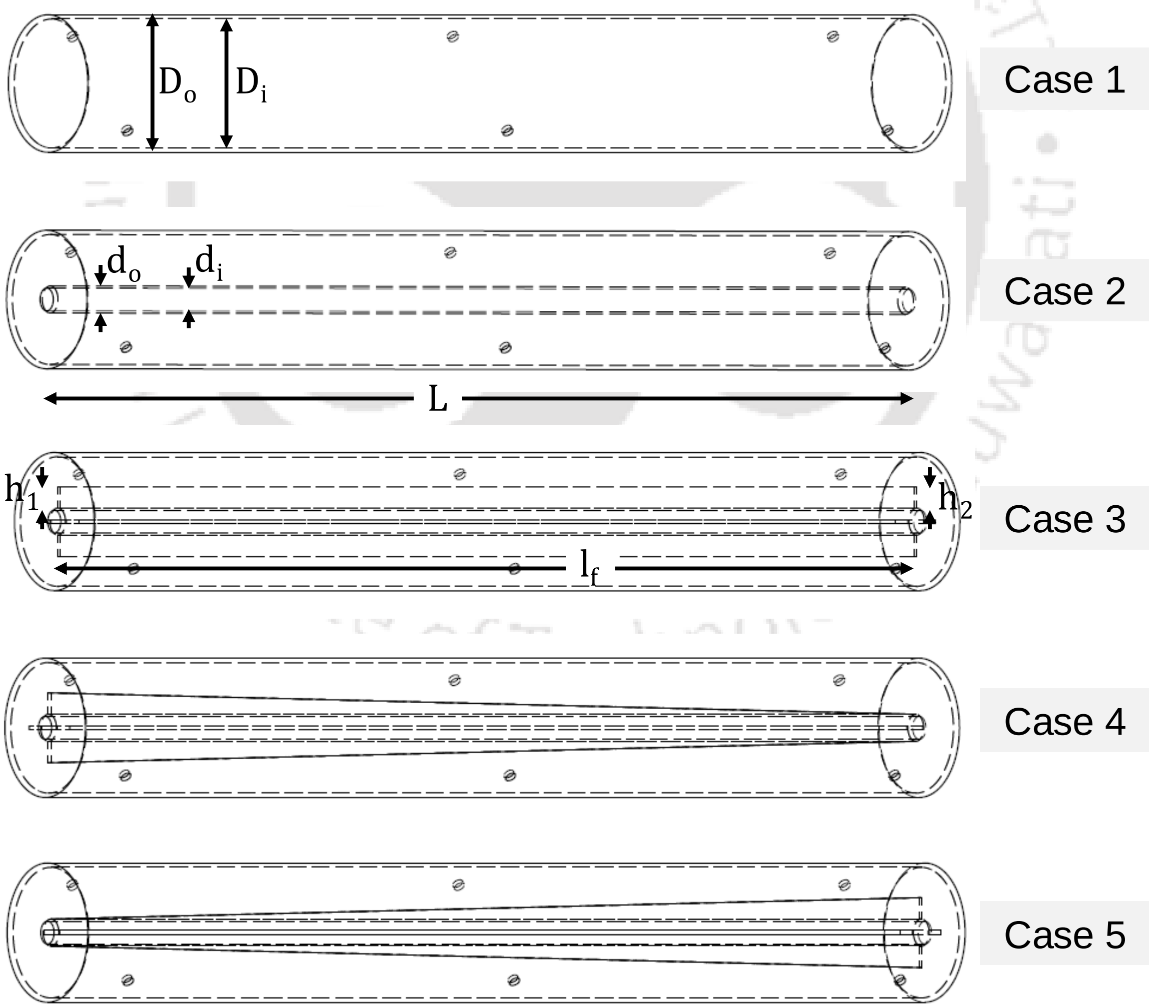

Figure 5.5. Dimensions of the different capsule modules (all dimensions in mm).

The HTF flows through the outer pipe, which has been insulated using a 4-inch thick ceramic wool insulation which prevents heat loss to the environment. The different PCM capsules shown in Figure 5.5 are denoted by different cases and their dimensions are shown in Table 5.1.

Table 5.1. Different PCM capsule modules and their dimensions.

Case no.	**Description**	**Dimensions (all dimensions in mm)**
Case 1	Basic capsule	$L = 500, D_o = 65, D_i = 61$
Case 2	Annular capsule	$L = 500, D_o = 65, D_i = 61, d_o = 13.7, d_i = 10.7$
Case 3	Annular capsule with straight longitudinal fins	$L = 500, D_o = 65, D_i = 61, d_o = 13.7, d_i = 10.7, h_1 = h_2 = 10, t = 2, l_f = 495$
Case 4	Annular capsule with tapered longitudinal fins having decreasing height	$L = 500, D_o = 65, D_i = 61, d_o = 13.7, d_i = 10.7, h_1 = 10, h_2 = 0, t = 2, l_f = 495$
Case 5	Annular capsule with tapered longitudinal fins having increasing height	$L = 500, D_o = 65, D_i = 61, d_o = 13.7, d_i = 10.7, h_1 = 0, h_2 = 10, t = 2, l_f = 495$

Sodium nitrate with a melting temperature of 305.1 ºC was filled in the different capsule modules. The thermo-physical properties of the sodium nitrate and air have been described in Section 3.3.2. The amount of PCM filled in the different capsule modules for Cases 1-5 were 2.41 kg, 2.4 kg, 2.36 kg, 2.38 kg and 2.37 kg, respectively. The total energy storage which is the sum of the sensible and latent heat of the PCM is described in Eq. (5.1).

$$E_{ch} = m_{PCM} C_p (\Delta T)_{ch} + m_{PCM} L_f \tag{5.1}$$

where m_{PCM}, C_p and L_f are the mass, specific heat and the latent heat of fusion of the PCM, respectively and ΔT is the temperature range of the charging process.

The corresponding total heat stored for Cases 1-5 in the charging temperature range between 275-330 ºC were 645 kJ, 645 kJ, 634.2 kJ, 639.6 kJ and 637 kJ, respectively.

The charging experiments were performed for all the PCM capsules by varying the inlet temperature and the air flow rate. The air flow rate was varied with values of 58.5, 73 and 87.5 m^3/h and the air inlet temperature was varied with values 360, 380 and 400 ºC. For all the charging experiments, the initial temperature of the PCM capsule was fixed as 275 ºC and the charging time was measured for charging in the temperature range of 275-330 ºC. Similarly, discharging experiments were performed for an initial PCM temperature of 330 ºC and the discharging time was measured in the temperature range 330-275 ºC. During discharging, the inlet air temperature was varied with values 250, 225 and 200 ºC for a fixed air flow rate of 87.5 m^3/h. Experiments were also performed by fixing the inlet temperature as 250 ºC and varying the inlet flow rate to the values 58.5, 73 and 87.5 m^3/h.

The experiments conducted in the present study were formulated based on rigorous preliminary assessment trials to determine the possible HTF inlet temperatures and flow rates. The operating HTF temperatures were selected based on the melting point temperature of the PCM suitable for high-temperature applications such as CSP and DSG. After deciding the maximum flow rate (87.5 m^3/h) and maximum temperature (400 ºC) conditions, the parametric investigations during charging and discharging were carried out for lower values of flow rates (58.5, 73 and 87.5 m^3/h) and temperatures (200-400 ºC). There is no obstruction in the flow in the 2 m length between the heater and the PCM capsule module. The calculated Reynolds number (Re_{HTF}) based on the HTF flow in the main channel (4-inch channel) lies in the range between ~4700 (87.5 m^3/h at 400 ºC) and ~7000 (87.5 m^3/h at 200 ºC).

Throughout the analysis, the PCM capsule temperature represents the average of all the temperatures measured by different thermocouples inserted in the capsule. K-type thermocouples were inserted in the capsule modules up to a fixed depth (12 mm) from the outer periphery of all the capsule modules. The LHS unit and the location of the thermocouples inserted inside the PCM capsule is described in Figure 5.6. While conducting the experiments, the uncertainty in estimating the flow rate of air occurs due to the pitot-tube meter having an accuracy of ±0.1 m/s, whereas, the K-type thermocouples used for temperature measurement have an accuracy of ±0.5 ºC. The uncertainties in the flow and energy storage estimated using the Kline McClintock method are ±2.92 m^3/h and ±3.261 kJ, respectively (Moffat, 1988) (refer Appendix B).

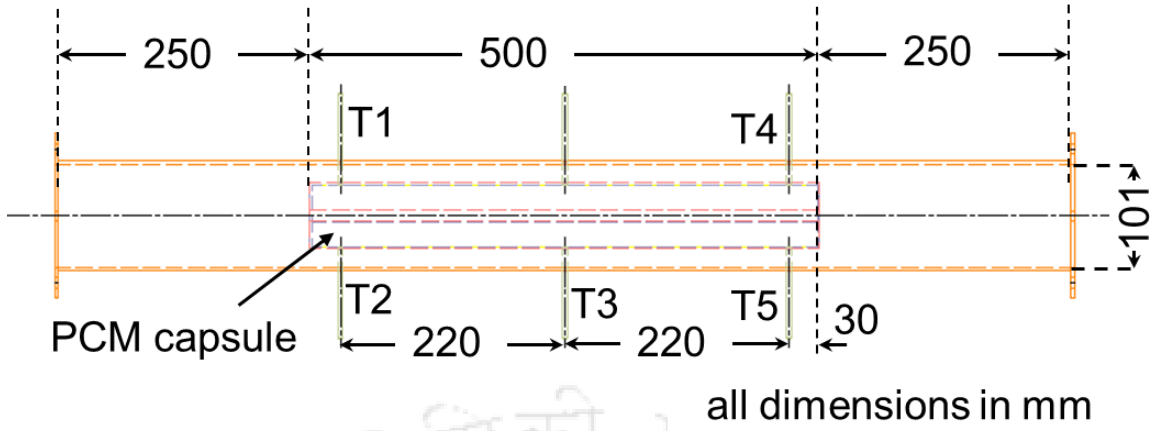

Figure 5.6. Schematic of the horizontal LHS unit and location of the thermocouples inside the PCM capsule.

5.4 Results and discussions

5.4.1 Comparison between the basic and annular capsule

The comparison between the basic capsule and the annular capsule was made by performing the charging experiment for the temperature range 50-330 ºC for an air flow rate and inlet temperature of 58.5 m^3/h and 360 ºC, respectively. The validation was performed for the basic capsule by comparing the experimentally measured temperature with the simulated data obtained from the numerical model at locations T2 and T5 (refer Figure 5.6) as shown in Figure 5.7(a). Similarly, Figure 5.7(b) shows the validation of the numerical model with the experimental data in case of the annular capsule. It can be observed that the numerical model data is in good agreement with the experimental data both in case of the basic capsule and the annular capsule.

Figure 5.8(a)-(b) shows the comparison between the average PCM temperature obtained as an arithmetic mean of all the temperatures at different locations (T1 to T5) for the basic capsule and the annular capsule. The average PCM temperature obtained from the numerical data is calculated based on same coordinates as that thermocouple locations (T1 to T5). The difference between the simulated data and the experimentally measured data is explained as below;

- It was observed that the inlet temperature had fluctuated by 7-8 ºC from the mean value (360 ºC) during the experiments, however, the inlet temperature in case of the model is kept as constant. This leads to some discrepancy between the experimental and the numerical results.

- It is important to note that even though the outer pipe enclosing the capsule module has been well insulated in case of the experimental system, the heat loss to the ambient cannot be neglected completely. On the other hand, the outer wall of the pipe in the developed numerical model is assumed to be adiabatic.
- Even as the capsule module was densely packed with the PCM, up to 10% of the volume was left void to allow for the expansion of PCM as it melts. Thus, there is a reduction in the thickness of the PCM layer in the top end of the actual capsule as the PCM settles down after the initial melting.

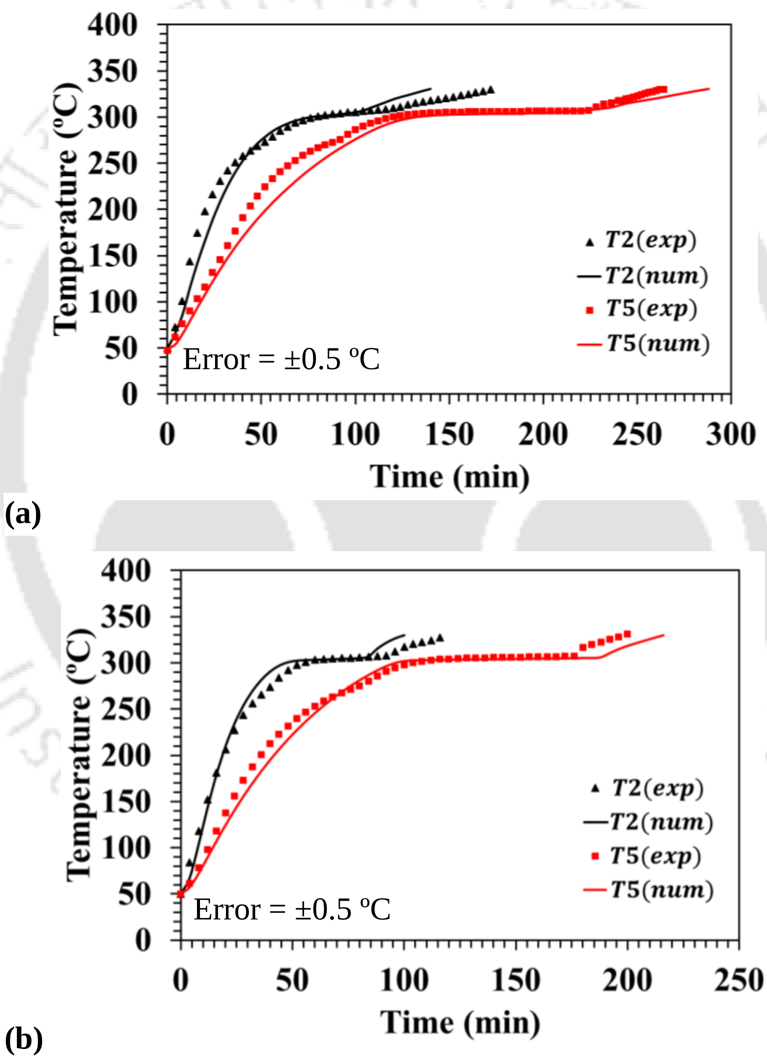

Figure 5.7. Validation of the numerical model data with the experimental data for thermocouples T2 and T5 for (a) basic capsule and (b) annular capsule.

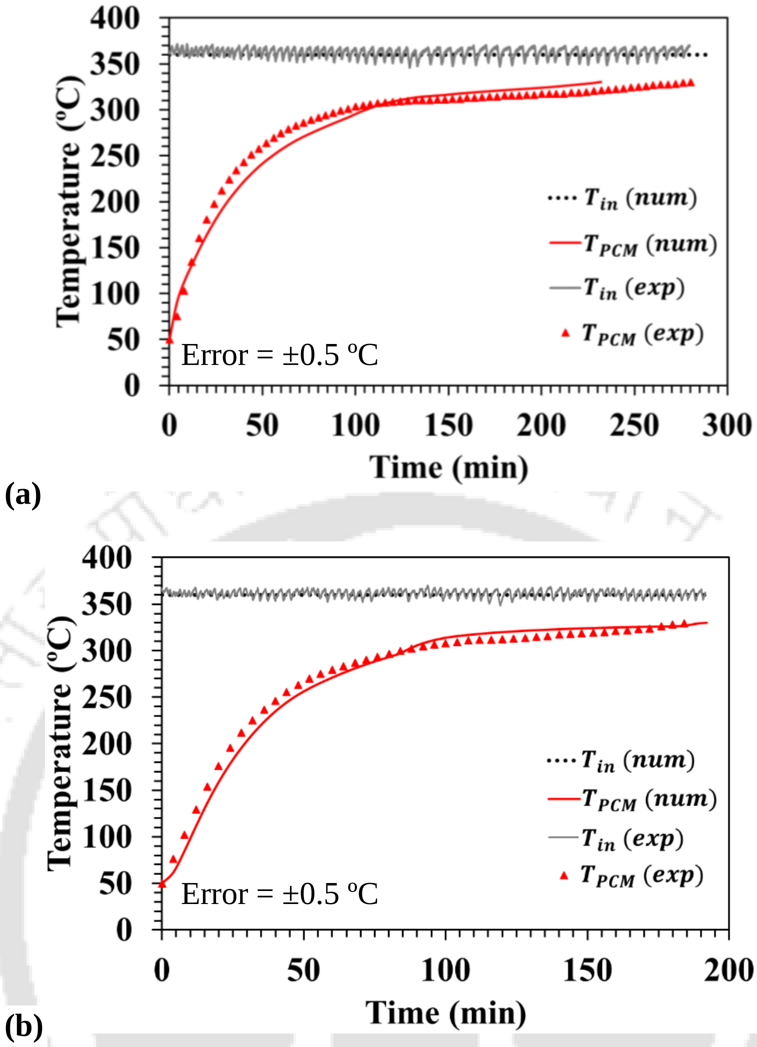

Figure 5.8. Comparison of the average PCM temperature (average of data T1-T5) obtained from the numerical model and experimental results for (a) basic capsule and (b) annular capsule.

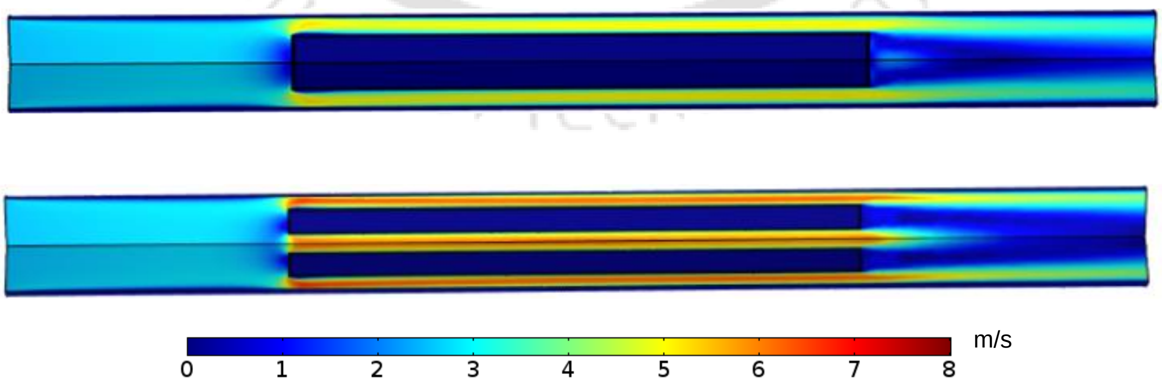

Figure 5.9. Comparison of velocity contours for basic capsule (top) and annular capsule (bottom).

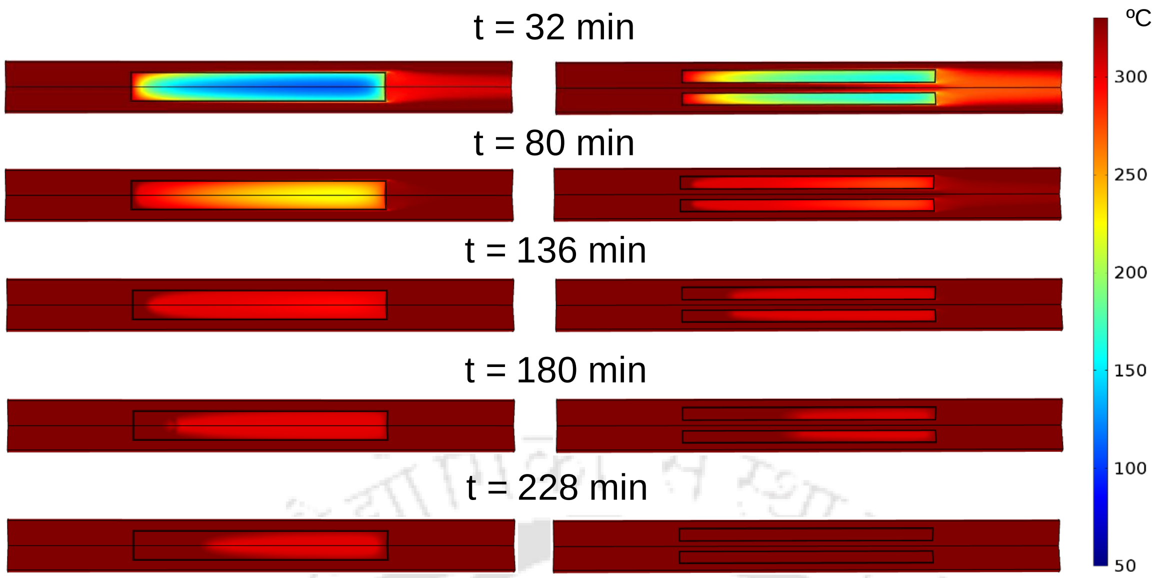

Figure 5.10. Comparison of temperature contours for the basic capsule (left) and annular capsule (right) at different time intervals

Based on the experiments, the times taken for the basic capsule and the annular capsule for the complete charging between 50-330 ºC were 280 min and 184 min, such that there was a reduction in charging time of 34.3% after introducing the annular capsule.

As the numerical model has been validated, it is useful in predicting the thermal performance of the capsule modules. The main reason for the improved charging performance of the annular capsule can be explained based on the velocity contours. Figure 5.9 shows the velocity contours of the basic capsule and the annular capsule for a fixed inlet air flow rate of 58.5 m^3/h. Two important observations can be made by changing the basic capsule design to the annular capsule;

i. The dynamics of air flow inside the system improves comprehensively. The velocity contours reflect that instead of one low velocity zone in case of basic capsule i.e. the air enclosed between the capsule and the outer pipe, there exists two high velocity zones both through the hole and the outer enclosure.

ii. The surface area of the air in contact with the capsule increases significantly after introducing the annular capsule. The heat transfer surface area for the annular capsule is found to increase by 16.5 % than the basic capsule.

The temperature contours for the charging process for the basic capsule and the annular capsule at different time intervals are shown in Figure 5.10. The heat transfer essentially takes place in both the axial and radial directions in both the cases, however, it is more predominant in the radial direction. It occurs in the axial direction due to flow of the HTF from the inlet to the outlet section, whereas, it occurs in the radial direction from the outer wall towards the centre of the PCM capsule. Initially, the heat transfer takes place due to conduction inside the solid PCM. The charging process initiates in the front end of the capsules as they come in contact with the incoming hot air as observed from the temperature contours at 32 min. It is evident that the heat transfer occurs inside the basic capsule from the outer wall towards the centre of the capsule. The shape of the temperature contours in the basic capsule is such that there is a development of an axial front which extends throughout the length. However, the temperature increase towards the centre of the capsule is slow as compared to the annular capsule.

In case of the annular capsule, the temperature near the inner wall of the capsule increases rapidly due to an increase in the surface area of heat transfer at the centre of the capsule. After 80 min, the temperature inside the basic capsule increases, however, there exists a significant temperature differential in the front and the rear end. In case of the annular capsule, the temperature throughout the length reaches the melting temperature and is uniform. After 136 min, the distinction between the melted and the un-melted layers can be clearly identified. The melting behaviour is similar in both the capsules with melting extending in the form of layers along the length of the system. The only distinction is in the rate of heat transfer which is faster in the annular capsule due to an additional high-temperature heat transfer surface at the centre. As the melting completes in case of the annular capsule, there is a sudden rise in the temperature due to conduction taking place in the liquid PCM. This phenomenon can be visualized from the change in the temperature contour from 180 min to 228 min, whereas, the melting in the basic capsule is incomplete till this time.

5.4.2 Charging and discharging performance of all capsule designs (Cases 1-5)

Different fin designs were incorporated in the annular capsule and the charging performance of all the cases shown in Figure 5.5 is analysed. The charging was conducted in the temperature range between 275-330 ºC for an air inlet flow rate and temperature of 58.5 m^3/h and 360 ºC, respectively. Figure 5.11 shows the temperature profile at the different thermocouple locations (T1 to T5) for all the cases (Cases 1, 2, 3, 4 and 5). Due to the experimental limitations, temperature at all locations was not uniform initially, however, the average temperature was fixed as 275 ºC.

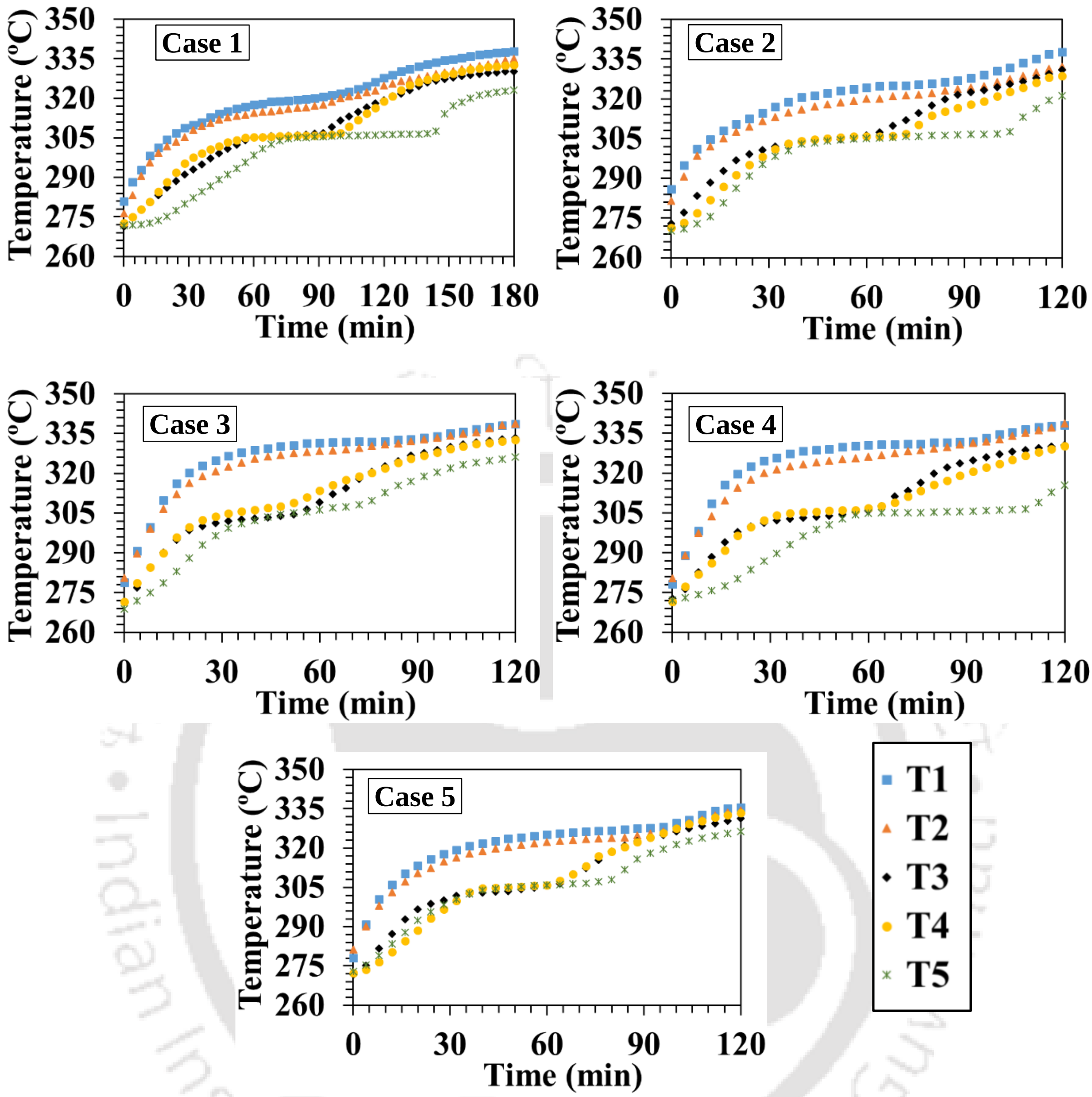

Figure 5.11. Temporal evolution of temperatures at different locations for all the Cases 1-5 during charging.

The heat transfer behaviour during charging for all the cases is explained as follows. The charging temperature profile comprises of conduction heat transfer which occurs initially as the PCM is solid. This is followed by its melting and heat transfer inside the liquid PCM due to conduction until the temperature reaches steady-state. Initially, the heat transfer initiates near the front end of all the capsules as the hot air comes in contact with the capsule. Due to a high temperature difference between the PCM and the air, the heat transfer rate is higher in the front end of the capsule. It is worthwhile noting that the temperature profiles for T1 and T2 located at the top and bottom of the capsule are almost similar throughout the charging process. This shows that there is a minimal effect of buoyancy driven natural convection heat transfer in the PCM capsule and the heat transfer occurs primarily due to conduction. The heat transfer then extends towards the middle section at location T3. It is evident that the heat transfer takes place from the outer wall in case of the basic capsule, and both through the inner and outer walls in rest of the cases. Finally, the heat transfer occurs at the rear end of the capsule with temperature rise at T4 and T5. The thickness of the PCM layer at the top end of the capsule is slightly lower than the bottom layer as the solid PCM leaves a void at top of the capsule. This reduces the PCM volume at top and hence the temperature rise at locations T1 and T4 is slightly higher than T2 and T5, respectively. Therefore, during the experiments, the charging process initiates near the front end of the system and completes towards the rear bottom end of the capsule. The behaviour during the charging phenomenon is also confirmed by the temperature contours obtained from the numerical models discussed above.

The improvement in heat transfer in Case 2 than Case 1 i.e. by changing to the annular capsule design is discussed previously in Section 5.4.1. By adding four longitudinal fins in the annular capsule, i.e. in Case 3, the heat transfer rate is substantially improved. This is evident from the rise in temperature at all the locations inside the PCM. However, as the weight of the fins is an important consideration while employing these capsules for practical applications, it is important to study the effect of adding tapered fins on the heat transfer rate. In Case 4, the fins are tapered from the inlet section towards the outlet section of the PCM capsule. In comparison to Case 3, the temperature profiles T1, T2 and T3 do not change significantly in Case 4, however, the rise in the temperature at the rear end of the capsule decreases comprehensively. This happens due to absence of fin surfaces at this location and the heat transfer rate is not affected as much. In Case 5 on the other hand, the heat transfer rate is already high in the front end due to a high temperature difference between the HTF and the PCM and thus, it is not affected due to the absence of fins at this location. The heat transfer rate at the front end is more affected due to the temperature difference between the air and the PCM. However, near the rear end, fins benefit the heat transfer rate and improve the overall charging rate inside the PCM.

Figure 5.12 shows the average PCM temperature for all the cases. The charging time for the basic capsule (Case 1) was 164 min, and that for Case 2 was 120 min, and there was a reduction by 26.8% in Case 2 than Case 1. By adding four straight longitudinal fins, the reduction in charging time in Case 3 than Case 2 was 16.67%. A higher rate of charging in Case 2 than Case 1 occurs due to improvement in the dynamics of air flow. However, by adding fins, the heat transfer rate improves due to reduction in thermal resistance inside the PCM. Therefore, it is evident that the major improvement in heat transfer enhancement occurs due to introduction of the annular capsule, however, fins only provide additional assistance to heat transfer rate. The charging time for Case 4 and Case 5 were 118 min and 108 min, respectively. The reduction in time for Case 4 and Case 5 than Case 2 were 1.4% and 10%, respectively. The charging time for Case 4 and Case 2 is almost similar, which shows that the addition of fins does not necessarily lead to improvement in the performance. However, fins when distributed effectively can improve the thermal performance as observed in Case 5.

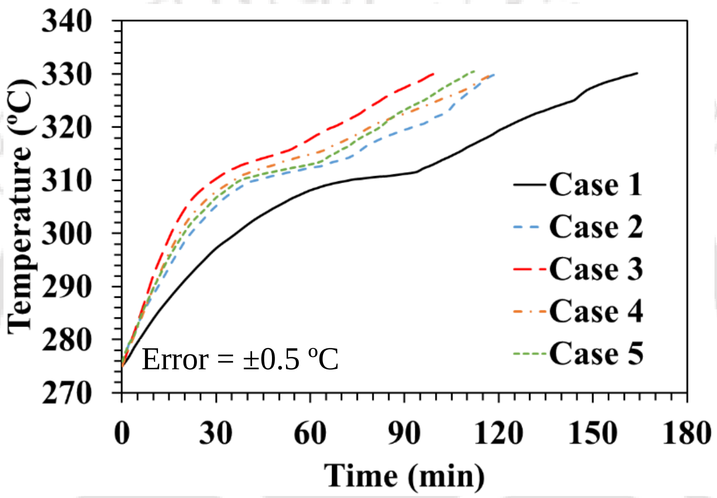

Figure 5.12. Temporal evolution of average PCM temperature for all the Cases 1-5 during charging.

The discharging experiment was performed within the temperature range 330-275 °C. The inlet air temperature and flow rate were fixed as 250 °C and 87.5 m^3/h, respectively. The temperatures at different thermocouple locations for all the cases (Cases 1-5) during the discharging experiment are shown in Figure 5.13. It can be observed that the heat transfer drops along the length of the system for all the cases, and is similar to that of the charging experiment. The heat transfer initiates at the front end of the PCM capsule at locations T1 and T2 and therefore, the temperature drops at a faster rate at these locations. This is followed by the discharging at the location T3 at the middle of the capsule. Finally, the heat transfer extends at the rear end of the PCM capsule and the discharging rate is slowest at location T5.

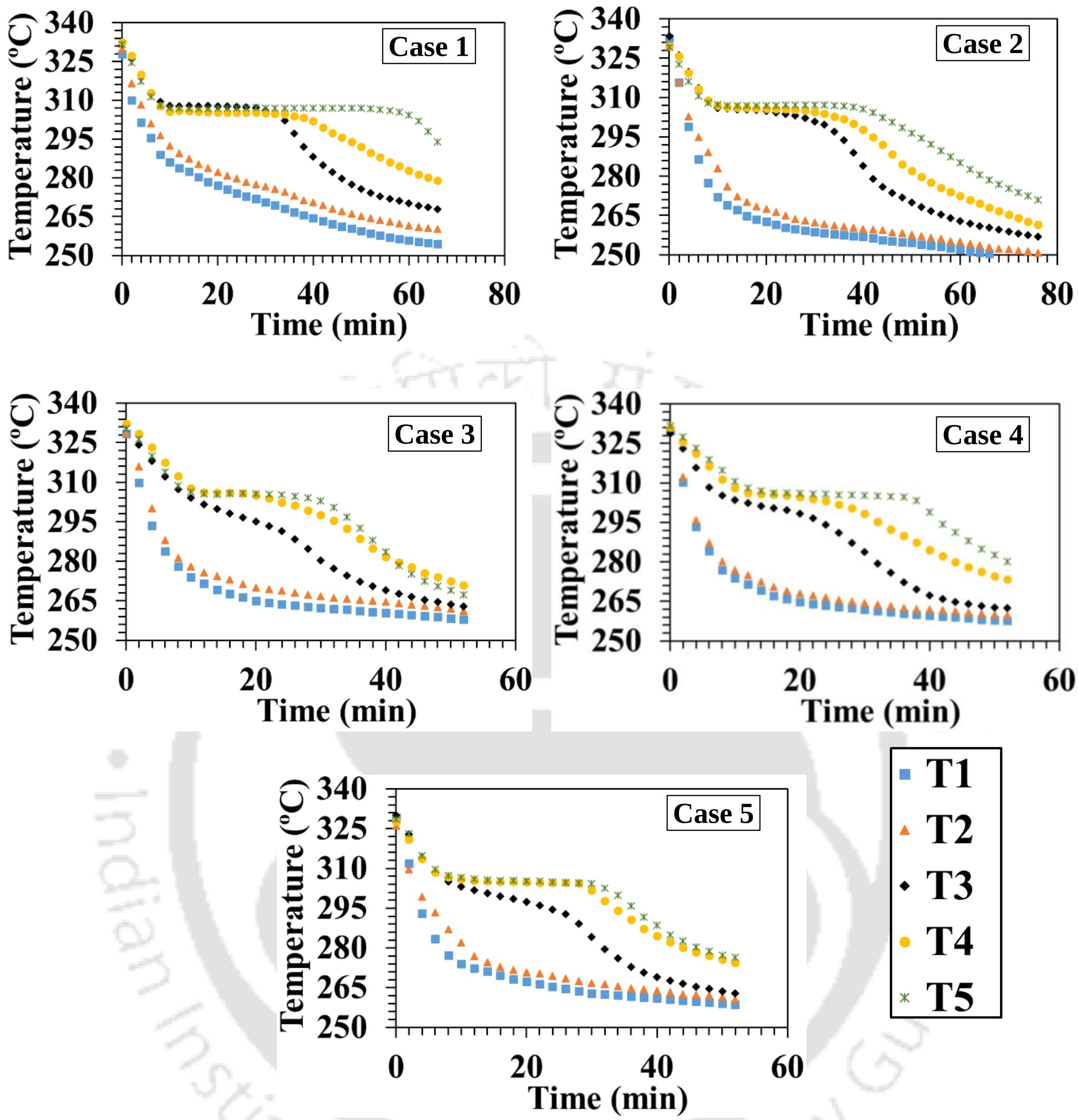

Figure 5.13. Temporal evolution of temperatures at different locations for all the Cases 1-5 during discharging.

In Case 1, the heat transfer rate at all the thermocouple locations is low throughout the discharging process as compared to the other cases. Significant improvement in the heat transfer rate is observed at all locations by changing from Case 1 to Case 2 due to an increase in the heat transfer surface area for the annular capsule. As indicated by the temperature profiles T3, T4 and T5, the heat transfer rate in Case 3, Case 4 and Case 5 is improved as compared to Case 2 due to further improvement in the heat transfer surface area with the addition of fins.

The temperature drop at location T5 decides the time of completion of the discharging process. The heat transfer rate at T5 is marginally faster in Case 3 than Case 4 and Case 5.

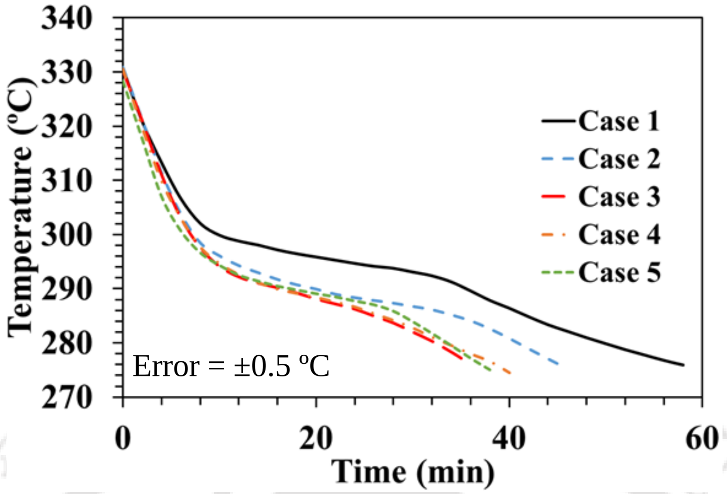

Figure 5.14. Temporal evolution of average PCM temperature for all the Cases 1-5 during discharging.

The average PCM temperature during discharging for all the cases (Cases 1-5) is shown in Figure 5.14. The discharging times for Case 1, Case 2, Case 3, Case 4 and Case 5 were 60 min, 46 min, 36 min, 39 min and 38 min, respectively. The discharging time by introducing the annular capsule design i.e. by changing from Case 1 to Case 2, was reduced by 23.3%. Further due to addition of longitudinal fins in the PCM capsule (Case 2 to Case 3), the discharging time was reduced further by 21.7%. It is observed that the overall heat transfer is not affected by the shape of the fins. The discharging time is similar for Case 3, Case 4 and Case 5, such that significant improvement in the heat transfer rate can be achieved by adding different fin designs.

Therefore, addition of fins is subjected to careful optimization based on the distribution of fins along the length of the capsule. The use of heat transfer surfaces such as fins is found to be favourable, however, it is subjected to a compromise between the system performance and weight. To reduce the overall system weight in the high capacity systems, fins can either be avoided or only the tapered fins with favourable charging and discharging performance can be utilized. To achieve a higher advantage with fins, high thermal conductivity fin materials such as copper or aluminium may be useful, however, their non-compatibility with molten salts used in the high-temperature storage is still a challenge.

5.4.3 Effect of inlet air flow rate

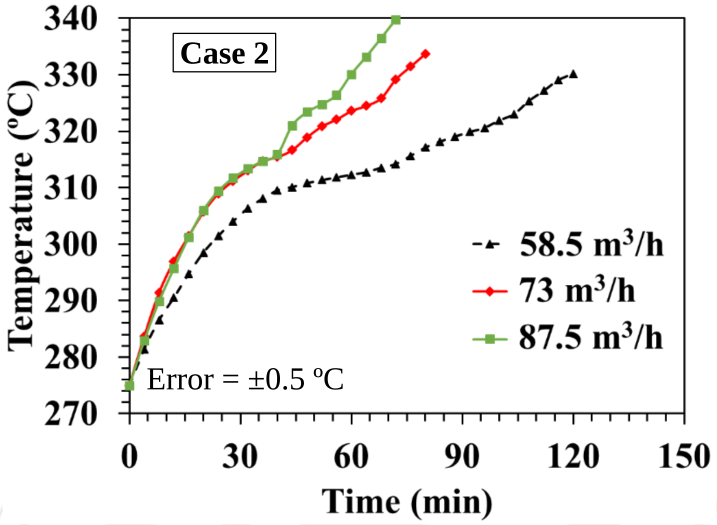

Figure 5.15. Effect of air flow rate on the average PCM temperature for Case 2 during charging.

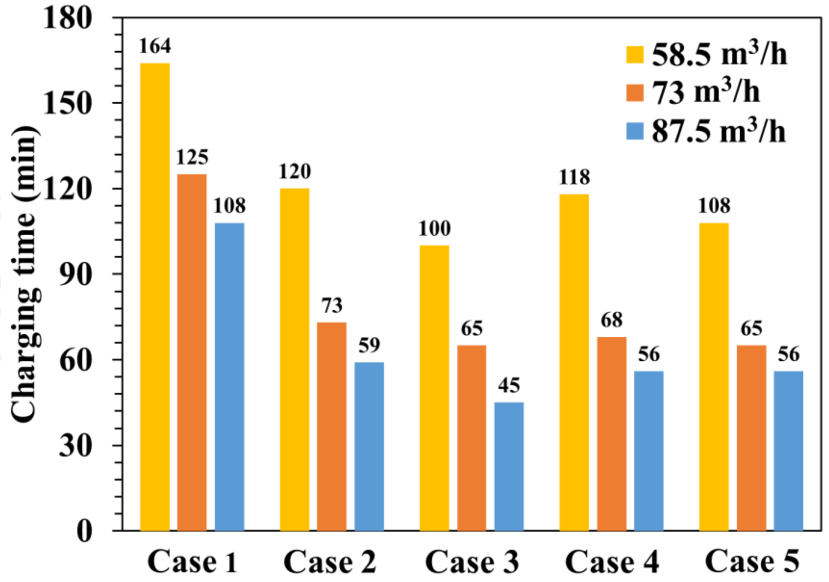

Figure 5.16. Charging times at different flow rates obtained for all the Cases 1-5.

Experiments were performed in the charging temperature range between 275-330 ºC for a fixed air inlet temperature of 360 ºC. The flow rates were varied to values of 58.5, 73 and 87.5 m^3/h. Figure 5.15 shows the effect of inlet flow rate on the thermal performance of the annular capsule (Case 2). Increasing the air flow rate from 58.5 m^3/h to 73 m^3/h, the charging time was reduced by 39.1%, however, there was a further reduction by 19.1% by increasing the air flow rate to 87.5 m^3/h. There was a substantial increase in the average PCM temperature by increasing the flow rate initially, however, as the flow rate was increased further, the improvement in the charging rate was less significant.

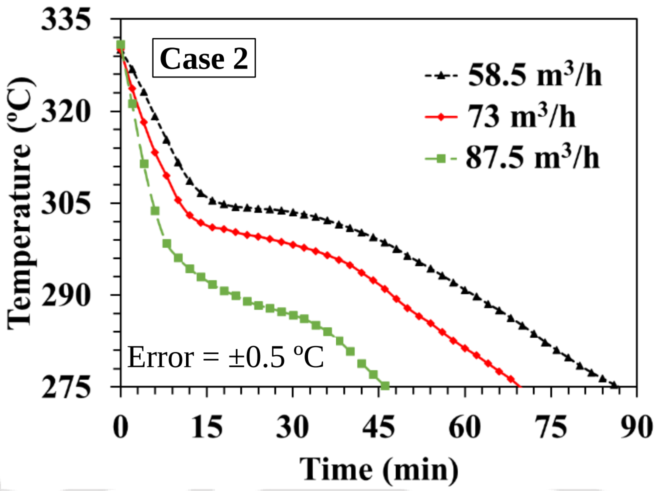

Figure 5.17. Effect of air flow rate on the average PCM temperature for Case 2 during discharging.

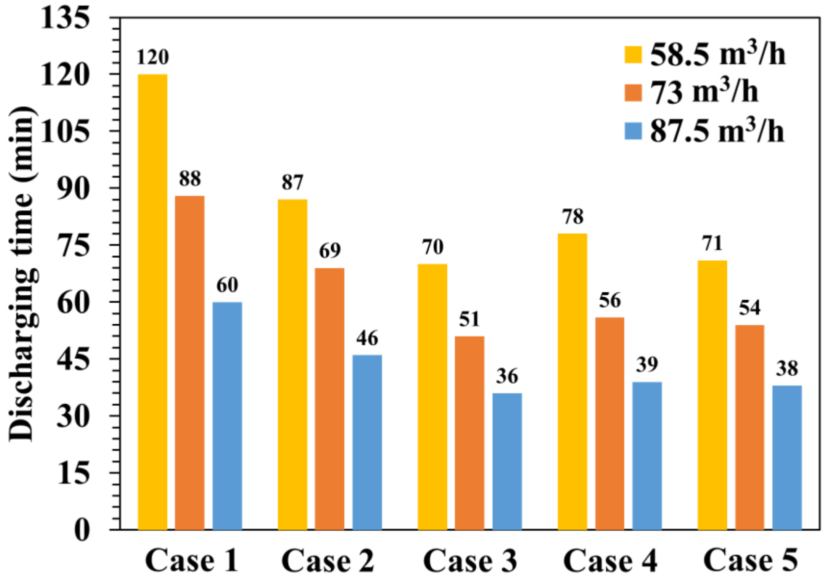

Figure 5.18. Discharging times at different flow rates obtained for all the cases 1-5.

Similarly, experiments were performed for all the cases (Cases 1-5) for different flow rates (58.5, 73 and 87.5 m^3/h) and the corresponding charging times are plotted in Figure 5.16. The least effect of increase in the flow rate on the charging time was observed in Case 1. However, the performance improved notably in the other cases having the annular design. The maximum impact of the flow rate was found in Case 3, wherein, increasing the flow rate from 58.5 m^3/h to 87.5 m^3/h, there was a reduction in the charging time by 55%. For Case 1, 2, 3 and 4, the charging time reduced by 47-55% by increasing the flow rate. In all the cases, notable charging time reduction occurred only up to a flow rate of 73 m^3/h, whereas, the reduction was not significant thereafter.

The effect of air flow rate on the discharging performance in Case 2 was analysed by varying the air flow rate to different values; 58.5 m^3/h, 73 m^3/h and 87.5 m^3/h as shown in Figure 5.17. The initial PCM temperature and inlet air temperature were fixed as 330 ºC and 250 ºC, respectively, and the discharging was performed in the temperature range 330-275 ºC. Increasing the flow rate from 58.5 m^3/h to 73 m^3/h in Case 2, the discharging time reduced by 21%, and reduced further by 33.3% by increasing the flow rate from 73 m^3/h to 87.5 m^3/h. Therefore, the heat transfer rate improves significantly by increasing the flow rate above a threshold value (73 m^3/h). The calculated Reynolds number based on standard air property charts (Incropera et al., 2007) increases from ~5000 to ~7000 by increasing the flow rate from 58.5 m^3/h to 87.5 m^3/h. This suggests that the air flow changes from transition regime to turbulent regime which leads to a significant improvement in the heat transfer rate. The discharging times for all the cases (Cases 1-5) for different flow rates is plotted in Figure 5.18. It is observed that for all the PCM capsules, the heat transfer rate improves with the increase in the air flow rate. Similar to Case 2, the heat transfer rate increases by increasing the inlet air flow rate from 58.5 m^3/h to 87.5 m^3/h in all the cases and thus, the discharging time reduces.

5.4.4 Effect of inlet air temperature

Figure 5.19 shows the average PCM temperature profiles for Case 2 at different inlet air temperatures (360, 380 and 400 ºC). The air flow rate was fixed as 58.5 m^3/h for the charging temperature range between 275-330 ºC. The results show that an increase in the inlet air temperature decreases the charging time. The outcomes can be attributed to the increase in the temperature difference between the air and the PCM, which accelerates the heat transfer rate especially at the front end of the capsule. However, it is worth noting that, increasing the air temperature by 20 ºC, there was a decrease in the charging time by 39.1%. Increasing the inlet temperature further by 20 ºC, the charging time decreased further by 19.1%. Therefore, increase in the air inlet temperature has a major influence in improving the heat transfer rate than increase in the air flow rate.

The charging times for all the cases (Cases1-5) at different air inlet temperatures are plotted in Figure 5.20. With a 40 ºC increase in the inlet temperature, the reduction in charging time for Cases 1, 2, 3, 4 and 5 were 40.3%, 58.3%, 62%, 59.3% and 56.5%. The behaviour is similar in all the cases such that the effect of inlet air temperature on the charging time is significant by increasing the inlet air temperature by 40 ºC.

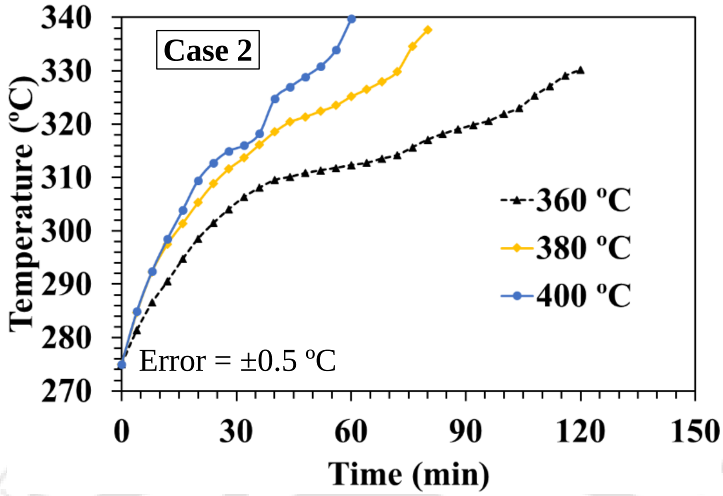

Figure 5.19. Effect of inlet air temperature on the average PCM temperature for Case 2 during charging.

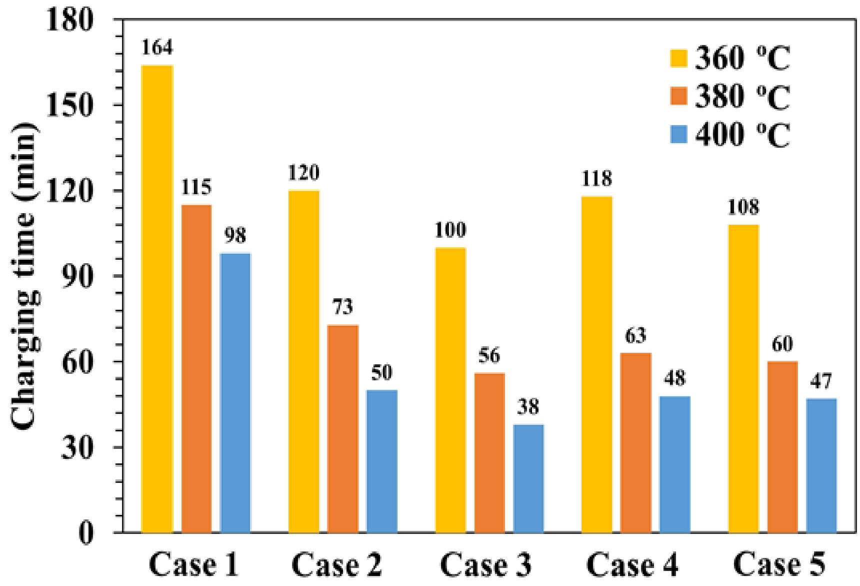

Figure 5.20. Charging times at different air inlet temperatures obtained for all the Cases 1-5.

The effect of inlet air temperature during the discharging was analysed by varying the temperature to different values; 250 ºC, 225 ºC and 200 ºC. The average initial PCM temperature and the inlet air flow rate were fixed as 330 ºC and 87.5 m^3/h, respectively, and the discharging was conducted in the temperature between 330-275 ºC.

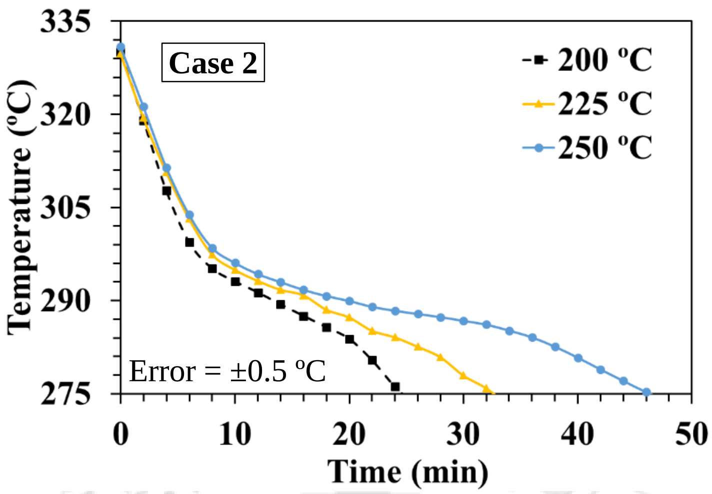

Figure 5.21. Effect of inlet air temperature on the average PCM temperature for Case 2 during discharging.

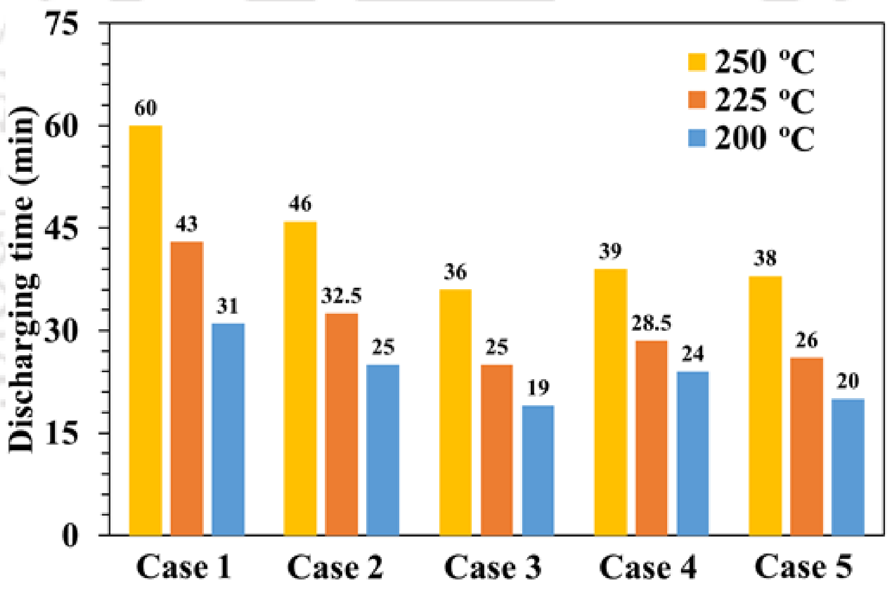

Figure 5.22. Discharging times at different air inlet temperatures obtained for all the Cases 1-5.

Figure 5.21 shows the variation of temperature versus time for Case 2 due to decrease in the inlet air temperature during discharging. The effect of inlet air temperature cannot be directly compared with the charging process as there was a significant variation in the density of air while operating at a lower temperature during discharging. Based on the standard property charts for air, the density increases by approximately 20% such that there is an increase in the mass flow rate of the air, even as the volumetric flow rate is fixed while conducting the experiments. Nevertheless, decreasing the inlet air temperature by 25 ºC from 250 ºC, there was a 29.3% reduction in the discharging time, followed by a further reduction of 23% with a decrease in the inlet temperature to 200 ºC. A similar effect is observed by decreasing the inlet air temperature for all the cases (Cases 1-5) as shown in Figure 5.22. There was a 38.5-48.3% reduction in the discharging time due to a 50 ºC drop in the inlet air temperature, where the maximum and minimum reduction occurred in Case 1 and Case 4.

5.4.5 Energy charged or discharged

The energy charged or discharged by the PCM capsules is calculated based on the temperature range of the charging and discharging experiments. The total energy charged or discharged is a sum of the latent heat and the sensible heat stored by the PCM and is calculated using Eq. (5.1). The corresponding total heat stored or discharged by the PCM encapsulations calculated for Cases 1-5 in the temperature range between 275-330 ºC were 647.6 kJ, 645 kJ, 634.2 kJ, 639.6 kJ and 637 kJ, respectively. The quantity of latent heat stored or discharged for Cases 1-5 was estimated as 66.2% of the total energy charged or discharged. The rates of energy charging or discharging are affected by the inlet air conditions such as flow rate and temperature and are consistent with the charging and discharging temperature profiles discussed in detail in Sections 5.4.3 and 5.4.4 previously.

5.5 Summary

In the present study, experimental and numerical investigations were carried out to study the charging and discharging performances of high-temperature phase change material (PCM) capsules. Sodium nitrate with melting point 305.1 ºC was used as the PCM and air was used as the heat transfer fluid. The capsules were manufactured from stainless steel (SS 310S) material suitable for highly corrosive and high-temperature environment. First, basic cylindrical capsule (Case 1) and the annular cylindrical capsule (Case 2) thermal storage performances were compared within the charging temperature range of 50-330 ºC. The developed numerical model has been validated with the experimental results. Introducing the annular design improves both the air flow dynamics and the heat transfer surface area and thus leads to a reduction in the charging time. The temperature contours show that the heat transfer takes place due to conduction in the axial and radial directions in both the cases, however, heat transfer accelerates in the radial direction due to an additional heat transfer surface at the centre of the annular capsule.

Additionally, experimental investigations were carried out to study the charging and discharging characteristics of three more annular capsule designs namely; annular capsule with straight longitudinal fins (Case 3), annular capsule with tapered longitudinal fins having decreasing height (Case 4) and annular capsule with tapered longitudinal fins having increasing height (Case 5). Experiments for different flow rates (58.5, 73 and 87.5 m^3/h) and different air inlet temperatures (360/380/400 ºC during charging and 200/225/250 ºC during discharging) were performed for all the cases in the charging/discharging temperature range of 275-330 ºC. A maximum reduction in charging time of 49% (for 58.5 m^3/h and 400 ºC) was obtained, whereas during discharging, there was maximum reduction in discharging time of 27.5% (for 58.5 m^3/h and 250 ºC) by changing design from Case 1 to Case 2. Employing Case 3 led to an additional reduction in the charging and discharging time by 11-24% and 20-26%, respectively. The performance for Case 4 was either similar or marginally faster than Case 2 during charging, however, during discharging, there was 4-19% reduction in the discharging time. The Case 5 performed reasonably good with an improvement in the heat transfer rate by 5-17.8% than Case 2 during charging, and 18-20% during discharging.

The work presented in this chapter describes the most practical scenario of utilizing PCM capsules for high-temperature thermal energy storage applications. The importance of using simple design techniques to improve the heat transfer surface area such as introducing a hole in the capsule or using tapered fins were projected. Implementing fins is subjected to the constraints such as weight and cost of manufacturing in the actual high-capacity storage system. Further, it is proposed to use tapered fins than conventional straight fins in order to reduce the PCM capsule weight for a similar charging/discharging performance. It may also be appropriate to avoid fins, and rather achieve a high heat transfer rate by varying the inlet air conditions such as flow rate and temperature during charging and discharging.

Chapter 6

Novel conical shell LHS system design[**]

Preface

The thermal performance of the LHS systems primarily depends upon the heat transfer characteristics in the PCM region. Using heat transfer augmentation techniques, especially adding fins is advantageous, but at the same time, it suppresses the natural convection and adds up to the system size and cost. Also, the heat transfer weakens along the length of a cylindrical tube in tube LHS system because of the diminishing thermal potential between the HTF and the PCM. Therefore, melting takes place rapidly near the inlet section of the storage system and is delayed at the rear end. Hence, there is a need to design a simple heat exchanger system with the heat transfer mechanism being intensified via natural convection and effective PCM distribution. This technique may accelerate the charging/discharging rates and maintain the compact size of the system.

In this work, a numerical model to analyse the charging and discharging characteristics of a horizontal shell and tube type Latent Heat Storage (LHS) prototype is presented. The design is optimized by modifying a cylindrical shell into a conical shell heat exchanger system and a performance comparison is made between the two systems for a fixed LHS capacity. 3-D numerical simulation performed on the proposed system revealed that an innovation in the design leads to enhanced heat transfer rate caused by uniform melting throughout the system. With the advent of advanced heat exchanger design, there is a greater scope of obtaining higher heat transfer rates employing the proposed conical shell and tube LHS system.

[**] The findings reported in this chapter are published as the following research article:

Sodhi GS, Jaiswal AK, Vigneshwaran K, Muthukumar P. Investigation of charging and discharging characteristics of a horizontal conical shell and tube latent thermal energy storage device. Energy Conversion and Management. 2019 May 15;188:381-97.

6.1 Design of LHS system

A cylindrical shell LHS system is designed for a storage capacity of 1 MJ. The PCM volume (V) required for this capacity depends on the heat storage capacity (Q_L), density (ρ) and latent heat of fusion (Δh_f), which is calculated using Eq. (3.1). Based on the length (L), outer diameter (d_o) of the HTF tube and the calculated PCM volume, the diameter of the cylindrical shell (D_o) is calculated using Eq. (3.2).

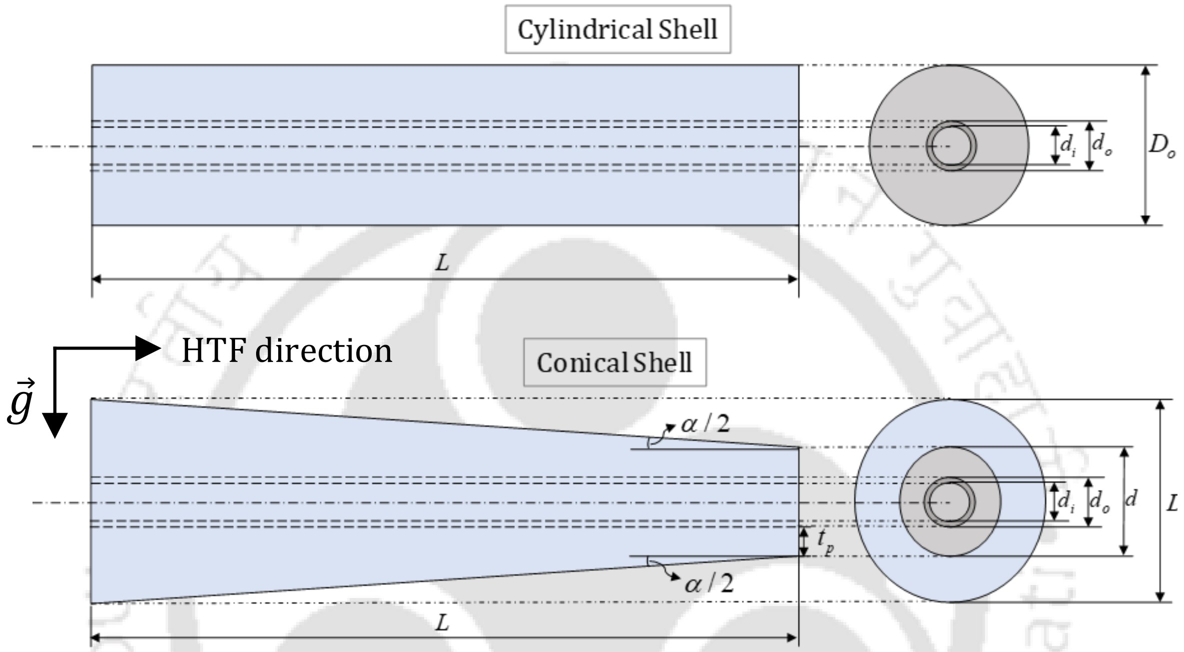

Figure 6.1. Dimensions of the horizontal cylindrical and conical shell LHS systems.

A conical shell model is developed by keeping the PCM volume same as that of a cylindrical model. The diameters D and d of the conical shell at inlet and outlet sections, respectively, can be calculated by equating the PCM volume inside the cylindrical and conical shell LHS systems. The physical models with dimensions are described in Figure 6.1. During the charging process, the air is passed through the HTF tube at a temperature higher than the initial system temperature. The energy lost by the air is absorbed by the storage model in the form of latent heat and the PCM starts melting. The dimensions of the models shown in Figure 6.1 are described in Table 6.1.

Table 6.1. Dimension values of LHS system.

Dimension	d_o(mm)	d_i(mm)	L(mm)	D_o(mm)	t_p(mm)	d(mm)	D(mm)	α (°)
Values	28.6	24.6	750	77.37	12.7	54	98.6	3.6

6.2 Numerical model

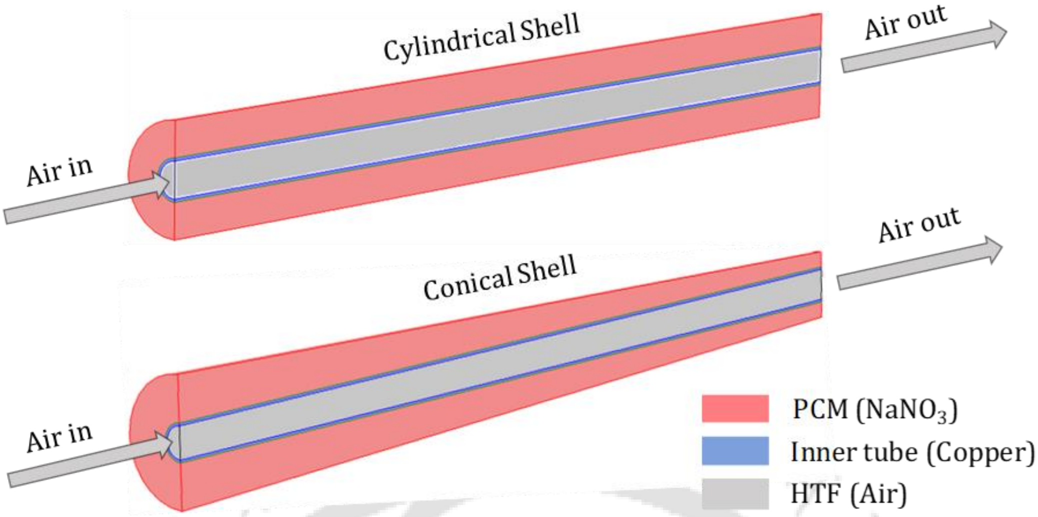

Figure 6.2. Computational domain of the horizontal cylindrical and conical shell LHS systems developed for the study.

The numerical models of the cylindrical shell and conical shell LHS systems are developed to investigate the performance of both the system and develop an optimum LHS geometry. The computational domain of the 3D models are shown in Figure 6.2. A conjugate heat transfer multi-physics problem is developed in the commercial modelling software COMSOL Multiphysics and only one half of the geometrical models are developed as both the heat transfer and fluid flow are symmetric about the vertical axes. The equations governing the HTF flow and the heat transfer between the HTF and the PCM, the basic assumptions for the HTF and PCM domains and the numerical procedure is described in detail in Section 3.2. The effective heat capacity method used to model the phase change is validated with the experimental data reported by Longeon et al. (Longeon et al., 2013) and has been reported previously in Section 3.2.4.

6.2.1 Boundary conditions

The numerical model is subjected to the boundary conditions as described in Table 6.2.

Table 6.2 Boundary conditions imposed on the system

For Charging: $T_{in} > T_M > T_i$ For Discharging: $T_{in} < T_M < T_i$	At t =0 s, $T = T_i$ (for all domains) At $t > 0$, $T_{HTF} = T_{in}$ and $v_{HTF} = v_{in}$
Adiabatic outer surface of shell	$\left.\frac{\partial T}{\partial r}\right\|_{r=D/2} = 0$ (Cylindrical or conical shell)
No slip boundary conditions	$v_{HTF} = 0$ and $\vec{v} = 0$ (walls)

Sodium nitrate ($NaNO_3$) and air are chosen as the PCM and the HTF, whereas, the heat transfer interface between the HTF and the PCM is of copper. The thermo-physical properties of the PCM and the HTF have been described previously in Section 3.3.2. The PCM is considered to melt in the temperature range of 4 °C ($|T_L - T_S|$). The performance of the LHS models is assessed based on the important parameters such as the melt fraction, charging/ discharging times and energy stored/ discharged and have been discussed previously in Section 4.1.

6.2.2 Meshing and grid independent test

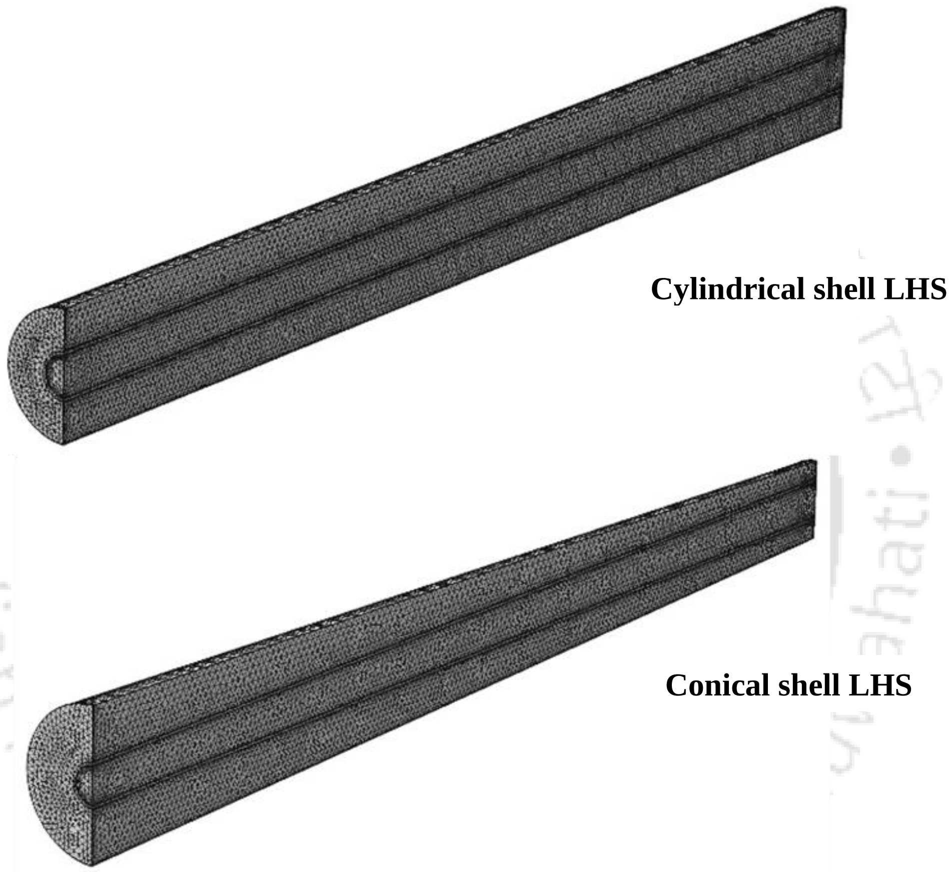

Figure 6.3. Model view after mesh development in both cylindrical and conical shell LHS system.

In the model, the mesh is developed with the help of free tetrahedral and triangular elements with special consideration to effective mesh distribution close to the walls and boundaries. The model view after meshing is shown in Figure 6.3. It is desired to make the numerical model independent of the grid so as to obtain best solution quality at a minimum computation cost.

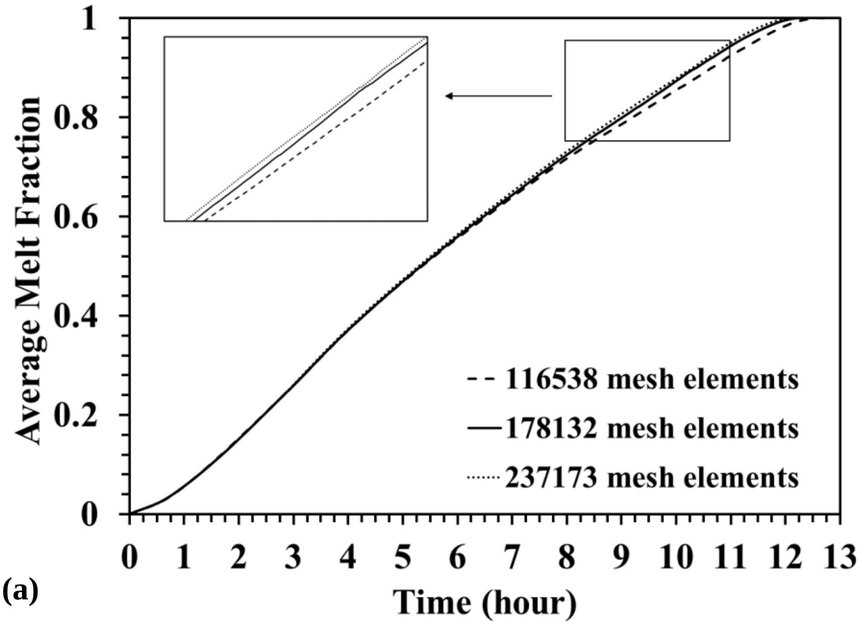

(a)

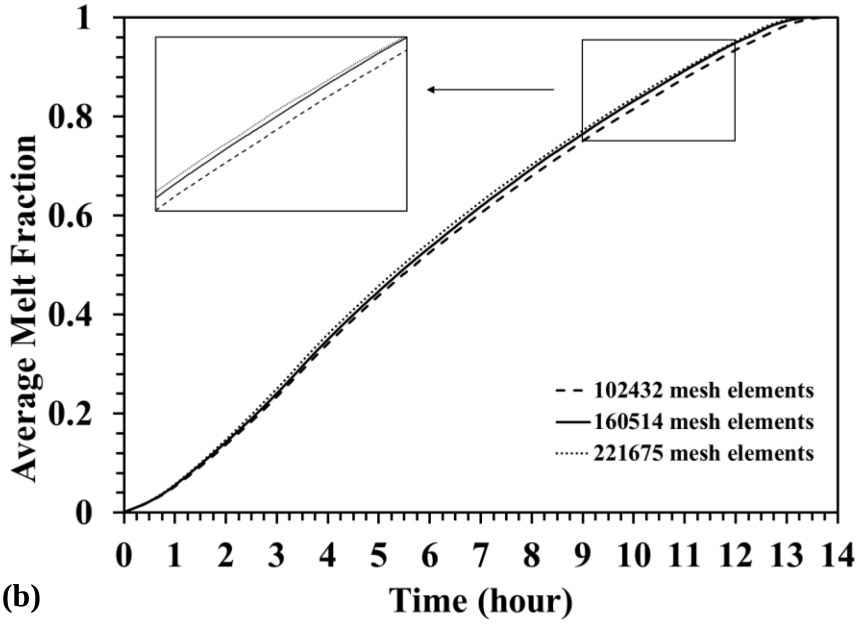

(b)

Figure 6.4. Grid independent test of the thermal model with (a) conical and (b) cylindrical shell system.

Figure 6.4(a) shows the variation of average melt fraction of PCM with time for the conical shell models with 116538, 178132 and 237173 mesh elements. It can be observed that the thermal models with 178132 and 237173 mesh elements are grid independent. Figure 6.4 (b). shows the average melt fraction of PCM of the cylindrical shell models with 102432, 160514 and 221675 mesh elements. It is found that the thermal models with 160514 and 221675 mesh elements are grid independent. The thermal model with 178132 mesh elements for conical model and 160514 mesh elements for cylindrical model has been selected to minimize the computational effort.

6.3 Results and Discussions

6.3.1 Optimization of PCM shell dimensions

Numerical simulations are carried out for the optimization of diameters of the conical shell system at the inlet and outlet sections, for both the charging and the discharging processes and the results are presented in this section.

Table 6.3. Dimensions of different conical shell configurations.

$t_p = \left(\frac{d-d_o}{2}\right)$ (mm)	d (mm)	D (mm)	$\alpha = 2tan^{-1}\left(\frac{D-d}{2L}\right)$ (°)
20.7	70	84.5	1.1
16.7	62	91.8	2.3
12.7	54	98.6	3.4
8.7	46	104.9	4.5
4.7	38	110.9	5.6

Table 6.3 describes the dimensions of five different conical shell configurations, all having a fixed PCM mass. For charging; HTF inlet temperature (T_{in}) = 326 ºC and initial temperature (T_i) = 286 ºC, whereas for discharging; T_{in} = 286 ºC and T_i = 326 ºC have been chosen. Table 6.4 presents the charging and discharging times for the conical shell system at different cone angles and at HTF inlet velocity (v_{in}) of 10 m/s. The variation of melt fraction is shown in Figure 6.5(a)-(b).

Table 6.4. Charging and discharging times for the conical and cylindrical shell LHS systems.

α (°)	Cylindrical	1.1	2.3	3.4	4.5	5.6
Charging time (h)	13.18	12.53	12.15	12.16	13.05	13.98
Discharging time (h)	16.1	12.9	12.76	12.23	14.29	14.68

During charging, it is observed that the configuration with cone angle (α) 3.4º melts faster than α = 2.3° for 96% of the process, whereas complete melting for both happens in same time. Discharging process for α = 3.4º is completed in very less time than other values of α. Therefore, α = 3.4º is chosen as an optimal value for both the charging and discharging processes.

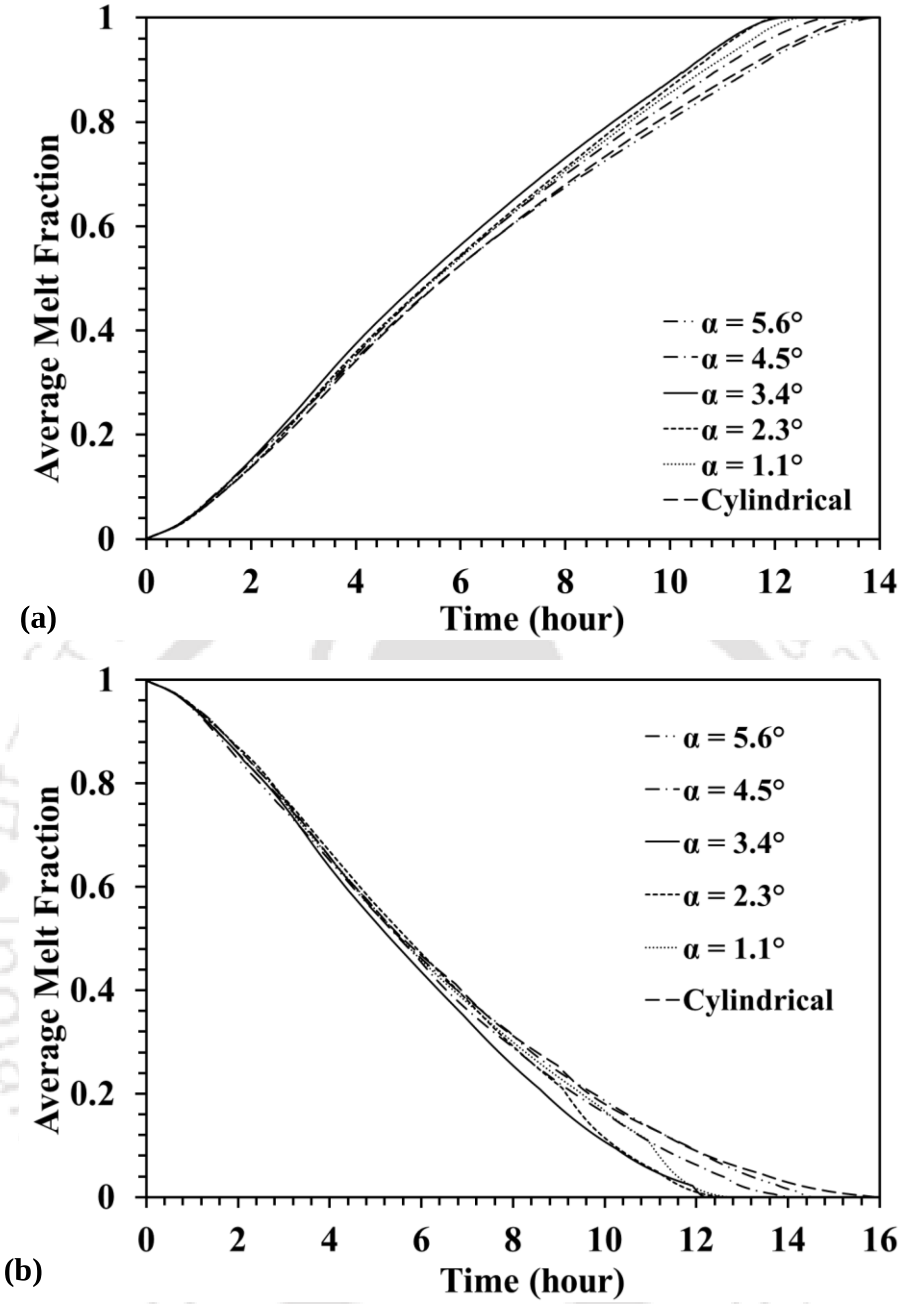

Figure 6.5. Variation of average melt fraction of storage system for different cone angles during (a) charging and (b) discharging.

Figure 6.6 shows the melt fraction contours for the charging process at 12.01 h and discharging process at 12.22 h. It is observed that, the cylindrical shell model is only 93.5/91.1% charged/discharged when the optimized model (α = 3.4°) is fully charged/discharged. As the cone angle decreases, the charging and discharging rates first increase and then decrease. The charging phenomenon characterised by PCM melting is explained as follows. For α=0° (cylindrical shell system) and α = 1.1°, the melt front initiates at the inlet section and travels axially in the flow direction. There is a regular melting behaviour with decreasing rate of melting from the inlet to outlet sections of the system and hence, the melting thoughout the LHS system is delayed. For α = 4.5° and 5.6°, a regular melt front travels axially in the flow direction. At the same time, due to very less PCM mass there is intensification of heat transfer near the outlet section, such that melting starts with movement of another melt front from the outlet section. Due to excessive PCM mass in the inlet section, melting takes place at a slower rate. Therefore, both the melt fronts meet near the inlet section, such that there is an overall delay in melting throughout the system. Hence, it is very important to distribute the PCM uniformly throughout the system, such that the average rate of melting is maximum. This happens for α = 3.4°, wherein the melt fronts initiated at the inlet and outlet section meet almost at the middle section leading to fast and uniform melting.

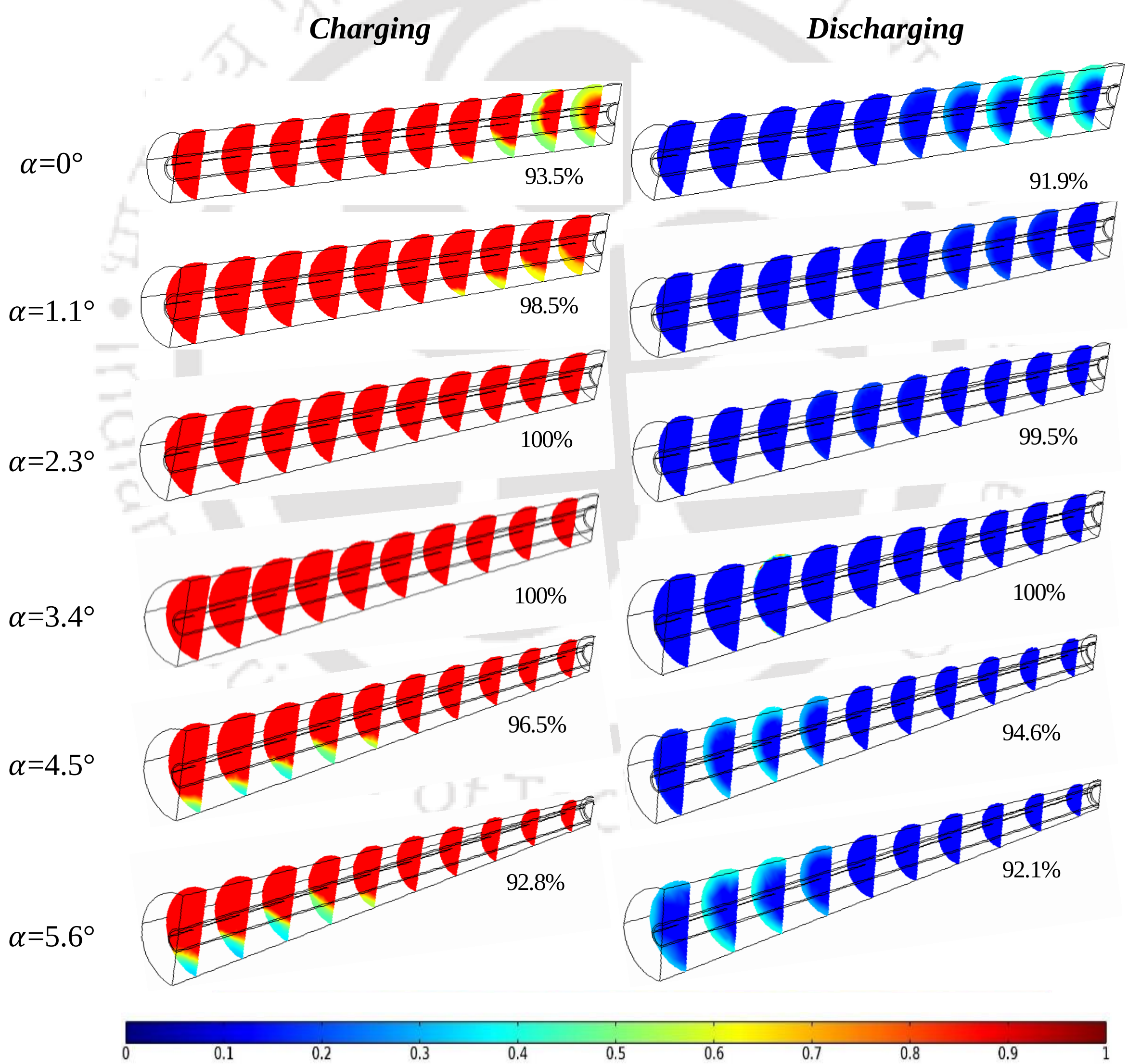

Figure 6.6. Melt fraction contours of storage system for different cone angles at t = 12.01 h for charging (left) and at 12.22 h for discharging (right).

During discharging process, the solidification fronts are almost symmetrical about both the horizontal and the vertical axes. Again, 3.4° is found out as the optimum cone angle, where, a similar reasoning equivalent to the charging process leads to this development.

6.3.2 Effect of HTF inlet conditions on the performance of conical shell system

6.3.2.1 Effect of inlet velocity of HTF

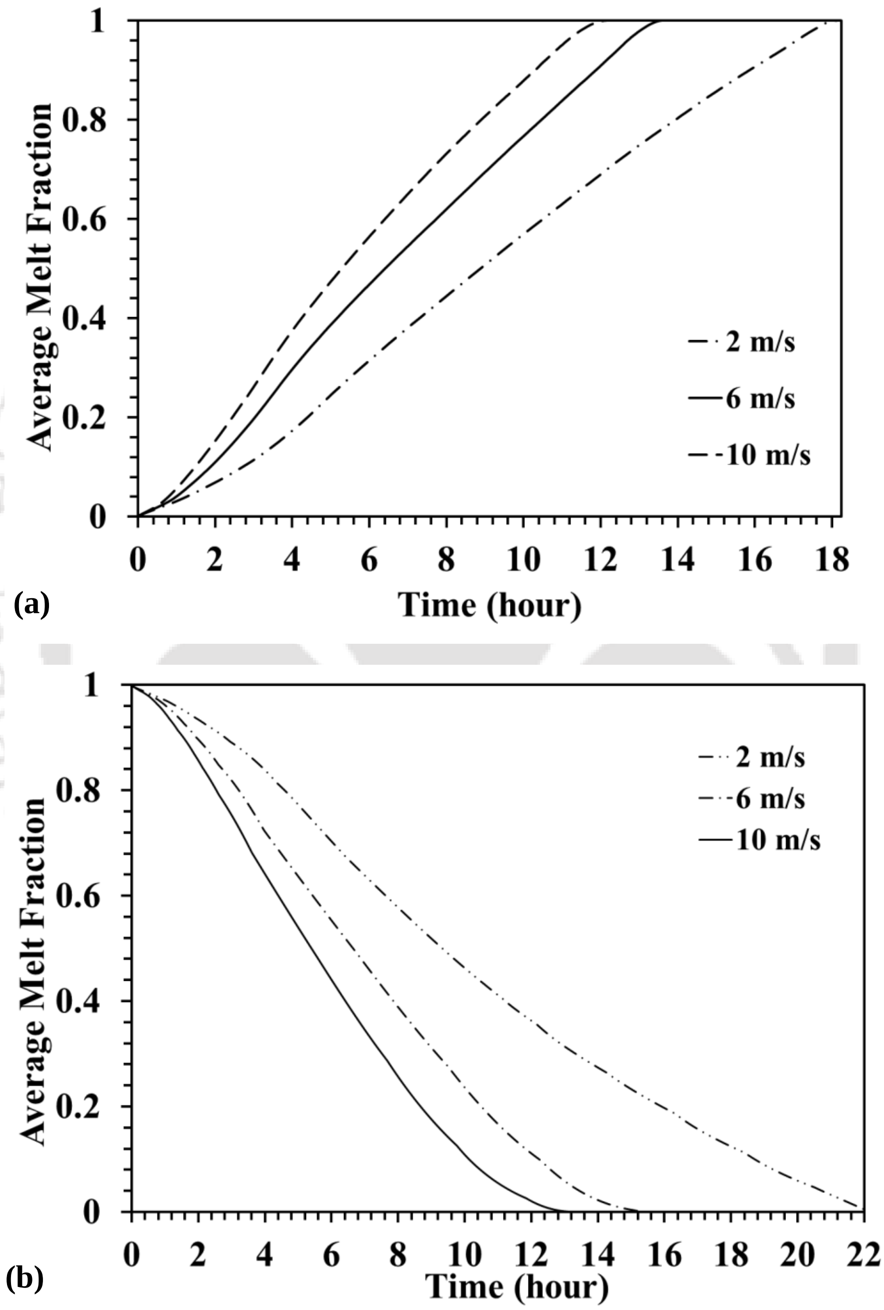

Figure 6.7. Average melt fraction variation of conical shell system for different HTF inlet velocities (v_{in}= 2, 4 and 10 m/s) for (a) charging and (b) discharging.

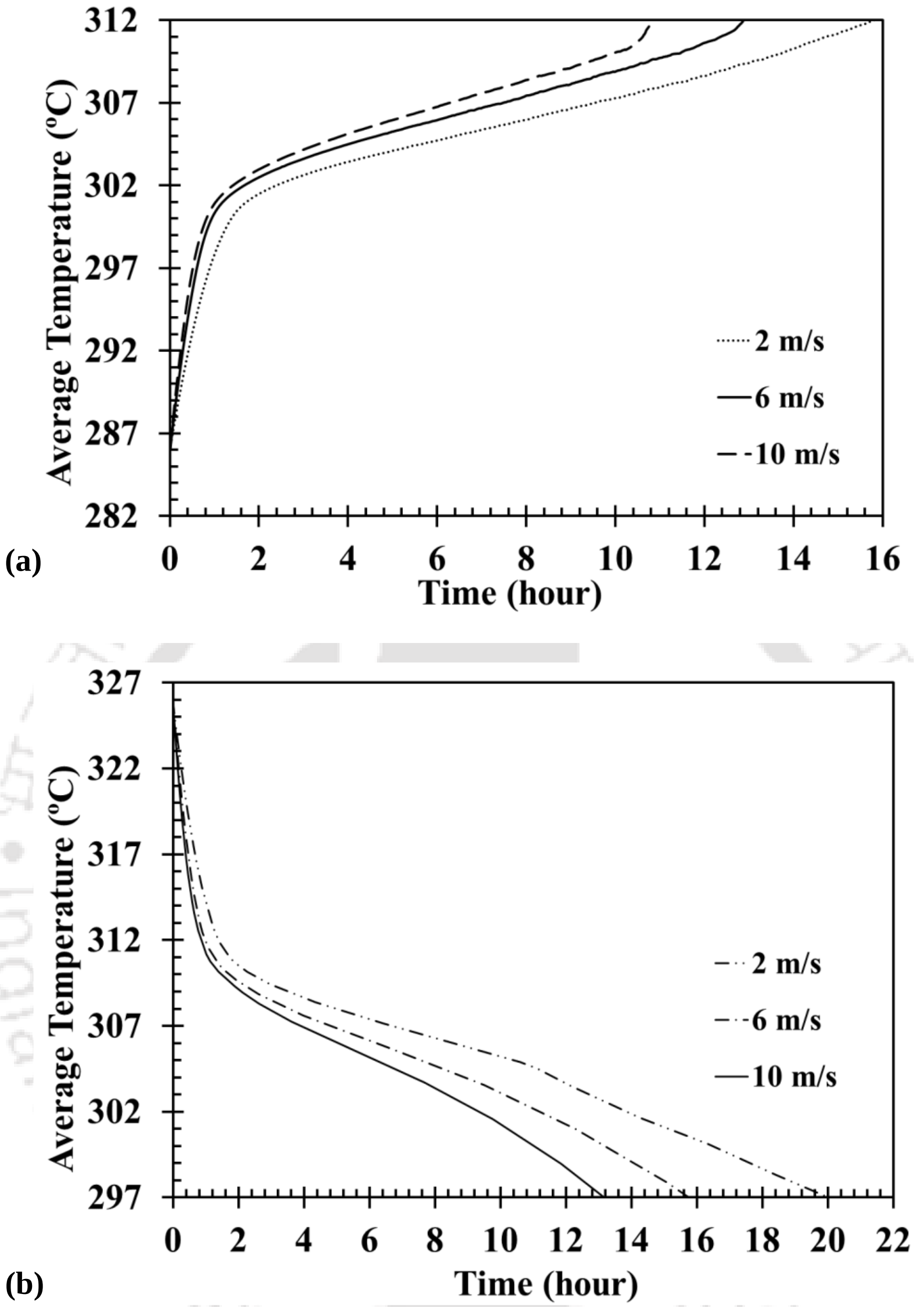

Figure 6.8. Average temperature variation of conical shell system at different HTF inlet velocities (v_{in}= 2, 4 and 10 m/s) for (a) charging and (b) discharging.

Figure 6.7(a)-(b) represents the average melt fraction of conical shell system (α = 3.4°) during charging (T_{in} = 326 ºC and T_i = 286 ºC) and discharging (T_{in} = 286 ºC and T_i = 326 ºC) at different velocities (v_{in} = 2 m/s, 6 m/s and 10 m/s). It is observed that the percentage reduction in charging time with increase in v_{in} from 2 m/s to 6 m/s is 25.1%, whereas with further increase from 6 m/s to 10 m/s, it is 10.5% only. During discharging the reduction in discharging time with increase in v_{in} from 2 m/s to 6 m/s and from 6 m/s to 10 m/s are 30%

and 14.4 % respectively. The variation in average PCM temperature during charging and discharging at different velocities is shown in Figure 6.8(a)-(b). Initially, the PCM temperature rises sharply due to significant temperature difference between the HTF and the PCM. As the PCM reaches the phase change temperature, an almost constant temperature profile is observed. Once the PCM melts completely, the temperature starts rising again due to sensible heat transfer between the HTF and the melted PCM.

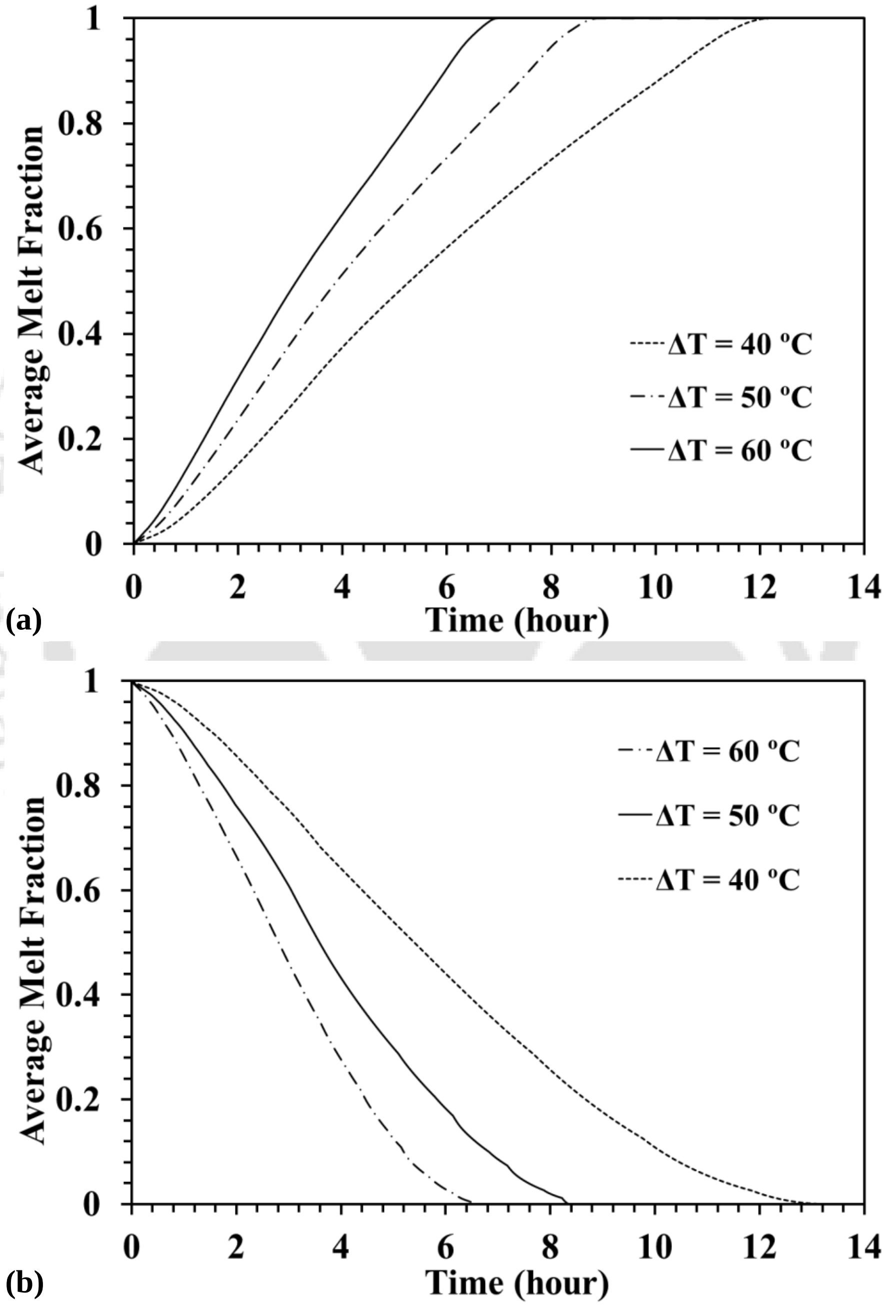

Figure 6.9. Average melt fraction variation of conical shell system for different ΔT for (a) charging and (b) discharging.

From Figure 6.7(a)-(b) and Figure 6.8(a)-(b), it is evident that increase in velocity to very high values, does not necessarily lead to significant reduction in charging and discharging times.

6.3.2.2 Effect of inlet temperature of HTF

During charging (T_i = 286 ºC and v_{in}=10 m/s) and discharging (T_i = 326 ºC and v_{in}=10 m/s), of the conical shell system (α=3.4°), the $\Delta T = |T_{in} - T_i|$ is changed from 40 ºC to 50 ºC and 60 ºC. The average melt fraction curves for different ΔT values are shown in Figure 6.9(a)-(b). With increase in ΔT from 40 ºC to 50 ºC, there is a reduction in charging time by 26.9% and discharging time by 36.7%. Further increasing ΔT to 60 ºC, the percentage reduction is 21.5% and 21.2%, respectively. With increase in ΔT, there is a definite improvement in system performance because of increase in thermal gradient for heat transfer between the HTF and the PCM. The effect of HTF inlet temperature is quite significant, and can be even employed to increase the heat transfer rate for low-cost HTF having poor thermal properties.

It can be observed that the inlet conditions of the HTF have a considerable impact on system performance. These parameters can change according to system requirements, and hence an optimal combination of these parameters has to be selected.

6.3.3 Performance comparison of cylindrical and conical shell systems

By now, it is evident from the study that the introduction of conical shell design leads to improvement in performance than cylindrical shell system. In this section, the relative improvement is studied in terms of charging and discharging times (described in Table 6.5).

Table 6.5. Charging and discharging times of the optimized conical and the cylindrical shell system at different HTF inlet velocities.

v_{in} (m/s)		2	6	10
Charging time, t_c (h)	Cylindrical	20.95	16.34	13.79
	Conical	18.13	13.58	12.15
	% t_c reduction	13.4	17.0	11.9
Discharging time, t_d (h)	Cylindrical	31.14	19.96	15.56
	Conical	22.16	15.5	13.26
	% t_d reduction	28.8	22.3	14.7

6.3.3.1 Charging and Discharging time

In case of conical shell design, the PCM mass is distributed in such a way that the decreasing temperature difference between HTF and PCM along the length of the LHS system does not affect the heat transfer significantly, which results in uniform melting of the PCM.

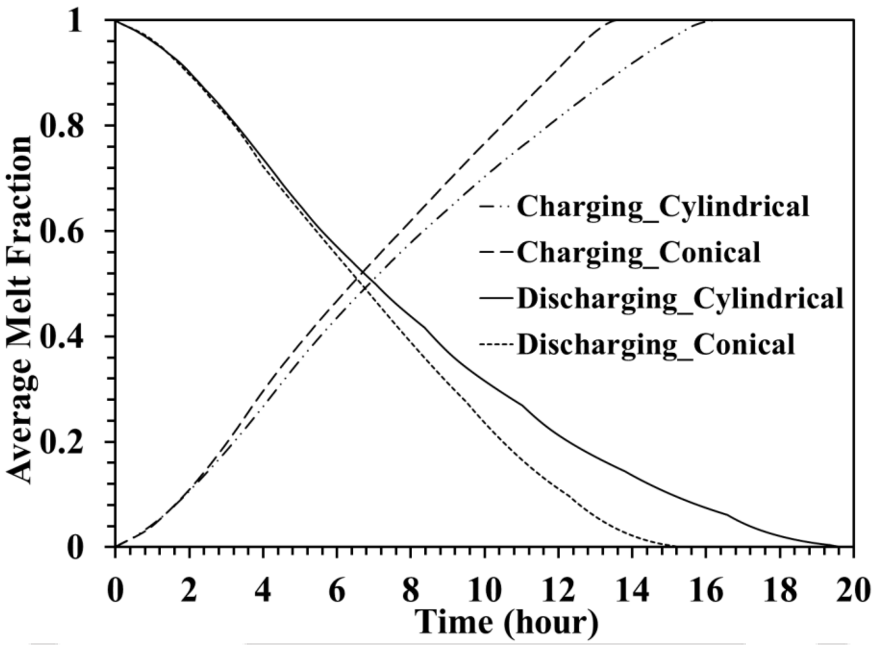

Figure 6.10. Average melt fraction variation for conical and cylindrical shell systems (v_{in}= 6 m/s).

The charging and discharging rates of the conical shell system are higher than the cylindrical shell system as shown in Figure 6.10. As compared to the charging times, the discharging times are significantly less. Since discharging is conduction dominated, it can be comprehended that by changing the design from cylindrical to conical shell system, there is much more enhancement in the conduction rate. Therefore, a similar effect leads to enhanced heat transfer during the charging process. Figure 6.11 and Figure 6.12 describe the percentage completion of melting and solidification of the conical and cylindrical shell systems with respect to time.

Initially, the melting behaviour of cylindrical and conical shell systems are identical. The behaviour continues till t = 5.43 h. Due to less PCM mass at the outlet section of the conical shell system, an additional melt front is initiated. Finally, at t = 13.33 h the melting in conical shell system is almost completed at the middle section, whereas the average melting in the cylindrical shell system is completed by 88.5%.

The solidification contours shown in Figure 6.12 are symmetrical about the horizontal and vertical axes for both the conical shell and cylindrical shell systems. Initially, the solidification behaviour of both the systems are identical. After *t* = 5.43 h, the solidification initiates at the outlet section of the conical shell. Finally, at *t* = 15.5 h the solidification is completed by 90% in the cylindrical shell system, with no comprehensive solidification at the outlet section. At the same time, the conical shell system is completely melted except the small amount of PCM left at the outer periphery of middle section. This concludes that the conical shell system is advantageous due to effective distribution of heat in the PCM region, both during the melting and solidification.

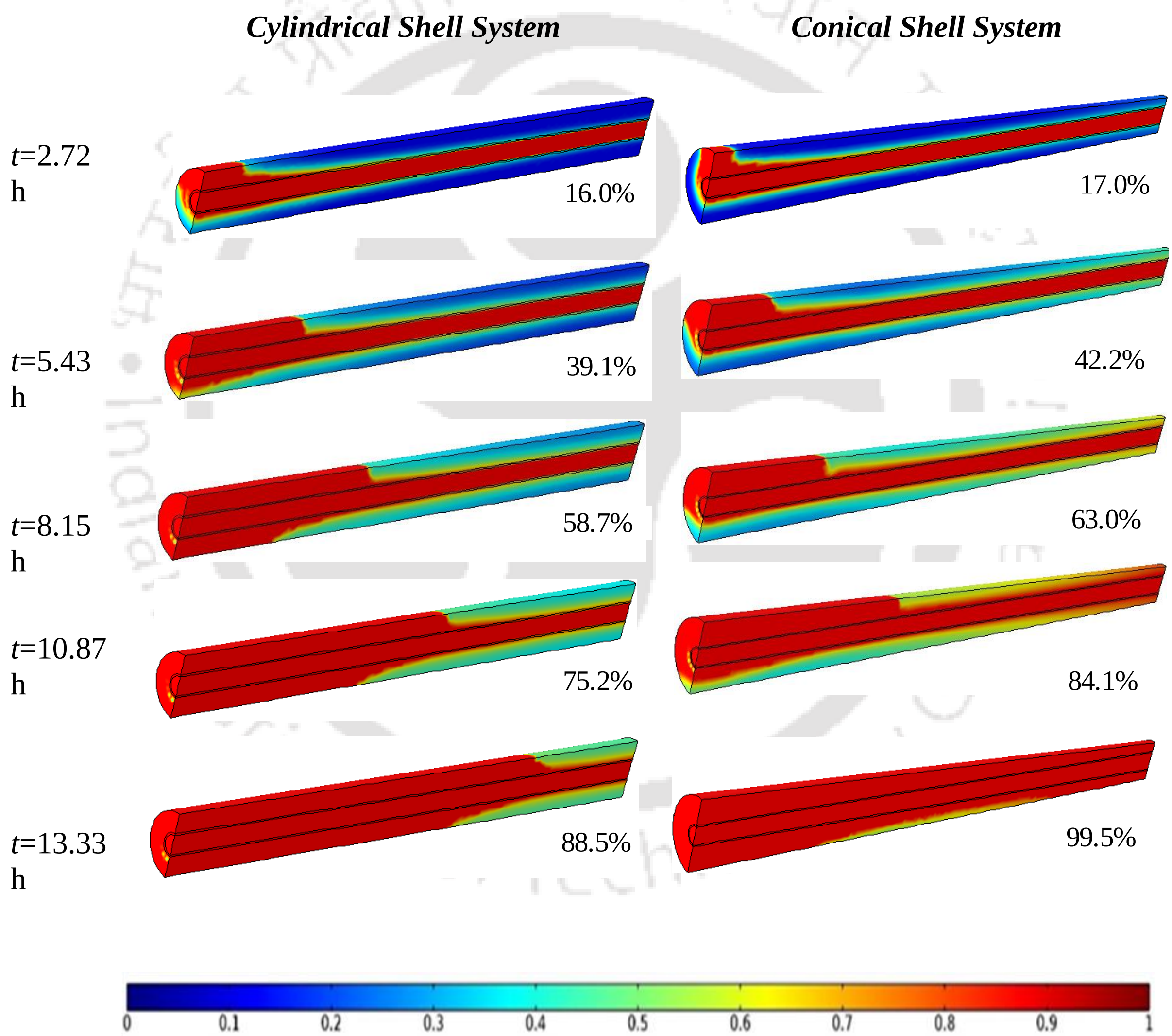

Figure 6.11. Comparison of solidification contours of cylindrical and conical shell systems at different time intervals.

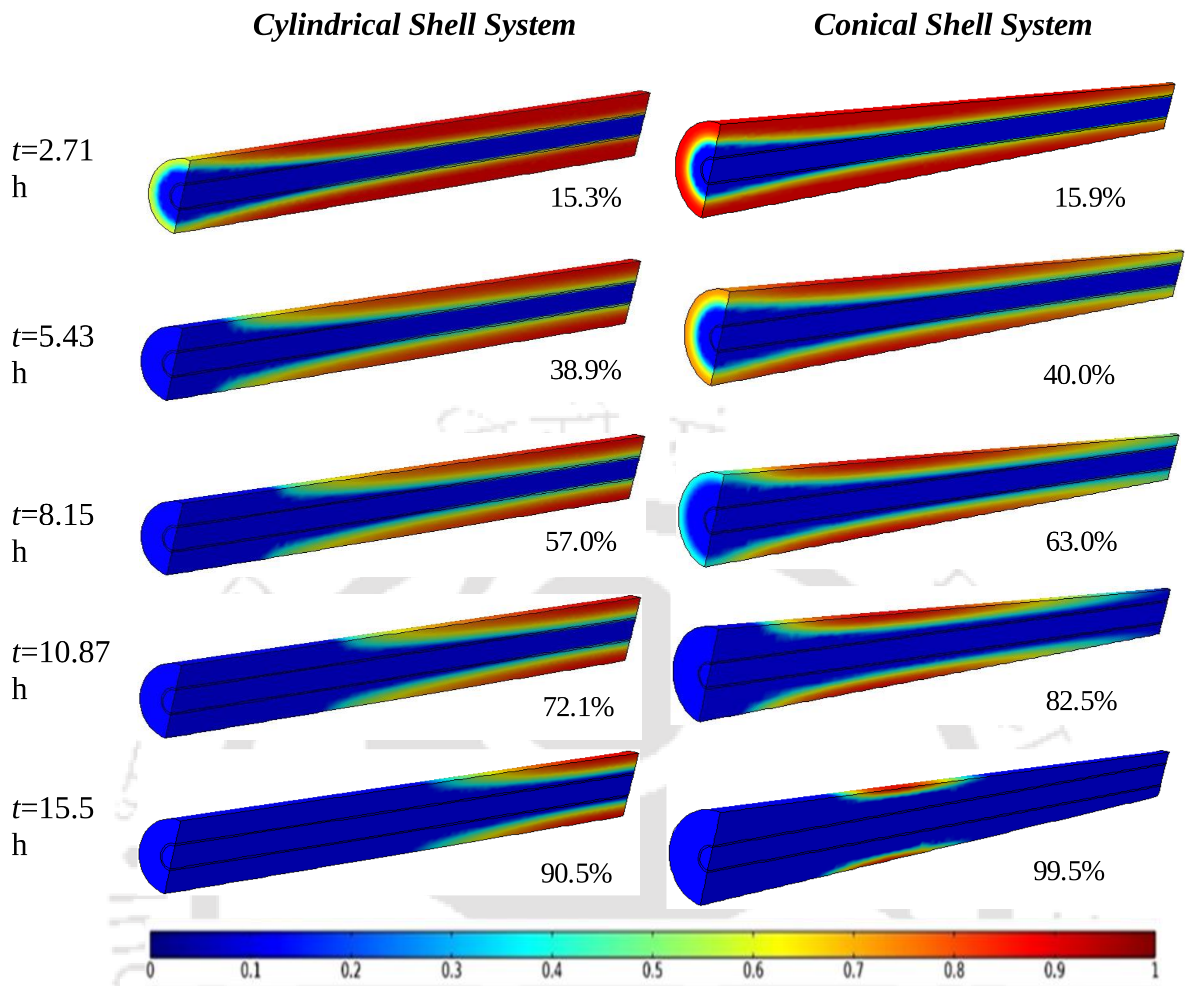

Figure 6.12. Comparison of solidification contours of cylindrical and conical shell systems at different time intervals.

6.3.3.2 Average PCM and HTF outlet temperatures

Figure 6.13(a)-(b) describes the variation of average PCM temperature and HTF outlet temperature of conical and cylindrical shell system. During the charging process, both the average temperature of the PCM and the HTF outlet temperature of the conical shell system reaches the HTF inlet temperature approximately 2 h earlier than cylindrical shell system. This indicates that the heat transfer rate is high in case of conical shell system. During discharging, the behaviour of average PCM temperature and HTF outlet temperature of conical and cylindrical shell system is identical till t = 13 h. Later, the heat transfer rate is relatively high in conical shell system and the HTF outlet temperature approaches the HTF inlet temperature.

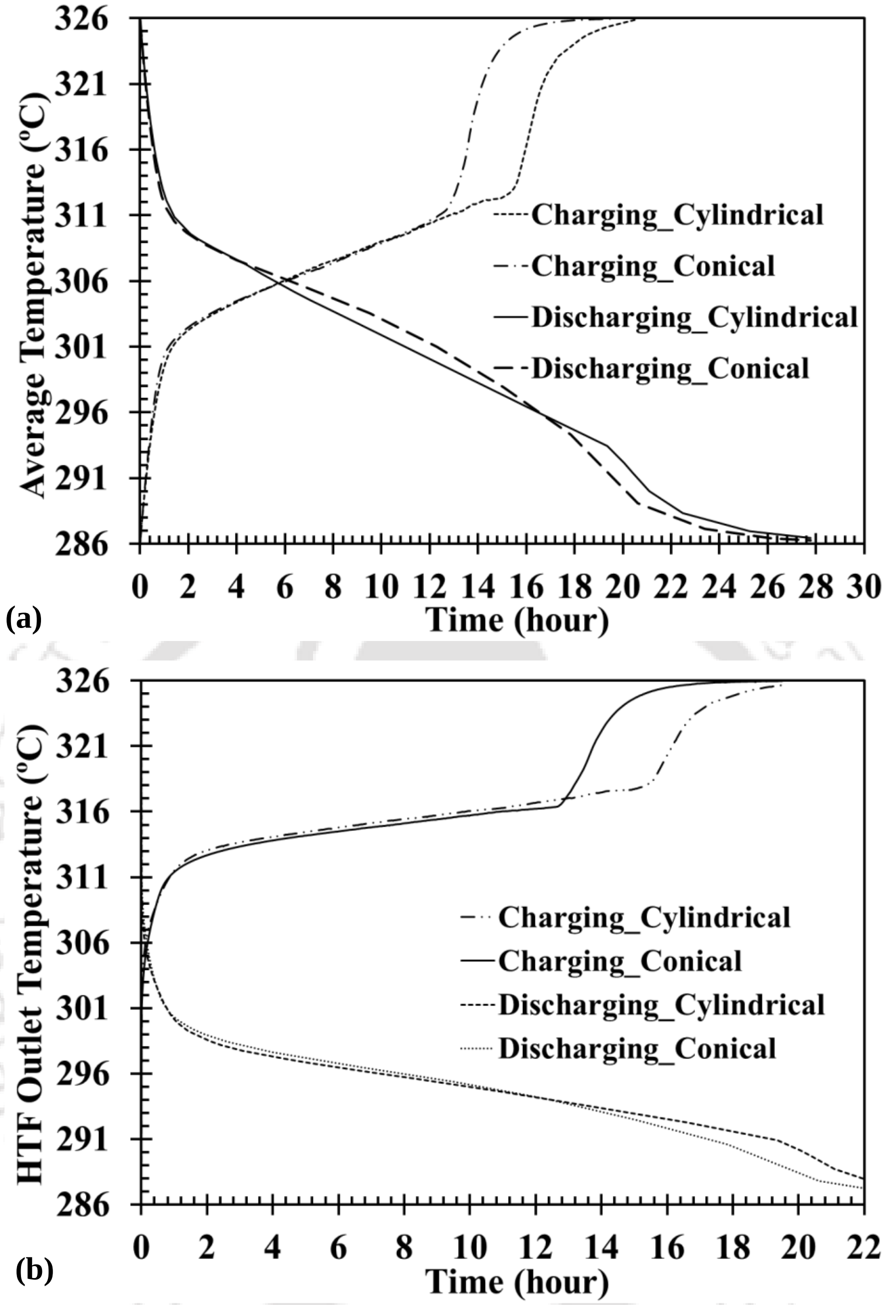

Figure 6.13. (a) Average PCM temperature and (b) HTF outlet temperature variation of conical and cylindrical shell systems during charging and discharging processes.

6.3.3.3 Energy storage and discharge rate

Figure 6.14(a)-(b) shows the rates of energy stored and discharged in the form of sensible and latent heat. The conical and cylindrical shell systems are developed for a latent heat capacity of 1 MJ, whereas, there is an additional 0.19 MJ sensible energy stored in both the cylindrical and conical shell systems due to temperature difference between the HTF and the PCM. It can be observed that the energy storage/discharge rate of the conical shell LHS system is higher than that of cylindrical shell system.

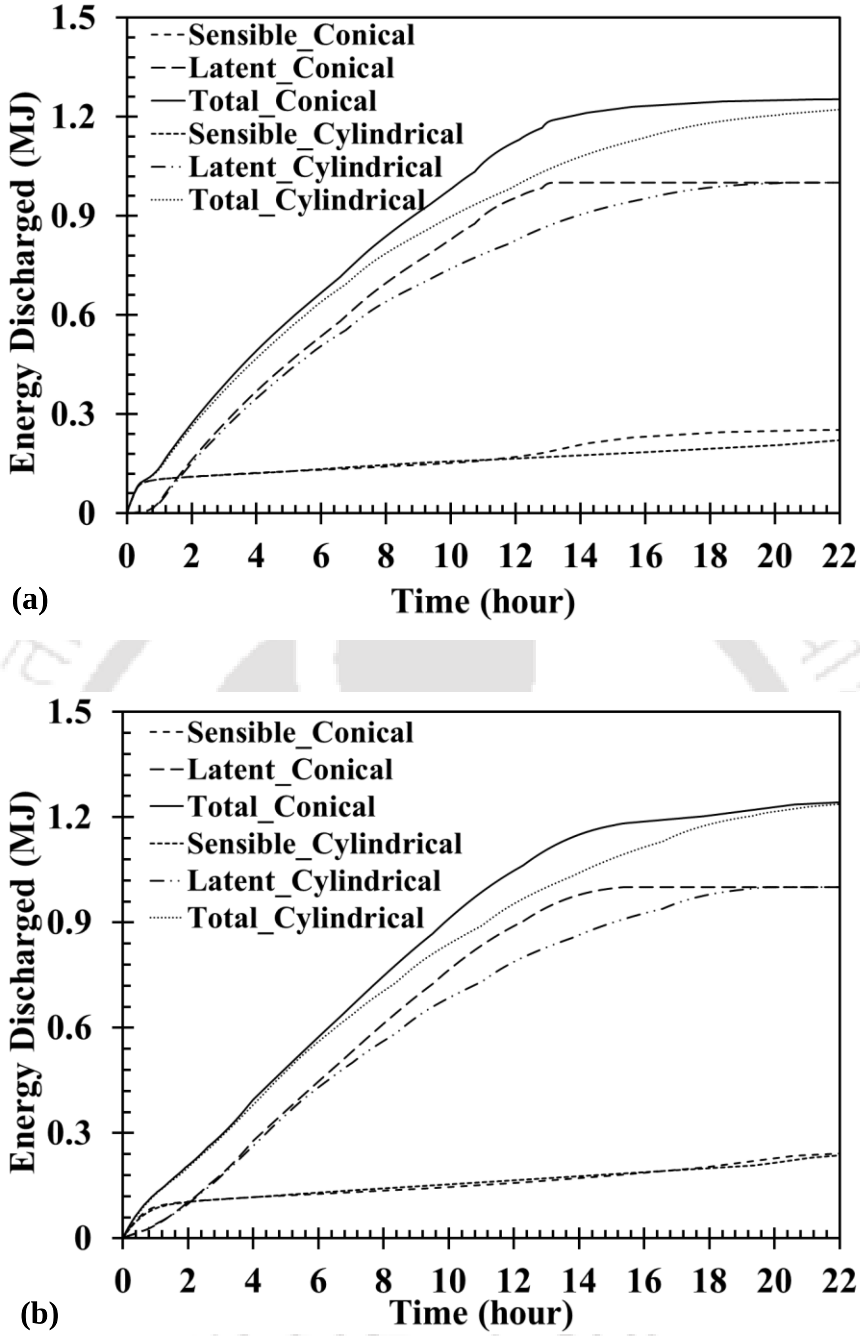

Figure 6.14. Energy stored/discharged rates of the conical shell and the cylindrical shell system for (a) charging and (b) discharging.

6.3.4 Inclusion of fins in the conical shell system

In this section, the current study has been further extended to analyse the effect of different fin designs implemented in the developed conical shell storage system. It has been observed from the reported research works that addition of fins on the HTF tubes lead to a faster rate of heat transfer in the LHS system. Addition of fins leads to increase in heat transfer surface area, and hence enhances the conduction heat transfer which dominates during the discharging process

(Rabienataj Darzi et al., 2016). Whereas, the charging process involves movement of the liquid PCM that is desired to have additional convection currents leading to enhancement of heat transfer rate. But, the size and shape of the fins has to be limited to a specific shape and number, in order to avoid the blockage of convection currents (Solomon and Velraj, 2013).

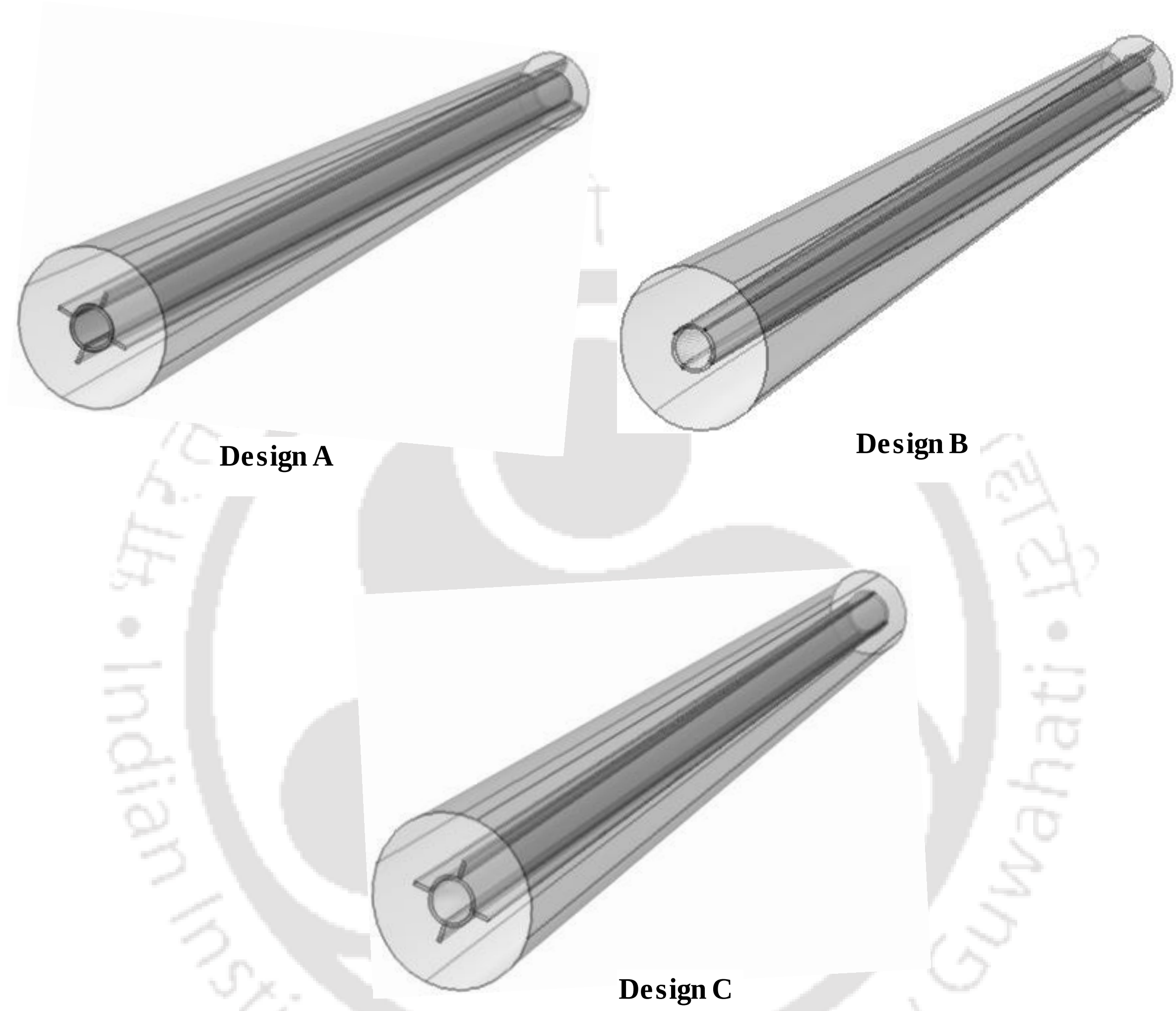

Figure 6.15. Different designs of conical shell system with fins.

The heat transfer and the fluid flow are symmetrical about the vertical axis during both the charging and the discharging processes. Therefore, only half of the model geometry is developed to save the computational effort. The height, length and width of fins is selected as 10 mm, 750 mm and 2 mm, respectively and the PCM mass is maintained as constant. Different fin designs as shown in Figure 6.15 are illustrated as follows:

A. Four longitudinal straight fins.
B. Four longitudinal fins with uniformly increasing tapered cross section from inlet to outlet.
C. Four longitudinal fins with uniformly decreasing tapered cross section from inlet to outlet.

The numerical simulations are carried out for charging (T_{in} = 326 ºC and T_i = 286 ºC) and discharging (T_{in} = 286 ºC and T_i = 326 ºC) at v_{in} = 6 m/s.

6.3.4.1 Charging and discharging

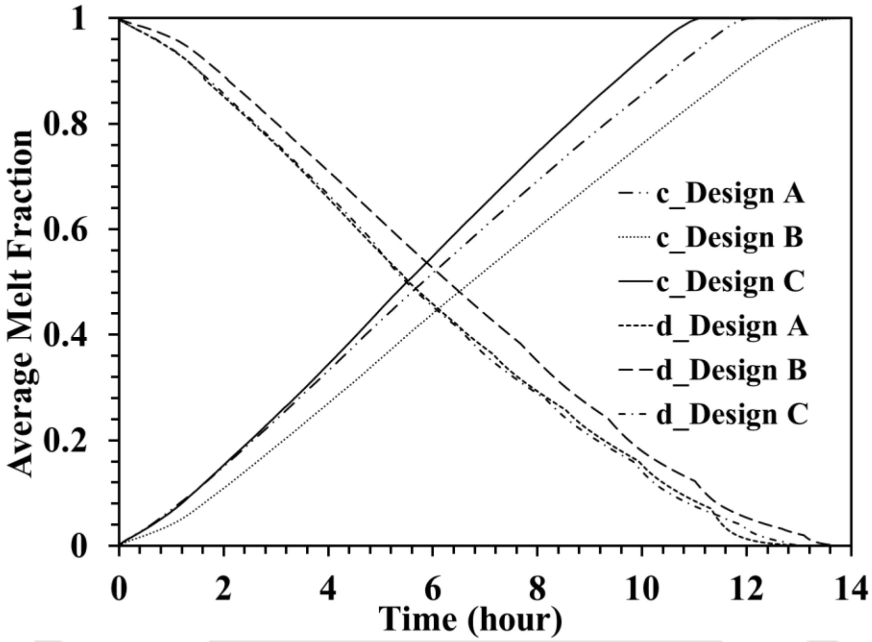

Figure 6.16. Variation of melt fraction with time during the charging and discharging of conical shell system with different fin designs.

Figure 6.16 illustrates the time taken for the charging and discharging processes for all the cases namely; Design A, Design B and Design C. The Design A melts in 12.06 h, whereas, Design B and Design C melt in 13.79 h and 11.01 h. As reported in Table 6.5, the charging time evaluated for conical shell system without fins is 13.58 h. It is observed that the time taken for charging of Design B is more than the system without fins, whereas Design A and C show a relative improvement over system without fins. Hence, the use of fins does not necessarily improve the heat transfer rate.

Further, the relative comparison of the effect of presence of fin surfaces on heat transfer rate at inlet and outlet sections is explained by evaluation of local temperature profile at two coordinates: X_{in}: x, y, z (0mm, 20mm, 45mm) and X_{out}: x, y, z (0mm, 730mm, 26mm).

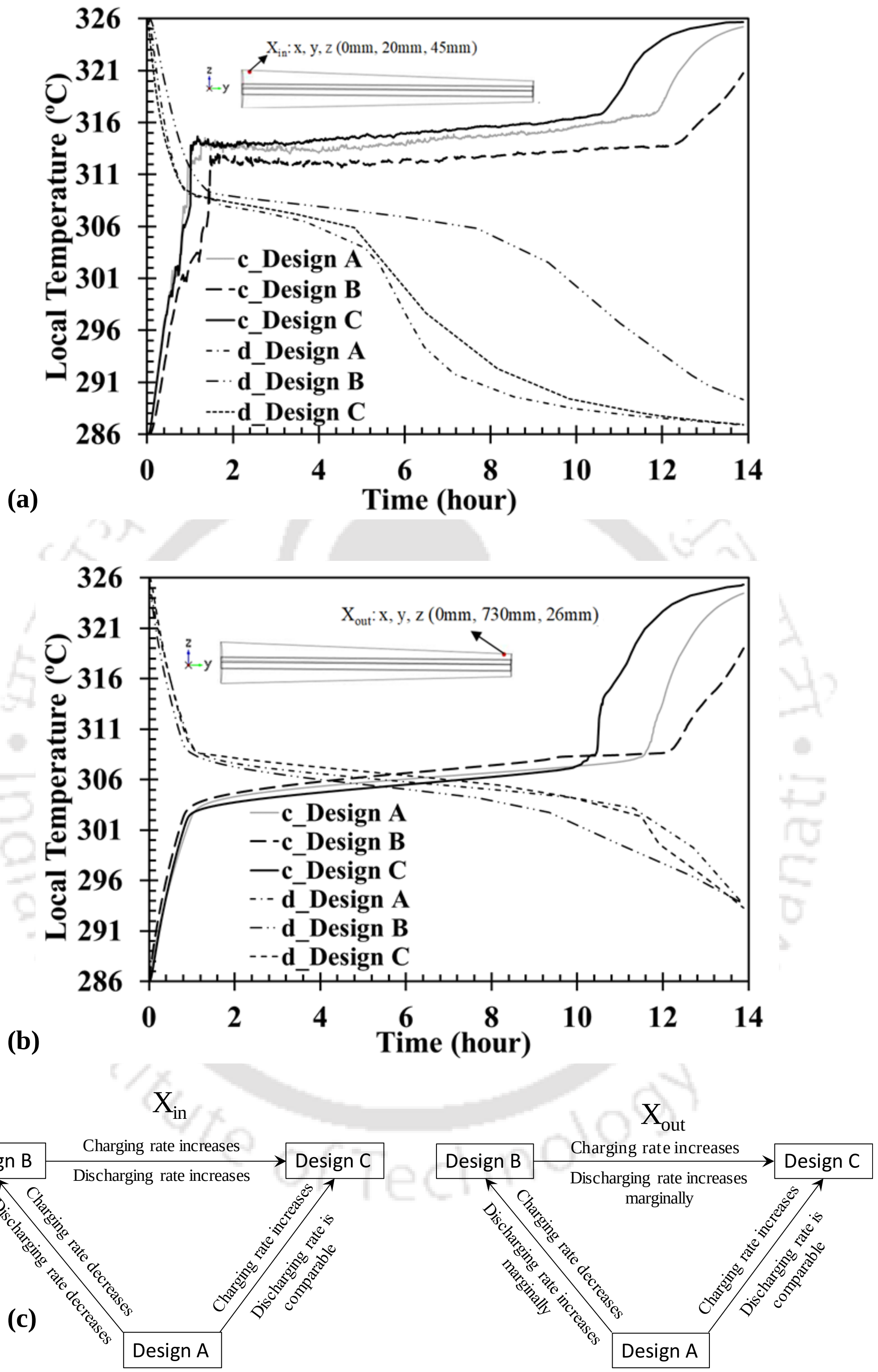

Figure 6.17. Local PCM temperature at inlet section (X_{in}), (b) Local PCM temperature at outlet section (X_{out}) and (c) variation in charging and discharging rates for different fin designs during the charging and discharging processes.

Figure 6.17(a)-(b) shows the local temperature variation at X_{in} and X_{out} during charging and discharging processes. Figure 6.17(c) represents the variation in charging and discharging rates for three different designs at X_{in} and X_{out}. It is observed that the rate of conduction heat transfer during discharging in Design C is higher than Design B at X_{in}, and marginally lower at X_{out}. This happens because of presence of more fin surface at X_{in} in Design C and at X_{out} in Design B. On the other hand, the charging rate in Design C is higher than Design B, both at X_{in} and X_{out}. This is possible due to relatively higher conduction heat transfer rate at X_{in} because of more fin surface. Whereas at X_{out}, even with presence of more fins in Design B, the charging rate is slower as the convection currents are affected adversely.

Therefore, the heat transfer rate between the HTF and PCM at inlet and outlet sections is effected by temperature gradient, fin surfaces and convection currents. The presence of fins is useful in the region of high thermal potential between HTF and PCM (near inlet) both during charging and discharging. Whereas, with the presence of fins in the region of lower thermal potential (near outlet), there is a compromise between conduction heat transfer and free movement of PCM.

The melting contours for conical shell system with different fin designs are plotted in Figure 6.18. Initially, fins accelerate the heat transfer rate in Design A and C near the inlet section. At t = 5.43 h, the melting initiates at the outlet section in all the three cases. Further, at t = 10.86 h, the melting is completed in half of the system starting from the inlet side of Design A and C. Whereas, due to very less fin surfaces at inlet section and blockage of convection currents at outlet section, melting is still incomplete in Design B. Finally, melting is only completed by 92.5% in Design B, whereas it has completed in Design A and C.

The discharging process is conduction dominated, thus having more fin surfaces is always beneficial. Initially, the solidification is faster due to presence of fins near the inlet section for Design A and C as shown in Figure 6.19. Further at t = 5.43 h, the solidification initiates in the outlet section in all the designs. In Design B, the fins do not give much advantage as more fin surfaces are present in the region of low temperature difference between the HTF and the PCM (near outlet section). The solidification completes in 13 h for Design A, followed by Design C and B in 13.2 h and 13.9 h, respectively. The maximum reduction in charging time as compared to system without fins is in Design C (approximately 19%), whereas the maximum reduction in discharging time as compared to system without fins is in Design A and C (approximately 16% and 15%).

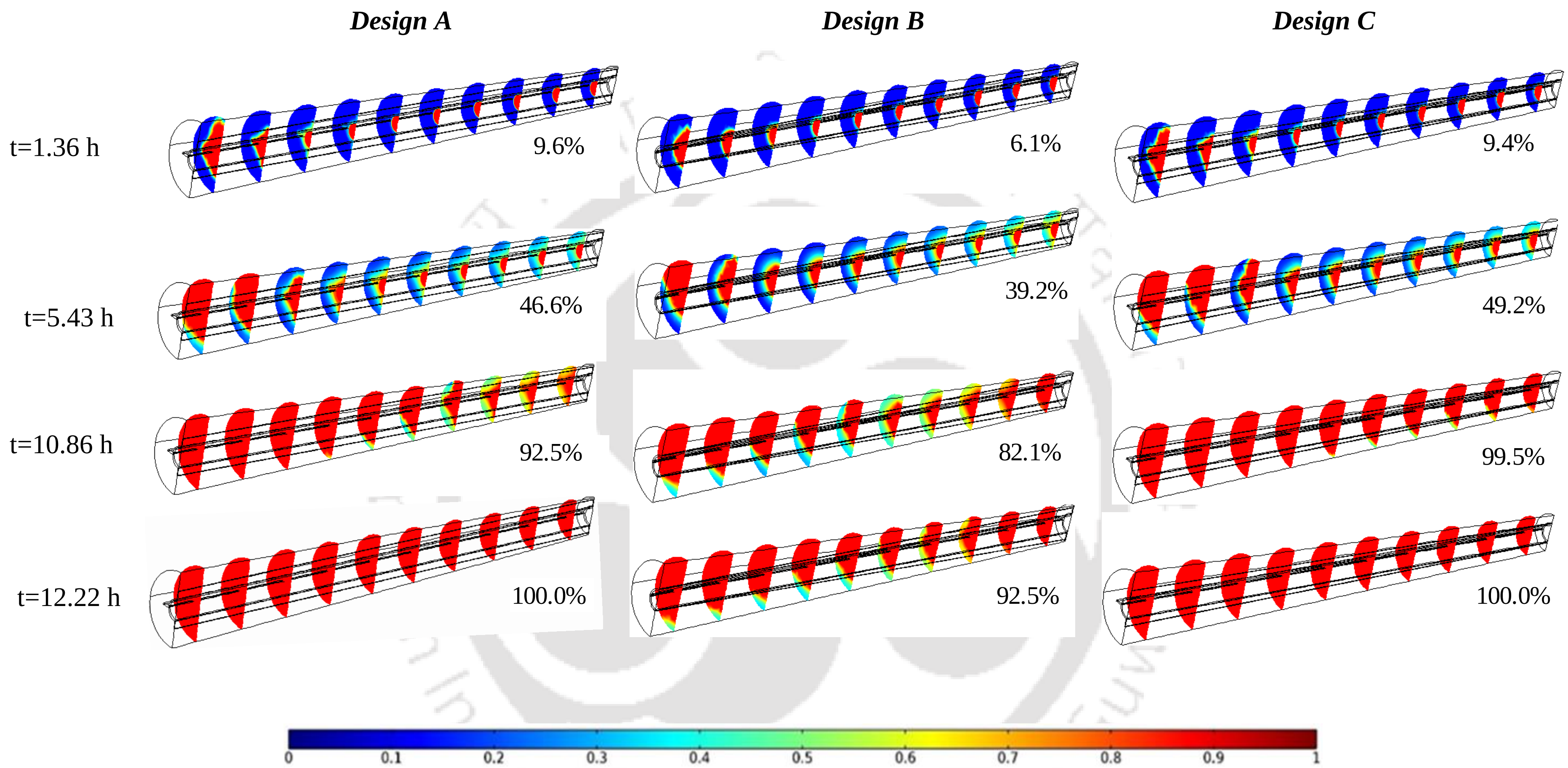

Figure 6.18. Melting contours of the conical shell system for different fin designs during the charging process.

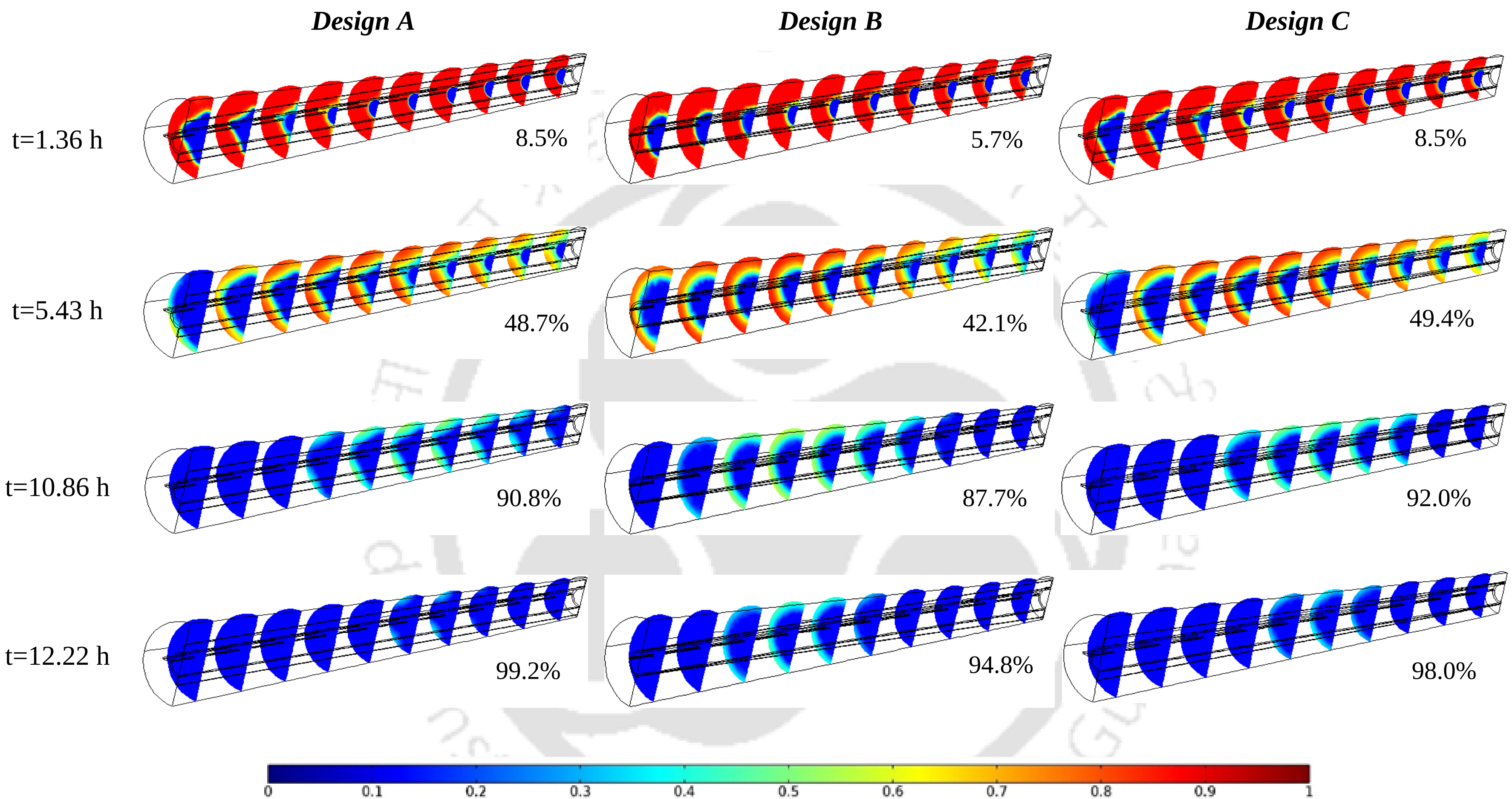

Figure 6.19. Solidification contours of the conical shell system for different fin designs during the discharging process.

6.3.4.2 Average PCM and HTF outlet temperature

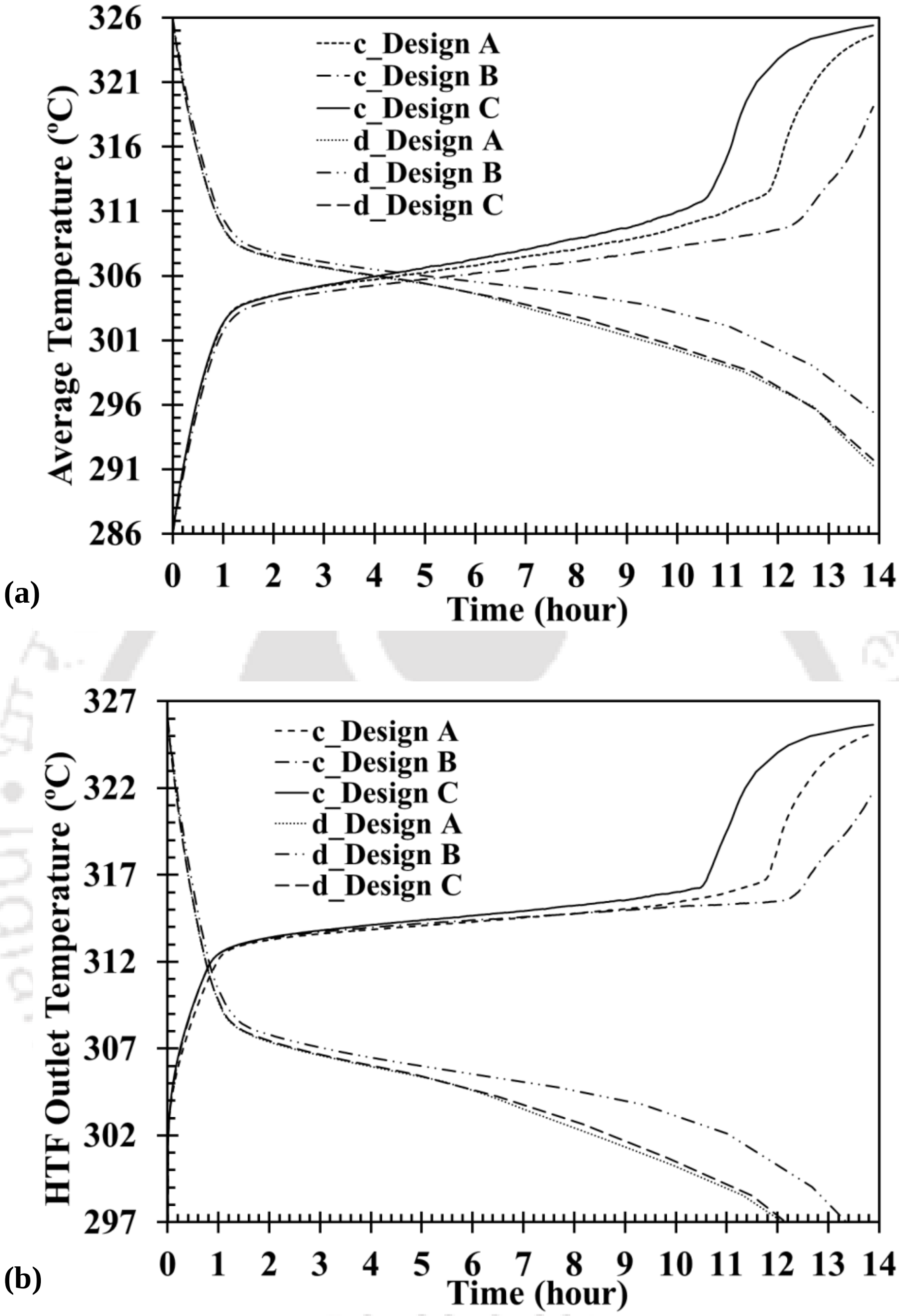

Figure 6.20. (a) Average PCM temperature and (b) HTF outlet temperature variation for different fin designs during the charging and discharging processes.

Figure 6.20(a) shows the average temperature of the PCM for both charging and discharging processes. The average temperature plots are consistent with the average melt fraction curves plotted in Figure 6.16. Due to faster rate of heat transfer throughout the charging process, the average temperature of the PCM is always higher in Design C followed by Design A and B. During discharging, due to higher rate of conduction heat transfer in Design A, the average

PCM temperature is always lower than Design B and C. Figure 6.20(b) shows the variation of HTF outlet temperature for all the fin designs. The HTF outlet temperature attains a temperature closer to HTF inlet temperature earlier in case of a higher heat transfer from HTF to PCM (Design C in charging) and vice versa (Design A in discharging).

The study of different fin designs concludes that the fins are advantageous for heat transfer, but their design is a crucial criterion to decide their feasibility with LHS system. The improvement in heat transfer during discharging process is merely dependent upon increasing the heat transfer surface area of the fins. At the same time, careful measures have to be taken to select the design of fins for the charging process.

6.4 Summary

In the present study, a numerical analysis is performed to develop a conical shell based LHS system. The adapted geometry is optimized after varying the cone angle, starting from a perfectly cylindrical geometry. After selecting an optimal shell design, the applicability of different fin designs and their effect on the melting/solidification rates are discussed. The following conclusions are drawn from the study;

- The conical shell system optimized for charging and discharging processes has a cone angle of 3.4° and diameter at inlet and outlet section of 98.6 mm and 54 mm, respectively.
- Due to less PCM mass near the outlet section of the conical shell system, melting and solidification starts earlier in this region than cylindrical shell system. The melting and solidification completes at the middle section of conical shell system due to merging of two melt fronts originating from inlet and outlet sections. There is a maximum reduction in charging and discharging times up to 17% and 28% due to better PCM distribution.
- HTF inlet conditions impact the system performance significantly. By increasing HTF inlet velocity from 2 m/s to 6 m/s, both charging and discharging rates increase comprehensively, but the influence of velocity is insignificant thereafter. Also, by changing the $\Delta T = |T_{in} - T_i|$ from 40 ºC to 50 ºC and later to 60 ºC, the percentage reduction in charging time are 26.7% and 21.5 %, whereas, the reduction in discharging time are 36.7% and 21.2%, respectively. Thus, even by using an HTF (air) with poor thermal properties, a higher ΔT is beneficial to improve the system performance.
- The fins are beneficial to increase the conduction heat transfer rate during the charging and discharging in the region of higher thermal potential (inlet section), but are inadequate in

the region with low thermal potential (outlet section). Near the outlet section, presence of fins leads to a compromise between conduction heat transfer and convection currents in liquid PCM. Proposed Design C for charging and discharging is found to be most effective with a reduction of ~ 19% and 15% in time over the system without fins.

This study provides an insight for improving charging and discharging performances of LHS system by alteration of simple design aspects of conventional cylindrical systems. Such modifications can be more useful than selecting highly complex structures, thereby controlling the overall size and cost incurred for designing and manufacturing. There is a possibility of extending this method to high capacity storage systems, where the advantages in terms of cost reduction will increase substantially.

Chapter 7

Heat transfer enhancement in the single and multi-PCM LHS systems using non-uniform fin distribution[††]

Preface

To enhance the heat transfer characteristic in the conventional LHS systems, there have been significant attempts to improve the effective thermal conductivity of PCMs, such as using snowflake-shaped fins, wavy-fins, spiral-wound and helical fins. However, these fin designs are not yet commercial and require high-cost manufacturing techniques such as 3D-printing. The distribution of fins plays a vital role in the natural convection and conduction heat transfer enhancement and therefore, relatively simpler fin shapes such as circular fins with effective distribution inside the PCM region can be utilized.

The charging/discharging rate enhancements in the multi-PCM (m-PCM) systems than single PCM systems are subjected to the following conditions; (i) optimum selection of PCMs based on the melting point temperature (T_M) and thermo-physical properties, (ii) optimum T_M difference between adjacent PCMs, and (iii) reduction in volumetric energy storage capacity. The improvement in the energy storage and discharge characteristics can be achieved by using effective fin distribution in different PCMs. In the present work, a numerical model of a vertical shell and tube latent heat storage system validated with the experimental data is presented. The developed model comprises of three blocks of phase change materials (PCMs) having melting point temperatures (T_M) 360 °C, 335.8 °C and 305.4 °C, respectively. By employing a compound enhancement technique, which is a combination of non-uniform fin-distribution and PCM volumes optimization for the m-PCM system, 30% and 9% reduction in the charging and discharging time, respectively, and 25% improvement in the specific energy over the single PCM system was achieved.

[††] The findings reported in this chapter are published as the following research article:

Sodhi GS, Muthukumar P. Compound charging and discharging enhancement in multi-PCM system using non-uniform fin distribution. Renewable Energy, 171, 2021.

7.1 Design and numerical modelling of the LHS system

A vertical shell and tube heat exchanger filled with single or multiple-phase change materials (m-PCMs) in three PCM blocks is developed. Fins are used to enhance the heat transfer rate during the charging and discharging processes. Further, the fin distribution is varied along the length of the system to study the enhancement in the heat transfer rate for the single and m-PCM systems. Air is chosen as the HTF with a fixed velocity of 16 m/s throughout the analysis. Three PCMs namely; PCM[a] (potassium hydroxide (KOH), T_m = 360 °C), PCM[b] (potassium nitrate (KNO_3), T_m = 335.8 °C) and PCM[c] (sodium nitrate ($NaNO_3$), T_m = 305.4 °C) are considered for developing the m-PCM LHS system. The thermo-physical property data for the PCMs were adopted from Michels and Pitz-Paal (Michels and Pitz-Paal, 2007).

Table 7.1. Thermo-physical properties of the PCMs.

Property	Value		
	PCM[a]	PCM[b]	PCM[c]
T_m (°C)	360	335.8	305. 4
Δh_f (Jkg^{-1})	135	97	175
ρ (kgm^{-3})	2040	2109	2261
c_p $(Jkg^{-1}K^{-1})$	1340	953	1100
k $(Wm^{-1}K^{-1})$	0.5	0.5	0.5

All the models are developed for a total LHS capacity (Q_L) of 500 kJ, whereas each of the three PCM blocks in the single or m-PCM systems has an equal LHS capacity of $Q_L/3$. For a fixed capacity of $Q_L/3$, the length of each block for the single PCM system is fixed as 250 mm. However, in the case of the m-PCM system, the lengths of the top block (PCM[a]), middle block (PCM[b]) and bottom block (PCM[c]) are calculated based on individual PCM volumes as given in Eqs. (7.1-7.2). The outer diameter (d_o) and thickness of the inner HTF tube of copper material are fixed as 19.05 mm and 1.5 mm, respectively. The diameter of all the models is same and is calculated on the basis of a single PCM block (PCM[b]) of length 250 mm and LHS capacity $Q_L/3$ using Eq. (7.2).

$$(Q_L)_{PCM^{a/b/c}} = (\rho V \Delta h_f)_{PCM^{a/b/c}} \tag{7.1}$$

$$l_{1/2/3} = \frac{4 \times V_{PCM^{a/b/c}}}{\pi(D_o^2 - d_o^2)} \tag{7.2}$$

where Q_L, $\rho, V, \Delta h_f$ and l are the LHS capacity, density, volume, latent heat and length of the PCM block, respectively.

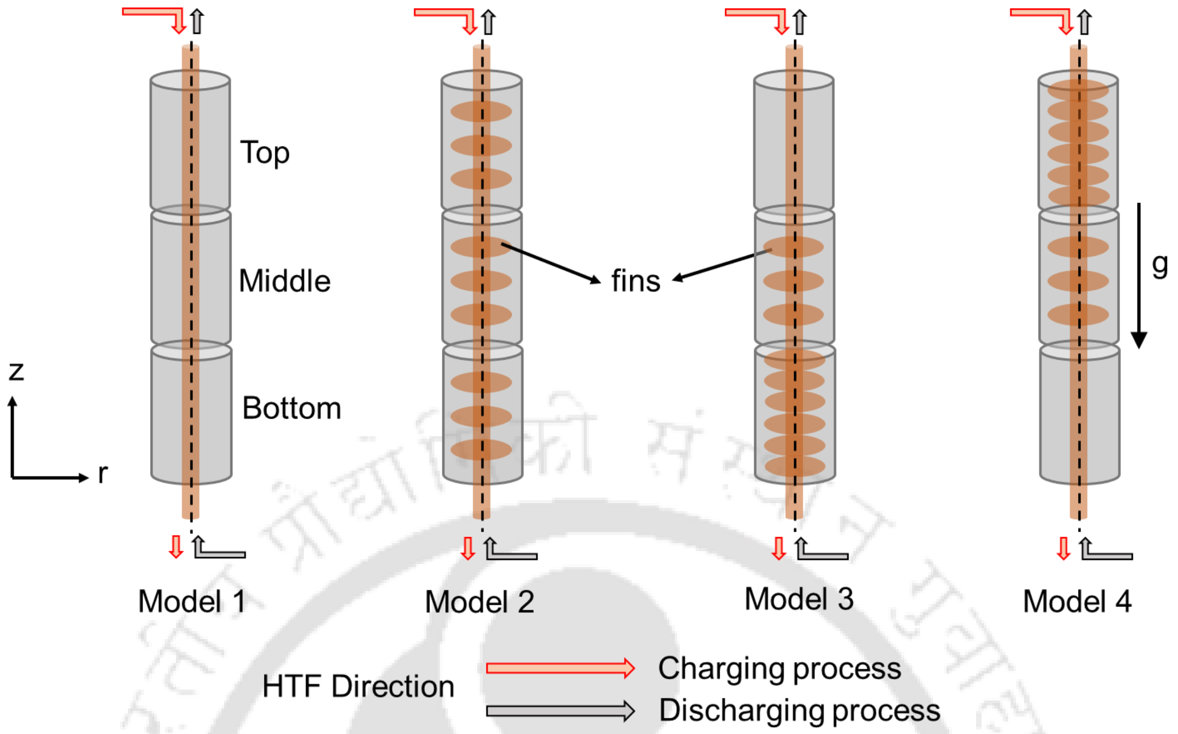

Figure 7.1. Studied physical models of the PCM system with uniform and non-uniform fin distribution.

Different cases shall be formulated based on these models to predict the charging and discharging characteristics of the single and m-PCM LHS systems. The PCM^a, PCM^b and PCM^c have different latent heat of phase change, however, the total latent heat storage capacity of the single and m-PCM systems are the same for any of the configurations shown in Figure 7.1. For charging, the HTF flows from top to bottom, whereas, during discharging the flow direction is reversed. For the developed models, the analysis for the effect of HTF inlet temperature is made by calculating the non-dimensionless parameters; Stefan number (Ste) and Rayleigh number (Ra) shown in Eqs. (7.3-7.5) and Eqs. (7.6-7.8). To compare the single and m-PCM systems, PCM^b is considered as reference.

The Ste_{ref} is defined as the ratio of the sensible heat to the latent heat charged and discharged by the reference PCM (PCM^b). The m-PCM shall be further optimized by varying the PCM blocks lengths ratio which is discussed at a later stage.

$$Ste_{PCM^a} = \left(\frac{c_p}{\Delta h_f}\right)_{PCM^a} \times (T_{in} - T_M^a) \tag{7.3}$$

$$Ste_{PCM^b} = Ste_{ref} = \left(\frac{c_p \Delta T}{\Delta h_f}\right)_{ref} = \left(\frac{c_p}{\Delta h_f}\right)_{PCM^b} \times \left(T_{in} - T_M^b\right) \tag{7.4}$$

$$Ste_{PCM^c} = \left(\frac{c_p}{\Delta h_f}\right)_{PCM^c} \times (T_{in} - T_M^c) \tag{7.5}$$

$$Ra_{PCM^a} = \left(\frac{\rho \beta l_c^3}{\mu \alpha}\right)_{PCM^a} \times g(T_{in} - T_M^a) \tag{7.6}$$

$$Ra_{PCM^b} = Ra_{ref} = \left(\frac{\rho \beta l_c^3}{\mu \alpha}\right)_{PCM^b} \times g\left(T_{in} - T_M^b\right) \tag{7.7}$$

$$Ra_{PCM^c} = \left(\frac{\rho \beta l_c^3}{\mu \alpha}\right)_{PCM^c} \times g(T_{in} - T_M^c) \tag{7.8}$$

Here, $\rho, \beta, \vartheta, \alpha \; and \; c$ are the density (kg/m^3), coefficient of thermal expansion (1/K), kinematic viscosity (m^2/s), thermal diffusivity (m^2/s) and specific heat (J/kg K) of the respective PCMs.

An important aspect of analysing the performance of the single or m-PCM system is to determine the specific energy. The specific energy charged and discharged is determined based on the total cumulative energy absorbed or delivered by the single or m-PCM system divided by the total mass of PCM in the system. The sensible and latent specific energies are given in Eqs. (7.9-7.10).

$$P_S = \frac{(Q_S)_{top} + (Q_S)_{middle} + (Q_S)_{bottom}}{(m_{PCM})_{top} + (m_{PCM})_{middle} + (m_{PCM})_{bottom}} = \frac{\sum \left\{m_{PCM}\left(c_p\right)_{PCM}(T_{max} - T_i)\right\}}{\sum m_{PCM}} \tag{7.9}$$

$$P_L = \frac{(Q_L)_{top} + (Q_L)_{middle} + (Q_L)_{bottom}}{(m_{PCM})_{top} + (m_{PCM})_{middle} + (m_{PCM})_{bottom}} = \frac{\sum \{m_{PCM}(\Delta h_f)_{PCM}\}}{\sum m_{PCM}} \tag{7.10}$$

where T_{max} is the maximum temperature up to which the sensible specific energy is estimated and T_i is the initial temperature of all the PCMs in the single or m-PCM system. The total specific energy is the sum of the sensible and latent specific energies as shown in Eq. (7.11).

$$P = P_S + P_L = \frac{Q_S + Q_L}{(m_{PCM})_{top} + (m_{PCM})_{middle} + (m_{PCM})_{bottom}} \tag{7.11}$$

The melt fraction for any PCM block is defined as;

$$\delta = \begin{cases} 0, for\ T < T_s \\ \frac{T-T_s}{T_l-T_s}, for\ T_s \le T \le T_l \\ 1, for\ T \ge T_l \end{cases} \tag{7.12}$$

where T_S and T_L are the solid and liquid temperatures of the PCM with phase change temperature range $|T_L - T_S|$.

The average melt fraction (δ_o) during the charging and discharging is defined as the average of melt fraction of the top, middle and bottom blocks as shown in Eq. (7.13).

$$\delta_o = \frac{\delta_{l_1} + \delta_{l_2} + \delta_{l_3}}{3} \tag{7.13}$$

where δ_{l_1}, $\delta_{l_2}$and δ_{l_3}, and l_1, l_2 and l_3 are the melt fractions and lengths of the top, middle and bottom PCM blocks, respectively.

The time incurred in complete charging ($\delta_o = 1$) and complete discharging ($\delta_o = 0$) is defined as the overall charging and discharging time, respectively.

The equations governing the HTF and PCM domains, the experimental validation of the numerical model and the assumptions have been described in detail in Section 3.2.

7.1.1 Boundary conditions

The boundary conditions for the model are described in Eqs. (7.14-7.18).

For charging (HTF flow from top to bottom); $T_{ch} > T_M > T_i$

At $t = 0\ s, T = T_i$ (for all domains) (7.14)

For $t > 0$, $T_{ch} = T_{in} = 385$ °C and $v_{HTF} = 16\ m/s$ (7.15)

For discharging (HTF flow from bottom to top); $T_{dch} < T_M < T_i$

At $t = 0\ s, T = T_i$ (for all domains) (7.16)

For $t > 0$, $T_{dch} = T_{in} = 280$ °C and $v_{HTF} = 16\ m/s$ (7.17)

Outer shell of the LHS is adiabatic; $\left.\frac{\partial T}{\partial r}\right|_{r=D_o/2} = 0.$ (7.18)

The no-slip boundary condition is imposed at the HTF tube and the PCM container wall such that the velocity at all walls is assumed as zero. The developed model is axisymmetric, such that the variation of any quantity around the vertical axes is zero.

The computations are performed using the commercial software tool COMSOL Multiphysics. A parallel direct linear solver (PARDISO) is used to obtain the numerical solution. The time step is varying with a minimum chosen value of $0.001\ s$. The solution convergence criterion is set as 10^{-3}.

7.1.2 Meshing and grid independent test

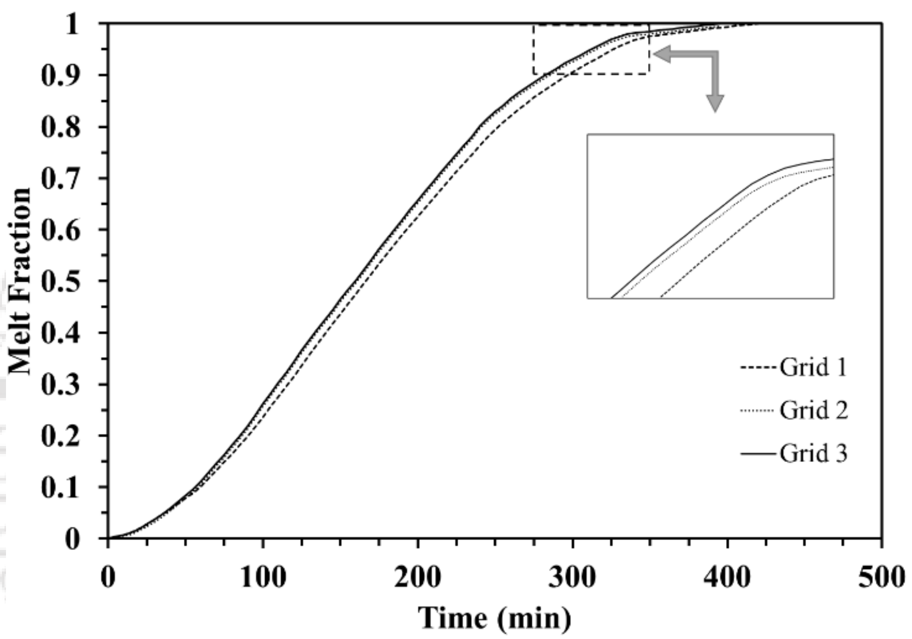

Figure 7.2. Grid-independency test showing the variation of the melt fraction due to change in the grid size.

The model is meshed using free triangular and tetrahedral elements, and special mesh-distribution feature is used for improving the mesh near the corners, edges and boundary layers. By improving the mesh quality, the solution quality is improved at the cost of a higher computational effort. Therefore, a grid-independency study has been conducted to determine the appropriate grid for which the solution quality is independent of the grid size. The study is performed by considering Model 2 i.e. model with 3 fins in each of the top, middle and bottom PCM blocks while carrying out the charging simulations. The mesh is developed with three grids having number of elements; 5873 (Grid 1), 9313 (Grid 2) and 13696 (Grid 3). The average melt fraction variation by employing the different grids is shown in Figure 7.2. It is observed that the solution varies by changing the grid from Grid 1 to Grid 2, however, it does not vary significantly thereafter by changing to Grid 3. Therefore, the Grid 2 with 9313 elements is selected as the appropriate one to obtain an optimum solution with minimum computational effort.

7.2 Results and discussion

In this section, the effect of employing the non-uniform fin distribution on the charging and discharging performances of the single PCM system is discussed initially. The charging and discharging characteristics of the single and m-PCM systems are compared and finally, the performance enhancements for the m-PCM system by optimizing the PCM blocks lengths ratio and employing the non-uniform fin distribution are discussed.

7.2.1 Effect of fin distribution on the performance of the single PCM system

The effect of fin distribution is studied for the charging and discharging processes for Models 1, 2, 3 and 4 shown in Figure 7.1. The HTF velocity (v_{HTF}) is fixed as 16 m/s, whereas, the difference between the HTF inlet and model initial temperatures ($T_{in} - T_i$) is fixed as 105 ºC. The calculated Ste_{ref} value using Eq. (7.4) is 0.5.

7.2.1.1 Melting characteristics

During charging, the HTF is injected from the top and the initial model temperature is fixed as 280 ºC. The melt fraction (δ) in the top, middle and bottom PCM blocks, and the average melt fraction for the single PCM system during charging are shown in Figure 7.3(a). The melt fraction varies due to fin distribution and the location of the PCM block i.e. top, middle or bottom.

In the top PCM block, Model 4 has the least charging time (242 min), which is less by 16.5%, 5% and 20.6% than Model 1, Model 2 and Model 3, respectively. It is to be noted that Model 1 and Model 3 have no fins in the top PCM block and the melting rate for Model 1 is marginally faster than Model 3. In the middle PCM block, the melting time of Model 2 and Model 3 is less than Model 1 by 12.6% and 10.1%, respectively. However, the melting rate for Model 4 is fastest, with melting time less than Model 1 by 17.7%. In the bottom PCM block, the Model 4 performance is affected significantly and the total charging time (510 min) is equal to the no-fin system (Model 1). However, the charging time for Model 3 (385 min) is least, and less than Model 1 by 24.5%.

A more detailed examination of the melting process can be made through melt fraction and temperature contours for the individual PCM blocks shown in Figure 7.3(b). At t=100 min, the melting of Model 1, Model 2, Model 3 and Model 4 is completed by 19.8%, 23.5%, 21% and

24.5%, respectively. Due to the presence of fin surfaces in the top blocks in Model 2 and Model 4, the heat transfer rate is enhanced in these regions. Another important observation is the formation of convection currents, especially near the fin surfaces. As the temperature gradient between fin surfaces and the surrounding PCM is high, the PCM melting fronts originate near the fin surface. The buoyant forces induce a natural convection heat transfer above the fins and hence, melting occurs in the space between the fins. As observed from the temperature contours, the temperature variations between all four models in the top block are marginal at this stage. However, upon close observation, the temperature near the fin surfaces in Model 2 and Model 3 is found to be higher and the melting fronts originate at the fin surfaces. In the bottom block, the PCM melting after 100 min is almost negligible in Model 1 and Model 4, whereas, melting initiates near fin surfaces in Model 2 and Model 3.

At t = 250 min, the melt fraction for Model 1, Model 2, Model 3 and Model 4 are 66%, 79.5% 79% and 75%, respectively. The faster melting in Model 2 and Model 3 happens due to heat transfer enhancement caused by the presence of fins in the bottom block, which may have otherwise melted at last. At t = 400 min, the melting is complete in Model 3, whereas it is 94% in Model 1, 99% in Model 2 and 96.1% in Model 4. The temperature variations throughout the LHS are more significant at this stage, where the PCM temperatures are high in the bottom blocks for Model 2 and Model 3 due to heat transfer enhancement caused by the fins.

The calculated Rayleigh number for the model is 8.41×10^7 ($Ra = Ra_{ref}$), and is the same for the individual PCM blocks as the single PCM is taken as reference. Therefore, the rate of natural convection in the individual PCM blocks does not vary significantly. The heat transfer rate only varies along the length of the system due to the location of the PCM blocks and the presence of fins. For example, the heat transfer rate in the top PCM block in Model 4 is exceptionally high due to high temperature difference between the HTF and the PCM combined with the effect of adding fins.

The average melt fraction variation in the single PCM system shows that adding fins may not always be advantageous in improving the heat transfer rate. For example, the performance enhancement achieved by Model 4 in the top PCM block is nullified by its poor performance in the bottom PCM block, such that the average melting in the system does not improve even with the addition of fins in Model 4. In Model 3, even though the fins are not present in the top PCM block, the average melting is improved significantly due to fins present in the bottom block.

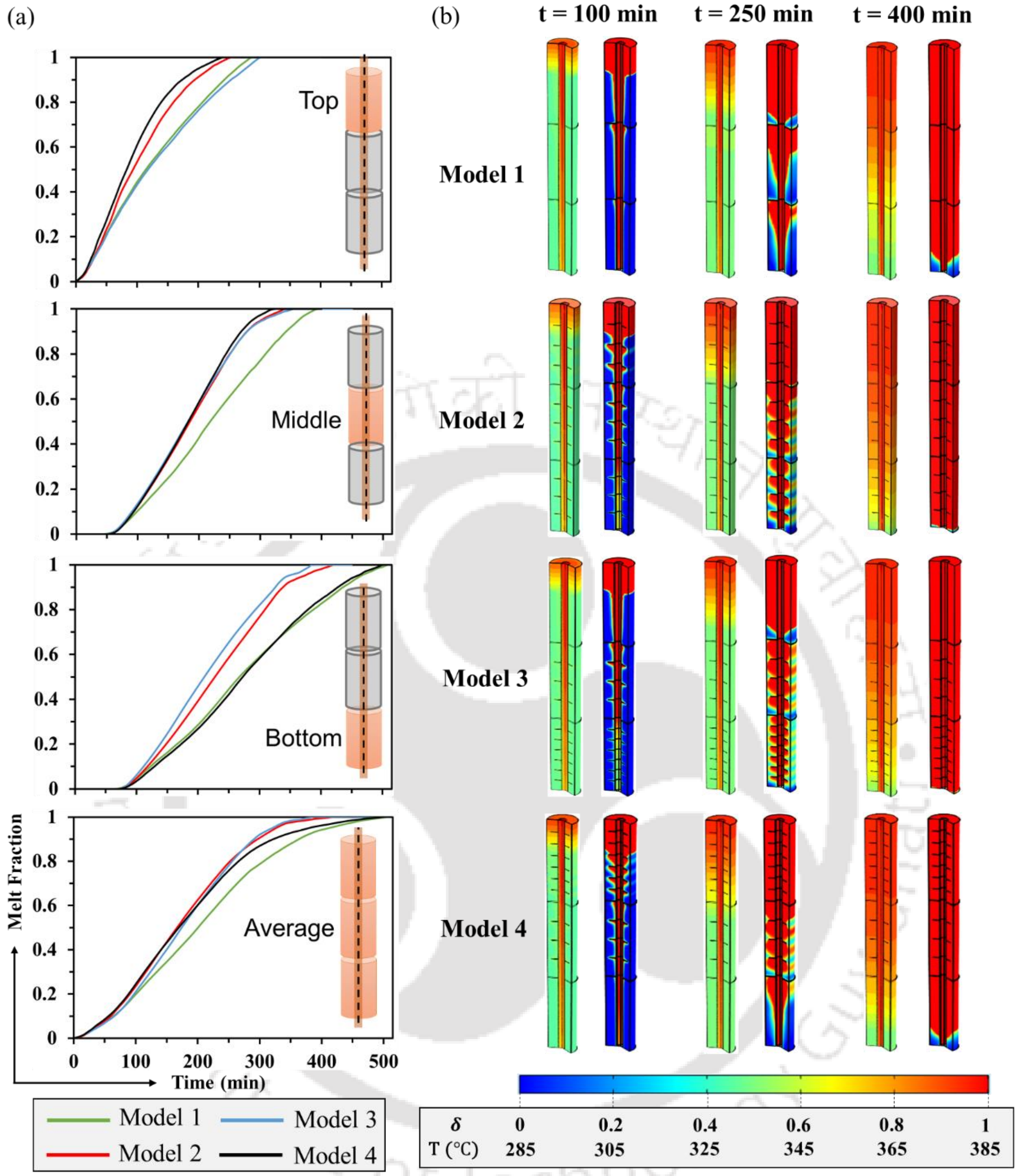

Figure 7.3. Effect of fin distribution on the single PCM system; (a) melt fraction variation with time in the top, middle and bottom PCM blocks and (b) temperature and melt fraction contours during charging.

Overall, the charging performance is improved due to the addition of fins in a vertical tube-in-tube LHS system. The uniform distribution of fins in the top, middle and bottom PCM blocks leads to a 17.5% reduction in charging time. A further improvement of 9% in the charging rate can be achieved using non-uniform fin distribution, which leads to a more uniform melting along the length.

7.2.1.2 Solidification characteristics

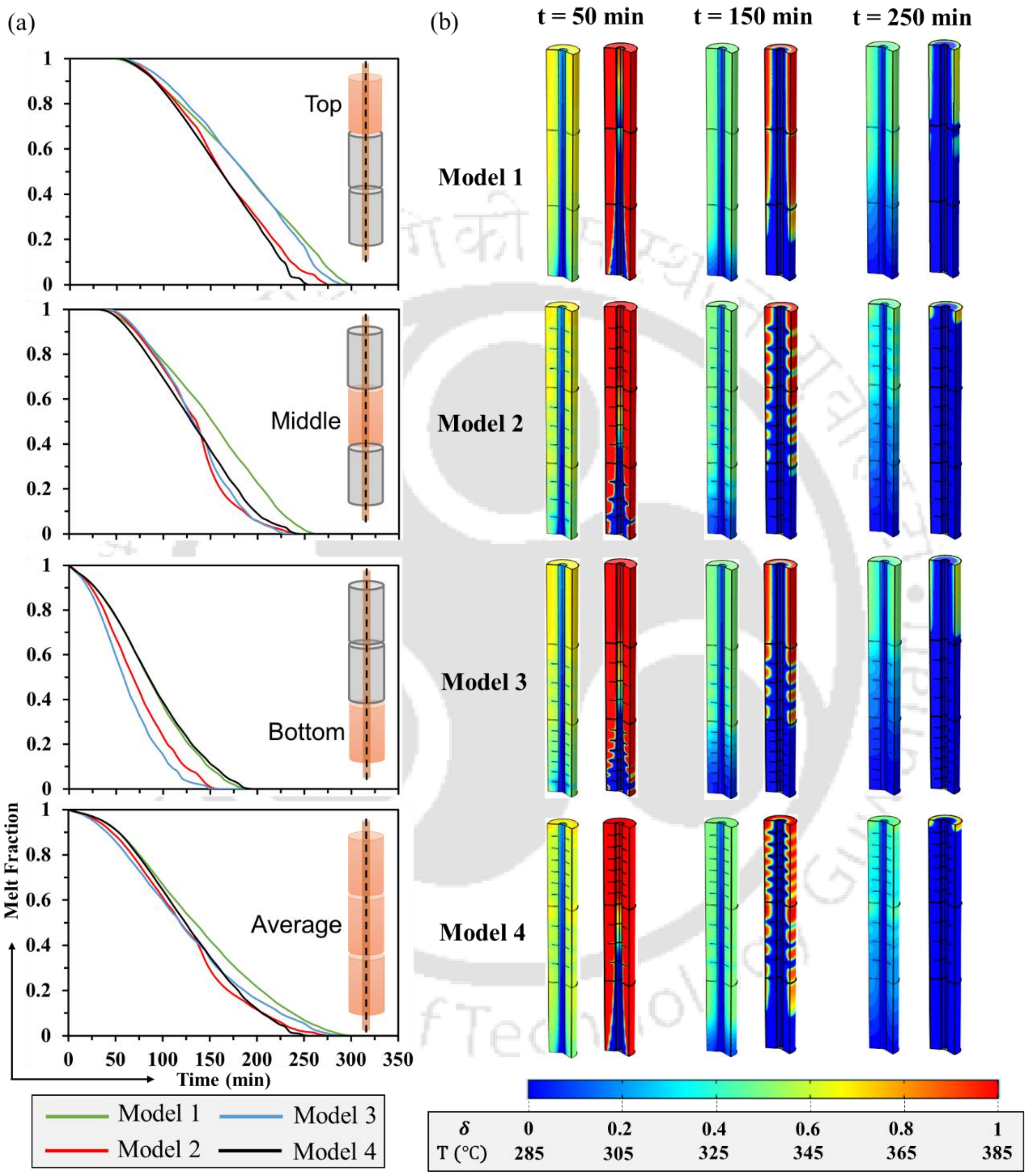

Figure 7.4. Effect of fin distribution on the single PCM system; (a) melt fraction variation with time in the top, middle and bottom PCM blocks and (b) temperature and melt fraction contours during discharging.

During discharging, the initial system temperature is 385 ºC and the HTF is injected at 280 ºC from the bottom. Therefore, the bottom PCM block interacts with the HTF initially. The natural convection effect of the PCMs is neglected during solidification and hence, the heat transfer takes place only due to conduction. The PCM solidifies from bottom to top i.e. along the direction of HTF flow. The melt fraction variation in the top, middle and bottom PCM blocks and the average melt fraction for the single PCM LHS system during discharging are plotted in Figure 7.4(a).

In the bottom PCM block, Model 4 and Model 1 have maximum discharging time (190 min), however, the discharging time for Model 3 is the least (155 min). The reduction in discharging time for Model 3 than Model 1, Model 2 and Model 4 is 18.5%, 6% and 20.5%, respectively. In the middle PCM block, the discharging time for Model 2, Model 3 and Model 4 is less than Model 1 by 7.5% (20 min), 9.5% (25 min) and 5.5% (15 min), respectively. In the top PCM block, Model 4 has the least discharging time, which is less by 16.5% than Model 1, 7.3% than Model 2, and 13.5% than Model 3. The overall discharging time is minimum for Model 4 having non-uniform fin distribution i.e. 6 fins in the top PCM block. The discharging time is highest for Model 1 i.e. the model without fins. The overall discharging time for Model 2, Model 3 and Model 4 is less than Model 1 by 10%, 3% and 16.5%, respectively. The melt fraction and temperature contours plotted in Figure 7.4(b) show the solidification and temperature variations along the length of the single PCM system.

Initially at t = 50 min, the amount of PCM solidified for each of the models is almost similar. At t = 150 min, the bottom block in Model 2 and Model 3 is solidified completely due to heat transfer enhancement caused by fins, however, it is partially solidified in Model 1 and Model 4. The solidification fronts are found to originate near the fin surfaces in the top PCM blocks in Model 2 and Model 4. The temperature varies significantly along the length due to the different fin configurations, where the temperature in the bottom block reaches close to the HTF inlet temperature. This happens due to a high temperature difference between the HTF and the PCM which drives the heat transfer substantially. In Model 2 and Model 3, the heat transfer rate is further improved due to the presence of fins. At t = 250 min, the solidification is almost completed in Model 2 and Model 4, whereas the absence of fins in top blocks delays the overall solidification in Model 1 and Model 3. The temperature contours show a similarity in Model 2, Model 3 and Model 4 having temperatures close to the HTF inlet temperature in the middle and bottom PCM blocks, whereas, Model 1 having no fins achieves this temperature condition only in the bottom PCM block.

The conduction heat transfer significantly influences the solidification process based on the location of PCM block and the fins. For example, in Model 4, enhancement in the heat transfer rate occurs due to fins in the top PCM block and a high temperature difference between the PCM and the HTF in the bottom PCM block. The average solidification rate is thus enhanced significantly due to uniformity of heat transfer throughout the system.

From the charging and discharging analysis of the single PCM system, it is inferred that the distribution of fins along the length of the system plays an important role in the heat transfer enhancement rate. The heat transfer reduces along the length from top to bottom during charging with HTF injection from the top, whereas, it reduces from bottom to top during discharging with HTF injected from the bottom. Uniform fin-distribution improves both the charging and discharging rates, however, further enhancements can be achieved by employing more fins in the PCM blocks which are opposite from the direction of HTF injection.

7.2.1.3 Specific energy charged and discharged

The variations in sensible, latent and total specific energies for all the models during both the charging and discharging processes are plotted in Figure 7.5. The values are estimated for maximum average PCM temperature (T_{max}) of 375 ºC during charging and minimum average PCM temperature (T_{min}) of 290 ºC during discharging. The total specific energy remains the same (~50.6 Wh/kg) for all the models in the specified temperature range as the same PCM is used in all the models. The rate of charging or discharging depends significantly on the temperature difference between the HTF and the PCM and the addition of fins.

During charging, the PCM is initially in the solid-state and hence, the heat transfer takes place due to conduction. However, as the PCM starts melting, it absorbs the latent heat followed by the sensible heating of the liquid PCM. The total charging rate is slow throughout the process in the absence of fins i.e. for Model 1. Upon close observation, it can be noticed that the rate of sensible heat transfer is higher in Model 2, Model 3 and Model 4 than Model 1, whereas, the rate of latent heat transfer is marginally lower than Model 1. The fins improve the overall heat transfer rate, however, they also lead to partial hindrance to the convection currents which are restricted in the spaces between the fins. However, the total charging rate is marginally affected by this development. The natural convection suppression caused by the fins has been reported extensively in the literature (Rabienataj Darzi et al., 2016; Solomon and Velraj, 2013), and also in the authors previous study (Sodhi et al., 2019a).

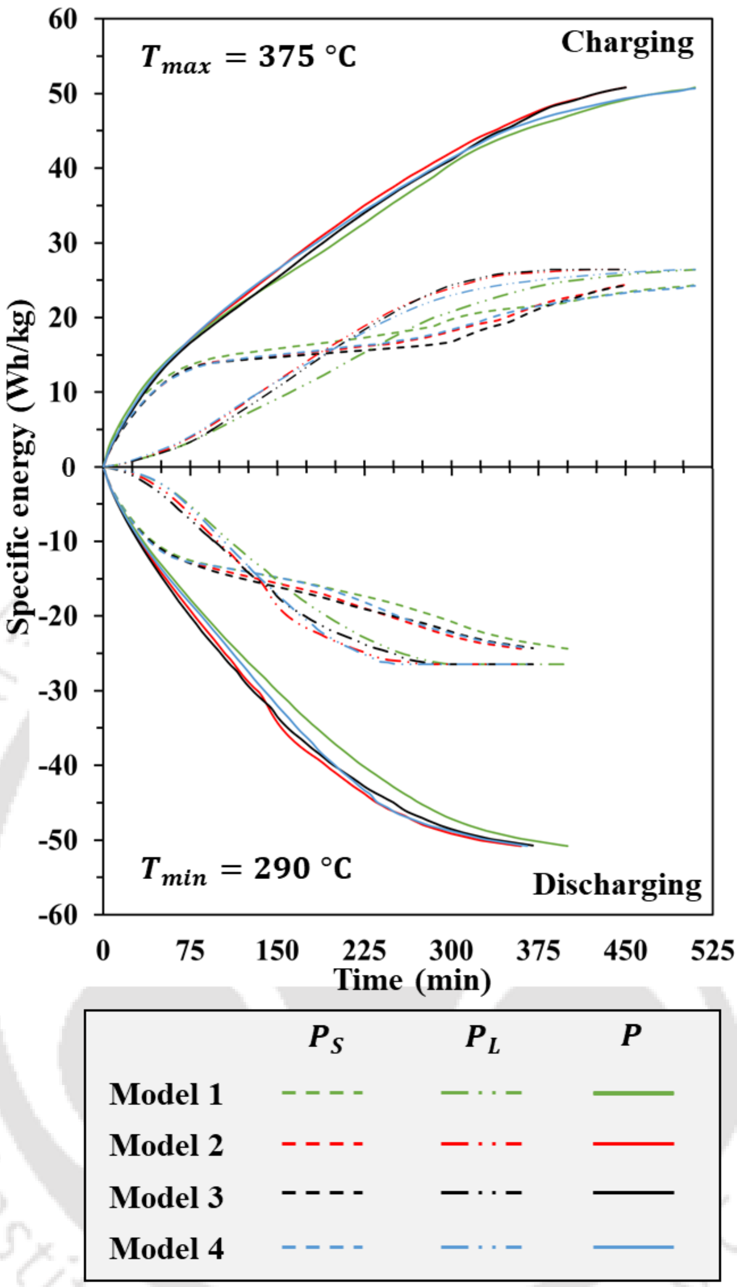

Figure 7.5. Sensible, latent and total specific energy charged and discharged by the single PCM systems with different fin distribution.

The discharging process starts with sensible heat discharged by the liquid PCM followed by its solidification. After discharging the latent heat, the PCM undergoes sensible cooling. Again, due to addition of fins, as in case of Model 2, Model 3 and Model 4, the total rate of discharging is improved significantly. Unlike charging, both the rate of sensible and latent heat discharged are enhanced. Since, the natural convection effect for the discharging process has been neglected, fins only affect the conduction heat transfer rate.

7.2.2 Comparison of the single and m-PCM systems

7.2.2.1 Charging and discharging time

The charging and discharging comparison between the single and m-PCM systems at different HTF inlet temperatures is analysed in this section. The single PCM system (with PCM[b] in all three PCM blocks) is taken as the reference and the corresponding Ste_{ref} values are calculated at different inlet temperatures and used as a reference for a convenient comparison. The average HTF velocity is fixed as 16 m/s. The total temperature range ($T_{in} - T_i$) for charging and discharging operation, and the latent heat capacity (individually for top, bottom and middle PCM blocks) for the single and m-PCM systems are equal in each of the cases with different Ste_{ref}. The reference Rayleigh number (Ra_{ref}) values are also calculated to compare the effect of natural convection heat transfer in the different PCM blocks. The charging time for the top, middle and bottom PCM block, and the overall charging time for the single and m-PCM system due to change in Ste_{ref} are plotted in Figure 7.6.

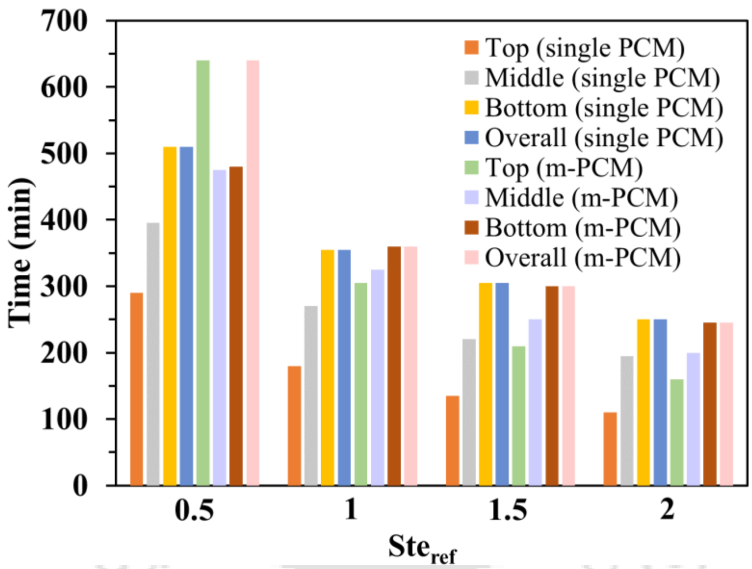

Figure 7.6. Variation in charging time for the single and m-PCM systems for different Ste_{ref} values.

The heat transfer rate between the HTF and the PCM (or PCMs) depends upon several factors such as the temperature difference between the HTF and the PCM, the length (or volume) of the PCM blocks, the melting point temperature of the PCM (or PCMs) and their thermo-physical properties. The charging performance of the single PCM system is superior than the m-PCM system for a low Ste_{ref} value of 0.5. The major performance bottleneck in the m-PCM system than the single PCM system is the slow melting in the top PCM block which happens due to a low temperature difference between the HTF and the PCM. Further, fixing the latent heat capacity of the single and m-PCM LHS systems, $Ra_{PCM^a}(8.8 \times 10^6$, m-PCM system) < $Ra_{ref}(8.4 \times 10^7$, single PCM system), which indicates a low rate of natural convection in the m-PCM system. The melting takes place at a faster rate in the bottom PCM block for the m-PCM system than the single PCM system due to high temperature difference between the HTF and the PCM. The heat transfer rate in the m-PCM system improves significantly by increasing the inlet temperature i.e. by increasing Ste_{ref} to 1.

As Ste_{ref} increases from 0.5 to 2, melting times in the top block for the single and m-PCM systems are reduced by 62% and 75%, whereas, 50% and 58% reductions are observed in the middle block. The corresponding melting time reduction in the bottom block are 51% and 49%, respectively. Therefore, by increasing the Ste_{ref} from 0.5 to 2, the charging performance is improved for both the single and m-PCM systems throughout the system length, however, the enhancements are more comprehensive for the m-PCM system.

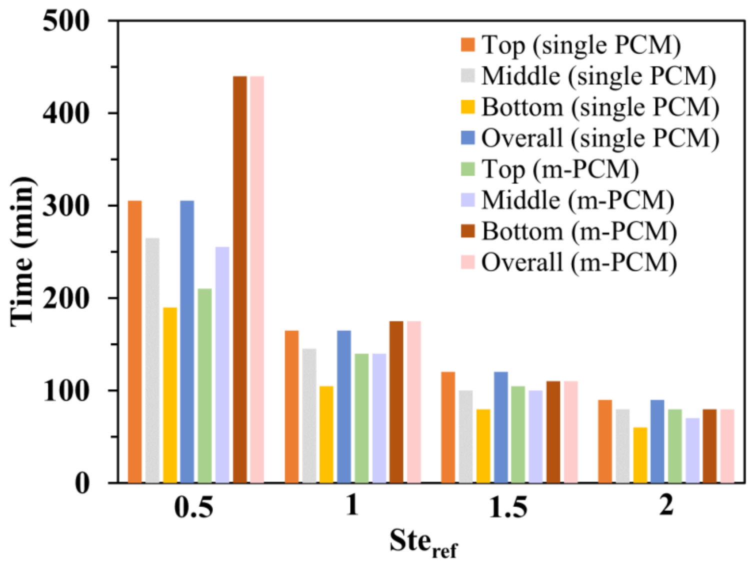

Figure 7.7. Variation in discharging time for the single and m-PCM systems for different Ste_{ref} values.

The overall melting time for the single or m-PCM system is estimated based on the PCM block which melts at last. It indicates the overall performance as it incorporates the effects of natural convection, conduction and lengths (or volumes) of different PCM blocks throughout the LHS system. The overall melting time is less for the single PCM system initially ($Ste_{ref} = 0.5$), however, it is similar to the m-PCM system for $Ste_{ref} = 1.0$. A higher $Ste_{ref} = 1.5$ leads to a lesser melting time for the m-PCM than the single PCM system by 11.5%. Increasing Ste_{ref} further, does not improve the m-PCM system performance any further.

During discharging, the performance improvements primarily depict the degree of improvement in the conduction heat transfer rate in the single or m-PCM system as the natural convection heat transfer is considered to be negligible. The HTF interacts with the PCM in the top block at last due to the bottom injection of HTF during discharging. The discharging times for the single and m-PCM systems due to variation in the Ste_{ref} is plotted in Figure 7.7. For $Ste_{ref} = 0.5$, the performance of the m-PCM exceeds that of the single PCM system in the top block with the discharging time less than the single PCM system by 31%. The rate of discharging in the middle block remains similar between the single and m-PCM systems at all Ste_{ref} values. The major variation in the discharging rate occurs in the bottom block, and the heat transfer depends upon a combination of factors i.e. the temperature difference between the HTF and the PCM, thermo-physical properties of PCM and lengths (or volumes) of the single or m-PCM blocks. During discharging, the temperature difference between the HTF and the PCM in the bottom PCM block is the major bottleneck that limits the heat transfer rate in the m-PCM system for $Ste_{ref} = 0.5$. Decreasing the inlet HTF temperature i.e. for $Ste_{ref} > 0.5$, improves the heat transfer rate.

The overall discharging time gives a better understanding of the overall improvement in the discharging rate of the single or m-PCM system with increase in Ste_{ref}. For $Ste_{ref} = 0.5$, the total discharging time for the single and m-PCM systems is 305 min and 440 min, respectively. For $Ste_{ref} = 1$, the overall discharging time for the single and m-PCM system is almost the same. However, for $Ste_{ref} = 1.5$, the discharging time for the m-PCM system is less than the single PCM system by 17%, and the variation is insignificant thereafter. Increasing the Ste_{ref} from 0.5 to 2, the discharging time for the single PCM system reduces by 70.5%, whereas that for the m-PCM system reduces by 82%.

Therefore, both the charging and the discharging performances of the m-PCM system are similar or higher than the single PCM system for $Ste_{ref} \geq 1$.

7.2.2.2 Specific energy charged and discharged

The variations in the total specific energy charged and discharged by the single and m-PCM systems at different Ste_{ref} values are shown in Figure 7.8. It is observed that the total specific energy delivered by the m-PCM is higher than the single PCM system for all the Ste_{ref} values.

With an increase in Ste_{ref} from 0.5 to 2, the total specific energy for the single PCM system increases from 50.8 to 90.5 Wh/kg, whereas that for the m-PCM system increases from 63.5 to 109.7 Wh/kg. The latent specific energy for the m-PCM system is 35 Wh/kg and is higher than the single PCM system (26.4 Wh/kg) by 32.5%. The latent heat specific energy does not change with Ste_{ref} as the total latent heat capacity for the single or m-PCM system is fixed. The rise in total specific energy due to an increase in the Ste_{ref} value for both the single and m-PCM systems is due to an increase in the sensible specific energy. For a fixed temperature range $(T_{in} - T_i)$ of charging and discharging operation, and a fixed total latent heat $((Q_L)_{top} + (Q_L)_{middle} + (Q_L)_{bottom})$ charged and discharged, the specific energy charged and discharged by the m-PCM system is always higher than the single PCM system.

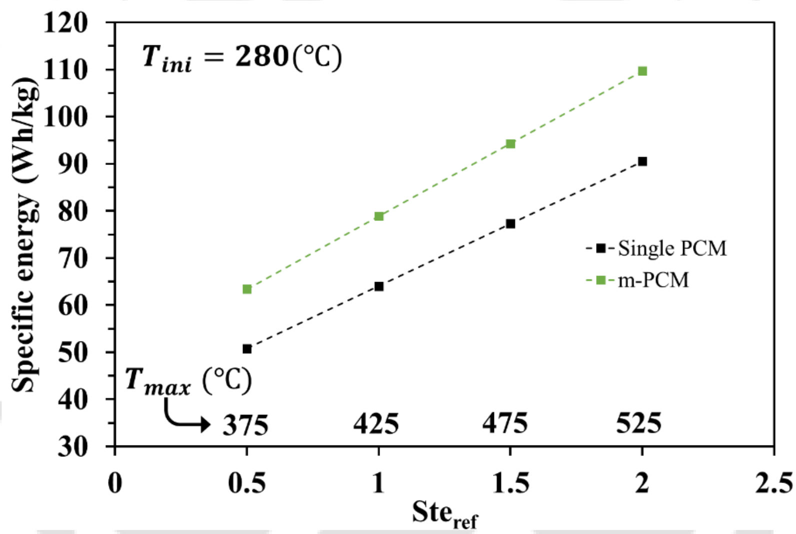

Figure 7.8. Maximum specific energy charged and discharged (shown for charging) by the single and m-PCM systems for different Ste_{ref} values.

It is evident from Figure 7.8-10, that for $Ste_{ref} = 0.5$, the performance of the m-PCM system is a compromise between the specific energy charged and discharged (higher than the single PCM system) and the rate of charging and discharging (lower than the single PCM system). The charging and discharging times for the m-PCM system are similar to the single PCM system for $Ste_{ref} \geq 1$, whereas, the specific energy delivered by the m-PCM system is significantly higher (>21-25%) at all Ste_{ref} values. Considering these advantages, the further enhancements in the charging and discharging rates of the m-PCM system by varying the lengths (or volumes) ratio of different PCM blocks is discussed in the upcoming section.

7.2.3 Effect of PCM block lengths ratio (LR) on the performance of m-PCM system

The main objective of varying the length ratio (LR) is to vary the volumes of different PCMs, which can be varied by changing the ratio of the amount of latent heats stored by the individual PCMs in the m-PCM system, keeping the total latent heat as fixed. The melt fraction profiles for the m-PCM systems with different lengths ratio are shown in Figure 7.9. It is observed that the charging melt fraction profile varies comprehensively up to an average melt fraction value of 0.95, however, the change is insignificant thereafter. The m-PCM system with LR4 ($l_1: l_2: l_3 = 0.73: 1: 1.03$) leads the other m-PCM systems throughout the charging process. For a melt fraction of 0.8, the m-PCM with LR4 melts faster than LR2 by ~20% and the melt fraction for the m-PCM with LR1 and LR3 lie in between. Any variation in the overall melting of the m-PCM system depends upon the melt fraction variation in the individual PCM blocks, which further depends on important factors such as, (i) length (or volume) of the PCM block, (ii) location i.e. top, middle or bottom, and (iii) thermo-physical properties of the PCM. The enhancement in the charging rate for LR4 up to the average melt fraction of 0.95 occurs due to a combination of factors discussed above.

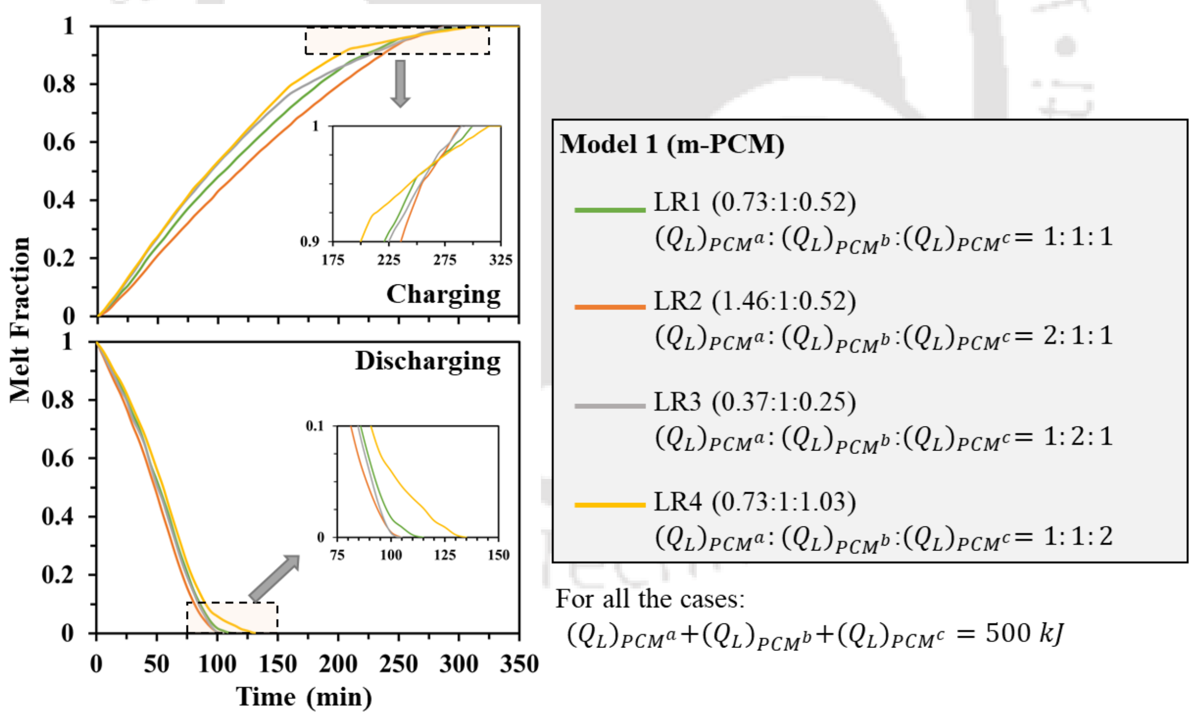

Figure 7.9. Variation in melt fraction with different lengths ratio of m-PCM systems during charging and discharging.

During discharging, the melt fraction profiles for the m-PCM with different LRs vary only marginally from each other as shown in Figure 7.9. The profiles are similar up to 90% of the solidification and therefore, any variations in melt fraction profile after this point can be ignored. Therefore, varying the LR in the m-PCM system does not affect the discharging performance significantly.

For a fixed Ste_{ref} ($Ste_{ref} = 1.5$) value, the total specific energies during the charging and discharging of the m-PCM systems with different LRs is plotted in Figure 7.10. During charging, it is observed that the m-PCM with LR2 and LR4 have a maximum specific charging and discharging energy of 97.5 Wh/kg and 96.7 Wh/kg, respectively, followed by LR1 and LR3 having values 94.1 Wh/kg and 89 Wh/kg, respectively. The rate of charging for the m-PCM with LR4 is higher than other systems during most of the charging process. During the discharging, the rate of discharging is similar up to 60% of the total specific energy discharged, however, the discharging rate for the m-PCM with LR4 is faster thereafter.

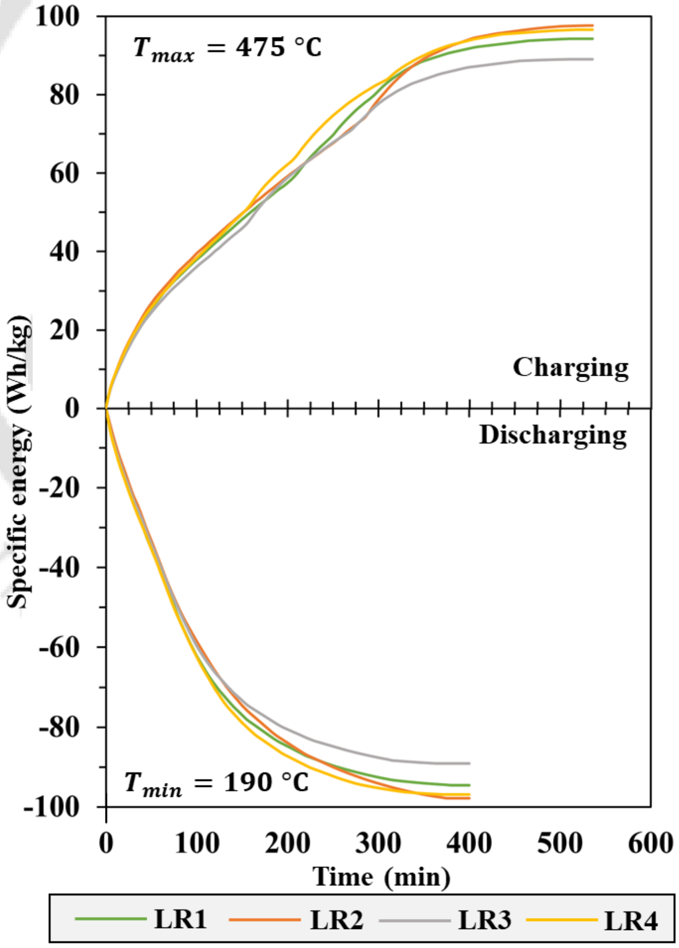

Figure 7.10. Specific energy charged and discharged for the m-PCM system with different lengths ratio.

The analysis identifies that the m-PCM with LR4 has the fastest charging and discharging rates, followed by the m-PCM with LR1 and LR2 having an intermediate charging and discharging rates, whereas, the m-PCM with LR3 has the poorest charging and discharging performances both in terms of the amount and rate of specific energy transferred.

7.2.4 Compound heat transfer enhancement in the m-PCM system

From the previous discussion, it is evident that the m-PCM with LR4 has the fastest charging rates and yields higher total specific energy charged and discharged and therefore, it is chosen as the best candidate for further enhancement in heat transfer rate using non-uniform fin distribution. The enhancement in the m-PCM systems in terms of melting and solidification times and charging or discharging specific energy outputs are further elaborated by comparing the following cases;

- Case 1: Model 1, single PCM system
- Case 2: Model 1, m-PCM system, LR1 ($l_1: l_2: l_3 = 0.73: 1: 0.52$)
- Case 3: Model 1, m-PCM system, LR4 ($l_1: l_2: l_3 = 0.73: 1: 1.03$)
- Case 4: Model 2, m-PCM system, LR4 ($l_1: l_2: l_3 = 0.73: 1: 1.03$)
- Case 5: Model 3, m-PCM system, LR4 ($l_1: l_2: l_3 = 0.73: 1: 1.03$)
- Case 6: Model 4, m-PCM system, LR4 ($l_1: l_2: l_3 = 0.73: 1: 1.03$)

In all the cases, the total latent heat capacity is fixed. Also, the temperature range of charging and discharging operation ($T_{in} - T_i$) is fixed at 205 °C ($Ste_{ref} = 1.5$). The Cases 1 and 2 are the standard single and m-PCM systems, whereas Cases 3, 4, 5 and 6 represent the variations in terms of optimized m-PCM lengths ratio (LR4) and addition of fins. The variations in melt fraction profiles in the top, middle and bottom PCM blocks, and the average melt fraction profiles for charging and discharging are plotted in Figure 7.11(a) and Figure 7.11(b), respectively, and the temporal variations in the melting contours are further elaborated in Figure 7.12 and Figure 7.13, respectively.

Melting and solidification in Top PCM block: During charging, the heat transfer enhancement in the top block for the m-PCM system (Cases 2-6) depends upon the temperature difference between the HTF and the PCM. The enhancement can be further achieved by adding fins in this section, as in Cases 4 and 6 which perform better than Cases 2, 3 and 5. The length ratio optimization discussed in the previous section leads to better performance in the m-PCM system, as the melting rate in Cases 3-6 is higher than Case 2. The melting time for Case 1 (single PCM system) is comparable to that for Case 4, but lesser than Case 3. Figure 7.12 shows that melting in the top PCM block is enhanced by adding 6 fins (Case 6). At time t = 75 min, the melting rate is enhanced in Case 6 by 15.5% and 78% than Cases 1 and 2, respectively. At 150 min, the melting is complete in Cases 1, 3 and 6, whereas the slowest melting rate occurs in Case 2.

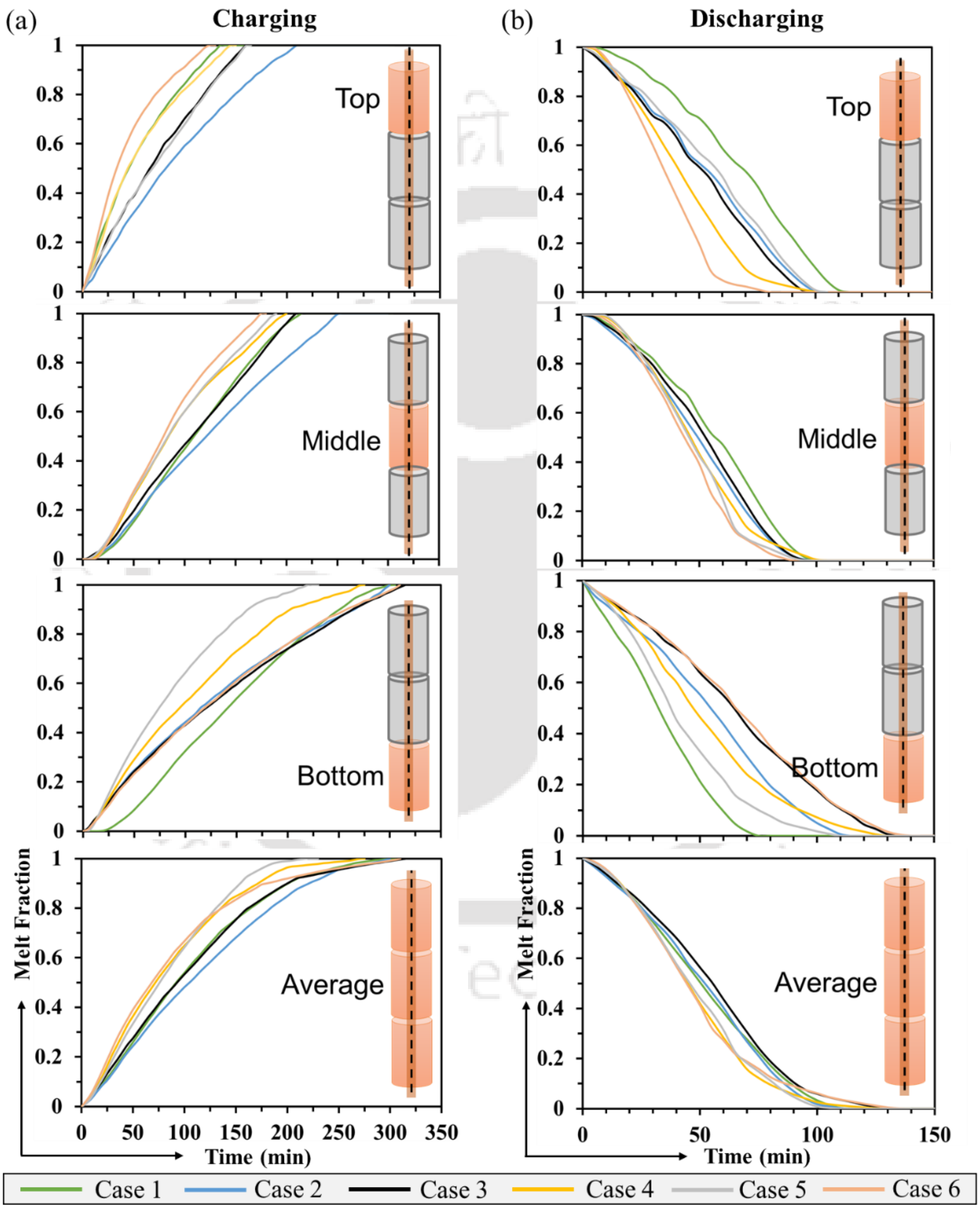

Figure 7.11. Melt fraction variation in top, middle and bottom PCM blocks for Cases 1-6 during (a) charging and (b) discharging.

During solidification, the heat transfer rate in the top block is enhanced due to the addition of fins as in Cases 4 and 6. At t = 25 min, the solidification rate in Cases 4 and 6 is faster than Case 1 by 18% and 23%, respectively. However, the overall solidification rate is fastest in Case 6 having 6 fins.

Melting and solidification in Middle PCM block: Both during charging and discharging, the melting and solidification rate for Case 6 is found to be highest.

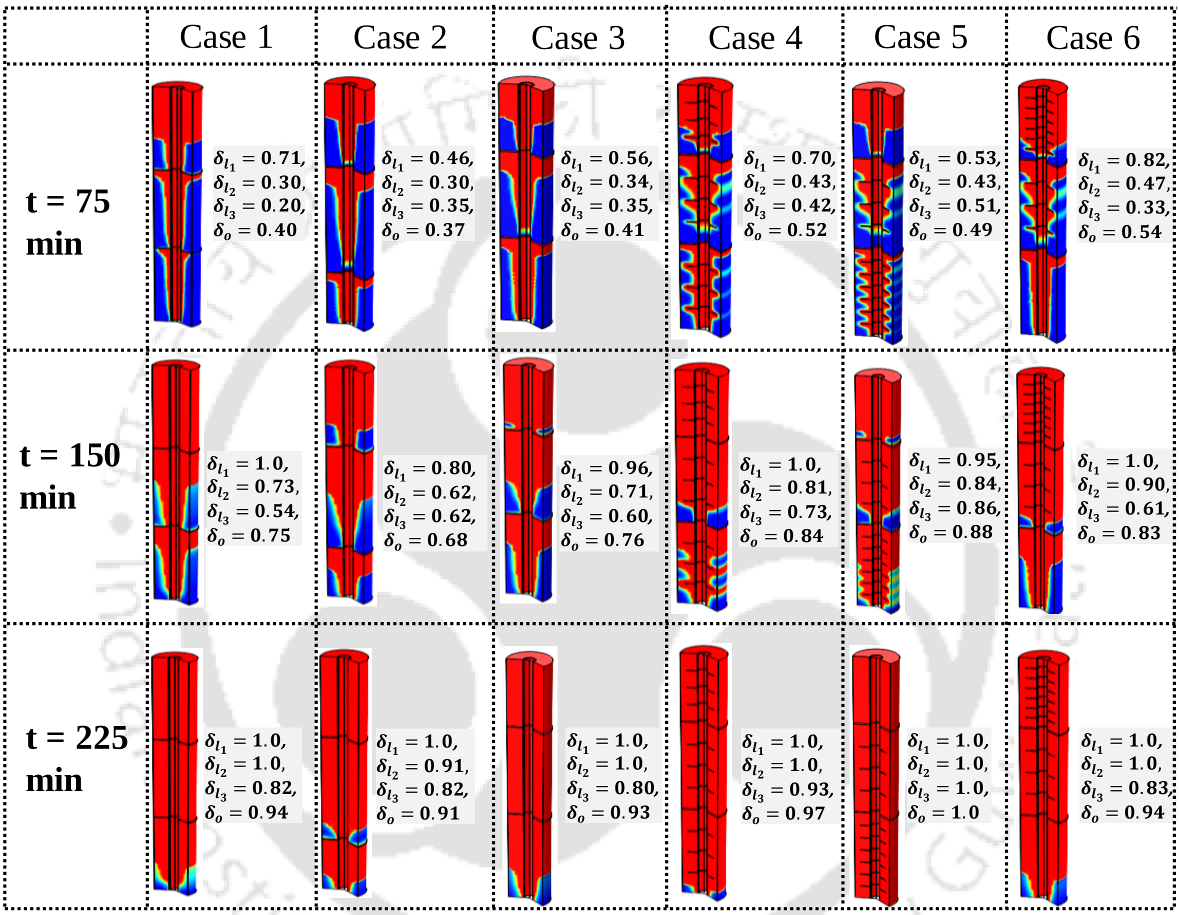

Figure 7.12. Melt fraction contours during charging for Cases 1-6 at different time intervals ($\delta_{l_1}, \delta_{l_2}, \delta_{l_3}$ *and* δ_o refer to top, middle, bottom and average melt fractions in the PCM blocks).

Melting and solidification in Bottom PCM block: The melting in the bottom block depends upon the temperature difference between the PCM and the HTF injected from top. A faster rate of melting is observed for Cases 4 and 6 due to the presence of 3 and 6 fins respectively, whereas the rate is slowest for Case 2. The melting time in Cases 4 and 6 is less than Case 2 by 13% and 30%, respectively. During discharging, the HTF is injected from the bottom, and interacts with the PCM in the bottom block. The LR optimization analysis discussed previously shows that the discharging time for Case 3 is marginally higher than Case 2. This can also be observed from the melt fraction contours shown in Figure 7.13, where the solidification in Cases 3 and 6 is the slowest. However, the discharging time can be reduced by employing the non-uniform fin distribution. For example, the heat transfer rate improves in Case 5 by adding fins in the bottom block, such that the discharging rate improves.

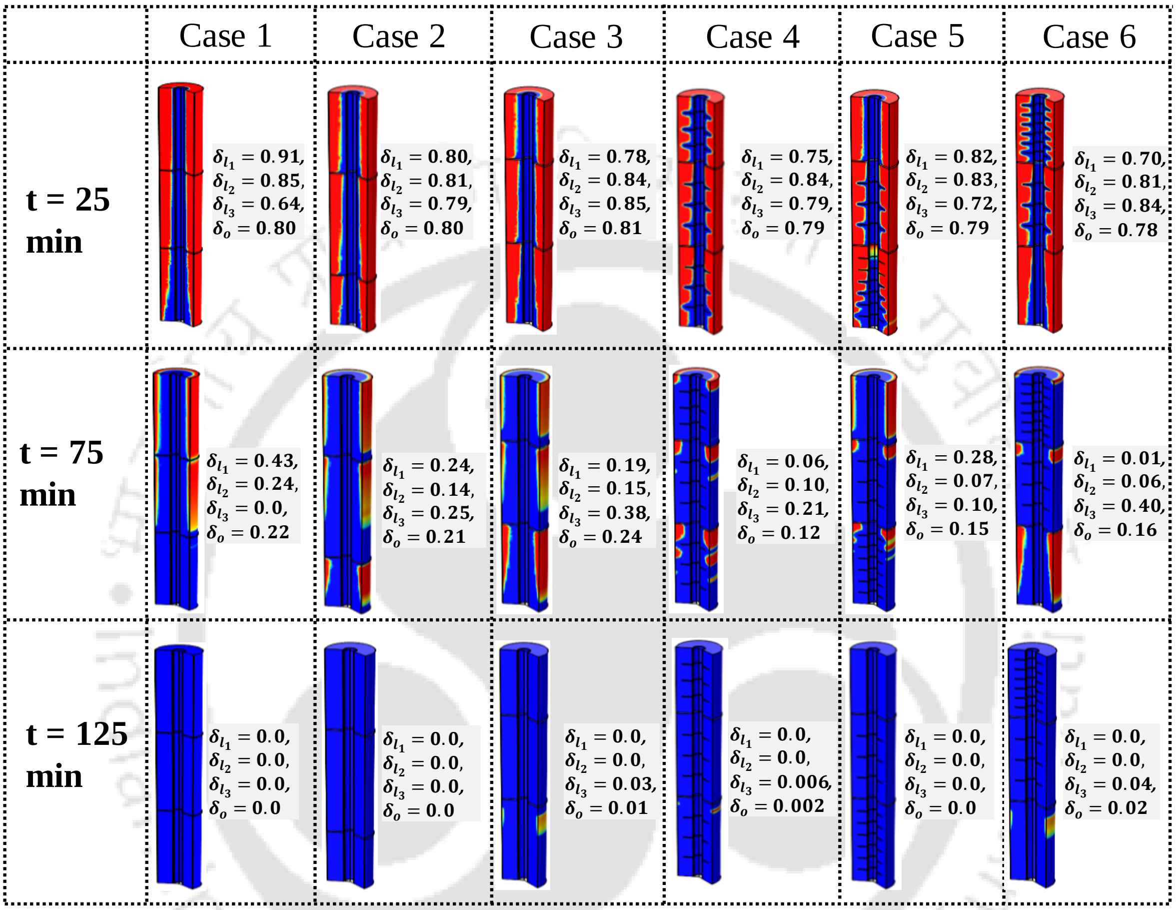

Figure 7.13. Melt fraction contours during discharging for Cases 1-6 at different time intervals ($\delta_{l_1}, \delta_{l_2}, \delta_{l_3}$ *and* δ_o refer to top, middle, bottom and average melt fractions in the PCM blocks).

Melting and solidification in the system: The melting and solidification performance depends upon a combination of factors such as; temperature difference between the HTF and the PCM (or PCMs) in the different single PCM or m-PCM blocks, the direction of HTF injection, lengths (or volumes) ratio of the m-PCM system, etc. The melting rate is fastest for Case 5 with least charging time followed by Case 4. The melting rate is slowest for Case 2 followed by Case 1 and Case 3. The overall charging time in Case 5 i.e. m-PCM system with non-uniform fin distribution having 6 fins in the bottom block is less than Case 1 by ~30%. The overall discharging time is least for Case 5 followed by Cases 2, 1, 4 and 3. The overall discharging time for Case 5 is less than Case 1 (single PCM system) by ~9%. The overall discharging time for Case 6 is highest even with the presence of fins, which shows that fins alone may not be advantageous to improve the performance of the m-PCM system. However, the appropriate distribution of the fins can improve the performance significantly in the PCM block which may otherwise suffer from a low heat transfer rate.

Overall, Case 5 is observed to have the best charging and discharging performances. The heat transfer enhancements due to non-uniform fin distribution and optimized LR are more profound during charging, however, the enhancements during discharging are only moderate.

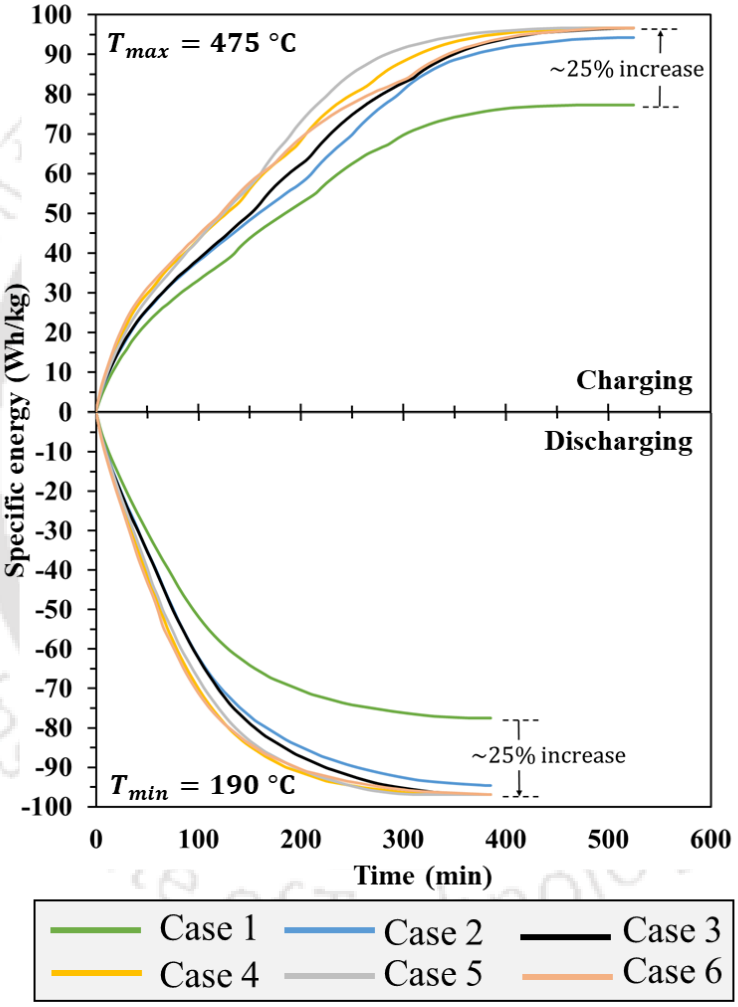

Figure 7.14. Specific energy charged and discharged for Cases 1-6.

The specific energy charged and discharged for all the six cases is shown in Figure 7.14. The maximum enhancement in the specific energy charged and discharged by the m-PCM system than the single PCM system is ~25%, and the rates of charging and discharging throughout the processes are found to be maximum for Case 5.

Therefore, the m-PCM system undergoes compound enhancement, both in terms of the rate of charging and discharging and the amount of total specific energy charged and discharged. The compound enhancement is achieved due to a combination of factors i.e. non-uniform fin distribution and optimizing the PCMs lengths ratio.

7.2.5 Design implications and application perspectives

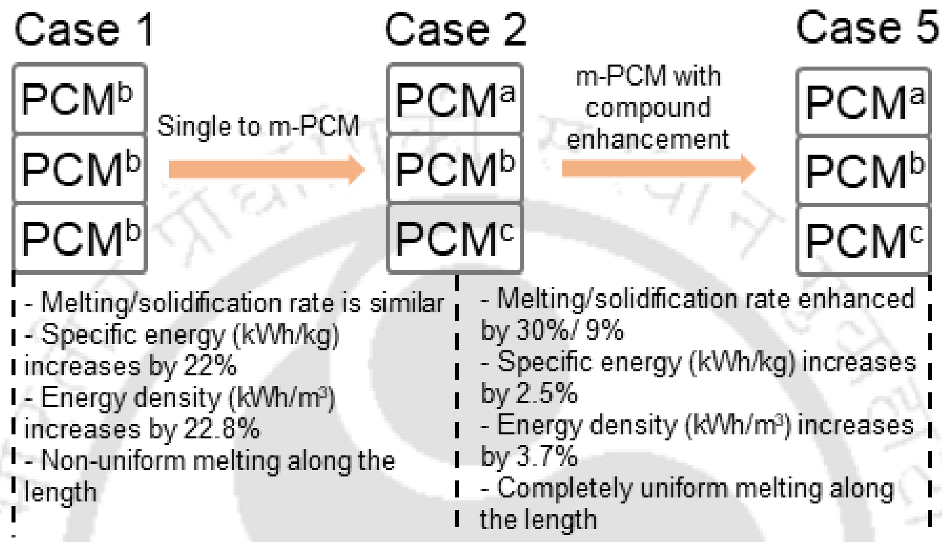

Figure 7.15. Hierarchy of design and improvements for the developed multi-PCM system.

The hierarchal development of the optimized m-PCM system starting from the single PCM system is described in Figure 7.15. By opting the multi-PCM design, the energy storage capacity per unit volume (kWh/m^3) and the specific energy (kWh/kg) increase, however, the charging and discharging rates are similar or even lower than the single PCM system depending upon the HTF conditions. The thermo-physical properties of the selected PCMs cannot be altered, however, identifying the bottlenecks, the charging and discharging rates in the m-PCM system can be enhanced further. This can be achieved without compromising the energy storage capacity per unit volume by using the proposed design methodology.

The numerical procedure and the design methodology are valid for all combination of PCMs, and can be integrated to any energy storage application. Based on the operational characteristics, the proposed system can be incorporated with a high temperature concentrated solar power application (CSP) such as the Ait-Baha CSP plant in Morocco (Zavattoni et al., 2018). The facility is having a 100 MWth thermal energy storage system for 5 h storage using sedimentary rocks as a storage medium. The solar collector field inlet and outlet HTF (air) temperatures are 270 °C and 570 °C, which are also the charging and discharging temperatures, respectively. The numerical simulations are conducted for the charging process by integrating the proposed design to the solar field output of the CSP application and the following benefits for the optimized m-PCM over the conventional single PCM system can be projected;

- The proposed m-PCM system can be compact with 21.2% increase in the energy storage capacity per unit volume.
- Specific energy can be increased by 20.5%.
- Uniform melting characteristics can be obtained with enhanced charging heat transfer rate by up to 25%.
- Based on the PCM costs of KOH (568 USD/kWh), KNO_3 (496 USD/kWh) and $NaNO_3$ (318 USD/kWh) reported by Liu et al (Liu et al., 2012), the required PCM material cost can be reduced up to 13%.

7.3 Summary

In the present study, an experimentally validated model of the m-PCM system with three PCM blocks (PCM^a, PCM^b and PCM^c) is developed. A non-uniform distribution of fins in different PCM blocks is introduced and the performance of the single PCM system (PCM^b) is initially analysed. Further, the single and m-PCM systems are compared on the basis of a reference Stefan number parameter (Ste_{ref}), which is calculated by considering the single PCM system as the reference and incorporates the effect of HTF inlet temperatures during the charging or discharging. For a fixed total latent heat capacity of the m-PCM system, varying the latent heat storage capacity of PCM^a, PCM^b and PCM^c in different ratios varies the lengths ratio (LR) of the PCM blocks, and the corresponding performance variations are analysed. Based on these developments, compound enhancement in the m-PCM systems using non-uniform fin distribution and optimum PCM block lengths ratio (LR) is studied. The following major conclusions are drawn from the study;

- The melting and solidification times for the single PCM system are reduced by 24.5% and 16.5% by incorporating the non-uniform fin distribution.
  The melting and solidification times for the single PCM system are reduced by 24.5% and 16.5% by incorporating the non-uniform fin distribution.
- For a fixed temperature range of operation (temperature difference between the HTF and the PCM initial temperature) and equal latent heat capacity (individually for all PCMs), a comparison between the single and m-PCM systems shows that at low Ste_{ref}(PCM^b as reference) value of 0.5, the performance of the m-PCM system is a compromise between

low charging and discharging rates and high specific energy charged and discharged. However, for $Ste_{ref} \geq 1$, the charging and discharging times for the m-PCM system are either similar or lower than the single PCM system. The specific energy for the m-PCM system is higher than the single PCM system by 21-25% in the complete range of Ste_{ref} values (0.5 to 2) considered. The overall system performance is influenced by several factors such as the degree of natural convection and conduction heat transfer, and location and volumes of the PCM blocks.

- The LR $l_1{:}\,l_2{:}\,l_3 = 0.73{:}\,1{:}\,1.03$ is found to be optimum with high charging and discharging rate and high specific energy charged and discharged.
- The compound heat transfer enhancement i.e. enhancement achieved by employing a non-uniform fin distribution in the m-PCM system with optimum PCM blocks LR, leads to reduction in charging and discharging times than the single PCM system by 30% and 9%, respectively. Further, there is a 25% increase in the charging and discharging specific energy for the m-PCM system than the single PCM system.
- The optimized m-PCM system proves beneficial over the single PCM when employed to a real time CSP application due to high energy storage capacity and specific energy, uniform melting and enhanced charging characteristics, and low PCM cost.

Chapter 8

Conclusions and future scope

Preface

The present thesis work is a resolute effort aimed towards the development of sustainable energy technologies. The research work is primarily focussed on the design and development of a high-temperature (~500 °C) latent heat storage (LHS) system and various aspects related to thermal storage such as thermal modelling, storage system design, experimental and numerical analysis on LHS modules, and their heat transfer enhancements are explored.

The thermal behaviour and the performances of the LHS system are studied by conducting experimental investigations on an in-house test setup developed at IIT Guwahati. The numerical models are developed to assist the designing of different LHS modules. Majorly, high-capacity (~20 MJ) storage modules and low-capacity (<1 MJ) encapsulated PCM modules with different fin designs are tested.

Based on the in-depth scrutiny of the recent literature on LHS systems, few heat transfer enhancement techniques such as novel conical LHS shell and tapered longitudinal fin designs, and non-uniform fin distribution are developed to facilitate uniform melting and solidification of the PCM.

The critical goal of all the sub-objectives covered in the thesis work is to improve the charging and discharging characteristics for developing efficient storage systems.

In this chapter, the major conclusions drawn from the thesis work are presented. Further, the scope of the research work in the future is discussed.

8.1 Performance investigations of high-temperature latent heat storage (LHS) modules

In the present thesis work, experimental and numerical investigations were conducted to analyse the performance of different LHS systems. Two different types of LHS systems namely; shell and tube heat exchanger design and PCM encapsulation design were analysed.

To achieve this objective, a high-temperature test facility with air as the source fluid at operating temperatures of up to 500 ºC was developed. In the tested LHS modules, sodium nitrate with a melting temperature of 305.1 ºC was used as the phase change material (PCM). The important PCM properties such as melting temperature and the latent heat were estimated using the Differential Scanning Calorimetry test.

Numerical models were developed using the finite element based modelling tool COMSOL Multiphysics. The interaction between the PCM and the HTF was modelled using the conjugate heat transfer physics. The effective heat capacity model was considered to solve the phase change problem. To incorporate the buoyancy occurring in the PCM flow, the boussinesq approximation was introduced as a source term in the Navier-Stokes equation. Further, the Kozeny-Carman equation was added as a source term to solve the two-phase (solid-liquid) PCM condition. The model was validated and found to be in good agreement with the experimental results obtained from the literature.

Some of the major outcomes and conclusions made from the two different LHS designs are described below.

8.1.1 Multi-tube LHS module

- The 2D numerical model developed to optimize the number of HTF tubes shows that for a fixed PCM volume to heat transfer surface area ratio, the conduction and convection heat transfer rate is improved by employing more number of smaller sized tubes than using less number of larger size tubes.
- Axial and radial distribution of temperature in the LHS module shows that the charging process was dominated by natural convection heat transfer, whereas, conduction was the dominant mode of heat transfer during charging.

- Charging times at flow rates of 43.8 m^3/h, 73 m^3/h and 102 m^3/h were 348 min, 296 min and 271 min, respectively, and the discharging times were 460 min, 336 min and 256 min, respectively.
- Melting initiated at the front end of the LHS module and occurred at a faster rate in the upper regions due to the natural convection heat transfer dominating throughout the process. The melting finishes at the rear end in the bottom region of the LHS module.
- Solidification initiates at the front end and finishes at the rear end of the LHS module, however, the heat transfer rate varies significantly only in the axial direction.
- Increasing the temperature difference between the inlet HTF temperature and initial PCM temperature during charging and discharging improves the heat transfer rate in the LHS module.
- Increasing the HTF flow rate improves both the charging and discharging rate only up to a threshold value of flow rate, whereas, the improvement is insignificant thereafter.
- During charging and discharging processes, the effect of varying the temperature difference between the HTF and PCM is more prevalent as compared to the increase in the flow rate.
- Maximum amount of energy charged and discharged by the LHS module were 19.5 MJ and 20.62 MJ, respectively.
- Power is charged or discharged at a faster rate initially, followed by a steady discharge later.

8.1.2 PCM encapsulation module

- The charging and discharging performances of the basic cylindrical PCM capsules can be improved by introducing the annular PCM encapsulation design which increases the heat transfer surface area.
- The numerical model was developed for the charging process and the results were found to be in good agreement with the charging experiments in the temperature range 50-330 ºC.
- The temperature contours show that the heat transfer takes place in both the axial and radial direction of the PCM capsules. The rate of heat transfer in the radial direction is particularly improved by employing the annular capsule design.
- A maximum reduction in the charging and discharging times of 49% and 27.5% was obtained by changing the design from basic to annular cylindrical capsule.
- Adding straight or tapered longitudinal fins in the annular capsules improve the discharging rate significantly as compared to the charging rate.

- The tapered fins with increasing height from inlet to the outlet has better charging and discharging performances as compared to fins with decreasing height from inlet to the outlet.
- In the actual high-capacity storage systems, implementing fins is subjected to constraints such as weight and cost of manufacturing. Therefore, it is proposed to use tapered fins than conventional straight fins in order to reduce the PCM capsule weight for a similar charging/discharging performance.

8.2 Novel methods to improve the heat transfer rate in conventional shell and tube LHS designs

Apart from the above-mentioned performance investigations on high-temperature LHS systems, novel techniques are proposed to improve the heat transfer rate in conventional LHS designs using numerical modelling.

8.2.1 Novel conical shell LHS design

- The shell dimensions of a conventional cylindrical shell and tube LHS system were optimized to a conical shell (cone angle 3.4°) design. The design leads to effective PCM distribution with less PCM mass near the outlet section and more PCM near the inlet.
- The conical shell LHS system leads to a uniform melting and solidification and a maximum reduction in charging and discharging times up to 17% and 28% can be achieved.
- The system performance is significantly affected by the inlet HTF velocity and temperature. The effect of increase in the HTF inlet velocity on the charging and discharging rates is comprehensive only up to a threshold value of velocity (6 m/s). Increasing the temperature difference between the HTF inlet temperature and initial PCM temperature by 10 ºC leads to a reduction in the charging and discharging times by 26.7% and 36.7%, respectively, whereas, further increase by 10 ºC leads to a further reduction by 21.5% and 21.2%. Thus, even by using an HTF (air) with poor thermal properties, a higher ΔT is beneficial to improve the system performance.
- Adding fins to the conical shell system improves the conduction heat transfer rate during the charging and discharging near the inlet section, but is inadequate near the outlet section. Near the outlet section, presence of fins leads to a compromise between the conduction heat transfer and convection currents in the liquid PCM.

8.2.2 Non-uniform fin distribution in single and multi-PCM shell and tube system

- The melting and solidification times for the single PCM system are reduced by 24.5% and 16.5% by incorporating the non-uniform fin distribution.
- Fixing the operating parameters such as the temperature range of operation and latent heat (individually for all PCMs), it is observed that for a low Ste_{ref} value of 0.5, the performance of the m-PCM system is a compromise between low charging and discharging rates and high specific energy charged and discharged. For $Ste_{ref} \geq 1$, the charging and discharging times for the m-PCM system are either similar or lower than the single PCM system. The rate of natural convection and conduction heat transfer, and location and volumes of the PCM blocks are the major factors influencing the performance of the m-PCM system.
- For different Ste_{ref} (0.5 to 2) values, the specific energy for the m-PCM system is higher than the single PCM system by 21-25%.
- Fixing the total LHS capacity of the m-PCM system, the individual capacities are varied in different ratios by varying the volumes (or lengths) of different PCM blocks. Optimizing the PCM volume ratio and implementing non-uniform fin distribution leads to a reduction in the charging and discharging times than the single PCM system by 30% and 9%, respectively.

8.3 Future scope

The studies conducted in the present thesis work provide several prospects and practical implications that can extend the research work to future possibilities. Based on the research objectives fulfilled, the following points are considered for exploration in the future;

- Combining different sensible and latent heat storage modules with higher storage temperatures in series and parallel configurations and test the thermal performance of high-capacity hybrid thermal energy storage systems.
- The heat transfer rates during charging and discharging processes in the multi-tube LHS module were high only up to partial melting and solidification conditions. Therefore, heat transfer enhancement techniques such as modifying the shell geometry can be explored further to obtain uniform melting and solidification throughout the LHS module.
- The developed PCM encapsulation designs and their improvements can be implemented to real-time thermal energy storage systems.

- Comparison of the performance of conical and cylindrical shell LHS systems through experimental investigations can be considered in the future. Further, numerical investigations can also be conducted to extend the design improvements to multi-tube high capacity storage systems.
- The performance improvements in conventional single and multi-PCM LHS systems will be explored and the fabrication of the developed non-uniform fin arrangement systems is presently in progress.

References

Ã–zisik MN, Özışık MN, 1993. Heat conduction. John Wiley & Sons, Ltd.

Ã, A.F.R., Solanki, S.C., Saini, J.S., 2008. Heat transfer characteristics of thermal energy storage system using PCM capsules : A review 12, 2438–2458. https://doi.org/10.1016/j.rser.2007.06.009

Abdulateef, A.M., Abdulateef, J., Mat, S., Sopian, K., Elhub, B., Mussa, M.A., 2018a. Experimental and numerical study of solidifying phase-change material in a triplex-tube heat exchanger with longitudinal/triangular fins. Int. Commun. Heat Mass Transf. 90, 73–84. https://doi.org/10.1016/j.icheatmasstransfer.2017.10.003

Abdulateef, A.M., Mat, S., Abdulateef, J., Sopian, K., Al-Abidi, A.A., 2018b. Geometric and design parameters of fins employed for enhancing thermal energy storage systems: a review. Renew. Sustain. Energy Rev. 82, 1620–1635. https://doi.org/10.1016/j.rser.2017.07.009

Abdulateef, A.M., Mat, S., Sopian, K., Abdulateef, J., Gitan, A.A., 2017. Experimental and computational study of melting phase-change material in a triplex tube heat exchanger with longitudinal/triangular fins. Sol. Energy 155, 142–153. https://doi.org/10.1016/j.solener.2017.06.024

Abhat, A., 1983. Low temperature latent heat thermal energy storage: Heat storage materials. Sol. Energy 30, 313–332. https://doi.org/10.1016/0038-092X(83)90186-X

Acar, C., Dincer, I., 2019. Better thermal management options with heat storage systems for various applications: An Evaluation. Energy Storage 1, e47. https://doi.org/10.1002/est2.47

Achkari, O., El Fadar, A., 2020. Latest developments on TES and CSP technologies – Energy and environmental issues, applications and research trends. Appl. Therm. Eng. 167, 114806. https://doi.org/10.1016/j.applthermaleng.2019.114806

Agyenim, F., Eames, P., Smyth, M., 2010a. Heat transfer enhancement in medium temperature thermal energy storage system using a multitube heat transfer array. Renew. Energy 35, 198–207. https://doi.org/10.1016/j.renene.2009.03.010

Agyenim, F., Hewitt, N., Eames, P., Smyth, M., 2010b. A review of materials, heat transfer and phase change problem formulation for latent heat thermal energy storage systems (LHTESS). Renew. Sustain. Energy Rev. 14, 615–628. https://doi.org/10.1016/j.rser.2009.10.015

Ahmadi, R., Hosseini, M.J., Ranjbar, A.A., Bahrampoury, R., 2018. Phase change in spiral coil heat storage systems. Sustain. Cities Soc. 38, 145–157. https://doi.org/10.1016/j.scs.2017.12.026

Ahuja, E., Smith, M., 2016. Energy Change - Insights from the 1st and 2nd Industrial Revolutions and Recent Developments to help achieve the next Low Carbon Industrial Revolution. https://doi.org/10.13140/RG.2.1.4022.4249

Al-Abidi, A.A., Bin Mat, S., Sopian, K., Sulaiman, M.Y., Mohammed, A.T., 2013. CFD applications for latent heat thermal energy storage: A review. Renew. Sustain. Energy

Rev. 20, 353–363. https://doi.org/10.1016/j.rser.2012.11.079

Al-Saadi, S.N., Zhai, Z., 2013. Modeling phase change materials embedded in building enclosure: A review. Renew. Sustain. Energy Rev. 21, 659–673. https://doi.org/10.1016/j.rser.2013.01.024

Alam, T.E., Dhau, J., Goswami, D.Y., Rahman, M.M., Stefankos, E., 2014. Experimental Investigation of a Packed-Bed Latent Heat Thermal. ASME 2014 Int. Mech. Eng. Congr. Expo. IMECE2014 1–6.

Alam, T.E., Dhau, J.S., Goswami, D.Y., Stefanakos, E., 2015. Macroencapsulation and characterization of phase change materials for latent heat thermal energy storage systems. Appl. Energy 154, 92–101. https://doi.org/10.1016/j.apenergy.2015.04.086

Aldoss, T.K., Rahman, M.M., 2014. Comparison between the single-PCM and multi-PCM thermal energy storage design. Energy Convers. Manag. 83, 79–87. https://doi.org/10.1016/j.enconman.2014.03.047

Alizadeh, M., Hosseinzadeh, K., Shahavi, M.H., Ganji, D.D., 2019. Solidification acceleration in a triplex-tube latent heat thermal energy storage system using V-shaped fin and nano-enhanced phase change material. Appl. Therm. Eng. 163, 114436. https://doi.org/10.1016/j.applthermaleng.2019.114436

Aly, K.A., El-Lathy, A.R., Fouad, M.A., 2019. Enhancement of solidification rate of latent heat thermal energy storage using corrugated fins. J. Energy Storage 24, 100785. https://doi.org/10.1016/j.est.2019.100785

Anisur, M.R., Mahfuz, M.H., Kibria, M.A., Saidur, R., Metselaar, I.H.S.C., Mahlia, T.M.I., 2013. Curbing global warming with phase change materials for energy storage. Renew. Sustain. Energy Rev. 18, 23–30. https://doi.org/10.1016/j.rser.2012.10.014

Archibold, A.R., Rahman, M.M., Goswami, D.Y., Stefanakos, E.L., 2014. High temperature latent-heat thermal energy storage module with enhanced combined mode heat transfer. Proc. ASME 2014 Int. Mech. Eng. Congr. Expo. 1–10.

Archibold, A.R., Yogi Goswami, D., Rahman, M.M., Stefanakos, E.K., 2015. Multi-mode heat transfer analysis during freezing of an encapsulated storage medium. Int. J. Heat Mass Transf. 84, 600–609. https://doi.org/10.1016/j.ijheatmasstransfer.2014.12.076

Avci, M., Yazici, M.Y., 2013. Experimental study of thermal energy storage characteristics of a paraffin in a horizontal tube-in-shell storage unit 73, 271–277. https://doi.org/10.1016/j.enconman.2013.04.030

Bains, P.S., Singh, H., 2018. Exploratory investigation of a new thermal energy storage system with different phase change materials having distinct melting temperatures. J. Energy Storage 19, 1–9. https://doi.org/10.1016/j.est.2018.07.002

Baker, J., 2008. New technology and possible advances in energy storage. Energy Policy 36, 4368–4373. https://doi.org/10.1016/j.enpol.2008.09.040

Bal, L.M., Satya, S., Naik, S.N., Meda, V., 2011. Review of solar dryers with latent heat storage systems for agricultural products. Renew. Sustain. Energy Rev. 15, 876–880. https://doi.org/10.1016/j.rser.2010.09.006

Bareiss, M., Beer, H., 1984. An analytical solution of the heat transfer process during melting of an unfixed solid phase change material inside a horizontal tube. Int. J. Heat Mass

Transf. 27, 739–746. https://doi.org/10.1016/0017-9310(84)90143-1

Barlev, D., Vidu, R., Stroeve, P., 2011. Innovation in concentrated solar power. Sol. Energy Mater. Sol. Cells 95, 2703–2725. https://doi.org/10.1016/j.solmat.2011.05.020

Bayón, R., Rojas, E., Valenzuela, L., Zarza, E., León, J., 2010. Analysis of the experimental behaviour of a 100 kWth latent heat storage system for direct steam generation in solar thermal power plants. Appl. Therm. Eng. 30, 2643–2651. https://doi.org/10.1016/j.applthermaleng.2010.07.011

Behar, O., Khellaf, A., Mohammedi, K., 2013. A review of studies on central receiver solar thermal power plants. Renew. Sustain. Energy Rev. 23, 12–39. https://doi.org/10.1016/j.rser.2013.02.017

Bellan, S., Alam, T.E., González-Aguilar, J., Romero, M., Rahman, M.M., Goswami, D.Y., Stefanakos, E.K., 2015. Numerical and experimental studies on heat transfer characteristics of thermal energy storage system packed with molten salt PCM capsules. Appl. Therm. Eng. 90, 970–979. https://doi.org/10.1016/j.applthermaleng.2015.07.056

Bénard, C., Gobin, D., Martinez, F., 1985. Melting in rectangular enclosures: Experiments and numerical simulations. J. Heat Transfer 107, 794–803. https://doi.org/10.1115/1.3247506

Bijarniya, J.P., Sudhakar, K., Baredar, P., 2016. Concentrated solar power technology in India: A review. Renew. Sustain. Energy Rev. 63, 593–603. https://doi.org/10.1016/j.rser.2016.05.064

Bland, A., Khzouz, M., Statheros, T., Gkanas, E.I., 2017. PCMs for residential building applications: A short review focused on disadvantages and proposals for future development. Buildings 7. https://doi.org/10.3390/buildings7030078

Bonacina, C., Comini, G., Fasano, A., Primicerio, M., 1973. Numerical solution of phase-change problems. Int. J. Heat Mass Transf. 16, 1825–1832. https://doi.org/10.1016/0017-9310(73)90202-0

Brent, A.D., Voller, V.R., Reid, K.J., 1988. Enthalpy-porosity technique for modeling convection-diffusion phase change: Application to the melting of a pure metal. Numer. Heat Transf. 13, 297–318. https://doi.org/10.1080/10407788808913615

Cabeza, L.F., Illa, J., Roca, J., Badia, F., Mehling, H., Hiebler, S., Ziegler, F., 2001. Immersion corrosion tests on metal-salt hydrate pairs used for latent heat storage in the 32 to 36 C temperature range. Werkstoffe und Korrosion 52, 140–146. https://doi.org/10.1002/1521-4176(200102)52:2<140::AID-MACO140>3.0.CO;2-R

Cao, X., Yuan, Y., Xiang, B., Highlight, F., 2018. Effect of natural convection on melting performance of eccentric horizontal shell and tube latent heat storage unit. Sustain. Cities Soc. 38, 571–581. https://doi.org/10.1016/j.scs.2018.01.025

Cerón, I., Neila, J., Khayet, M., 2011. Experimental tile with phase change materials (PCM) for building use. Energy Build. 43, 1869–1874. https://doi.org/10.1016/j.enbuild.2011.03.031

Charriau, P., Lapillonne, B., Crenes, M., 2020. Global Energy Trends 2020 Edition.

Chen, Y.J., Nguyen, D.D., Shen, M.Y., Yip, M.C., Tai, N.H., 2013. Thermal characterizations of the graphite nanosheets reinforced paraffin phase-change composites. Compos. Part A Appl. Sci. Manuf. 44, 40–46. https://doi.org/10.1016/j.compositesa.2012.08.010

Cheng, J., Zhou, Y., Ma, D., Li, S., Zhang, F., Guan, Y., Qu, W., Jin, Y., Wang, D., 2020. Preparation and characterization of carbon nanotube microcapsule phase change materials for improving thermal comfort level of buildings. Constr. Build. Mater. 244, 118388. https://doi.org/10.1016/j.conbuildmat.2020.118388

Cheng, X., Zhai, X., 2018. Thermal performance analysis of a cascaded cold storage unit using multiple PCMs. Energy 143, 448–457. https://doi.org/10.1016/j.energy.2017.11.009

Chiu, J.N.W., Martin, V., 2013. Multistage latent heat cold thermal energy storage design analysis. Appl. Energy 112, 1438–1445. https://doi.org/10.1016/j.apenergy.2013.01.054

Chung, T.J., 2018. Computational Fluid Dynamics, Nihon Bika Gakkai Kaishi (Japanese Journal of Rhinology). https://doi.org/10.7248/jjrhi.57.79

Comité Internacional De La Cruz Roja (CRIC), 2007. Informe anual 2007. Colombia.

COMSOL Inc., www.comsol.com

Conference, I., Storage, T.E., 2009. The 11th International Conference on Thermal Energy Storage – Effstock 14-17 June 2009 in Stockholm, Sweden 1–8.

Copernicus, 2021. 2020 warmest year on record for Europe; globally, 2020 ties with 2016 for warmest year recorded. Copernicus - Eur. Union’s Earth Obs. Program.

Crespo, A., Barreneche, C., Ibarra, M., Platzer, W., 2018. Latent thermal energy storage for solar process heat applications at medium-high temperatures – A review. Sol. Energy 1–32. https://doi.org/10.1016/j.solener.2018.06.101

CSH India, 1999. Steam Cooking System for 10000 people using Scheffler Dishes at Shantivan, Brahma Kumaris, Mount Abu 2, 2.

Cui, H., Yuan, X., Hou, X., 2003. Thermal performance analysis for a heat receiver using multiple phase change materials. Appl. Therm. Eng. 23, 2353–2361. https://doi.org/10.1016/S1359-4311(03)00210-2

Delgado, M., Lázaro, A., Mazo, J., Zalba, B., 2012. Review on phase change material emulsions and microencapsulated phase change material slurries: Materials, heat transfer studies and applications. Renew. Sustain. Energy Rev. 16, 253–273. https://doi.org/10.1016/j.rser.2011.07.152

Demuren, A., Grotjans, H., 2009. Buoyancy-driven flowsbeyond the boussinesq approximation. Numer. Heat Transf. Part B Fundam. 56, 1–22. https://doi.org/10.1080/10407790902970080

Deng, Y., Feng, C., E, J., Zhu, H., Chen, J., Wen, M., Yin, H., 2018. Effects of different coolants and cooling strategies on the cooling performance of the power lithium ion battery system: A review. Appl. Therm. Eng. 142, 10–29. https://doi.org/10.1016/j.applthermaleng.2018.06.043

Dhaidan, N.S., Khodadadi, J.M., 2015. Melting and convection of phase change materials in different shape containers: A review. Renew. Sustain. Energy Rev. 43, 449–477. https://doi.org/10.1016/j.rser.2014.11.017

Dickinson, R.M., Cruickshank, C.A., Harrison, S.J., 2013. Charge and discharge strategies for a multi-tank thermal energy storage. Appl. Energy 109, 366–373. https://doi.org/10.1016/j.apenergy.2012.11.032

Dugaria, S., Padovan, A., Sabatelli, V., Del Col, D., 2015. Assessment of estimation methods of DNI resource in solar concentrating systems. Sol. Energy 121, 103–115. https://doi.org/10.1016/j.solener.2015.07.043

Dutil, Y., Rousse, D.R., Salah, N. Ben, Lassue, S., Zalewski, L., 2011. A review on phase-change materials: Mathematical modeling and simulations. Renew. Sustain. Energy Rev. 15, 112–130. https://doi.org/10.1016/j.rser.2010.06.011

Elfeky, K.E., Ahmed, N., Wang, Q., 2018. Numerical comparison between single PCM and multi-stage PCM based high temperature thermal energy storage for CSP tower plants. Appl. Therm. Eng. 139, 609–622. https://doi.org/10.1016/j.applthermaleng.2018.04.122

Elmozughi, A.F., Solomon, L., Oztekin, A., Neti, S., 2014. Encapsulated phase change material for high temperature thermal energy storage - Heat transfer analysis. Int. J. Heat Mass Transf. 78, 1135–1144. https://doi.org/10.1016/j.ijheatmasstransfer.2014.07.087

EPA, 2020. Levelized Cost and Levelized Avoided Cost of New Generation Resources in the Annual Energy Outlook 2020. Us Eia Lcoe 1–20.

Esapour, M., Hosseini, M.J., Ranjbar, A.A., Pahamli, Y., Bahrampoury, R., 2016. Phase change in multi-tube heat exchangers. Renew. Energy 85, 1017–1025. https://doi.org/10.1016/j.renene.2015.07.063

Esen, M., Durmuş, Aydin, Durmuş, Ayla, 1998. Geometric design of solar-aided latent heat store depending on various parameters and phase change materials. Sol. Energy 62, 19–28. https://doi.org/10.1016/S0038-092X(97)00104-7

Espinosa-Rueda, G., Navarro Hermoso, J.L., Martínez-Sanz, N., Gallas-Torreira, M., 2016. Vacuum evaluation of parabolic trough receiver tubes in a 50 MW concentrated solar power plant. Sol. Energy 139, 36–46. https://doi.org/10.1016/j.solener.2016.09.017

Fang, X., Ding, Q., Li, L.Y., Moon, K.S., Wong, C.P., Yu, Z.T., 2015. Tunable thermal conduction character of graphite-nanosheets-enhanced composite phase change materials via cooling rate control. Energy Convers. Manag. 103, 251–258. https://doi.org/10.1016/j.enconman.2015.06.062

Farid, M.M., Kim, Y., Kansawa, A., 1990. Thermal performance of a heat storage module using PCM's with different melting temperature: Experimental. J. Sol. Energy Eng. Trans. ASME 112, 125–131. https://doi.org/10.1115/1.2929644

Farmer, G.T., Cook, J., 2013. Climate Change Science: A Modern Synthesis, Climate Change Science: A Modern Synthesis. https://doi.org/10.1007/978-94-007-5757-8

Farrell, A.J., Norton, B., Kennedy, D.M., 2006. Corrosive effects of salt hydrate phase change materials used with aluminium and copper. J. Mater. Process. Technol. 175, 198–205. https://doi.org/10.1016/j.jmatprotec.2005.04.058

Frank Kreith, Raj M. Manglik, M.S.B., 2011. Principles of Heat Transfer Seventh Edition, Handbook of Phase Change: Boiling and Condensation.

Frazzica, A., Manzan, M., Sapienza, A., Freni, A., Toniato, G., Restuccia, G., 2016. Experimental testing of a hybrid sensible-latent heat storage system for domestic hot water applications. Appl. Energy 183, 1157–1167. https://doi.org/10.1016/j.apenergy.2016.09.076

Fuqiang, W., Zhennan, G., Jianyu, T., Lanxin, M., Zhenyu, Y., Heping, T., 2016. Transient thermal performance response characteristics of porous-medium receiver heated by multi-dish concentrator. Int. Commun. Heat Mass Transf. 75, 36–41. https://doi.org/10.1016/j.icheatmasstransfer.2016.03.028

Gao, L., Gegentana, Liu, Z., Sun, B., Che, D., Li, S., 2020. Multi-objective optimization of thermal performance of packed bed latent heat thermal storage system based on response surface method. Renew. Energy 153, 669–680. https://doi.org/10.1016/j.renene.2020.01.157

Gasia, J., Maldonado, J.M., Galati, F., De Simone, M., Cabeza, L.F., 2019. Experimental evaluation of the use of fins and metal wool as heat transfer enhancement techniques in a latent heat thermal energy storage system. Energy Convers. Manag. 184, 530–538. https://doi.org/10.1016/j.enconman.2019.01.085

Gil, A., Medrano, M., Martorell, I., Lázaro, A., Dolado, P., Zalba, B., Cabeza, L.F., 2010. State of the art on high temperature thermal energy storage for power generation. Part 1-Concepts, materials and modellization. Renew. Sustain. Energy Rev. 14, 31–55. https://doi.org/10.1016/j.rser.2009.07.035

Goldstein, R.J., Ibele, W.E., Patankar, S. V, Simon, T.W., Strykowski, P.J., Tamma, K.K., Kuehn, T.H., Heberlein, J.V.R., Hofeldt, D.L., Davidson, J.H., Bischof, J., Kulacki, F., Lane, H., Congress, A., Depart-, M.E., 1997. Heat transfer - a review of 1994 literature. Heat Mass Transf. 40, 3729–3804. https://doi.org/10.1016/0017-9310(94)90183-X

Gong, Z.-X., Mujumdar, A.S., 1997. Thermodynamic optimization of the thermal process in energy storage using multiple phase change materials. Appl. Therm. Eng. 17, 1067–1083. https://doi.org/10.1016/S1359-4311(97)00012-4

González-Roubaud, E., Pérez-Osorio, D., Prieto, C., 2017. Review of commercial thermal energy storage in concentrated solar power plants: Steam vs. molten salts. Renew. Sustain. Energy Rev. 80, 133–148. https://doi.org/10.1016/j.rser.2017.05.084

GÜREL, B., 2020. A numerical investigation of the melting heat transfer characteristics of phase change materials in different plate heat exchanger (latent heat thermal energy storage) systems. Int. J. Heat Mass Transf. 148. https://doi.org/10.1016/j.ijheatmasstransfer.2019.119117

Haller, M.Y., Cruickshank, C.A., Streicher, W., Harrison, S.J., Andersen, E., Furbo, S., 2009. Methods to determine stratification efficiency of thermal energy storage processes - Review and theoretical comparison. Sol. Energy 83, 1847–1860. https://doi.org/10.1016/j.solener.2009.06.019

Hamdan, M.A., Al-Hinti, I., 2004. Analysis of heat transfer during the melting of a phase-change material. Appl. Therm. Eng. 24, 1935–1944. https://doi.org/10.1016/j.applthermaleng.2003.12.008

Hariharan, K., Kumar, G.S.S., Kumaresan, G., Velraj, R., 2018. Investigation on Phase Change Behavior of Paraffin Phase Change Material in a Spherical Capsule for Solar Thermal Storage Units. Heat Transf. Eng. 39, 775–783. https://doi.org/10.1080/01457632.2017.1341227

He, M., Yang, L., Lin, W., Chen, J., Mao, X., Ma, Z., 2019. Preparation, thermal characterization and examination of phase change materials (PCMs) enhanced by carbon-based nanoparticles for solar thermal energy storage. J. Energy Storage 25, 100874. https://doi.org/10.1016/j.est.2019.100874

Herrmann, U., Geyer, M., 2002. The AndaSol Project.

Herrmann, U., Kearney, D.W., 2002. Survey of Thermal Energy Storage for Parabolic Trough Power Plants. J. Sol. Energy Eng. 124, 145. https://doi.org/10.1115/1.1467601

Herrmann, U., Kelly, B., Price, H., 2004. Two-tank molten salt storage for parabolic trough solar power plants. Energy 29, 883–893. https://doi.org/10.1016/S0360-5442(03)00193-2

Hong, S.W., Lee, Y.T., Chung, J.D., 2015. Restrictions on the analytic approach of unconstrained melting inside a spherical capsule. J. Mech. Sci. Technol. 29, 5035–5042. https://doi.org/10.1007/s12206-015-1052-7

Hosseini, M.J., Ranjbar, A.A., Rahimi, M., Bahrampoury, R., 2015. Experimental and numerical evaluation of longitudinally finned latent heat thermal storage systems. Energy Build. 99, 263–272. https://doi.org/10.1016/j.enbuild.2015.04.045

Hosseinizadeh, S.F., Rabienataj Darzi, A.A., Tan, F.L., Khodadadi, J.M., 2013. Unconstrained melting inside a sphere. Int. J. Therm. Sci. 63, 55–64. https://doi.org/10.1016/j.ijthermalsci.2012.07.012

Hosseinzadeh, K., Moghaddam, M.A.E., Asadi, A., Mogharrebi, A.R., Ganji, D.D., 2020. Effect of internal fins along with Hybrid Nano-Particles on solid process in star shape triplex Latent Heat Thermal Energy Storage System by numerical simulation. Renew. Energy 154, 497–507. https://doi.org/10.1016/j.renene.2020.03.054

Hu, X., Zhu, F., Gong, X., 2019. Experimental and numerical study on the thermal behavior of phase change material infiltrated in low porosity metal foam. J. Energy Storage 26, 101005. https://doi.org/10.1016/j.est.2019.101005

Huang, X., Zhu, C., Lin, Y., Fang, G., 2019. Thermal properties and applications of microencapsulated PCM for thermal energy storage: A review. Appl. Therm. Eng. 147, 841–855. https://doi.org/10.1016/j.applthermaleng.2018.11.007

Inagaki, M., Kaburagi, Y., Hishiyama, Y., 2014. Thermal management material: Graphite. Adv. Eng. Mater. 16, 494–506. https://doi.org/10.1002/adem.201300418

Incropera, F.P., Dewitt, D.P., Bergman, T.L., Lavine, A.S., 2007. Fundamentals of Heat and Mass Transfer, 6th ed. John Wiley & Sons.

Informe anual 2006 -Plataforma Solar de Almeria, 2006.

International Energy Agency [IEA], India 2020 Policy Energy Review.

International Energy Agency, https://www.iea.org/

International Renewable Energy Agency, 2020. Renewable Energy Statistics 2020.

International Renewable Energy Agency - IRENA, 2019. Future of solar photovoltaic:Deployment, investment, technology, grid integration and socio-economic aspects, Irena.

Iradukunda, A.C., Huitink, D.R., Luo, F., 2020. A review of advanced thermal management solutions and the implications for integration in high-voltage packages. IEEE J. Emerg. Sel. Top. Power Electron. 8, 256–271. https://doi.org/10.1109/JESTPE.2019.2953102

Islam, M.T., Huda, N., Abdullah, A.B., Saidur, R., 2018. A comprehensive review of state-of-the-art concentrating solar power (CSP) technologies: Current status and research trends. Renew. Sustain. Energy Rev. 91, 987–1018. https://doi.org/10.1016/j.rser.2018.04.097

Jegadheeswaran, S., Pohekar, S.D., 2009. Performance enhancement in latent heat thermal storage system: A review. Renew. Sustain. Energy Rev. 13, 2225–2244. https://doi.org/10.1016/j.rser.2009.06.024

Jin, H.Q., Fan, L.W., Liu, M.J., Zhu, Z.Q., Yu, Z.T., 2017. A pore-scale visualized study of melting heat transfer of a paraffin wax saturated in a copper foam: Effects of the pore size. Int. J. Heat Mass Transf. 112, 39–44. https://doi.org/10.1016/j.ijheatmasstransfer.2017.04.114

Joseph, M., Sajith, V., 2019. Graphene enhanced paraffin nanocomposite based hybrid cooling system for thermal management of electronics. Appl. Therm. Eng. 163, 114342. https://doi.org/10.1016/j.applthermaleng.2019.114342

Joshi, V., Rathod, M.K., 2020. Experimental and numerical assessments of thermal transport in fins and metal foam infused latent heat thermal energy storage systems : A comparative evaluation. Appl. Therm. Eng. 178, 115518. https://doi.org/10.1016/j.applthermaleng.2020.115518

Ju, X., Xu, C., Hu, Y., Han, X., Wei, G., Du, X., 2017. A review on the development of photovoltaic/concentrated solar power (PV-CSP) hybrid systems. Sol. Energy Mater. Sol. Cells 161, 305–327. https://doi.org/10.1016/j.solmat.2016.12.004

Jurkowska, M., Szczygieł, I., 2016. Review on properties of microencapsulated phase change materials slurries (mPCMS). Appl. Therm. Eng. 98, 365–373. https://doi.org/10.1016/j.applthermaleng.2015.12.051

Kabbara, M., Groulx, D., Joseph, A., 2018. A parametric experimental investigation of the heat transfer in a coil-in-tank latent heat energy storage system. Int. J. Therm. Sci. 130, 395–405. https://doi.org/10.1016/j.ijthermalsci.2018.05.006

Kabbara, M., Groulx, D., Joseph, A., 2016. Experimental investigations of a latent heat energy storage unit using finned tubes. Appl. Therm. Eng. 101, 601–611. https://doi.org/10.1016/j.applthermaleng.2015.12.080

Kalapala, L., Devanuri, J.K., 2020. Energy and exergy analyses of latent heat storage unit positioned at different orientations – An experimental study. Energy 194, 116924. https://doi.org/10.1016/j.energy.2020.116924

Karami, R., Kamkari, B., 2020. Experimental investigation of the effect of perforated fins on thermal performance enhancement of vertical shell and tube latent heat energy storage systems. Energy Convers. Manag. 210, 112679. https://doi.org/10.1016/j.enconman.2020.112679

Kazemi, M., Hosseini, M.J., Ranjbar, A.A., Bahrampoury, R., 2018. Improvement of longitudinal fins configuration in latent heat storage systems. Renew. Energy 116, 447–457. https://doi.org/10.1016/j.renene.2017.10.006

Kelvii Wei Guo, 2011. Green nanotechnology of trends in future energy: a review. Int. J. energy Res. 36, 1–17. https://doi.org/10.1002/er.1928

Kenisarin, M., Mahkamov, K., 2016. Salt hydrates as latent heat storage materials:Thermophysical properties and costs. Sol. Energy Mater. Sol. Cells 145, 255–286. https://doi.org/10.1016/j.solmat.2015.10.029

Khalifa, A., Tan, L., Date, A., Akbarzadeh, A., 2014. A numerical and experimental study of solidification around axially finned heat pipes for high temperature latent heat thermal energy storage units. Appl. Therm. Eng. 70, 609–619. https://doi.org/10.1016/j.applthermaleng.2014.05.080

Khan, M.R., Swierczynski, M.J., Kær, S.K., 2017. Towards an ultimate battery thermal management system: A review. Batteries 3. https://doi.org/10.3390/batteries3010009

Khan, Z., Khan, Z.A., 2020. Role of extended fins and graphene nano-platelets in coupled thermal enhancement of latent heat storage system. Energy Convers. Manag. 224, 113349. https://doi.org/10.1016/j.enconman.2020.113349

Khan, Zakir, Khan, Zulfiqar, Ghafoor, A., 2016. A review of performance enhancement of PCM based latent heat storage system within the context of materials, thermal stability and compatibility. Energy Convers. Manag. 115, 132–158. https://doi.org/10.1016/j.enconman.2016.02.045

Koohi-Fayegh, S., Rosen, M.A., 2020. A review of energy storage types, applications and recent developments. J. Energy Storage 27, 101047. https://doi.org/10.1016/j.est.2019.101047

Korti, A.I.N., Tlemsani, F.Z., 2016. Experimental investigation of latent heat storage in a coil in PCM storage unit. J. Energy Storage 5, 177–186. https://doi.org/10.1016/j.est.2015.12.010

Koukou, M.K., Vrachopoulos, M.G., Tachos, N.S., Dogkas, G., Lymperis, K., Stathopoulos, V., 2018. Experimental and computational investigation of a latent heat energy storage system with a staggered heat exchanger for various phase change materials. Therm. Sci. Eng. Prog. 7, 87–98. https://doi.org/10.1016/j.tsep.2018.05.004

Krishna, J., Kishore, P.S., Solomon, A.B., 2017. Heat pipe with nano enhanced-PCM for electronic cooling application. Exp. Therm. Fluid Sci. 81, 84–92. https://doi.org/10.1016/j.expthermflusci.2016.10.014

Kumar, A., Prakash, O., Dube, A., 2017. A review on progress of concentrated solar power in India. Renew. Sustain. Energy Rev. 79, 304–307. https://doi.org/10.1016/j.rser.2017.05.086

Kumar, M., Krishna, D.J., 2017. Influence of Mushy Zone Constant on Thermohydraulics of a PCM. Energy Procedia 109, 314–321. https://doi.org/10.1016/j.egypro.2017.03.074

Kuravi, S., Trahan, J., Goswami, D.Y., Rahman, M.M., Stefanakos, E.K., 2013. Thermal energy storage technologies and systems for concentrating solar power plants. Prog. Energy Combust. Sci. 39, 285–319. https://doi.org/10.1016/j.pecs.2013.02.001

Kurnia, J.C., Sasmito, A.P., Jangam, S. V., Mujumdar, A.S., 2013. Improved design for heat transfer performance of a novel phase change material (PCM) thermal energy storage (TES). Appl. Therm. Eng. 50, 896–907. https://doi.org/10.1016/j.applthermaleng.2012.08.015

Kuznik, F., David, D., Johannes, K., Roux, J.J., 2011. A review on phase change materials integrated in building walls. Renew. Sustain. Energy Rev. 15, 379–391. https://doi.org/10.1016/j.rser.2010.08.019

Laing, D., Bahl, C., Bauer, T., Lehmann, D., Steinmann, W.D., 2011. Thermal energy storage for direct steam generation. Sol. Energy 85, 627–633.

https://doi.org/10.1016/j.solener.2010.08.015

Lakshmi Narasimhan N, 2019. Assessment of latent heat thermal storage systems operating with multiple phase change materials. J. Energy Storage 23, 442–455. https://doi.org/10.1016/j.est.2019.04.008

Lanahan, M., Tabares-Velasco, P.C., 2017. Seasonal thermal-energy storage: A critical review on BTES systems, modeling, and system design for higher system efficiency. Energies 10. https://doi.org/10.3390/en10060743

Leong, K.Y., Abdul Rahman, M.R., Gurunathan, B.A., 2019. Nano-enhanced phase change materials: A review of thermo-physical properties, applications and challenges. J. Energy Storage 21, 18–31. https://doi.org/10.1016/j.est.2018.11.008

Li, M.J., Jin, B., Ma, Z., Yuan, F., 2018. Experimental and numerical study on the performance of a new high-temperature packed-bed thermal energy storage system with macroencapsulation of molten salt phase change material. Appl. Energy 221, 1–15. https://doi.org/10.1016/j.apenergy.2018.03.156

Li, Q., Li, C., Du, Z., Jiang, F., Ding, Y., 2019. A review of performance investigation and enhancement of shell and tube thermal energy storage device containing molten salt based phase change materials for medium and high temperature applications. Appl. Energy 255. https://doi.org/10.1016/j.apenergy.2019.113806

Li, X.Y., Yang, L., Wang, X.L., Miao, X.Y., Yao, Y., Qiang, Q.Q., 2018. Investigation on the charging process of a multi-PCM latent heat thermal energy storage unit for use in conventional air-conditioning systems. Energy 150, 591–600. https://doi.org/10.1016/j.energy.2018.02.107

Liang, H., You, S., Zhang, H., 2015. Comparison of different heat transfer models for parabolic trough solar collectors. Appl. Energy 148, 105–114. https://doi.org/10.1016/j.apenergy.2015.03.059

Lim, C.S.L., Weaver, R., Sobhansarbandi, S., 2019. Heat transfer enhancement of phase change materials for thermal energy storage systems. Am. Soc. Mech. Eng. Power Div. POWER 2019-July, 26–50. https://doi.org/10.1115/power2019-1880

Lin, K., Zhang, Y., Xu, X., Di, H., Yang, R., Qin, P., 2005. Experimental study of under-floor electric heating system with shape-stabilized PCM plates. Energy Build. 37, 215–220. https://doi.org/10.1016/j.enbuild.2004.06.017

Lin, Y., Jia, Y., Alva, G., Fang, G., 2018. Review on thermal conductivity enhancement, thermal properties and applications of phase change materials in thermal energy storage. Renew. Sustain. Energy Rev. 82, 2730–2742. https://doi.org/10.1016/j.rser.2017.10.002

Liu, J., Xu, C., Ju, X., Yang, B., Ren, Y., Du, X., 2017. Numerical investigation on the heat transfer enhancement of a latent heat thermal energy storage system with bundled tube structures. Appl. Therm. Eng. 112, 820–831. https://doi.org/10.1016/j.applthermaleng.2016.10.144

Liu, L., Su, D., Tang, Y., Fang, G., 2016. Thermal conductivity enhancement of phase change materials for thermal energy storage: A review. Renew. Sustain. Energy Rev. 62, 305–317. https://doi.org/10.1016/j.rser.2016.04.057

Liu, M., Saman, W., Bruno, F., 2012. Review on storage materials and thermal performance enhancement techniques for high temperature phase change thermal storage systems.

Renew. Sustain. Energy Rev. 16, 2118–2132. https://doi.org/10.1016/j.rser.2012.01.020

Lomonaco, A., Haillot, D., Pernot, E., Franquet, E., Bédécarrats, J.P., 2016. Sodium nitrate thermal behavior in latent heat thermal energy storage: A study of the impact of sodium nitrite on melting temperature and enthalpy. Sol. Energy Mater. Sol. Cells 149, 81–87. https://doi.org/10.1016/j.solmat.2015.12.043

Longeon, M., Soupart, A., Fourmigué, J.F., Bruch, A., Marty, P., 2013. Experimental and numerical study of annular PCM storage in the presence of natural convection. Appl. Energy 112, 175–184. https://doi.org/10.1016/j.apenergy.2013.06.007

Lv, Y., Zhou, W., Jin, W., 2016. Experimental and numerical study on thermal energy storage of polyethylene glycol/expanded graphite composite phase change material. Energy Build. 111, 242–252. https://doi.org/10.1016/j.enbuild.2015.11.042

Madaeni, S.H., Sioshansi, R., Denholm, P., 2012. Capacity value of concentrating solar power plants. Conc. Sol. Power Data Dir. an Emerg. Sol. Technol. 149–186.

Mahdi, J.M., Lohrasbi, S., Nsofor, E.C., 2019. Hybrid heat transfer enhancement for latent-heat thermal energy storage systems: A review. Int. J. Heat Mass Transf. 137, 630–649. https://doi.org/10.1016/j.ijheatmasstransfer.2019.03.111

Mahdi, J.M., Nsofor, E.C., 2018. Solidification enhancement of PCM in a triplex-tube thermal energy storage system with nanoparticles and fins. Appl. Energy 211, 975–986. https://doi.org/10.1016/j.apenergy.2017.11.082

Mahdi, M.S., Mahood, H.B., Campbell, A.N., Khadom, A.A., 2020. Experimental study on the melting behavior of a phase change material in a conical coil latent heat thermal energy storage unit. Appl. Therm. Eng. 175, 114684. https://doi.org/10.1016/j.applthermaleng.2019.114684

Mantilla Gilart, P., Yedra Martínez, Á., González Barriuso, M., Manteca Martínez, C., 2012. Development of PCM/carbon-based composite materials. Sol. Energy Mater. Sol. Cells 107, 205–211. https://doi.org/10.1016/j.solmat.2012.06.014

Mark Mehos, C.T., Jorgenson, J., , Paul Denholm, C.H., Armijo, and K., 2016. Advancing Concentrating Solar Power Technology, Performance, and Dispatchability. Natl. Renew. Energy Lab. 1–66. https://doi.org/2016-2237 R

Mastani, M., Seddegh, S., Wang, X., Haghighat, F., 2019. Experimental investigation of multiple tube heat transfer enhancement in a vertical cylindrical latent heat thermal energy storage system. Renew. Energy 140, 234–244. https://doi.org/10.1016/j.renene.2019.03.037

Mat, S., Al-Abidi, A.A., Sopian, K., Sulaiman, M.Y., Mohammad, A.T., 2013. Enhance heat transfer for PCM melting in triplex tube with internal-external fins. Energy Convers. Manag. 74, 223–236. https://doi.org/10.1016/j.enconman.2013.05.003

Medrano, M., Gil, A., Martorell, I., Potau, X., Cabeza, L.F., 2010. State of the art on high-temperature thermal energy storage for power generation. Part 2-Case studies. Renew. Sustain. Energy Rev. 14, 56–72. https://doi.org/10.1016/j.rser.2009.07.036

Mehrali, Mohammad, Latibari, S.T., Mehrali, Mehdi, Metselaar, H.S.C., Silakhori, M., 2013. Shape-stabilized phase change materials with high thermal conductivity based on paraffin/graphene oxide composite. Energy Convers. Manag. 67, 275–282. https://doi.org/10.1016/j.enconman.2012.11.023

Mehta, D.S., Solanki, K., Rathod, M.K., Banerjee, J., 2019. Thermal performance of shell and tube latent heat storage unit: Comparative assessment of horizontal and vertical orientation. J. Energy Storage 23, 344–362. https://doi.org/10.1016/j.est.2019.03.007

Mehta, D.S., Vaghela, B., Rathod, M.K., Banerjee, J., 2020. Thermal performance augmentation in latent heat storage unit using spiral fin: An experimental analysis. J. Energy Storage 31, 101776. https://doi.org/10.1016/j.est.2020.101776

Michels, H., Pitz-Paal, R., 2007. Cascaded latent heat storage for parabolic trough solar power plants. Sol. Energy 81, 829–837. https://doi.org/10.1016/j.solener.2006.09.008

Milián, Y.E., Gutiérrez, A., Grágeda, M., Ushak, S., 2017. A review on encapsulation techniques for inorganic phase change materials and the influence on their thermophysical properties. Renew. Sustain. Energy Rev. 73, 983–999. https://doi.org/10.1016/j.rser.2017.01.159

MNRE, Govt. of India, https://www.mnre.gov.in/

Moffat, R.J., 1988. Describing the uncertainties in experimental results. Exp. Therm. Fluid Sci. 1, 3–17. https://doi.org/10.1016/0894-1777(88)90043-X

Mohamed, S.A., Al-Sulaiman, F.A., Ibrahim, N.I., Zahir, M.H., Al-Ahmed, A., Saidur, R., Yılbaş, B.S., Sahin, A.Z., 2017. A review on current status and challenges of inorganic phase change materials for thermal energy storage systems. Renew. Sustain. Energy Rev. 70, 1072–1089. https://doi.org/10.1016/j.rser.2016.12.012

Mosaffa, A.H., Garousi Farshi, L., Infante Ferreira, C.A., Rosen, M.A., 2014. Energy and exergy evaluation of a multiple-PCM thermal storage unit for free cooling applications. Renew. Energy 68, 452–458. https://doi.org/10.1016/j.renene.2014.02.025

Mostafavi Tehrani, S.S., Shoraka, Y., Nithyanandam, K., Taylor, R.A., 2018. Cyclic performance of cascaded and multi-layered solid-PCM shell-and-tube thermal energy storage systems: A case study of the 19.9 MWe Gemasolar CSP plant. Appl. Energy 228, 240–253. https://doi.org/10.1016/j.apenergy.2018.06.084

Murray, R.E., Groulx, D., 2014. Experimental study of the phase change and energy characteristics inside a cylindrical latent heat energy storage system: Part 1 consecutive charging and discharging. Renew. Energy 62, 571–581. https://doi.org/10.1016/j.renene.2013.08.007

Myers, P.D., Alam, T.E., Kamal, R., Goswami, D.Y., Stefanakos, E., 2016. Nitrate salts doped with CuO nanoparticles for thermal energy storage with improved heat transfer. Appl. Energy 165, 225–233. https://doi.org/10.1016/j.apenergy.2015.11.045

Myers, P.D., Goswami, D.Y., 2016. Thermal energy storage using chloride salts and their eutectics. Appl. Therm. Eng. 109, 889–900. https://doi.org/10.1016/j.applthermaleng.2016.07.046

Myers, P.D., Goswami, D.Y., Bhardwaj, A., Stefanakos, E., 2015. Chloride salt systems for high temperature thermal energy storage: Properties and applications. ASME 2015 9th Int. Conf. Energy Sustain. ES 2015, collocated with ASME 2015 Power Conf. ASME 2015 13th Int. Conf. Fuel Cell Sci. Eng. Technol. ASME 2015 Nucl. Forum 1, 1–10. https://doi.org/10.1115/ES2015-49460

Natural Resources Canada, 2018, n.d. Energy Fact Book 2018/19.

Nazir, H., Batool, M., Bolivar, F.J., Isaza-ruiz, M., Xu, X., Vignarooban, K., Phelan, P., Kannan, A.M., 2019. Recent developments in phase change materials for energy storage applications : A review. Int. J. Heat Mass Transf. 129, 491–523. https://doi.org/10.1016/j.ijheatmasstransfer.2018.09.126

Nepustil, U., Laing-nepustil, D., Lodemann, D., Sivabalan, R., 2016. High Temperature Latent Heat Storage with Direct Electrical Charging – Second Generation Design. Energy Procedia 99, 314–320. https://doi.org/10.1016/j.egypro.2016.10.121

Ng, K.W., Gong, Z.X., Mujumdar, A.S., Group, T.S., Quebec, M., 1998. Heat transfer in free convection-dominated melting of a phase change material in a horizontal annulus. Int. Commun. Heat Mass Transf. 25, 631–640.

Nithyanandam, K., Pitchumani, R., Mathur, A., 2014. Analysis of a latent thermocline storage system with encapsulated phase change materials for concentrating solar power. Appl. Energy 113, 1446–1460. https://doi.org/10.1016/j.apenergy.2013.08.053

Niyas, H., Prasad, S., Muthukumar, P., 2017a. Performance investigation of a lab – scale latent heat storage prototype – Numerical results. Energy Convers. Manag. 135, 188–199. https://doi.org/10.1016/j.enconman.2016.12.075

Niyas, H., Ravi, C., Rao, C., Muthukumar, P., 2017b. Performance investigation of a lab-scale latent heat storage prototype – Experimental results. Sol. Energy 155, 971–984. https://doi.org/10.1016/j.solener.2017.07.044

Nomura, T., Okinaka, N., Akiyama, T., 2010a. Technology of Latent Heat Storage for High Temperature Application: A Review. ISIJ Int. 50, 1229–1239. https://doi.org/10.2355/isijinternational.50.1229

Nomura, T., Okinaka, N., Akiyama, T., 2010b. Waste heat transportation system, using phase change material (PCM) from steelworks to chemical plant. Resour. Conserv. Recycl. 54, 1000–1006. https://doi.org/10.1016/j.resconrec.2010.02.007

Ogoh, W., Groulx, D., 2012. Effects of the heat transfer fluid velocity on the storage characteristics of a cylindrical latent heat energy storage system: a numerical study. Heat Mass Transf. 48, 439–449. https://doi.org/10.1007/s00231-011-0888-3

Pahamli, Y., Hosseini, M.J., Ranjbar, A.A., Bahrampoury, R., 2017. Effect of nanoparticle dispersion and inclination angle on melting of PCM in a shell and tube heat exchanger. J. Taiwan Inst. Chem. Eng. 81, 316–334. https://doi.org/10.1016/j.jtice.2017.09.044

Palacios, A., Barreneche, C., Navarro, M.E., Ding, Y., 2020. Thermal energy storage technologies for concentrated solar power – A review from a materials perspective. Renew. Energy 156, 1244–1265. https://doi.org/10.1016/j.renene.2019.10.127

Palanisamy, M., Niyas, H., 2018. Comparison of Thermal Characteristics of Sensible and Latent Heat Storage Materials Encapsulated in Different Capsule Configurations 11–20. https://doi.org/10.1007/978-981-10-4576-9_2

Palomba, V., Brancato, V., Frazzica, A., 2019. Thermal performance of a latent thermal energy storage for exploitation of renewables and waste heat: An experimental investigation based on an asymmetric plate heat exchanger. Energy Convers. Manag. 200, 112121. https://doi.org/10.1016/j.enconman.2019.112121

Parabolic trough power plants, https://www.mtholyoke.edu

Pasupathy, A., Athanasius, L., Velraj, R., Seeniraj, R. V., 2008. Experimental investigation and numerical simulation analysis on the thermal performance of a building roof incorporating phase change material (PCM) for thermal management. Appl. Therm. Eng. 28, 556–565. https://doi.org/10.1016/j.applthermaleng.2007.04.016

Patel, J.R., Rathod, M.K., 2020. Recent developments in the passive and hybrid thermal management techniques of lithium-ion batteries. J. Power Sources 480, 228820. https://doi.org/10.1016/j.jpowsour.2020.228820

PCM Products, 2020. Global PCM based Building Services Application Examples 1–12.

Peinado Gonzalo, A., Pliego Marugán, A., García Márquez, F.P., 2019. A review of the application performances of concentrated solar power systems. Appl. Energy 255, 113893. https://doi.org/10.1016/j.apenergy.2019.113893

Peiró, G., Gasia, J., Miró, L., Cabeza, L.F., 2015. Experimental evaluation at pilot plant scale of multiple PCMs (cascaded) vs. single PCM configuration for thermal energy storage. Renew. Energy 83, 729–736. https://doi.org/10.1016/j.renene.2015.05.029

Pelay, U., Luo, L., Fan, Y., Stitou, D., Rood, M., 2017. Thermal energy storage systems for concentrated solar power plants. Renew. Sustain. Energy Rev. 79, 82–100. https://doi.org/10.1016/j.rser.2017.03.139

Peng, G., Dou, G., Hu, Y., Sun, Y., Chen, Z., 2020. Phase change material (PCM) microcapsules for thermal energy storage. Adv. Polym. Technol. 2020. https://doi.org/10.1155/2020/9490873

Peng, H., Dong, H., Ling, X., 2014. Thermal investigation of PCM-based high temperature thermal energy storage in packed bed. Energy Convers. Manag. 81, 420–427. https://doi.org/10.1016/j.enconman.2014.02.052

Pereira da Cunha, J., Eames, P., 2016. Thermal energy storage for low and medium temperature applications using phase change materials - A review. Appl. Energy 177, 227–238. https://doi.org/10.1016/j.apenergy.2016.05.097

Pirasaci, T., Goswami, D.Y., 2016. Influence of design on performance of a latent heat storage system for a direct steam generation power plant. Appl. Energy 162, 644–652. https://doi.org/10.1016/j.apenergy.2015.10.105

Pirasaci, T., Wickramaratne, C., Moloney, F., Goswami, D.Y., Stefanakos, E., 2018. Influence of design on performance of a latent heat storage system at high temperatures. Appl. Energy 224, 220–229. https://doi.org/10.1016/j.apenergy.2018.04.122

Pirasaci, T., Wickramaratne, C., Moloney, F., Yogi Goswami, D., Stefanakos, E., 2017. Dynamics of phase change in a vertical PCM capsule in the presence of radiation at high temperatures. Appl. Energy 206, 498–506. https://doi.org/10.1016/j.apenergy.2017.08.187

Pizzolato, A., Sharma, A., Ge, R., Maute, K., Verda, V., Sciacovelli, A., 2020. Maximization of performance in multi-tube latent heat storage – Optimization of fins topology, effect of materials selection and flow arrangements. Energy 203, 114797. https://doi.org/10.1016/j.energy.2019.02.155

Pizzolato, A., Sharma, A., Maute, K., Sciacovelli, A., Verda, V., 2017. Design of effective fins for fast PCM melting and solidification in shell-and-tube latent heat thermal energy storage through topology optimization. Appl. Energy 208, 210–227.

https://doi.org/10.1016/j.apenergy.2017.10.050

Powell, K.M., Rashid, K., Ellingwood, K., Tuttle, J., Iverson, B.D., 2017. Hybrid concentrated solar thermal power systems: A review. Renew. Sustain. Energy Rev. 80, 215–237. https://doi.org/10.1016/j.rser.2017.05.067

Power, C.S., 2010. Technology Roadmap Concentrating Solar Power 5, 1–52. https://doi.org/10.1787/9789264088139-en

Pramanik, S., Ravikrishna, R. V., 2017. A review of concentrated solar power hybrid technologies. Appl. Therm. Eng. 127, 602–637. https://doi.org/10.1016/j.applthermaleng.2017.08.038

Praveen, B., Suresh, S., 2018. Experimental study on heat transfer performance of neopentyl glycol/CuO composite solid-solid PCM in TES based heat sink. Eng. Sci. Technol. an Int. J. 21, 1086–1094. https://doi.org/10.1016/j.jestch.2018.07.010

Praveen, B., Suresh, S., Pethurajan, V., 2019. Heat transfer performance of graphene nano-platelets laden micro-encapsulated PCM with polymer shell for thermal energy storage based heat sink. Appl. Therm. Eng. 156, 237–249. https://doi.org/10.1016/j.applthermaleng.2019.04.072

Prieto, C., Cabeza, L.F., 2019. Thermal energy storage (TES) with phase change materials (PCM) in solar power plants (CSP). Concept and plant performance. Appl. Energy 254, 113646. https://doi.org/10.1016/j.apenergy.2019.113646

Qureshi, Z.A., Ali, H.M., Khushnood, S., 2018. Recent advances on thermal conductivity enhancement of phase change materials for energy storage system: A review. Int. J. Heat Mass Transf. 127, 838–856. https://doi.org/10.1016/j.ijheatmasstransfer.2018.08.049

Rabha, D.K., Muthukumar, P., 2017. Performance studies on a forced convection solar dryer integrated with a paraffin wax–based latent heat storage system. Sol. Energy 149, 214–226. https://doi.org/10.1016/j.solener.2017.04.012

Rabienataj Darzi, A.A., Jourabian, M., Farhadi, M., 2016. Melting and solidification of PCM enhanced by radial conductive fins and nanoparticles in cylindrical annulus. Energy Convers. Manag. 118, 253–263. https://doi.org/10.1016/j.enconman.2016.04.016

Rady, M., 2009. Thermal performance of packed bed thermal energy storage units using multiple granular phase change composites. Appl. Energy 86, 2704–2720. https://doi.org/10.1016/j.apenergy.2009.04.027

Rathod, M.K., Banerjee, J., 2013. Thermal stability of phase change materials used in latent heat energy storage systems: A review. Renew. Sustain. Energy Rev. 18, 246–258. https://doi.org/10.1016/j.rser.2012.10.022

Raul, A.K., Bhavsar, P., Saha, S.K., 2018. Experimental study on discharging performance of vertical multitube shell and tube latent heat thermal energy storage. J. Energy Storage 20, 279–288. https://doi.org/10.1016/j.est.2018.09.022

Reddy, K.S., Mudgal, V., Mallick, T.K., 2018. Review of latent heat thermal energy storage for improved material stability and effective load management. J. Energy Storage 15, 205–227. https://doi.org/10.1016/j.est.2017.11.005

Rehman, T. ur, Ali, H.M., Janjua, M.M., Sajjad, U., Yan, W.M., 2019. A critical review on heat transfer augmentation of phase change materials embedded with porous materials/foams. Int. J. Heat Mass Transf. 135, 649–673. https://doi.org/10.1016/j.ijheatmasstransfer.2019.02.001

REN21, 2020. Renewables 2020 Global Status Report, REN21 Secretariat.

REN21, 2019. Conference Renewables 2019 Global Status Report.

Renewable, I., Agency, E., 2013. Thermal Energy Storage Technology Brief E17.

Riahi, S., Saman, W.Y., Bruno, F., Belusko, M., Tay, N.H.S., 2018. Performance comparison of latent heat storage systems comprising plate fins with different shell and tube configurations. Appl. Energy 212, 1095–1106. https://doi.org/10.1016/j.apenergy.2017.12.109

Rozenfeld, A., Kozak, Y., Rozenfeld, T., Ziskind, G., 2017. Experimental demonstration, modeling and analysis of a novel latent-heat thermal energy storage unit with a helical fin. Int. J. Heat Mass Transf. 110, 692–709. https://doi.org/10.1016/j.ijheatmasstransfer.2017.03.020

Rubitherm, 2017. Remarks on subcooling, hysteresis and other properties of the SP products 1–2.

Sari, A., Karaipekli, A., 2007. Thermal conductivity and latent heat thermal energy storage characteristics of paraffin/expanded graphite composite as phase change material. Appl. Therm. Eng. 27, 1271–1277. https://doi.org/10.1016/j.applthermaleng.2006.11.004

Sciacovelli, A., Gagliardi, F., Verda, V., 2015. Maximization of performance of a PCM latent heat storage system with innovative fins. Appl. Energy 137, 707–715. https://doi.org/10.1016/j.apenergy.2014.07.015

Seddegh, S., Wang, X., Henderson, A.D., 2015a. Numerical investigation of heat transfer mechanism in a vertical shell and tube latent heat energy storage system. Appl. Therm. Eng. 87, 698–706. https://doi.org/10.1016/j.applthermaleng.2015.05.067

Seddegh, S., Wang, X., Henderson, A.D., Xing, Z., 2015b. Solar domestic hot water systems using latent heat energy storage medium: A review. Renew. Sustain. Energy Rev. 49, 517–533. https://doi.org/10.1016/j.rser.2015.04.147

Sefidan, A.M., Sojoudi, A., Saha, S.C., Cholette, M., 2017. Multi-layer PCM solidification in a finned triplex tube considering natural convection. Appl. Therm. Eng. 123, 901–916. https://doi.org/10.1016/j.applthermaleng.2017.05.156

Shahsavar, A., Goodarzi, A., Mohammed, H.I., Shirneshan, A., Talebizadehsardari, P., 2020. Thermal performance evaluation of non-uniform fin array in a finned double-pipe latent heat storage system. Energy 193, 116800. https://doi.org/10.1016/j.energy.2019.116800

Shamsundar, N., Sparrow, E.M., 1975. Analysis of Multidimensional Conduction Phase Change Via the Enthalpy Model. J. Heat Transfer 97, 333. https://doi.org/10.1115/1.3450375

Shao, J., Darkwa, J., Kokogiannakis, G., 2015. Review of phase change emulsions (PCMEs) and their applications in HVAC systems. Energy Build. 94, 200–217. https://doi.org/10.1016/j.enbuild.2015.03.003

Sharma, A., Tyagi, V. V., Chen, C.R., Buddhi, D., 2009. Review on thermal energy storage with phase change materials and applications. Renew. Sustain. Energy Rev. 13, 318–345.

https://doi.org/10.1016/j.rser.2007.10.005

Shen, G., Wang, X., Chan, A., 2019. Experimental investigation of heat transfer characteristics in a vertical multi-tube latent heat thermal energy storage system. Energy Procedia 160, 332–339. https://doi.org/10.1016/j.egypro.2019.02.165

Singh, H., Saini, R.P., Saini, J.S., 2010. A review on packed bed solar energy storage systems. Renew. Sustain. Energy Rev. 14, 1059–1069. https://doi.org/10.1016/j.rser.2009.10.022

Singh, S.K., Verma, S.K., 2020. Numerical investigation of thermal storage unit using multiple phase changing materials. Mater. Today Proc. https://doi.org/10.1016/j.matpr.2020.02.299

Sodhi, G.S., Botting, C., Lau, E., 2020. Hybrid heat sinks for thermal management of passively cooled battery chargers 1–17. https://doi.org/10.1002/er.6260

Sodhi, G.S., Jaiswal, A.K., Vigneshwaran, K., Muthukumar, P., 2019a. Investigation of charging and discharging characteristics of a horizontal conical shell and tube latent thermal energy storage device. Energy Convers. Manag. 188, 381–397. https://doi.org/10.1016/j.enconman.2019.03.022

Sodhi, G.S., Vigneshwaran, K., Kumar Jaiswal, A., Muthukumar, P., Jaiswal, A.K., Muthukumar, P., 2019b. Assessment of Heat Transfer Characteristics of a Latent Heat Thermal Energy Storage System: Multi Tube Design. Energy Procedia 158, 22–25. https://doi.org/10.1016/j.egypro.2019.01.737

Solar PACES, https://www.solarpaces.org/

Solomon, G.R., Velraj, R., 2013. Analysis of the heat transfer mechanisms during energy storage in a Phase Change Material filled vertical finned cylindrical unit for free cooling application. Energy Convers. Manag. 75, 466–473. https://doi.org/10.1016/j.enconman.2013.06.044

Sparrow, E.M., Larson, E.D., Ramsey, J.W., 1981. Freezing on a finned tube for either conduction-controlled or natural-convection-controlled heat transfer. Int. J. Heat Mass Transf. 24, 273–284. https://doi.org/10.1016/0017-9310(81)90035-1

Sparrow, E.M., Ramsey, J.W., Kemink, R.G., 1979. Freezing Controlled by Natural Convection. J. Heat Transfer 101, 578–584. https://doi.org/10.1115/1.3451040

Steinmann, W.D., Eck, M., 2006. Buffer storage for direct steam generation. Sol. Energy 80, 1277–1282. https://doi.org/10.1016/j.solener.2005.05.013

Stephanie Weckend, Andreas Wade, Garvin Heath, 2016. End of Life Management Solar PV Panels.

Su, W., Darkwa, J., Kokogiannakis, G., 2015. Review of solid-liquid phase change materials and their encapsulation technologies. Renew. Sustain. Energy Rev. 48, 373–391. https://doi.org/10.1016/j.rser.2015.04.044

Sumathi, S., Ashok Kumar, L., Surekha, P., 2015. Solar PV and Wind Energy Conversion Systems, Green Energy and Technology. https://doi.org/10.1007/978-3-319-14941-7

Sunku Prasad, J., Muthukumar, P., Anandalakshmi, R., Niyas, H., 2018. Comparative study of phase change phenomenon in high temperature cascade latent heat energy storage system using conduction and conduction-convection models. Sol. Energy 176, 627–637.

https://doi.org/10.1016/j.solener.2018.10.048

Sunku Prasad, J., Muthukumar, P., Desai, F., Basu, D.N., Rahman, M.M., 2019. A critical review of high-temperature reversible thermochemical energy storage systems. Appl. Energy 254, 113733. https://doi.org/10.1016/j.apenergy.2019.113733

Tao, Y.B., Lin, C.H., He, Y.L., 2015. Preparation and thermal properties characterization of carbonate salt/carbon nanomaterial composite phase change material. Energy Convers. Manag. 97, 103–110. https://doi.org/10.1016/j.enconman.2015.03.051

Tao, Y.B., Liu, Y.K., He, Y.L., 2019. Effect of carbon nanomaterial on latent heat storage performance of carbonate salts in horizontal concentric tube 185, 994–1004. https://doi.org/10.1016/j.energy.2019.07.106

Trahana, J., Grazianib, A., Goswami, D.Y., Stefanakosa, E., Jotshia, C., Goelc, N., 2014. Evaluation of pressure drop and particle sphericity for an air-rock bed thermal energy storage system. Energy Procedia 57, 633–642. https://doi.org/10.1016/j.egypro.2014.10.218

Trieb, F., 2009. Global Potential of Concentrating Solar Power. Conf. Proc. 1–11.

Umair, M.M., Zhang, Y., Iqbal, K., Zhang, S., Tang, B., 2019. Novel strategies and supporting materials applied to shape-stabilize organic phase change materials for thermal energy storage–A review. Appl. Energy 235, 846–873. https://doi.org/10.1016/j.apenergy.2018.11.017

Veerappan, M., Kalaiselvam, S., Iniyan, S., Goic, R., 2009. Phase change characteristic study of spherical PCMs in solar energy storage. Sol. Energy 83, 1245–1252. https://doi.org/10.1016/j.solener.2009.02.006

Velraj, R., Seeniraj, R.V., Hafner, B., Faber, C., Schwarzer, K., 1999. Heat Transfer Enhancement in a Latent Heat Storage System. Sol. Energy 65, 171–180. https://doi.org/10.1016/S0038-092X(98)00128-5

Vignarooban, K., Xu, X., Arvay, A., Hsu, K., Kannan, A.M., 2015. Heat transfer fluids for concentrating solar power systems – A review. Appl. Energy 146, 383–396. https://doi.org/10.1016/J.APENERGY.2015.01.125

Vigneshwaran, K., Sodhi, G.S., Muthukumar, P., Guha, A., Senthilmurugan, S., 2019a. Experimental and numerical investigations on high temperature cast steel based sensible heat storage system. Appl. Energy 251, 113322. https://doi.org/10.1016/j.apenergy.2019.113322

Vigneshwaran, K., Sodhi, G.S., Muthukumar, P., Subbiah, S., 2019b. Concrete based high temperature thermal energy storage system: Experimental and numerical studies. Energy Convers. Manag. 198, 111905. https://doi.org/10.1016/j.enconman.2019.111905

Wang, C., Lin, T., Li, N., Zheng, H., 2016. Heat transfer enhancement of phase change composite material: Copper foam/paraffin. Renew. Energy 96, 960–965. https://doi.org/10.1016/j.renene.2016.04.039

Wang, P., Wang, X., Huang, Y., Li, C., Peng, Z., Ding, Y., 2015. Thermal energy charging behaviour of a heat exchange device with a zigzag plate configuration containing multi-phase-change-materials (m-PCMs). Appl. Energy 142, 328–336. https://doi.org/10.1016/j.apenergy.2014.12.050

Wang, X., Yu, H., Li, L., Zhao, M., 2016. Experimental assessment on a kind of composite wall incorporated with shape-stabilized phase change materials (SSPCMs) 128, 567–574. https://doi.org/10.1016/j.enbuild.2016.07.031

Wang, Y., Wang, L., Xie, N., Lin, X., Chen, H., 2016. Experimental study on the melting and solidification behavior of erythritol in a vertical shell-and-tube latent heat thermal storage unit. Int. J. Heat Mass Transf. 99, 770–781. https://doi.org/10.1016/j.ijheatmasstransfer.2016.03.125

Warming Stripes for GLOBE from 1850-2019, https://showyourstripes.info/

Watanabe, T., Kanzawa, A., 1995. Second law optimization of a latent heat storage system with PCMS having different melting points. Heat Recover. Syst. CHP 15, 641–653. https://doi.org/10.1016/0890-4332(95)90044-6

Wei, L.L., Ohsasa, K., 2010. Supercooling and solidification behavior of phase change material. ISIJ Int. 50, 1265–1269. https://doi.org/10.2355/isijinternational.50.1265

Whittingham, M.S., 2012. History, evolution, and future status of energy storage. Proc. IEEE 100, 1518–1534. https://doi.org/10.1109/JPROC.2012.2190170

Wickramaratne, C., Dhau, J.S., Kamal, R., Myers, P., Goswami, D.Y., Stefanakos, E., 2018. Macro-encapsulation and characterization of chloride based inorganic Phase change materials for high temperature thermal energy storage systems. Appl. Energy 221, 587–596. https://doi.org/10.1016/j.apenergy.2018.03.146

Wickramaratne, C., Moloney, F., Pirasaci, T., Kamal, R., Goswami, D.., Stefanakos, E., Dhau, J., 2016. Experimental study on thermal storage performance of cylindrically encapsulated PCM in a cylindrical storage tank with axial flow. Proc. ASME 2016 Power Conf. collocated with ASME 2016 10th Int. Conf. Energy Sustain. ASME 2016 14th Int. Conf. Fuel Cell Sci. Eng. Technol. ASME 2016 Power Conf. 11–14.

Wu, L., Zhang, X., Liu, X., 2020. Numerical analysis and improvement of the thermal performance in a latent heat thermal energy storage device with spiderweb-like fins. J. Energy Storage 32, 101768. https://doi.org/10.1016/j.est.2020.101768

Xia, L., Zhang, P., Wang, R.Z., 2010. Preparation and thermal characterization of expanded graphite/paraffin composite phase change material. Carbon N. Y. 48, 2538–2548. https://doi.org/10.1016/j.carbon.2010.03.030

Xie, N., Huang, Z., Luo, Z., Gao, X., Fang, Y., Zhang, Z., 2017. Inorganic Salt Hydrate for Thermal Energy Storage. Appl. Sci. 7, 1317. https://doi.org/10.3390/app7121317

Xiong, T., Zheng, L., Shah, K.W., 2020. Nano-enhanced phase change materials (NePCMs): A review of numerical simulations. Appl. Therm. Eng. 178, 115492. https://doi.org/10.1016/j.applthermaleng.2020.115492

Xu, B., Li, P., Chan, C., 2015. Application of phase change materials for thermal energy storage in concentrated solar thermal power plants: A review to recent developments. Appl. Energy 160, 286–307. https://doi.org/10.1016/j.apenergy.2015.09.016

Yagci, O.K., Avci, M., Aydin, O., 2019. Melting and solidification of PCM in a tube-in-shell unit: Effect of fin edge lengths' ratio. J. Energy Storage 24, 100802. https://doi.org/10.1016/j.est.2019.100802

Yan, J., Yang, X., 2019. Thermal energy storage. Appl. Energy A1–A6.

https://doi.org/10.1016/j.apenergy.2018.03.001

Yang, H., He, Y., 2010. Solving heat transfer problems with phase change via smoothed effective heat capacity and element-free Galerkin methods. Int. Commun. Heat Mass Transf. 37, 385–392. https://doi.org/10.1016/j.icheatmasstransfer.2009.12.002

Yang, J., Zhao, C.Y., Hutchins, D., 2012. Modelling the effect of binary phase composition on inward solidification of a particle. Int. J. Heat Mass Transf. 55, 6766–6774. https://doi.org/10.1016/j.ijheatmasstransfer.2012.06.084

Yang, L., Zhang, X., Xu, G., 2014. Thermal performance of a solar storage packed bed using spherical capsules filled with PCM having different melting points. Energy Build. 68, 639–646. https://doi.org/10.1016/j.enbuild.2013.09.045

Yang, L., Zhang, X.S., 2012. Performance of a new packed bed using stratified phase change capsules. Int. J. Low-Carbon Technol. 7, 208–214. https://doi.org/10.1093/ijlct/cts027

Yinping, Z., Yi, J., 1999. A simple method, the T-history method, of determining the heat of fusion, specific heat and thermal conductivity of phase-change materials. Meas. Sci. Technol. 10, 201–205. https://doi.org/10.1088/0957-0233/10/3/015

Yusuf Yazici, M., Avci, M., Aydin, O., Akgun, M., 2014. Effect of eccentricity on melting behavior of paraffin in a horizontal tube-in-shell storage unit: An experimental study. Sol. Energy 101, 291–298. https://doi.org/10.1016/j.solener.2014.01.007

Zalba, B., Marı́n, J.M., Cabeza, L.F., Mehling, H., 2003. Review on thermal energy storage with phase change: materials, heat transfer analysis and applications, Applied Thermal Engineering. https://doi.org/10.1016/S1359-4311(02)00192-8

Zanganeh, G., Pedretti, A., Zavattoni, S., Barbato, M., Steinfeld, A., 2012. Packed-bed thermal storage for concentrated solar power - Pilot-scale demonstration and industrial-scale design. Sol. Energy 86, 3084–3098. https://doi.org/10.1016/j.solener.2012.07.019

Zauner, C., Hengstberger, F., Mörzinger, B., Hofmann, R., Walter, H., 2017. Experimental characterization and simulation of a hybrid sensible-latent heat storage. Appl. Energy 189, 506–519. https://doi.org/10.1016/j.apenergy.2016.12.079

Zavattoni, S.A., Zanganeh, G., Pedretti, A., Barbato, M.C., 2018. Numerical analysis of the packed bed TES system integrated into the first parabolic trough CSP pilot-plant using air as heat transfer fluid 090027. https://doi.org/https://doi.org/10.1063/1.5067121

Zhang, C., Li, J., Chen, Y., 2020. Improving the energy discharging performance of a latent heat storage (LHS) unit using fractal-tree-shaped fins. Appl. Energy 259, 114102. https://doi.org/10.1016/j.apenergy.2019.114102

Zhang, H.L., Baeyens, J., Degrève, J., Cacères, G., 2013. Concentrated solar power plants: Review and design methodology. Renew. Sustain. Energy Rev. 22, 466–481. https://doi.org/10.1016/j.rser.2013.01.032

Zhang, Y., Du, K., He, J.P., Yang, L., Li, Y.J., 2014. Impact factors analysis of the enthalpy method and the effective heat capacity method on the transient nonlinear heat transfer in phase change materials (pcms). Numer. Heat Transf. Part A Appl. 65, 66–83. https://doi.org/10.1080/10407782.2013.811153

Zhang, Y.W., Faghri, a, 1996. Heat transfer enhancement in latent heat thermal energy storage system by using the internally finned tube. Int. J. Heat Mass Transf. 39, 3165–3173.

https://doi.org/10.1016/0017-9310(95)00402-5

Zhang, Z., Cheng, J., He, X., 2017. Numerical simulation of flow and heat transfer in composite PCM on the basis of two different models of open-cell metal foam skeletons. Int. J. Heat Mass Transf. 112, 959–971. https://doi.org/10.1016/j.ijheatmasstransfer.2017.05.012

Zhao, C.Y., Zhang, G.H., 2011. Review on microencapsulated phase change materials (MEPCMs): Fabrication, characterization and applications. Renew. Sustain. Energy Rev. 15, 3813–3832. https://doi.org/10.1016/j.rser.2011.07.019

Zheng, Y., Wang, Z., 2019. Study on the heat transfer characteristics of a shell-and-tube phase change energy storage heat exchanger. Energy Procedia 158, 4402–4409. https://doi.org/10.1016/j.egypro.2019.01.777

Zhou, D., Zhao, C.Y., Tian, Y., 2012. Review on thermal energy storage with phase change materials (PCMs) in building applications. Appl. Energy 92, 593–605. https://doi.org/10.1016/j.apenergy.2011.08.025

Zipf, V., Neuhäuser, A., Willert, D., Nitz, P., Gschwander, S., Platzer, W., 2013. High temperature latent heat storage with a screw heat exchanger: Design of prototype. Appl. Energy 109, 462–469. https://doi.org/10.1016/j.apenergy.2012.11.044

Zou, B., Dong, J., Yao, Y., Jiang, Y., 2017. A detailed study on the optical performance of parabolic trough solar collectors with Monte Carlo Ray Tracing method based on theoretical analysis. Sol. Energy 147, 189–201. https://doi.org/10.1016/j.solener.2017.01.055

Appendix A

Components of the experimental system

The technical specifications of the important components of the experimental test facility are described below;

- To maintain the supply of the heat transfer fluid throughout the system, a centrifugal blower of capacity 120 m^3/h was employed. The blower was powered by a 3-phase motor of capacity 2 hp driven by a variable frequency drive. The flow directions and quantity were regulated using butterfly and spherical ball valves.
- To record the temperature variations in the LHS modules and in the storage system, calibrated K-type thermocouples with an accuracy of ±0.5 ºC were fitted. The data was recorded and processed using a Data Acquisition System of make Keysight, Agilent 34970A.
- To monitor the velocity of air, a pitot tube based differential pressure meter of make Testo, 512 was used.
- The capacity of air heater used for heating the HTF was 48 kW comprising of 48 elements of 1 kW each. A temperature controller of make Selec was connected to the heater to maintain the air supply at the required temperature conditions.
- The system was wrapped in a 102 mm thick ceramic wool thermal insulation blanket having thermal conductivity 0.12 W m^{-1} K^{-1}.
- The differential scanning calorimetry (DSC) analysis of the phase change material (PCM) samples was conducted using two different DSC Analyzer equipment namely: (i) Perkin Elmer and (ii) NETZSCH.

Appendix B

Error Analysis

The uncertainties while calculating different quantities such as mass flow rate, energy charged/discharged occur due to accuracy of various instruments that are used to measure different quantities such as velocity, temperature and weight of the PCM. In the present analysis, the accuracy of pitot tube velocity meter and K-type thermocouples used for temperature measurement are ±0.1 m/s and ±0.5 °C, respectively. The uncertainties are calculated using the Kline and McClintock Method (Moffat, 1988) described as follows.

The calculated quantity R which depends upon independent measured quantities X_1, X_2, X_3……X_n can be expressed as a function of the measured quantities as given in Eq. B.1.

$$R = R\,(X_1, X_2, X_3 \ldots\ldots\ldots . X_n) \tag{B.1}$$

The total uncertainty of the calculated quantity R is given by Eq. B.2.

$$\Delta R = \sqrt{\left(\frac{\partial R}{\partial X_1}\Delta X_1\right)^2 + \left(\frac{\partial R}{\partial X_2}\Delta X_2\right)^2 + \cdots + \left(\frac{\partial R}{\partial X_n}\Delta X_n\right)^2} \tag{B.2}$$

where $\Delta X_1, \Delta X_2, \Delta X_3 \ldots\ldots \Delta X_n$ are the errors in the measured quantities.

The sample calculation for calculating the error in the melt fraction of the PCM, energy stored, energy discharged and mass flow rate using the Kline and McClintock Method are shown below.

(i) ***Melt Fraction***

The melt fraction is a non-dimensional quantity and is represented as percentage of PCM melted or solidified as given by Eq. (B.3).

$$\delta = \frac{T - T_S}{T_L - T_S} = \frac{T - T_S}{2 \times \Delta T_M} \tag{B.3}$$

According to the Kline and McClintock Method,

$$\Delta\delta = \sqrt{\left(\frac{\partial\delta}{\partial T}\Delta T\right)^2 + \left(\frac{\partial\delta}{\partial T_S}\Delta T_S\right)^2 + \left(\frac{\partial\delta}{\partial \Delta T_M}\Delta(\Delta T_M)\right)^2}$$

$$= \sqrt{(0.03846 \times 0.5)^2 + (-0.03846 \times 0.5)^2 + (-0.03846 \times 1)^2}$$

$$= \pm 0.047$$

where,

$\frac{\partial\delta}{\partial T} = \frac{1}{2\times\Delta T_M} = 0.03846$, $\frac{\partial\delta}{\partial T_S} = \frac{-1}{2\times\Delta T_M} = -0.03846$, $\frac{\partial\delta}{\partial\Delta T_M} = \frac{-(T-T_S)}{2\times(\Delta T_M{}^2)} = -0.03846$

(ii) Energy stored and discharged by the LHS module

The energy stored and discharged by the LHS module are given by Eqs. (B.4-B.5).

$$Q_{ch} = m_{pcm}(c(T_f - T_i) + (\delta)\Delta h_f) = m_{pcm}(c\Delta T_{ch} + (\delta)\Delta h_f) \quad \text{(B.4)}$$

$$Q_{dch} = m_{pcm}(c(T_i - T_f) + (1-\delta)\Delta h_f) = m_{pcm}(c\Delta T_{dch} + (1-\delta)\Delta h_f) \quad \text{(B.5)}$$

The uncertainty in the mass of the PCM is assumed as 1%. The uncertainty in the calculation of the energy stored and discharged are calculated as below.

$$\Delta Q_{ch} = \sqrt{\left(\frac{\partial Q_{ch}}{\partial m_{pcm}}\Delta m_{pcm}\right)^2 + \left(\frac{\partial Q_{ch}}{\partial \Delta T_{ch}}\Delta(\Delta T_{ch})\right)^2 + \left(\frac{\partial Q_{ch}}{\partial \delta}\Delta(\delta)\right)^2}$$

$$= \sqrt{(315.9 \times 0.01)^2 + (97.6 \times 0.5)^2 + (10681.1 \times 0.047)^2} = \pm 504.4\ kJ$$

$$= \pm 0.5044\ MJ$$

$$\Delta Q_{dch} = \sqrt{\left(\frac{\partial Q_{dch}}{\partial m_{pcm}}\Delta m_{pcm}\right)^2 + \left(\frac{\partial Q_{dch}}{\partial \Delta T_{dch}}\Delta(\Delta T_{dch})\right)^2 + \left(\frac{\partial Q_{dch}}{\partial \delta}\Delta(\delta)\right)^2}$$

$$= \sqrt{(341.5 \times 0.01)^2 + (97.6 \times 0.5)^2 + (10681.1 \times 0.047)^2} = \pm 504.3\ kJ$$

$$= \pm 0.5043\ MJ$$

where,

$$\frac{\partial Q_{ch}}{\partial m_{pcm}} = c\Delta T_{ch} + \Delta h_f \delta = 315.9$$

$$\frac{\partial Q_{dch}}{\partial m_{pcm}} = c\Delta T_{dch} + \Delta h_f \delta = 341.5$$

$$\frac{\partial Q_{ch}}{\partial \Delta T_{ch}} = \frac{\partial Q_{dch}}{\partial \Delta T_{dch}} = m_{pcm} c = 97.6$$

$$\frac{\partial Q_{ch}}{\partial \delta} = \frac{\partial Q_{dch}}{\partial \delta} = m_{pcm} \Delta h_f = 10681.1$$

(iii) Mass flow rate

The mass flow rate of the HTF (air) is given by Eq. (B.6).

$$\dot{m} = \rho A v \tag{B.6}$$

The error in calculating the mass flow rate is calculated as below.

$$\Delta \dot{m} = \sqrt{\left(\frac{\partial \dot{m}}{\partial \rho}\Delta \rho\right)^2 + \left(\frac{\partial \dot{m}}{\partial A}\Delta A\right)^2 + \left(\frac{\partial \dot{m}}{\partial v}\Delta v\right)^2}$$

Here ρ and A are constant quantities such that $\Delta\rho = 0$ and $\Delta A = 0$.

$$\Delta \dot{m} = \rho A \Delta v$$

$$= 1.225 \times 8.10732 \times 10^{-3} \times 0.1 = \pm 0.0596\ kg/min$$

Therefore, the uncertainties associated with the calculation of melt fraction, energy charged, energy discharged and mass flow rate of air are ±0.047, ±0.5044 MJ, ±0.5043 MJ and ±0.0596 kg/min, respectively.

Appendix C

Derivation of energy discharged in different units

In order to compare the discharging performance of sodium nitrate ($NaNO_3$) with commonly used sensible heat storage mediums such as concrete and cast steel, the energy discharged by the storage module is formulated in terms of different units for a material-level or system-level comparison. The energy discharged in different units is given by Eqs. (C.1-C.4) below.

Thermal energy discharged by the TES medium ($Q_{discharged}$)

$$(\boldsymbol{in\ MJ}) = \left(\left(m\ [kg] \times c\ \left[\frac{J}{kg\ K}\right] \times (T_f - T_i)[K]\right) + \left(m\ [kg] \times \Delta h \left[\frac{J}{kg}\right]\right)\right) \times \frac{1}{10^6} \tag{C.1}$$

$$(\boldsymbol{in\ kWh}) = \left(\left(m\ [kg] \times c\ \left[\frac{J}{kg\ K}\right] \times (T_f - T_i)[K]\right) + \left(m\ [kg] \times \Delta h \left[\frac{J}{kg}\right]\right)\right) \times \frac{1}{3600 \times 1000} \tag{C.2}$$

$$\left(\boldsymbol{in}\,\frac{\boldsymbol{kWh}}{\boldsymbol{kgK}}\right) = \left(c + \frac{\Delta h}{(T_f - T_i)}\right)\left[\frac{J}{kg\ K}\right] \times \frac{1}{3600 \times 1000} \tag{C.3}$$

$$\left(\boldsymbol{in}\,\frac{\boldsymbol{kWh}}{\boldsymbol{m^3K}}\right) = \rho\left[\frac{kg}{m^3}\right]\left(c + \frac{\Delta h}{(T_f - T_i)}\right)\left[\frac{J}{kg\ K}\right] \times \frac{1}{3600 \times 1000} \tag{C.4}$$

Appendix D

Convergence criteria and numerical procedure

- Software tool: The finite element based software COMSOL Multiphysics 4.3a ("COMSOL Inc.,") has been employed to perform the numerical analysis.
- Solver used: The parallel direct linear solver (PARDISO) was the most common solver employed during the simulation work.
- Discretization and time-stepping: For the time-stepping, the Euler Backward difference formula (BDF) is employed. An adaptive time-step is adopted as an inherent feature of COMSOL Multiphysics 4.3a and the time-step varies based on the error values at previous iterations. The initial minimum and maximum time steps chosen are 0.001 s and 0.1 s, respectively. The chosen maximum time step helps to solve the problem in minimum computational time.
- Convergence criteria: Considering the high non-linearity of the phase-change problem, the convergence criterion is set as 10^{-3}.
- Workstation/Machine configuration: The simulations were performed using a Dell precision T7610 workstation, equipped with two Intel Xeon E5-2650 v2 processors and 64 GB 1866 MHz RAM.

List of publications

The significant outcomes from the present thesis work have been published/ communicated to many renowned international journals and presented in several reputed Int conferences. The list of all the publications are provided below.

Journals

1. **Sodhi GS**, P. Muthukumar. Experimental and numerical investigations on the charging and discharging performances of high-temperature cylindrical phase change material encapsulations. **Solar Energy**. 2021;224:411-424.
2. **Sodhi GS,** Muthukumar P. Compound charging and discharging enhancement in multi-PCM system using non-uniform fin distribution. **Renewable Energy**. 2021;171:299-314.
3. **Sodhi GS**, Botting C, Lau E, Palanisamy M, Rouhani M, Bahrami M. Hybrid heat sinks for thermal management of passively cooled battery chargers. **International Journal of Energy Research**. 2021;45:6333–6349.
4. **Sodhi GS**, Jaiswal AK, Vigneshwaran K, Muthukumar P. Investigation of charging and discharging characteristics of a horizontal conical shell and tube latent thermal energy storage device. **Energy Conversion and Management**. 2019 May 15;188:381-97.
5. **Sodhi GS**, Vigneshwaran. K, Muthukumar. P. Assessment of Heat Transfer Characteristics of a Latent Heat Thermal Energy Storage System: Multi Tube Design. **Energy Procedia** (2019) 158, 4677-4683.
6. Vigneshwaran K, **Sodhi GS**, Guha A, Muthukumar P, Subbiah S. Coupling strategy of multi-module high temperature solid sensible heat storage system for large scale application. **Applied Energy**. 2020 Nov 15;278:115665.
7. Vigneshwaran K, **Sodhi GS**, Muthukumar P, Guha A, Senthilmurugan S. Experimental and numerical investigations on high temperature cast steel based sensible heat storage system. **Applied Energy**. 2019 Oct 1;251:113322.
8. Vigneshwaran K, **Sodhi GS**, Muthukumar P, Subbiah S. Concrete based high temperature thermal energy storage system: Experimental and numerical studies. **Energy Conversion and Management**. 2019 Oct 15;198:111905.
9. Vigneshwaran. K, **Sodhi GS**, Muthukumar. P, V. K. Arvind, G. Balamurugan, S. Sriram, S. Senthilmurugan (2018). Experimental investigation of a Cast-Steel based Thermal Energy Storage System. **Energy Procedia (2019) 158,** 4664-4670.

Submitted and under review

1. **Sodhi GS**, K. Vigneshwaran, P. Muthukumar. Experimental investigations of high-temperature shell and multi-tube latent heat storage system (Submitted to **Applied Thermal Engineering**, Feb 2021).
2. **Sodhi GS**, Kumar Vishnu, P. Muthukumar. Design Assessment of a Horizontal Shell and Tube Latent Heat Storage System: Alternative to Fin Designs (Submitted to **Journal of Energy Storage**, April 2021).

Book Chapters

1. **Gurpreet Singh Sodhi**, K. Vigneshwaran, Vishnu Kumar, P. Muthukumar. Effect of Longitudinal Fin Configuration on the Charging and Discharging Characteristics of a Horizontal Cylindrical Latent Heat Storage System (Springer Book Series: Advances in Sustainability Science and Technology).
2. Vishnu Kumar, **Gurpreet Singh Sodhi**, Tat Suraj Arun and P Muthukumar. Numerical Investigation of a multi-tube conical shell and tube based Latent Heat Energy Storage system (Springer Book Series: Advances in Sustainability Science and Technology).

Conferences

1. **Gurpreet Singh Sodhi**, Tat Suraj Arun, Umapathi N, and Muthukumar Palanisamy. 2021. "Performance Investigations of the Energy Discharge Characteristics of High-temperature Phase Change Material Capsules." International ISHMT-ASTFE Heat and Mass Transfer Conference. Madras: IHMTC **(Accepted)**.
2. N, Umapathi, **Gurpreet Singh Sodhi**, Tat Suraj Arun, and Muthukumar Palanisamy. 2021. "Numerical Study on Optimization of the Discharging Characteristics of Three-PCM Cascaded Latent Heat Storage System with Non-uniform Fin Distribution." International ISHMT-ASTFE Heat and Mass Transfer Conference. Madras: IHMTC **(Accepted)**.
3. Arun, Tat Suraj, **Gurpreet Singh Sodhi**, Umapathi N, and Palanisamy Muthukumar. 2021. "Numerical Investigation of a Multi tube Combined Latent and Sensible Heat Thermal Storage System." International ISHMT-ASTFE Heat and Mass Transfer Conference. Madras: IHMTC **(Accepted)**.
4. **Sodhi GS**, K. Vigneshwaran, Vishnu Kumar, P. Muthukumar. Effect of Longitudinal Fin Configuration on the Charging and Discharging Characteristics of a Horizontal Cylindrical Latent Heat Storage System. First National Conference on Innovations in Sustainable Energy and Technology 2020 (Virtual), RGIPT Bangalore, 3rd December 2020
5. **Sodhi GS**, Vigneshwaran. K, P. Muthukumar. Thermal modeling and investigation of multi-tube latent heat storage system. Research Conclave' 19, Indian Institute of Technology.
6. **Sodhi GS**, Muthukumar P (2018). Effect of eccentricity on the charging of a multi-tube Latent Heat Storage System. Presented at 5th International Conference on Computational Methods for Thermal Problems. IISc Bangalore - 9-11 July, 2018.
7. **Sodhi GS**, Vigneshwaran. K, Muthukumar. P (2018). Assessment of Heat Transfer Characteristics of a Latent Heat Thermal Energy Storage System: Multi Tube Design. Presented at 10th International Conference on Applied Energy (ICAE2018), 22-25 August 2018, Hong Kong, China.
8. Vishnu Kumar, **Sodhi GS**, Tat Suraj Arun and P Muthukumar. Numerical Investigation of a multi-tube conical shell and tube based Latent Heat Energy Storage system. First National Conference on Innovations in Sustainable Energy and Technology 2020 (Virtual), RGIPT Bangalore, 3rd December 2020.
9. Vigneshwaran. K, **Sodhi GS**, P. Muthukumar, S. Senthilmurugan. Performance Study of Cast-Steel Based Medium Temperature Thermal Energy Storage System: Experiment.

Research Conclave' 19, Indian Institute of Technology Guwahati, Guwahati, 14-17 March, 2019.

10. Vigneshwaran K, **Sodhi GS**, Muthukumar P, Guha A, Senthilmurugan S. Experimental study and dynamic thermal modeling of solid sensible heat storage system. Proceedings of 11th international conference on Applied energy, Sweden, 2019.
11. Vigneshwaran K, **Sodhi GS**, Muthukumar P, Senthilmurugan S, Concrete based sensible heat storage system: Experimental investigations, 5th International Conference on Polygeneration (ICP2019) 15-17th May 2019, Japan.
12. Vigneshwaran. K, **Sodhi GS**, Muthukumar. P, V. K. Arvind, G. Balamurugan, S. Sriram, S. Senthilmurugan (2018). Experimental investigation of a Cast-Steel based Thermal Energy Storage System. Presented at 10th International Conference on Applied Energy (ICAE2018), 22-25 August 2018, Hong Kong, China.